Electromagnetic Modeling of Integrated Optical Wave Controlled Microstrip Discontinuities

Essam Shouhdy Tony Keddis

A thesis
presented to the University of Waterloo
in fulfillment of the
thesis requirement for the degree of
Doctor of Philosophy
in
Electrical Engineering

Waterloo, Ontario, Canada, 1998

©Essam Shouhdy Tony Keddis 1998

National Library of Canada
Acquisitions and Bibliographic Services
395 Wellington Street
Ottawa ON K1A 0N4
Canada

Bibliothèque nationale du Canada
Acquisitions et services bibliographiques
395, rue Wellington
Ottawa ON K1A 0N4
Canada

Your file Votre référence

Our file Notre référence

The author has granted a non-exclusive licence allowing the National Library of Canada to reproduce, loan, distribute or sell copies of this thesis in microform, paper or electronic formats.

L'auteur a accordé une licence non exclusive permettant à la Bibliothèque nationale du Canada de reproduire, prêter, distribuer ou vendre des copies de cette thèse sous la forme de microfiche/film, de reproduction sur papier ou sur format électronique.

The author retains ownership of the copyright in this thesis. Neither the thesis nor substantial extracts from it may be printed or otherwise reproduced without the author's permission.

L'auteur conserve la propriété du droit d'auteur qui protège cette thèse. Ni la thèse ni des extraits substantiels de celle-ci ne doivent être imprimés ou autrement reproduits sans son autorisation.

0-612-38273-7

Canada

The University of Waterloo requires the signatures of all persons using or photocopying this thesis. Please sign below, and give address and date.

Abstract

The technological maturity in the area of microwaves, and the rapid advances of optics, coupled with the added advantage of the larger bandwidths of microwave systems compared to those of electronic circuits, has lead to the emergence of new fast-growing areas of research. The area of optical control of microwave devices and signals is one of these areas. This class of devices is potentially capable of performing the high-speed/high-frequency functions demanded by the new communication systems applications.

This thesis envisions a future generation of optically controlled microwave structures that uses guided optical wave excitation in an integrated optical-microwave environment. The building block of these future devices is an optically-controlled microwave switch which is essentially a microstrip transmission line with a series gap. The optical signal is brought into the gap region using an optical waveguiding system buried in the semiconductor substrate of the microwave transmission line. Photo-generated carriers in the gap region produce a change in the transmission characteristics of the microstrip line.

One of the contributions of this Ph.D. work is the study and development of a systematic knowledge base for the technology of guided wave optical control of microwave devices. The introduction of guided optical waves as a replacement of bulk optics creates an integrated version of these devices and enhances the fabrication yield. This also leads to the improvement in the overall performance of the device or system that is being optically controlled. More complex devices and systems and complicated control mechanism could be implemented using guided wave optics. Examples of the proposed complex devices are presented.

The bulk of this thesis is dedicated to developing an accurate model of the microwave component of the switch. To model the propagation characteristics and the microwave discontinuity, an analysis that utilizes spatial Green's functions formulations is developed. This analysis is capable of modeling continuous and discontinuous shielded microstrip multi-conductor transmission lines with lossy multi-layer substrates. The formulation utilizes the concepts of the Green's function in the space domain and the principle of

scattering superposition to obtain the propagation characteristics. The analysis is kept broad enough to allow for multi-layered substrates in which one or more of the layers are lossy.

The Green's functions of the enclosing shielding structure along with the boundary condition imposed by the transmission line metalization yield a complex function representing the dispersion equation for the transmission line. This equation is solved using Muller Method to yield the unknown complex propagation constant, the characteristic impedance and the EM field patterns for the microwave signals propagated on the continuous microstrip transmission line. Samples of the results obtained using this method are presented.

Using the Method of Moments (MOM) coupled with the Electric Field Integral equation (EFIE), another formulation is developed to analyze the discontinuities in the transmission line. The MOM along with the EFIE, yield the current distribution on a transmission line with a certain discontinuity for a given excitation of the system. Using a curve fitting and optimization routine, the essential design and performance parameters are extracted from the current distribution and are used to compute the scattering ([S]) matrix and Impedance ([Z]) matrix of the structure. This analysis is kept general enough to allow for studying a variety of discontinuities and microstrip topologies.

The above analyses are developed into computer codes, and are used to conduct accurate modeling of a series gap discontinuity in the microstrip line. This series gap is a model of the microwave switch. The gap transmission behavior is studied for varied substrate conductivity, gap separations, and frequency ranges. The substrate conductivity represents the effect of photo-excitation generated by the optical control element.

Using the developed accurate model, the current approach of modeling optically controlled microwave switches using equivalent circuit models based on quasi-TEM assumptions is assessed and compared to the more accurate Green's function formulation. The domain of validity of these simplified models is defined.

The optical component of the proposed devices is also studied. The optical power

distribution within the microstrip gap region is accurately modeled using a Vector Beam Propagation Method (VBPM) and a Vector Finite Difference Time Domain (VFDTD) numerical simulators. Means to most effectively use the available optical power are studied. The optical guiding system proposed is an optical directional coupler. An iterative exact solution for the fields and effective index of the propagating optical power within the structure is presented and utilized in computing the input optical excitation field profile for the noted numerical simulators. The algorithm presented is particularly suited for modeling highly lossy optical waveguides, such as those utilized in the proposed structure.

Abstrait

La supériorité technologique des micro-ondes au-dessus du systeme optique d'une part, et les avances rapides du systeme optique d' autre part, couplées à l'avantage ajouté des largeurs de bande plus grandes des systèmes de micro-onde comparés à ceux des circuits électroniques, a pour mener à l'apparition de nouveaux domaines de recherche à croissance rapide. Le domaine de la commande optique des dispositifs et des signaux de micro-onde est un de ces zones. Cette classe des dispositifs est potentiellement capable d'exécuter les fonctions de haute fréquence/grande vitesse exigées par les nouvelles applications de systèmes de transmission.

Cette thèse envisage une future génération des structures à commande optique de micro-onde qui utilise l'excitation optique guidée de vague dans un environnement intégré d'optique-micro-onde. Le module de ces futurs dispositifs est un commutateur à commande optique à micro-ondes qui est essentiellement une ligne de transmission de microruban avec une série lacune. Le signal optique dedans introduit dans la région d'intervalle en utilisant un système waveguiding optique enterré dans le substrat de semi-conducteur de la ligne de transmission de micro-onde. les porteurs Photo-produits dans la région d'intervalle produisent un changement des caractéristiques de transmission de la ligne de microruban.

Un des contributions de ce travail de Ph.D. est l'étude et le développement d'une base de connaissance systématique pour la technologie de la commande optique guidée de vague des dispositifs à micro-ondes. L'introduction des vagues optiques guidées comme remplacement de systeme optique en bloc crée une version intégrée de ces dispositifs et met en valeur le rendement de fabrication. Ceci mène également à l'amélioration de l'exécution globale du dispositif ou du système qui sont à commande optique. Des dispositifs et des systèmes plus complexes et le mécanisme compliqué de commande ont pu être mis en application en utilisant le systeme optique guidé de vague. Des exemples des dispositifs complexes proposés sont présentés.

La majeure partie de cette thèse est consacrée à développer un modèle précis du

composant de micro-onde du commutateur. Pour modeler et les caractéristiques de propagation la discontinuité de micro-onde, une analyse qui utilise des formulations de Green spatiales de fonctions est développée. Cette analyse est capable de modeler les lignes protégées continues et discontinues de transmission de multi-conducteur de microruban avec les substrats multicouche de lossy. La formulation utilise les concepts dans de la fonction de Green le domaine de l'espace et le principe de disperser la superposition pour obtenir les caractéristiques de propagation. L'analyse est maintenue assez large pour tenir compte des substrats multicouche en lesquels un ou plusieurs des couches est lossy.

Les fonctions de Green de la structure d' armature entourante avec l'état de borne ont imposé par le rendement de metalization de ligne de transmission une fonction complexe représentant l'équation de dispersion pour la ligne de transmission. Cette équation est résolue en utilisant la méthode de muller pour rapporter la constante de propagation complexe inconnue, l'impédance caractéristique et les configurations de zone de fin de support pour les signaux de micro-onde propagés sur la transmission continue de microruban rayent. Des échantillons des résultats obtenus en utilisant cette méthode sont présentés.

En utilisant la méthode de moments (MOM) couplés à l'équation intégrale de champ électrique (EFIE), une autre formulation est développée pour analyser les discontinuités dans la ligne de transmission. Les MOM avec l'EFIE, rapportent la distribution courante sur une ligne de transmission avec une certaine discontinuité pour une excitation donnée du système. En utilisant un sous-programme d'ajustement et d'optimisation de courbe, la conception et les paramètres d'exécution essentiels sont extraits à partir de la distribution courante et sont employés pour calculer la matrice de dispersion ([S]) et la matrice d'impédance ([Z]) de la structure. Cette analyse est assez général gardé à tenir compte d'étudier une variété de discontinuités et de topologies de microruban.

Les analyses ci-dessus sont développées en codes machine, et sont employées pour conduire modeler précis d'une discontinuité d'intervalle de série dans la ligne de microruban. Cet intervalle de série est un modèle du commutateur à micro-ondes. Le comportement de transmission d'intervalle est étudié pour la conductivité de substrat, les séparations

d'intervalle, et les intervalles de fréquence divers. La conductivité de substrat représente l'effet de l'photo-excitation produit par l'élément optique de commande.

En utilisant le modèle précis développé, l'approche courante de modeler les commutateurs à commande optique à micro-ondes utilisant des modèles de circuit équivalent fondés sur des hypothèses de quasi-TEM est évaluée et comparée à la formulation de Green plus précise de fonction. Le domaine de la validité de ces modèles simplifiés est défini. On l'établit que les modèles quasistatiques sont seulement valides à de basses fréquences, et pour l'injection optique très élevée nivelle. Ces deux conditions s'assurent qu'un intervalle optiquement lumineux aura une résistivité qui est beaucoup plus petite que les capacités d' accompagnement de shunt. Pour les niveaux optiques pratiques d'excitation à des fréquences plus élevées, les effets de ces capacités deviennent significatifs, et modeler lié à la fréquence plus précis devient nécessaire.

sant optique des dispositifs proposés est également étudié et modelé. La distribution d'énergie optique dans la région d'intervalle de microruban est exactement modelée. Des moyens d'utiliser le plus pertinemment la puissance optique disponible sont étudiés. Le système optique de guidage proposé est un coupleur directionnel optique. Une solution exacte itérative pour les zones et l'incrément pertinent de la puissance optique de propagation dans la structure est présentée et utilisée dans l'étude. La simulation du système optique proposé en utilisant la méthode de propagation de faisceau (BPM) et le domaine de temps fini de différence (FDTD) sont conduites.

Acknowledgments

It was fun being a graduate student for the past few years. Now that I am working in the real world, I truly long for the freedom that comes with being a graduate student. For me, These will be the good old days when you can declare any sunny day as a national holiday. Waterloo is a nice little city to live in, and the University of Waterloo is a great university to study in, and I have enjoyed both.

This work was completed with the assistance and support of many others. Of those, I would like to acknowledge the assistance, guidance, and encouragement of my MASc and PhD research supervisor, Prof. Sujeet Chaudhuri. I will remain truly indebted for him for affording me an opportunity to do my graduate studies, and to come to this great country, Canada.

I would like to thank the members of my PhD Oral Defense and Comprehensive Exam Committees for taking the time to evaluate and provide insight into this research. Those are Prof. K. C. Gupta of the University of Colorado at Boulder, Colorado, USA, Prof. R. H. MacPhie, Prof. W. P. Huang, Prof. S. Safavi-Neini, Prof. A. E. Dixon and Prof. Y. L. Chow, along with Prof. S. K. Chaudhuri, all of the University of Waterloo. Prof. R. H. MacPhie devoted a lot of time to reviewing this manuscript suggesting editorial changes that has made it a well written thesis, and I thank him for his dedication.

Thanks to all who taught me a course here and they were many.

I would like to thank Prof. A. Vannelli, the current department chair, and the past associate chair for graduate studies, for lots of support and encouragement on numerous occasions. I appreciate the way he handles his job with zeal and dedication. Thanks also for Prof. James A. Barby who stopped by on the day of my PhD oral defense to wish me luck. Many thanks to Prof. Magdy M. A. Salama.

The staff of the E&CE Department are well deserving the thanks for lots of support. I would like to thank Wendy Boles for taking care of a lot of paper work on my behalf since I left here for Nortel. Thanks also to Karen Tergovac, who used to work here, as well as

Monica Ruppert, Gini Ivan-Roth, and Donna J. O'Brecht, the administrative secretary. Wendy was the first person I met when I first came to Waterloo on January 9th, 1992, and Donna was the last person I saw when I handed her the keys on October 26, 1998.

I would like to acknowledge the financial support I received from several sources throughout the duration of my graduate studies. Those were the ITRC research assistantship, the Ontario Graduate Scholarship (OGS), as well as several Faculty of Engineering (FOE) scholarships, the University Graduate scholarships, and many Teaching Assistantships.

I would like to acknowledge the moral support I received from the members of my family; my Mom and Dad, and my sisters Nevene and Irene, and especially Nevene who joined me for the most part of my PhD journey. I also realize that by getting this PhD degree I have made a dream by my late Grandma come true. May she rest in peace, for she has laboured a lot for me.

I was fortunate to be surrounded by a host of friends who appreciated my friendship, and together we shared lots of happy times I will always vividly remember: Akram Ibrahim, Amgad Bassili, Dr. Emad Farag, Medhat Roshdi, Micheal Youssef, Dr. Moheb Fam, Dr. Rafik Guindi, Rafik Refaat, and Dr. Serag GadelRab.

Vivien, like a morning star, so loving and caring, indeed full of life, who has brought all the happiness into my life. I would like to thank you, my lovely wife, for chosing to share your life with me. How could I ever be so lucky to meet you. Of all the great gifts that God has given me, you are the greatest. Thank you.

Finally, and above all, all thanks are unto the LORD who assigns to us more than we ask or understand.

Thou shalt guide me with thy counsel, and afterward receive me to glory

(Pslam 73:34).

This work is
dedicated To
Vivien and To
My Child who
is on his Way

Contents

List of Figures

List of Tables

List of Symbols

Symbol	Meaning
α	Absorption coefficient
β	Phase constant of transmission line
γ	Reduction factor in conductance due shaded semiconductor zones
δ	The microwave skin depth
ϵ_o	Free space permittivity
$\epsilon_r{}'$	Real part of the dielectric constant
$\epsilon_r{}''$	Imaginary part of the dielectric constant
η	The quantum efficiency
η_{lens}	The focusing lens efficiency
λ, λ_{opt}	Optical wavelength
λ_m, λ_g	The microwave signal's wavelength
μ	Permeability of free space
μ_e	Electron mobility in bulk
μ_h	Hole mobility in bulk
$\mu_n{}'$	The surface mobility of electrons
$\mu_p{}'$	The surface mobility of holes
ν	Optical Wavelength
ρ	Resistivity
ω	Angular frequency
ω_{mic}	Microwave angular frequency

σ The conductivity of a semiconductor

σ_c capture cross-section

τ_c Carrier decay time in a semiconductor (capture time)

τ_e Energy relaxation rise time

τ_m Momentum relaxation rise time

Γ_{in} Voltage reflection coefficient for the input port

$\Delta\sigma$ The change in conductivity due to illumination

Δt The optical pulse duration

$\vec{\Pi}_e$ The electric Hertz vector,$\vec{\Pi}_e = \hat{x}\psi_e$

$\vec{\Pi}_h$ The magnetic Hertz vector,$\vec{\Pi}_h = \hat{x}\psi_h$

$\vec{E}$ Electric field

a Waveguide and cavity dimension in the $x-$ direction

b Waveguide and cavity dimension in the $y-$ direction

c Waveguide and cavity dimension in the $z-$ direction

e The electron charge

f Microwave frequency

f_t Amplifier current-gain cutoff frequency

h Planck's Constant

h_x Basis function wavenumber for expansion in the x direction

h_z Basis function wavenumber for expansion in the z direction

k_i The wave number for the i-th layer of the substrate

$k_x{}^i$ The eigen value in the x direction for the i-th layer of the substrate

k_o	Free space propagation constant
l_y	Subsection length in the y direction
l_z	Subsection length in the z-direction
n_i	Imaginary part of the refractive index of a material
n_r	Real part of the refractive index of a material
n, h	Electron and hole carrier densities
p	Discrete summation index in the y-direction for field points
p'	Discrete summation index in the y-direction for source points
q	Discrete summation index in the z-direction for field points
q'	Discrete summation index in the z-direction for source points
$\tan\delta$	Loss tangent
$< v_{th} >$	Mean thermal carrier velocity
z_{in}^{even}	Normalized input impedance for even excitation
z_{in}^{odd}	Normalized input impedance for odd excitation
$x_{i,i+1}$	Planar interface of the two dielectric layers i and $i+1$ of the multi-layered substrate
y_p	Discrete coordinate along the y-axis for a field point
$y_{p'}$	Discrete coordinate along the y-axis for a source point
z_q	Discrete coordinate along the z-axis for a field point
$z_{q'}$	Discrete coordinate along the z-axis for a source point

C_a	Shunt Capacitance between a transmission line and the ground plane
C_b	Capacitance of a series gap in a transmission line
$\mathcal{D}$	Displacement vector
$\mathbf{E}$	The electric field
$\mathcal{E}_g$	Band-gap energy
$\mathcal{E}_{ph}$	Photon energy
$G(\vec{r}, r')$	Electric Green's function
$G_b(t)$	Time-dependent conductance representing an optically excited series gap
$\vec{H}$	Magnetic field
I_z^-	Reflected current in the z direction due to a discontinuity
I_z^+	Incident current in the z direction into a discontinuity
$\mathbf{J}$	The current density
$\vec{J}_s(r')$	Surface current
$\vec{J}_c$	Conduction current
KT	Thermal energy with K being Boltzman's Constant
K_z	Propagation constant of an ideal transmission line current
F_{ph}	Photon Flux
M	Highest index in the summation over m for waveguide and cavity modes
N	Highest index in the summation over n for cavity modes
N_t	Trap density
P	Subsectioning index maximum = $\frac{b}{l_y}$
P_{abs}	Optical absorbed power in the gap
Q	Subsectioning index maximum = $\frac{c}{l_z}$
Q_v	The photon flux density in vacuum

R	Optical Reflectance at an interface
S_{11}	Scattering parameter in the scattering matrix representation of a two port network
S_{12}	Scattering parameter in the scattering matrix representation of a two port network
U	The unitary matrix
V_g	The voltage across the gap
Z_{11}	Impedance parameter in the impedance representation of a two port network
Z_{12}	Impedance parameter in the impedance representation of a two port network
Z_{in}	Input impedance
Z_o, Z_c	Transmission line Characteristic impedance

Chapter 1

Introduction

1.1 Introduction and Motivation

With the emergence of optical fibers in early 1970s as means of communication links, the field of guided wave optics as well as the related fields such as semiconductor lasers and optoelectronic and optical devices have advanced at a considerable pace. The future of the area of optical guided waves envisions an all-optical communication network. To achieve this goal, it is recognized that the area of guided-wave optics is facing, mainly, two challenges:

1. Technology limitations: The Processing and fabrication technology of all-optical devices has not yet matured enough to provide the viable and reliable devices that are being envisioned in the research literature. It is being observed that the current technology cannot provide the complicated structures envisioned and satisfy the tight tolerances required.

2. Speed limitations of electronic control elements: In general, most optical devices are controlled electronically. Advanced electronic circuits have traditionally played a crucial role in the practical realization and commercialization of optical communication systems. In the 1980's, rapid advances in high speed IC technologies and design tech-

niques marched in phase with the requirements and the corresponding advances on the optical side leading to an impressive rate of increase in optical channel capacity. In the 1990's, however, as the bandwidth capability of optical components increased beyond 10 Gbit/s, the electronics represented the bottle neck that is challenging the advancement and improvement in the area of all-optical networks. As lightwave communication systems advance towards even higher bandwidths, the integrated circuits used to provide signals to the optical sources at the transmitter end and to process the photodetected signals at the receiver end are becoming increasingly critical system components, if not impeding the overall system capabilities.

On the other hand, microwave technology has matured considerably since the 1930s, and has evolved into a well established fabrication technology ranging from microwave guides to submicron feature sized VLSI microwave and RF circuits and monolithic microwave integrated circuits (MMICs) [1]. In the past few years, tremendous strides were realized in this area fueled by the following factors [2]:

1. The availability of III-V compound semiconductors, such as $GaAs$ and InP, which have very high mobility and scatter limited velocity.

2. The ability to grow semi-insulator substrates for low-loss planar microwave circuitry.

3. Progress in epitaxial growth techniques such as Molecular Beam epitaxy (MBE), vapor phase epitaxy (VPE) and liquid phase epitaxy (LPE). These are used for the growth of ternary and quaternary compounds such as $GaAlAs$ and $InGaAsP$ to form multilayer heterostructures.

4. Availability of computer aided design software for device performance optimization.

5. Availability of test equipments for on-wafer characterization of devices.

As a result of these advances, fast devices such as discrete field effect transistors with unity current-gain cutoff frequency (f_t) greater than 125 GHz with noise figure of 1.5 dBs and a gain of 6 dBs have been realized [2].

The technological superiority of microwaves over optics on one hand, and the rapid advances of optics on the other hand, coupled with the added advantage of the larger bandwidths of microwave systems compared to those of electronic circuits, has lead to the emergence of a new fast-growing area of research which is the area of optical control of microwave devices and signals [3]. This class of devices is capable of performing the high-speed/high-frequency functions demanded by the communication systems applications. Optical control of microwaves have landed applications in a wide spectrum of old and new areas such as the rapidly emerging field of optically fed wireless communications [4] [5] as well as the more established fields of Cable television (CATV) distributions. Other applications include those in the areas of high definition television (HDTV) and interactive television (ITV)[6] as well as optically controlled phased array antennas [7] [8] and antenna remoting [9]. Further, the progress in the application of ultrafast optics to microwaves and millimeter-wave technology using picosecond photo-conductors was extended to the generation, control, and characterization of both pulsed and CW high frequency waves [3] [10].

The growing interest in optical control of microwave and millimeter-wave devices and systems over the past decade was generated partially by the availability of high speed electrooptic devices that can provide the optical control elements, and partially by the development of more sophisticated and more ambitious microwave systems which require better and faster control. With the advent of femto-second lasers, we envision such devices to work in the picosecond time domain.

As a short term goal, optical control of microwave signals lends itself as a faster and better control mechanism. Further, in the long term, there is a possibility of monolithic integration of optical devices with microwave devices and subsystems to realize microwave control functions such as switching, limiting, phase shifting, tuning of oscillators, and amplifiers gain control among others. In the future, optical control of microwave devices would lead to new applications such as light weight and low cost airborne phased array radar, which is difficult to realize with current technologies, because of various limitations.

The term "optical control of microwaves" describes such a mechanism where an incident optical signal alters the performance characteristics of a microwave device. One of the means of achieving this is through photo-conductivity. Incident optical energy is absorbed in a semiconductor material within a microwave device, thus generating electrical carriers that alters the state of the microwave device. The speed of response of the device materials to the incident optical energy is dictated by the material relaxation time, which is in the order of less than a picosecond. Further, the typical duration of the optical pulse is in the picosecond range as well. Hence, in response to such a small optical pulse, the material can switch its characteristics from an insulator to a conductor in a time frame of a picosecond or less. The term "picosecond photo-conductivity" was coined to describe such behavior. Picosecond photo-conductivity is becoming more and more the dominant means of optical control of microwave signals and systems.

1.2 Types of optically controlled devices

Optical control of microwave devices can fall into one of two categories based on the type of device being controlled:

1. Control of passive components such as microstrip lines or dielectric resonators. [3]
2. Control of active devices such as IMPATT diodes, TRAPATT diodes, MESFETs and HFETs among others [2].

The controlling optical signal may be of two types:

1. Pulsed optical signal.
2. Continuous illumination.

Within the last decade, the pulse induced optical control of microwaves and millimeter-wave components has been established as a very attractive and practical technique of

high flexibility allowing a wide scope for more device concepts. Considerable success was realized in Optoelectronic Microwave Switching (OMS) using pulsed optical signals owing to the numerous features of the pulsed light such as broad-band capability, subnanosecond optical pulse duration, simplicity of operation, and near-perfect isolation between the controlled microwave signal and the controlling optical signal [11].

Further, picosecond optical pulses have the additional advantage of enabling the generation of extremely high density plasma without damaging the material. The generation of very short microwave or millimeter wave bursts of high energy using optical pulsed signals is utilized in optoelectronic sampling devices [12].

In general, the utilization of switched optical excitation is more advantageous than continuous illumination, from the point of view of devices functionality, the practicality of the devices, and the existence of more freedom to design new devices. This thesis is concerned with suggesting novel structures for optical microwave switching, with extended applications. The novel topology is aimed at integrating the optical control element and the microwave controlled element onto the same chip. A theoretical study of the performance characteristics and an accurate model for the proposed microwave switch is conducted.

In the following section, concentration is devoted to explaining the concept of switching of microwave devices by picosecond photo-conductivity.

1.3 Microwave Switching by Picosecond Photoconductivity

Microwave switching by picosecond optical pulses utilizes the bulk conductivity produced by these optical pulses. An optical beam is incident on a segment of a planar microstrip transmission line, where a series gap is located, as shown in Figure 1.1. In the absence of the optical energy, the gap interrupts the passage of the microwave signal, hence reflecting

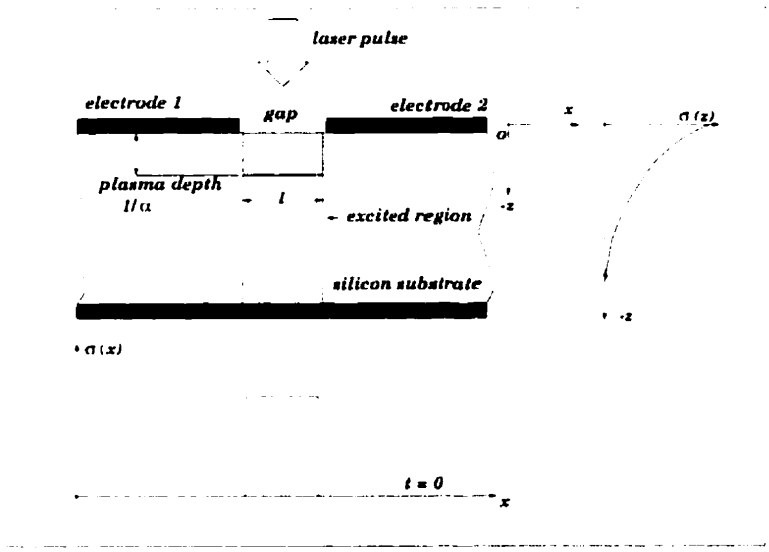

Figure 1.1: Optically controlled microstrip switch

it back. The incident optical energy is generated by an external source and is aimed at the gap region where it penetrates through the gap into a semiconductor substrate. The wavelength of the incident optical energy is chosen to match the semiconductor band gap, and hence the optical energy is absorbed and a plasma of photo-generated electrical carriers is created in place. The high density of carriers located within the series gap region alters the transmission characteristics of the microstrip line, allowing for an uninterrupted passage for the microstrip signal. This technique is used to gate and switch microwave signals propagating along the transmission line.

Further, this technique can be used in the generation of microwave and millimeter-wave pulses as short as a single cycle with an optical energy requirement of few μJoules [13].

It has been demonstrated [14] that plasma densities in excess of 10^{20} cm^{-3} can be readily generated by the absorption of single-picosecond optical pulses in semiconductors. Plasma densities as high as these convert the semiconductor region into a quasi-metallic area (i.e., the incident light converts the semiconductor into a degenerate semiconductor that acts as a conductor with quasi-metallic properties). This high conductivity makes

this technique an ideal one for high speed bulk switching.

This idea has been employed to realize some functions such as the gating of microwave signals [15], the generation of very short microwave or millimeter wave bursts [13] - [18] and optoelectronic sampling [19]- [21].

In most cases, the series gap is illuminated by a low-duty pulsed excitation. As the pulse widths of the applied laser pulses are predominantly much smaller than the excess carrier life time of the semiconductor material used, carrier diffusion and surface recombination effects may be neglected and hence the DC and RF performance of the optoelectronic microwave switch could be analyzed using a lumped-parameter approach [11] [16].

In comparison with conventional electronic switching junction devices such as Schottky diodes, step-recovery diodes or high speed transistors, the use of semiconductor microstrip switches offer a significant improvement in both speed and power handling, especially when switching high-power microwave CW signals of up to few watts [13] or pulsed DC signals of up to 1 KV [22] with high speed precision. This comes as a consequence of the absence of the junction breakdown and thermal dissipation limitations, a characteristic inherent to all junction devices. Other advantages are the simple structure of the device, its extreme broad band feature, and the inherently high isolation of the switched electrical signal and the switching laser pulse [23].

1.4 Identifying Deficiencies in The Area

The extent of the applications of the concept of optical control of microwave devices and signals suggests a considerable interest in the area. Despite that considerable interest, most of the current work utilizes microwave devices that are not specifically designed or packaged for optical control. In these devices, the injection efficiency of an optical beam into that part of the device which is most sensitive to light and actually performs the control function is low and usually unspecified. Several reasons could be given for

the low efficiency. First, air-semiconductor interface constitutes a high refractive index discontinuity, which reflects a sizable portion of the incident light. Second, not all of the coupled energy is utilized effectively, because of metalization overshadowing and other reasons that will be explained later. Hence, it becomes clear that the problem of efficient optical energy coupling and utilization needs to be addressed with considerable attention, should the full potential of optical control be realized.

Another central issue is the integration of the optical and microwave components. Most of the current devices operate by using bulk optics to couple light from a laser source that is separate from the microwave device or circuit. Thus, another area that requires investigation is the possibility of realizing integrated optically controlled microwave circuits. As will be explained in later chapters, the issues of integration and efficiency are correlated.

Another major impediment to the wider use of this technology is the cost and reliability of the components. The problems of cost and reliability can be addressed through the integration of photonic and microwave components on the same chip, hence increasing the fabrication yield.

The above three deficiencies can be categorized as technological deficiencies that need to be addressed. Further, an accurate modeling of the optical-microwave interaction is still lacking. Current modeling techniques are either quasi-static approximations or empirical and experimental in nature.

1.5 Current Contribution

It has been noted that the injection efficiency of the optical energy into the microwave device is generally low, because the air-semiconductor interface constitutes a high refractive index discontinuity and because not all the coupled energy is utilized effectively, for various reasons, as will be explained.

It has also been noted that unless an integrated version of these devices is available,

the commercialization of these devices is not an easy task. Hence, it becomes important to address these issues in any future contribution.

This thesis envisions the future generation of optically controlled microwave structures to use guided optical wave excitation. The building block of these future devices is a microwave optically-controlled switch which is essentially a microstrip transmission line with a series gap. The optical signal in brought into the gap region using an optical waveguiding system buried in the semiconductor substrate of the microwave transmission line. Photo-generated carriers in the gap region produce a change in the transmission characteristics of the microstrip line.

One of the contributions of this Ph.D. work is the study and development of a systematic knowledge base for the technology of guided wave optical control of microwave devices. The introduction of guided optical waves as a replacement of bulk optics creates an integrated version of these devices and enhances the fabrication yield. This also leads to the improvement in the overall performance of the device or system that is being optically controlled. More complex devices and systems and complicated control mechanisms could be implemented using guided wave optics. These issues are discussed in Chapter 3.

The bulk of this thesis is dedicated to developing an accurate model of the microwave switch. The analysis utilizes spatial Green's functions formulations of continuous and discontinuous shielded microstrip multi-conductor transmission lines with lossy multilayer substrates. The formulation utilizes the concepts of the Green's function in the space domain and the principle of scattering superposition to obtain the propagation constant, the characteristic impedance and the field patterns for the continuous transmission lines. The analysis is kept broad enough to allow for multi-layered substrates in which one or more of the layers are lossy.

The Green's function of the enclosing shielding structure along with the boundary condition imposed by the transmission line metalization yield a complex function representing the dispersion equation for the transmission line. This equation is solved using Muller Method to yield the unknown complex propagation constant. Samples of the

results obtained using this method are presented.

Using the Method of Moments (MOM) coupled with the Electric Field Integral Equation (EFIE), another formulation is developed to analyze the discontinuities in the transmission line. The MOM along with the EFIE, yield the current distribution on a transmission line with a certain discontinuity for a given excitation of the system. Using a curve fitting and optimization routine, the essential parameters are extracted from the current distribution and are used to compute the scattering ([S]) matrix and Impedance ([Z]) matrix of the structure. This analysis is kept general enough to allow for studying a variety of discontinuities and microstrip topologies. This analysis is presented in Chapter 4.

The above analyses are developed into computer codes, and are used to conduct accurate modeling of a series gap discontinuity in the microstrip line. This series gap is a model of the microwave switch. The gap transmission behavior is studied for varied substrate conductivity. The substrate conductivity represents the effect of photo-excited carriers generated by the optical control element. Effects of changing various parameters such as the microwave frequency, the gap length and width are studied.

Using the developed accurate model, the current approach of modeling optically controlled microwave switches using equivalent circuit models based on quasi-TEM assumptions is assessed and compared to the more accurate Green's function formulation. The domain of validity of these simplified models is identified. It is established that the quasi-static models are only valid at low frequencies, and for very high optical injection levels. These two conditions ensure that an optically illuminated gap will have a resistivity which is much smaller than the accompanying shunt capacitances. For practical optical excitation levels at higher frequencies, effects of these capacitances become significant, and the more accurate frequency-dependent modeling becomes necessary. Chapter 5 is dedicated to presenting the results of this study.

The optical component of the proposed devices is also studied and modeled. The optical power distribution within the microstrip gap region is accurately modeled. Means

to most effectively use the available optical power are studied. The optical guiding system proposed is a directional coupler. An iterative exact solution for the fields and effective index of the propagating optical power within the structure is presented and utilized in the study. Simulation of the proposed optical system using the Beam Propagation Method (BPM) and the Finite Difference Time Domain (FDTD) are conducted.

The thesis also presents a study and proposes a model for the guided optical energy conversion into electronic plasma. The plasma distribution in space and its relation to the optical field distribution leads to suggesting specific guiding characteristics and optimized optical field distribution patterns that can be more effective in achieving the control function and hence enhancing the device performance. Through guiding of optical energy, profiling of both the optical beam and the resulting plasma distribution is possible, which reduces optical losses, and reduces the optical energy requirement, among other advantages.

The thesis explores novel device concepts enabled by the integration of photonic and microwave systems. The availability of the optical energy in a guided format enables the design of complex optically controlled devices and systems.

A comparison and an assessment of the proposed guided-control technique versus existing bulk-optics devices from point of view of integrability, efficiency, capability of more complex integration and more complex structure is presented.

1.6 Organization of the Thesis

The rest of this document is organized as follows: **Chapter 2** discusses the physics behind light generated plasmas, and its application in creating picosecond conductivity for utilization in microwave switching. An overview of the various applications of optical control of microwaves, and an analytical description of optoelectronic microwave switching are also presented in this chapter.

Chapter 3 is intended to demonstrate the proposed approach of using optical guided wave control in an integrated environment with the microstrip device. Basic configurations of devices and their operation principles are discussed. The use of optical guided waves provides opportunities for the design of microwave devices with complex optical control functionality such as optoelectronic logic elements. These devices are described in Chapter 3. A comparison and an assessment of the proposed guided-control technique versus existing bulk-optics devices from point of view of integrability, efficiency, capability of more complex integration and more complex structure is also presented in this chapter. Further, an algorithm for modeling highly lossy optical guiding structures is also presented. This analysis is an iterative exact solution for the fields and effective index of the propagating optical power within the structure. This algorithm is utilized in computing accurate input excitation fields for the numerical simulators utilized in the study.

In **Chapter 4**, a detailed analysis of the microwave component of the proposed device is conducted. A theoretical analysis of a shielded lossy multi-layered-substrate microstrip transmission line is detailed for both a uniform line and for discontinuities within that line.

Overall device performance characteristics are studied in **Chapter 5**. To achieve this end, the tools developed in chapters 3 and 4 are utilized. Conclusions and suggestions for future work are presented in Chapter 6.

Chapter 2

Picosecond Photoconductivity and Optical Control of Microwaves

2.1 Introduction

In this chapter, the physics behind light generated carriers in semiconductors, and its dependence on various parameters is outlined. Different microwave switching circuits utilizing photogenerated plasmas are explained in detail. Detailed treatment of photoconductivity could be found in texts such as [24] [25] [26] [27] [28].

2.2 Photoconductivity

Optical energy can be absorbed in a semiconductor if the photon energy is greater than the band-gap energy, $\mathcal{E}_g$. The absorbed energy generates electron-hole pairs, which produce a current referred to as the photocurrent. If the photosensitive material is a $p-n$ junction, a potential difference is established across the space charge layer (depletion layer) and the incident optical energy is stored in the form of an electric potential energy. This is called the *photovoltaic* effect, which is the basic concept behind photocells and photodetectors.

When a semiconductor is illuminated, only photons with energy greater than $\mathcal{E}_g$ are absorbed. Photons with energy smaller than $\mathcal{E}_g$ are not absorbed because there is no energy states in the forbidden energy gap to accommodate an electron. For these photons, the material is transparent in the optical sense. For photons with energy greater than $\mathcal{E}_g$, an amount of energy equal to $\mathcal{E}_g$ is consumed to generate an electron-hole pair and the rest is delivered as kinetic energy for the carriers and is subsequently dissipated as heat. The wavelength of the incident light, λ, is related to the photon energy, $\mathcal{E}_{ph}$, and the optical frequency, ν, by

$$\mathcal{E}_{ph} = h\nu = h\frac{c}{\lambda}, \tag{2.1}$$

where h is Planck's constant. Using electron volts (eV) as units of energy and μm as units of length, the relationship between the photon energy and the optical wavelength is given by the following familiar formula:

$$\lambda = \frac{1.24}{\mathcal{E}_{ph}(eV)}\mu m. \tag{2.2}$$

2.2.1 Absorption coefficient

Consider a monochromatic light with $h\nu > \mathcal{E}_g$ is incident along a certain direction, say the x-axis, of a semiconductor. The number of absorbed photons, N, will be proportional to the number of incident photons, F_{ph}, and the thickness Δx of the semiconductor. Mathematically, this is expressed as,

$$N = \alpha F(x)\Delta x, \tag{2.3}$$

where α is a proportionality constant known as the absorption coefficient. Hence, from the concept of continuity of light,

$$F(x+\Delta x) - F(x) = \frac{dF(x)}{dx}\Delta x = -\alpha F(x)\Delta x, \tag{2.4}$$

and by solving for $F(x)$;

$$F(x) = F_{ph}e^{-\alpha x} \tag{2.5}$$

where the absorption coefficient, α, is a function of the photon energy, $h\nu$, and varies from one material to the other. Figure 2.1 shows the dependence of the absorption coefficient on the wavelength of the incident light, for some selected semiconductor materials. In this figure, abrupt changes in the value of α correspond to values of photon energies matching the band-gap energy of the material.

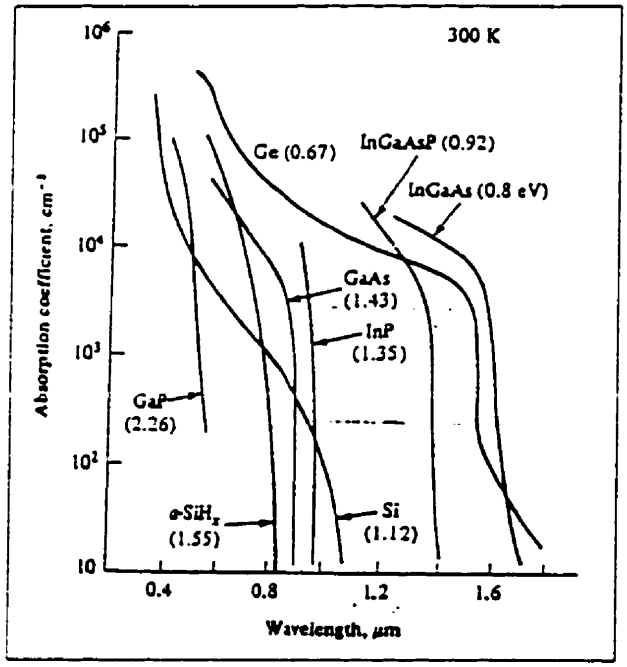

Figure 2.1: Absorption coefficients of some important optoelectronic semiconductors as a function of wavelength [28].

2.2.2 Surface Reflection

Consider the surface of the semiconductor exposed to illumination. The number of photons penetrating the surface of the semiconductor is less than that of the incident photons because of reflection at the surface. The percentage of light reflected is determined by the angle of incidence and the dielectric constant of the material. For normal incidence, the reflectance is given by

$$R = \frac{(n_r - 1)^2 + {n_i}^2}{(n_r + 1)^2 + {n_i}^2} = \frac{(n_r - 1)^2 + (\frac{\lambda\alpha}{4\pi})^2}{(n_r + 1)^2 + (\frac{\lambda\alpha}{4\pi})^2} \tag{2.6}$$

where n_i is the imaginary part of the semiconductor refractive index, also known as the extinction coefficient, $n_r = \frac{n_2}{n_1}$ where n_1 and n_2 are the real parts of the refractive indices of air and the semiconductor, respectively. It could be shown, using simple optical power propagation consideration, that n_i is given by $(\frac{\lambda\alpha}{4\pi})^2$. For Silicon, the term $\frac{\alpha\lambda}{4\pi}$ is negligible compared to n_r (for Si, $n_r \approx 3.5$). Therefore the reflected light in the case of Si is $\approx$30%. Methods to reduce reflectance include coating the absorbing surface with a matching index material whose refractive index lie between n_1 and n_2. This antireflective coating would idealy have a refractive index of $(n_1 n_2)^{1/2}$. Also using "texturized" surfaces (i.e. increasing the surface roughness) reduces the reflection from the surface.

2.3 Photoconducting Materials for Ultrafast Optoelectronics

A wide variety semiconductor materials have been deployed for the fabrication of picosecond photoconductors. Table 2.1 [29] shows a summary of the key properties of some of the most important semiconductor materials used. They are either intrinsic, impurity doped, radiation damaged, polycrystalline or amorphous semiconductors. For this table, p: denotes polycrystalline, a: denotes amorphous, and d: denotes radiation damaged.

Material	Band Gap $\mathcal{E}_g$ [eV]	Resistivity ρ [Ωcm]	Mobility μ $[cm^2/Vs]$	Decay Time τ_c [ps]
Si	1.12	$4x10^4$	1950	10^7 - 10^3
GaAs:Cr	1.43	10^6 - 10^7	2000	300
InP:Fe	1.29	$2x10^8$	2200	150 - 1000
$CdS_{0.5}Se_{0.5}$	2.0	10^7	400	$2x10^4$
GaP	2.24	10^8	240	60 - 500
Diamond	5.5	10^{13} - 10^{15}	1800	50-300
d-SOS	1.12	10^5	10 - 100	1 - 300
d-GaAs	1.43	10^7	100	5
d-InP	1.29	10^6	100 - 1000	1 - 100
d-InGaAs	0.75	1	800 - 4000	40 - 800
p-Si	1.1	10^5		2 - 5
p-Ge	0.85		3	50
p-CdTe	1.5	$3x10^7$	60	4
a-Si	1.4	$10^5 - 10^7$	10	330

Table 2.1: **Materials for picosecond photoconductors**

Detailed properties of photoconductive materials could be found in references such as [27].

2.3.1 Intrinsic speed of response of Semiconductors

The absorption of a photon by a semiconductor and the subsequent generation of an electron-hole pair is intrinsically a fast process, being limited by the uncertainty principle and the requirement that the frequency spectrum of the optical pulse falls within the absorption bands corresponding to electronic transition from bound to free states. Since

the width of these bands for semiconductors is about 1 eV [see table 2.1], this time can be as short as a femto-second, in principle. Hence, it is less than the duration of one optical cycle in the infrared range and consequently does not limit the rise time of the photocurrent.

The quantum efficiency of the light generated current is determined by the probability that an electron-hole pair will escape its mutual coulomb field. In high mobility semiconductors, this probability is essentially 100%. In low mobility materials, such as amorphous silicon, the quantum efficiency is significantly lower.

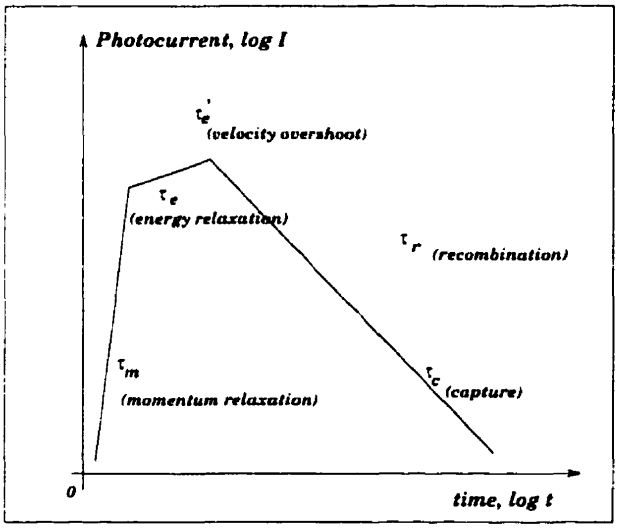

Figure 2.2: Schematic Illustration of the temporal response of a semiconductor due to an incident optical impulse. The initial rise time is limited by the elastic scattering of the free carriers. Energy relaxation then occurs and enhances or slows down the response depending on the electric field and photon energy. The decay of the photocurrent is dominated by recombination, but may be accelerated by the introduction of defects to produce rapid trapping (capture) of free carriers.

Although the onset of the current is very rapid, a number of effects can influence the subsequent evolution of the current following excitation by a very short optical pulse. Figure 2.2 shows the temporal behavior of a photocurrent generated by an optical impulse. The time scale is a logarithmic scale. The initial rise-time is limited by the elastic

scattering rate of the photogenerated free electrons and holes, also known as momentum relaxation time or material relaxation time. This is denoted on the figure by the momentum relaxation rise time, τ_m. If the incident photon energy is greater than the energy gap, which is the threshold for photoconduction, by an amount greater than the thermal energy KT, the photon-generated electron-hole pair will impart the excess energy in the form of kinetic energy. Since most scattering mechanisms are stronger at higher energies, the initial mobility of carriers will be less than the equilibrium (steady state) mobility. The transfer of this excess energy to the lattice by phonon emission produces an additional mobility transient with a rise time in the range of a picosecond to a nano second depending on several factors such as the material, the excitation density, the amount of excess energy, and the lattice temperature. This is denoted in Figure 2.2 by the energy relaxation rise time, τ_e. Further, if the bias voltage applied to the photoconductor is very large, the photo-generated carriers will be accelerated by the electric field and their transient behavior will be modified due to velocity overshoot as shown in Figure 2.2.

On longer time scales, once an equilibrium carrier distribution has been established, higher electric fields can produce a substantially lower mobility due to the saturation of the drift velocity. In Silicon, for example, the electrons and hole drift velocities saturate at approximately 10^5 m/sec for electric fields higher than 10^6 V/sec. In GaAs and other materials with *satellite* valleys in the conduction band, the steady state drift velocity reaches a maximum at fields of $3x10^5$ and decreases for higher fields, in what is known as the negative resistance property. It can lead to electric field instabilities due to the Gunn effect, and can limit the maximum DC bias that can be placed across a photoconductor.

These events that contribute to the overall rise time of the photo-generated current are relatively short in time, and are in the picosecond range. Hence, they do not pose a speed limitation on the envisioned optically controlled microwave devices. It is the decay time that pose the limitation on the switching speed of these devices. The decay of the photocurrent is dominated by recombination, which is inherently a slow phenomena, as explained in the next section. The decay time can be accelerated by the introduction of

material defects to produce rapid trapping and capture of the free carriers.

2.3.2 Recombination and Trapping

In an intrinsic semiconductor, recombination is determined by the radiative transitions. These are relatively slow, which leads to a sustained photocurrent. This is a major problem for the applications of picosecond photoconductors. Direct gap semiconductors have radiative life times that are few nanoseconds. Indirect gap materials, such as silicon, can have life times that are a few milliseconds. Clearly, alternative materials and techniques must be used to produce the fast current decays that are necessary for picosecond applications.

Carrier removal may be assisted by the presence of a large electric fields that sweep the carriers to the contact, where they recombine quickly. For a substrate like Silicon, where the saturated drift velocity is only $1.6\text{x}10^5$ m/sec at 300K, so the gap dimensions would play a role. For a 10 μ gap in silicon, it is possible to realize switching speeds in the vicinity of 100 GHz. This situation could be enhanced be considering alloys such as $Si - Ge$ and other materials like $GaAs$ where the saturation drift velocity is higher. It is important to note, however, that it will become increasingly difficult for free-space optics to illuminate an aperture of 10 μ with light of wavelengths about 1 μ. The guided wave optics control approach proposed in this thesis can be advantageous in this respect as will be explained later.

For example, in p-n junction diodes, carrier sweep out determines the speed of response, which is substantially faster that the intrinsic recombination time. On the other hand, maximum sweep-out rates are limited by the drift velocity saturation. For a path length of 1 μm and a saturation velocity of 10^5 m/sec, as that of Silicon, the sweep-out time is 10 psec. As a result, sweep-out is primarily used in semiconductor devices where extremely high speeds is not required. Also the photovoltaic behavior of p-n junctions and the need for large reverse bias make them unsuitable for some picosecond devices such as sampling gates.

An effective method of reducing the free carrier life time is to introduce a moderate density of defects into the semiconductor which act as traps and recombination centers. This can be achieved by radiation damage, impurities, or the use of materials with large densities of naturally occurring defects such as polycrystalline and amorphous semiconductors. Table 2.1 shows some examples of materials in these classes which indicates a much faster times compared to intrinsic materials.

The capture time, τ_c, can be estimated from the expression:

$$\tau_c = \frac{1}{N_t \sigma_c < v_{th} >} \tag{2.7}$$

where N_t is the trap density, σ_c is the capture cross-section, and $< v_{th} >$ is the mean thermal carrier velocity. According to the above equation, trap densities of 10^{18} to 10^{20} cm^{-3} are sufficient to produce free carrier life times of approximately one picosecond. This estimate is obtained assuming the typical capture cross-sections of 10^{-13} for GaAs and 10^{-15} cm^2 for Silicon.

2.3.3 Radiation Damage

The specific nature of the defects produced by radiation damage has been extensively studied. The type, density, and stability of the defects depend on the material, type of radiation, background impurities, and temperature.

Experiments with picosecond photoconductors have shown that extremely fast photocurrent decay times can be produced with moderate levels of radiation damage, as shown in table 2.1 [29].

Figure 2.3 shows the carrier life time of a radiation damaged silicon-on-Saphire film is plotted as a function of radiation dose [30]. This measurement used femto-second optical pulses to probe the free carrier absorption following excitation. The minimum decay rate of 0.7 ps was produced with damage levels that are close to the point of rendering the material completely amorphous.

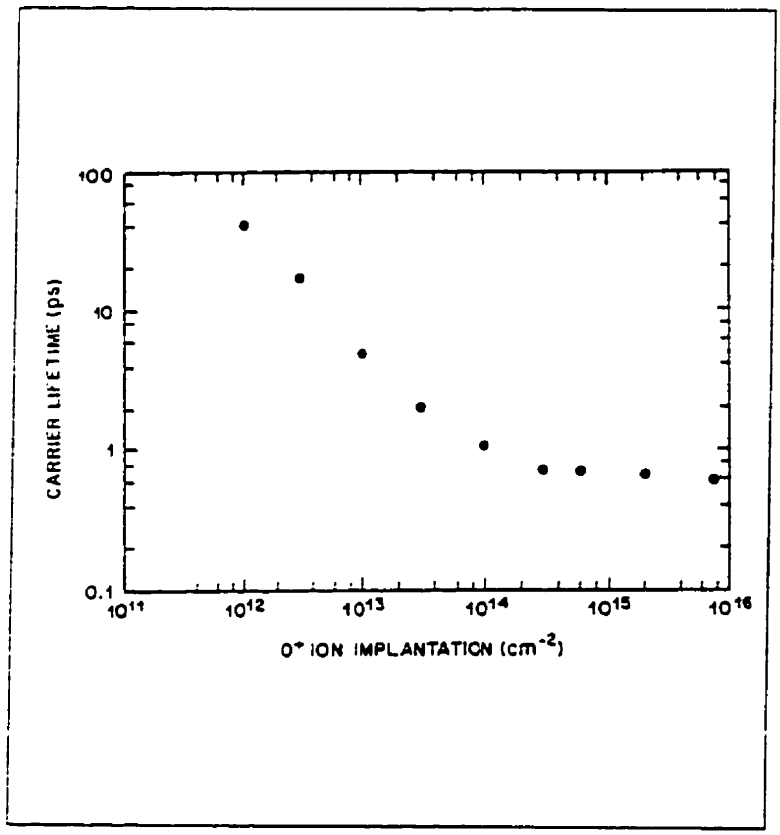

Figure 2.3: The relaxation time of optically injected carriers in radiation damaged silicon-on-Saphire, as measured by time-resolved optical reflectivity with femto-second optical pulses [28].

The introduction of moderately large densities of defects into crystalline semiconductors has a number of additional effects, some of which are advantageous and the others are not. If the defect traps lie deep within the band gap, free carriers due to dopants are removed from the transport bands moving the Fermi level close to the mid-gap and greatly increasing the resistivity. For most applications of photoconductors this is a desirable property since it reduces the dark current. Further, high defect densities enhance optical absorption in the spectral region below the edge for direct transitions due to the introduction of new states. This effect is more pronounced in indirect-gap materials such as Silicon.

Another advantage for the use of high defect density materials is the ease of fabrication of ohmic contacts. Semi-insulating materials are generally very difficult to contact with low-resistance non-rectifying contacts. A Shottky barrier usually forms at the metal semiconductor interface which produces a non-ohmic (rectifying) behavior along with an internal electrostatic field which produces a photovoltaic response in addition to the photoconductive signal. This problem of contacts become even more difficult if the injected carrier densities are higher than the background carrier density, as usually occurs in picosecond photoconductivity applications. It is important in these situations to have ohmic contacts for both types of carriers, a condition that is very hard to achieve.

2.3.4 Carrier Mobilities

The major disadvantage of the use of high defect densities is the reduction in the carrier mobilities due to increased elastic scattering from the defects. The lack of a strong temperature dependence of the mobilities suggests also that most of the defects are neutral rather than charged if relatively high doses of radiation damage are used. Estimates of the influence of elastic scattering from neutral defects have been made by Erginsoy [31].

To produce capture times of 1ps in Silicon, and using $\sigma_c = 10^{-15}\ cm^2$, the mobility, μ is about 5 $cm^2/V.sec$. For GaAs, with $\sigma_c = 10^{-13}$, μ is 350 $cm^2/V.sec$. The clear advantage

of GaAs over Si arises primarily from the larger capture cross section. This conclusion is borne out by experiments.

Although the introduction of relatively high densities of defects has a dramatic effect on the free carrier life time, it is also important that recombination paths be provided to prevent thermal emission of trapped carriers which can produce sustained photocurrent in the form of long tails for the generated pulses. If the defect density is sufficiently high, trapped carriers can tunnel between defects sites, and recombination will occur without reemission. For this reason, it is usually better to use a defect density that is higher than necessary to achieve short capture times.

In general, a particular method of introducing defects results in a variety of traps, each having different energies and capture cross sections. Some of these will be deep levels with fast capture times and slow emission rates, but others may be too slow to use for picosecond applications. It is important that different combinations of materials and methods of introducing defects be explored to optimize this approach. The use of annealing to remove shallow defects and retain deep traps is a potentially useful technique for improving the mobility without loss of speed.

Other methods of achieving fast photocurrent decay times are the use of compensating impurities such as Fe in InP, the use of polycrystalline materials such as p-Ge and amorphous semiconductors. In the later case, the mobilities are very small (1-10 $cm^2/V.sec$) and although the response time can be very fast, radiation damage appears to provide a better compromise between speed and sensitivity than the use of completely disordered (i.e. amorphous) materials.

2.4 Applications of Optical Control of Microwaves

The interest in the area of optical control of microwaves is getting more attractive because of several factors. Some of these factors are the distinct advantages of these systems in terms of performance, design and manufacturing [2], the increasing use of microwave fre-

quencies within the general communication system, and the ability to integrate microwave and optical components onto a single chip. These have stimulated considerable interest in the development of microwave-optoelectronic systems in general [3], and microwave devices controlled via photoconductivity in particular. The extent of the areas in which optical control of microwave have found potential application is a testimony of its vitality. A sample of the typical applications of the area are [2]:

1. Beam steering in Phased Arrays [7] [8]
2. Reference frequency distribution in phased arrays
3. Remoting of antennas [9]
4. Signal processing and electronic warfare
5. Missile guidance
6. Cable television
7. High definition TV (HDTV) and Interactive TV [6]
8. Cellular telephony [4] [5] [32]
9. Instrumentation [12]
10. Generation, control, and characterization of pulsed and CW high frequency waves [33] [3] [10] [13].

Some of these applications are outlined below.

2.4.1 Optically Controlled Antenna Systems

Future phased array radar systems and satellite-borne communication systems might need several thousand radiating elements to form a pencil beam for tracking and communications [2]. In addition, advanced phased array radars for aircrafts will require distributed

transmitter-receiver modules constructed from GaAs MMICs and arranged in an antenna architecture that conforms to the skin of the fuselage[2]. The beam steering in these arrays is done electronically. This can be done optically by using a fiber optic link to carry control signal to MMIC phase shifters [34] or by using optical fibers for RF distribution and phase shifting.

Both coherent techniques, such as heterodyne methods, and non-coherent techniques, such as true time delay (TTD), are in progress to realize optically controlled phased array antennas [7] [8]. A collection of papers on this topic can be found in [35] and [36].

Since the low loss and low dispersion characteristics of optical fiber makes the system much easier to implement in the optical domain, the TTD method usually uses an optical fiber distribution network. For example, Esman [9] reports experimental results of an optical control technique for implementing a true time delay function for array antennas. A microwave signal is transmitted on a wavelength-tunable optical carrier through a fiber-optic prism to photodetectors that feed each antenna element. The fiber-optic prism is a set of nominally equal-delay fibers with different net dispersion. The relative inter-element time-delay adjustment between array elements, which in turn control the beam angle, is accomplished by tuning the optical carrier wavelength. Antenna patterns for a two element array measurements clearly demonstrated beam steering and true time delay (TTD) over a two-octave bandwidth of 2-8 GHz.

Other proposals combine planar optical switching networks and different-length optical fibers. Many of these proposals rely on using polarization-dependent devices built of materials like Lithium Niobate ($LiNbO_3$) and Gallium Arsenide ($GaAs$) and polarization-maintaining fibers. To address cost and technological issues, Silicon based systems have also been proposed [8]. Fujiang reports a novel optically controlled phased array antenna system architecture in [37] where a new beam forming network (BFN) and steering technique is given. Reference [38] also reports on an optical control system for millimeter wave phased-array antennas. A high-precision detector switched monolithic GaAs time-delay network for the control of phased arrays was proposed in [39]. An optically

controlled push-pull self-oscillating mixer for phased array antennas was reported in [40]. This mixer can perform functions such as oscillation, frequency and phase locking to a reference signal, and mixing with data signal.

In radioastronomy, an optical control structure was reported in [41] that can control long baseline space interferometers. An overview of the evolution of optics in radars is presented [7].

2.4.2 Optically controlled Wireless Systems

Microwave optical systems were also extended to cellular and mobile systems, where analog optical fiber transmitters were deployed in fiber-fed wireless microcells used for antenna remoting [4]. An optical link that operates in the 2 GHz band for cellular telephone microcell was reported in [32]. The wide-band low-loss transmission capability of optical fiber systems has led to considerable interest in their use for distributing microwave signals for Wireless Communication Systems. This technology also promises a much wider dynamic range than conventional ones [42].

A recent application of optics in Wireless systems is using fiber optics to extend cellular telephone coverage to shadow zones that are obscured from the main antenna of the local cell such as bridges, tunnels and underground parking areas. Fiber optic lines connect a transmission node to an antenna covering the shadow area [43].

2.4.3 Optically controlled Microwave and Millimeter Wave Passive and Active Components

Several excellent articles that provide an overview on many of these devices are [29] [44] [45] [50] [27]. The following is a brief description of some of the main device concepts presented in the literature.

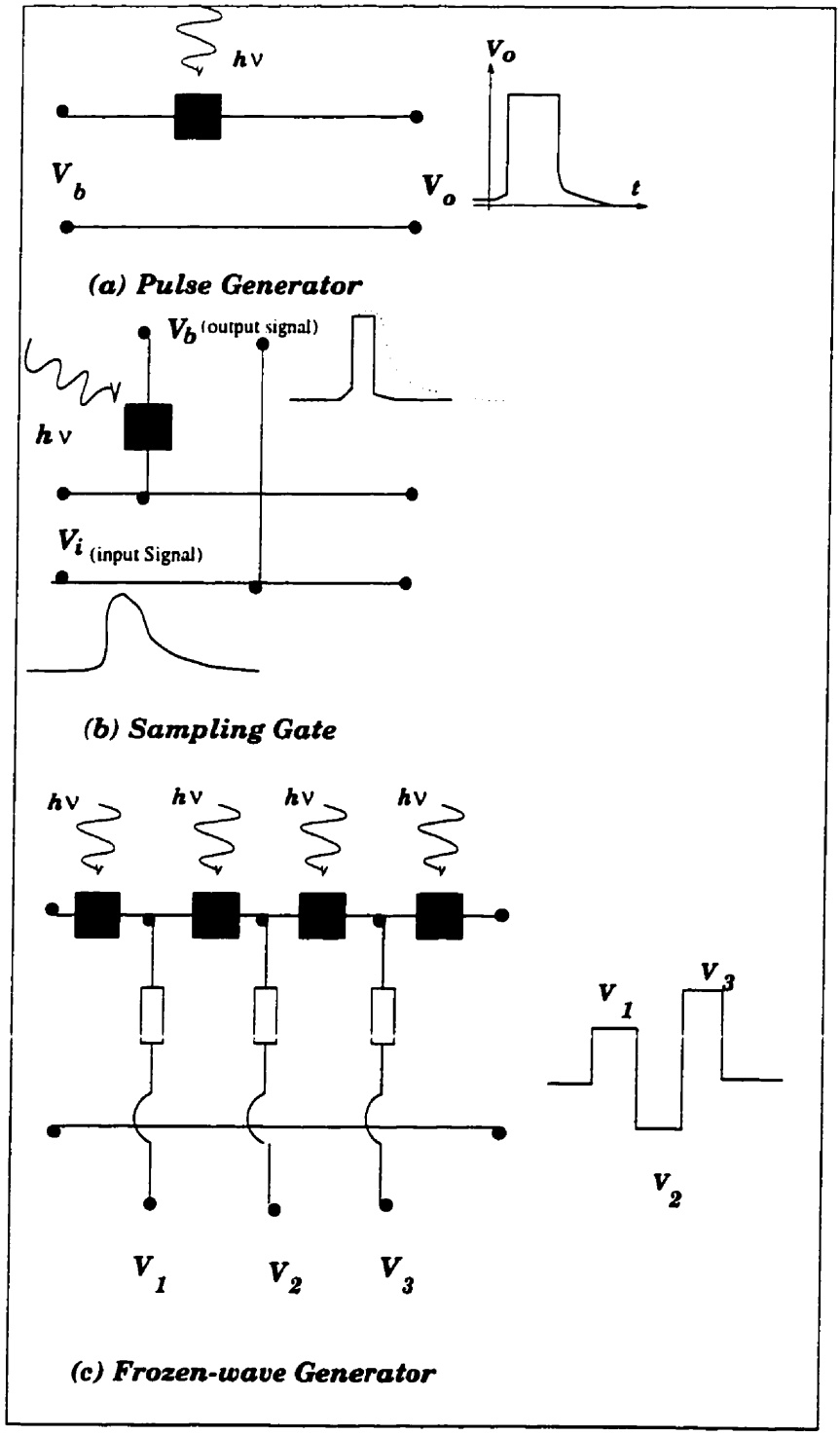

Figure 2.4: Schematic illustration of basic optoelectronic device concepts: (a) photoconducting electrical pulse generator (b) photoconducting electrical sampling gate, and (c) photoconducting frozen wave generator. In each case, an ultrashort optical pulse illuminates a photoconductor to produce a fast conducting transient in a transmission line.

Optoelectronic Pulse Generator

Consider a microstrip transmission line with a semiconductor substrate and a series gap in the top metalization [13]. With moderate optical pulse energies, it is possible to produce a photoresistance within the gap that is relatively low compared to the characteristic impedance of the transmission line. This results in a switching action which permits a fast optical pulse to initiate a high speed electrical signal at one end of the transmission line in response to a DC excitation at the other end of the line [16], [17], [18]. Figure 2.4.a shows a schematic illustration of a basic photoconducting electronic pulse generator. The amplitude and shape of the electrical pulse depends on the details of the device geometry and the materials as well as on the optical pulse [51]. With proper choice of these parameters, extremely fast electrical pulses having relatively large amplitudes can be generated. Similar other proposals can be found in [52] and [53]

Optoelectronic Sampling Gate

Figure 2.4.b illustrates a sampling gate, which is a variation of the pulse generator. In this case, the input electrical signal is a time varying waveform which is sampled by the optical signal incident on the photoconductor, by diverting a small portion of the signal to a sampling electrode. By varying the relative timing between the incoming electrical waveform and the optical pulse, the amplitude of the sampled pulse gives a replica of the desired waveform [54], [15], [19], [20], [21].

Optoelectronic Frozen-wave Generator

Another variation of the pulse generator is the use of multiple switches to form a frozen wave generator as shown in Figure 2.4.c. Simultaneous illumination of the photoconductors releases the "frozen" waveform which can have an arbitrary shape determined by the number of photoconductors and the DC bias applied to them. In this case, a long photoconductivity recombination time is required to enable each section to discharge in

tandem. A relatively high optical pulse energy is required to ensure a low resistance for each photoconductor. The amplitude and duration of each segment of the waveform can in principle be adjusted arbitrarily by changing the bias voltages and lengths of the transmission line separating each photoconductor.

Optoelectronic RF mixer

Figure 2.5.a shows an RF mixer in which the input microwave signal is a high frequency sinusoidal signal whose amplitude can be modulated by the light pulse. The optical signal has an envelope modulation at a frequency equal to the local so that the output signal at the intermediate frequency is proportional to the product of the electrical input signal and optical envelope signals.

Optoelectronic RF burst generator

Figure 2.5.b shows an RF burst generator. In this case, a resonant circuit controls the frequency of the generated waveform. The coupling of the circuit to an external transmission system causes the signal to decay rapidly resulting in short bursts of RF energy. With the use of high bias voltages and large optical pulse energies, this method can produce relatively high power RF signals.

Optoelectronic measurement antennas

When the rise time of the photocurrent is extremely short, the photoconductor can directly radiate an electromagnetic signal into free space as illustrated in Figure 2.5.c. As such, photoconductors can also be used as receiving antennas by sampling an RF pulse when illuminated by an optical pulse. The combination of optically triggered transmitting and receiving antennas antennas forms a measurement system which is phase coherent and has extremely good time resolution.

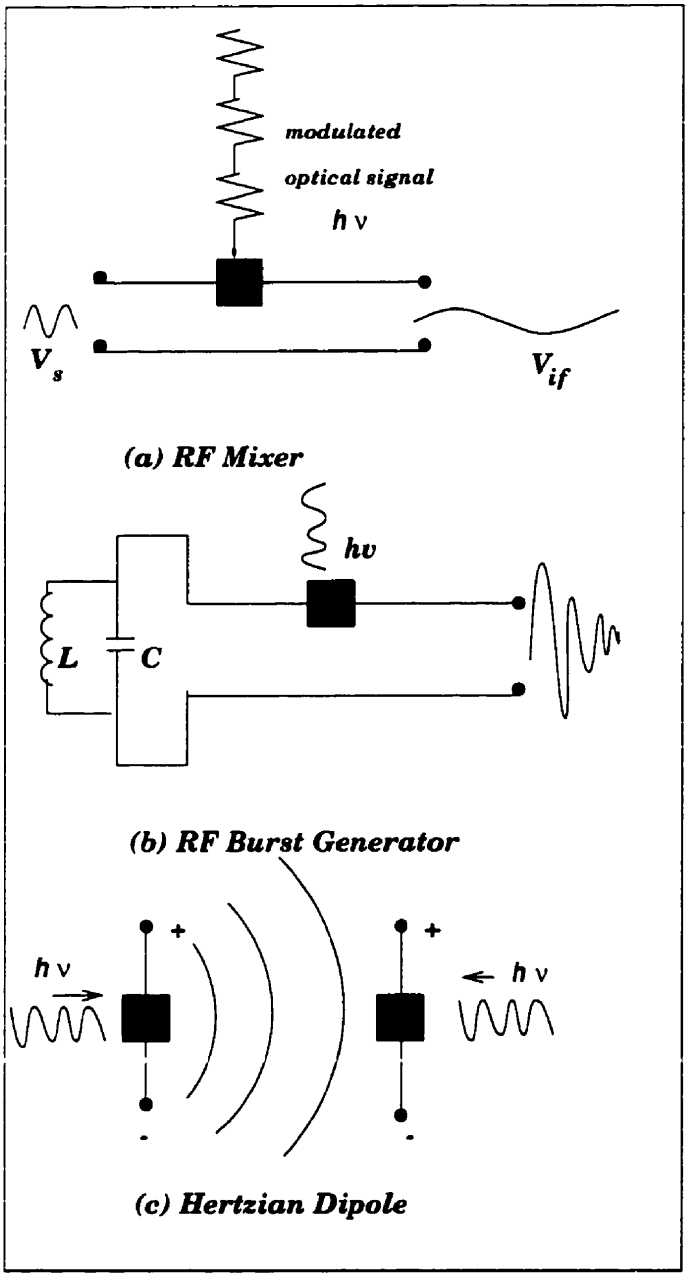

Figure 2.5: Schematic illustration of basic optoelectronic device concepts: (a) photoconducting RF frequency mixer, where a local oscillator signal is encoded in the envelope of the optical signal. Mixing with the input signal, V_s, produces an IF output. (b) photoconducting RF burst generator, which produces a damped oscillation at the frequency of the tank circuit in which the photoconductor is mounted. (c) photoconductors in which a rapid current transient radiates into free space, and is detected by the second receiving photoconducting antenna.

Optical control of other passive components

Further, in planar microwave circuits, optical illumination was used to control a short-terminated microstrip filter utilizing current distribution of the standing wave on the terminated microstrip line [55]. In a similar approach, the same author demonstrated in [56] the optical control of microstrip band elimination filter utilizing semiconductor plasma. The device utilizes an optically controlled small gap on a resonant section for the shift of the eliminated frequency range using semiconductor plasmas. An optically controlled planar attenuator was demonstrated [57].

A high-quality microwave signal is generated by heterodyning two diode-laser-pumped Nd:YAG lasers [58]. A III-V semiconductor optical waveguide containing a doping superlattice is used to manipulate the phase and amplitude of one of the laser outputs before mixing. This leads to a corresponding change in the phase and amplitude of the resultant microwave signal. This approach was used to generate microwave signals up to 52 GHz with 42 dB amplitude change and 8 π phase change using a 1.2 mm-long optical waveguide and less than 3 V of voltage control [58].

Full-wave analysis of optically controlled semiconductor coplanar waveguides was reported in [59]. The incident optical illumination results in a change in the propagation characteristics of the microwave signal such as its phase or propagation loss [60].

Optical control of active components

Direct optical control of microwave semiconductor devices has been an area of growing interest. Various RF control functions including gain control of amplifiers, oscillator tuning, locking and frequency modulation, switching, mixing, limiting and phase shifting have already been demonstrated optically [12], [61], [62] [65]. Optically controlled modulators and demodulators have also been reported [66] [67] as well as optical/RF transducers [68]. Integrated optically driven millimeter wave sources and receivers were demonstrated in various configurations such as [69] [70] [71]. Another application reported in [72] is the

optical control of polarity of short electrical pulses generated from coplanar waveguide metal-semiconductor-metal photodetector.

Optical control of solid-state semiconductor microwave devices include optical control of High Electron Mobility Transistors (HEMT) [73] [74], MESFETs, MODFETs [75] and HFETs [76]. MODFETs are an advance design of MESFETs known as the two dimensional electron gas FETs.

The idea of using photo-conductivity for the control of microwave solid-state devices was also extented to controlling other devices such as TRAPATT [77] and transferred-electron devices (TEDs) such as Gunn diodes [78].

Optical control of microwave signals using GaAs FETs was reported in many applications [79] [37]. It is reported in [37] that using optical phase locking, the phase and frequency of the FET oscillation can be independently controlled. The principle of an optically controlled phase shifter is described in [37]. Other Optically controlled MESFETs were reported in [80] [81]

Other references such as [82] show the possibility of direct optical control and tuning of IMPATT n^+ip^+ avalanche diode oscillators. Other optically controlled IMPATT oscillators were reported in [83] - [85].

In [86] it is suggested to control the microwave transmission of $n-i-p-i$ structure by illuminating it with a CW Argon ion laser. Tests in a broad-band microwave modulator wave spectrometer show that an optical intensity of 900 mW/cm^2 produced a 50% change in the transmission for microwave signals between 10 GHz and 50 GHz.

Broad-band low-loss optical fiber links for concurrent detection and down-conversion of phase-sensitive analog microwave signals at 16 GHz were reported in [87]. Another system is described in [88]

As stated earlier, picosecond photo-conductivity is becoming more and more the dominant means of optical control of microwave signals. In the following section, concentration is devoted to explaining the concept of switching of microwave devices by picosecond

photo-conductivity. It will attempt to explain how an Optoelectronic microwave switch functions, and will cite the various structures reported in the literature.

2.5 Optoelectronic Microwave Switching

Picosecond Photoconductors were first demonstrated by *Auston* [89] and by *Lawton* and *Scavannec* [90] along with later contributions by many others [91] [15]. Various materials and geometric configurations have been proposed for picosecond photoconductors. Most, however, have in common a design which optimizes the speed of response by directly coupling the photocurrent to a high speed transmission line structure. This is usually accomplished by making the electrodes of the photoconductor an integral part of the transmission line. A typical example is illustrated in Figure 2.6. It consists of an insulating substrate on which metallic electrodes have been deposited in the configuration of a microstrip transmission line. A picosecond light pulse is focused on the active region of the photoconductor which consists of a small gap in the top microstrip metalization. Other transmission line configurations such as coaxial and coplanar waveguides [59] have also been proposed. The photoconductor may be used as a substrate material if it is a semi-insulating material.

The detailed analytical description of the device performance was discussed sparingly in the literature. By conducting a thorough literature survey, the following comprehensive analytical description is provided.

An expression for the output voltage waveform could be obtained by solving the time-varying electromagnetic equations for the electric fields produced by the radiating currents and charges in the gap, which is a fairly complex approach. A simpler approach is to represent the photoconductor by a time-varying circuit element and proceed to analyze the device using a lumped parameter circuit representation. This simplification is valid for the case where the gap dimensions and the transmission line cross-section are much smaller than the microwave wavelength. For gap dimensions and transmission line widths

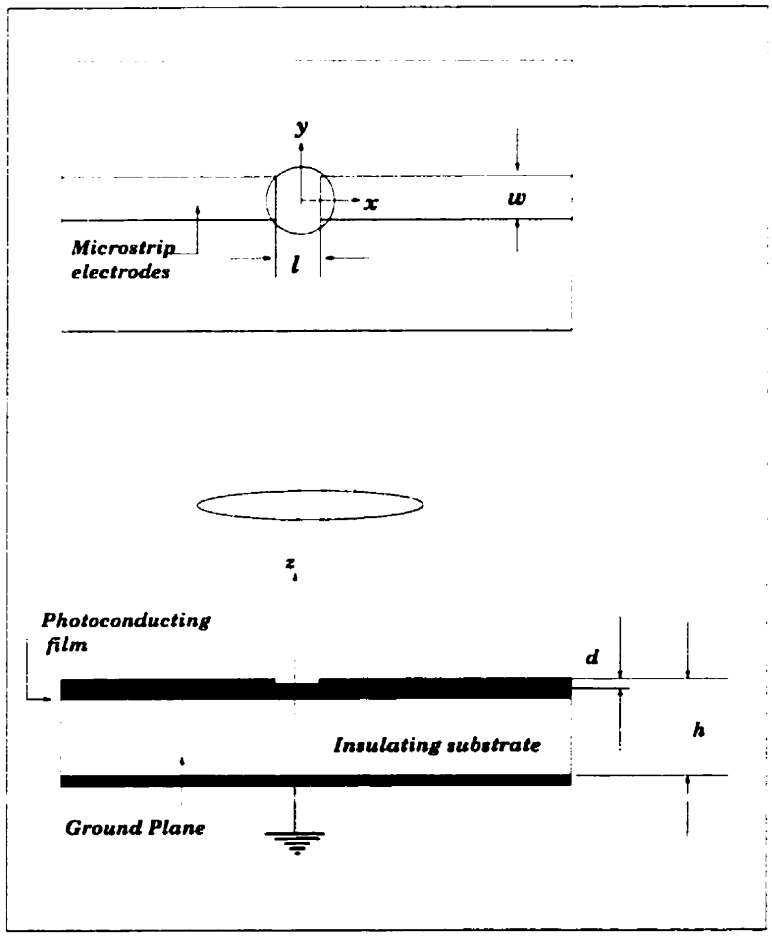

Figure 2.6: A Schematic diagram of a thin film photoconductor as an integral part of a high-speed microstrip microwave transmission line. The active region is the gap in the upper conductor, at which light is focussed.

less than 1 mm, this approach is accurate for signals up to 30 GHz.

Considering the later approach, the photoconductor is modeled as a time-dependent conductance, $G_b(t)$, in parallel with a capacitance, C_b, connecting the two ends of the transmission line. The capacitance C_b is the static capacitance of the gap, and is in the range of 10-100 fF for the geometries and dimensions of interest. This capacitance is a speed limiting factor for the device. It can be shown that the capacitance increases only logarithmically as we decrease the gap length, l [see Figure 2.6]. On the other hand, the sensitivity of the device increases with $\frac{1}{l^2}$. Hence, it is possible to minimize the gap length and increase the sensitivity of the device, without much sacrifice of the speed [15]. Using bulk optics excitation techniques, however, poses limitation on the miniaturization of the gap size. The proposed integrated approach of this thesis can address this issue, as explained later. The lumped-parameter circuit model becomes more accurate for smaller gap sizes.

There is also a very small shunt capacitance, C_a, that connects the upper and lower metalizations of the microstrip transmission line. Further, the leakage current through the substrate between the upper and lower metalizations can be modeled as a conductance G_a, which again could be neglected given its small magnitude. A higher value of G_a, due to a low dark resistivity or due to light leakage through the substrate, reduces the switching effectiveness of the the incident light. The circuit model of the device is depicted in Figure 2.7. Several accounts in the literature [13] [51] [92] [91] [93] [94] ignore the effect of these capacitances alltogether. It is shown in this thesis that for higher frequency ranges, and for moderate optical energy levels, the effect of these capacitances becomes more prominent.

A general expression for the time varying conductance $G_b(t)$ can be derived from the rate of dissipation of electrical energy:

$$G_b(t)V_g^2 = \int_v \mathbf{E}.\mathbf{J}dv \tag{2.8}$$

where V_g is the voltage across the gap, $\mathbf{E}$ is the electric field of the microwave signal,

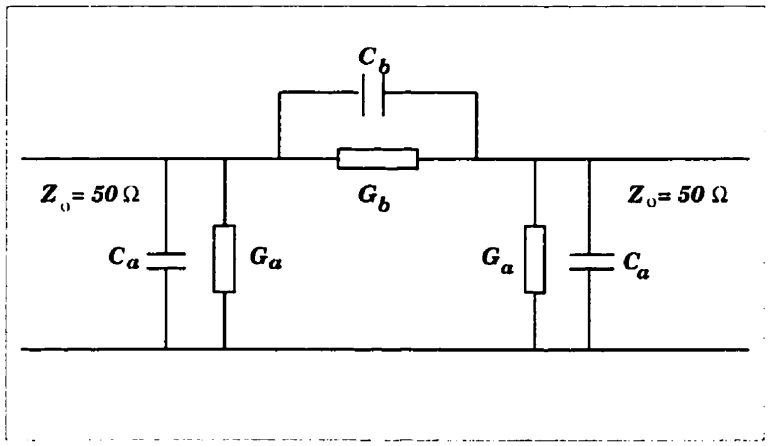

Figure 2.7: The π equivalent circuit of the configuration shown in the previous figure

and **J** is the current density. The integration extends over the entire active volume of the photoconductor. For linear dependence between the current density and the electric field, i.e. Ohm's law applies,

$$G_b(t) = \frac{1}{V_g^2}\int_v \sigma|\mathbf{E}|^2 dv = G_o + g(t) = G_o + \frac{1}{V_g^2}\int_v \delta\sigma\,|\mathbf{E}|^2\,dv\,. \qquad (2.9)$$

As shown, $G_b(t)$ can be expressed as the summation of two components. The first is the dark conductivity, G_o, which is a constant depending on the material, size and shape of the gap, and represents the conductivity of the gap in absence of light. The Second is the time varying term, $g(t)$, which is due to photoconductance. In absence of optical excitation, $G_b = G_o$ which is designed to be a very small value leading to an open circuit condition (if the shunt capacitive susceptance, ωC_b, is also negligible). In the case of optical illumination, $G_b \approx g(t)$ which is designed to be a very large quantity. If $G_b Z_o << 1$, where Z_o is the transmission line characteristic impedance, the gap is considered to be a short circuit (provided that the shunt capacitive susceptance is again very small compared to G_b and Z_o). In the above expression, σ is the overall conductivity, and $\delta\sigma$ is the change in conductivity due to illumination.

An incident optical pulsed excitation will generate a distribution of electrons and holes at the onset of the pulse given by

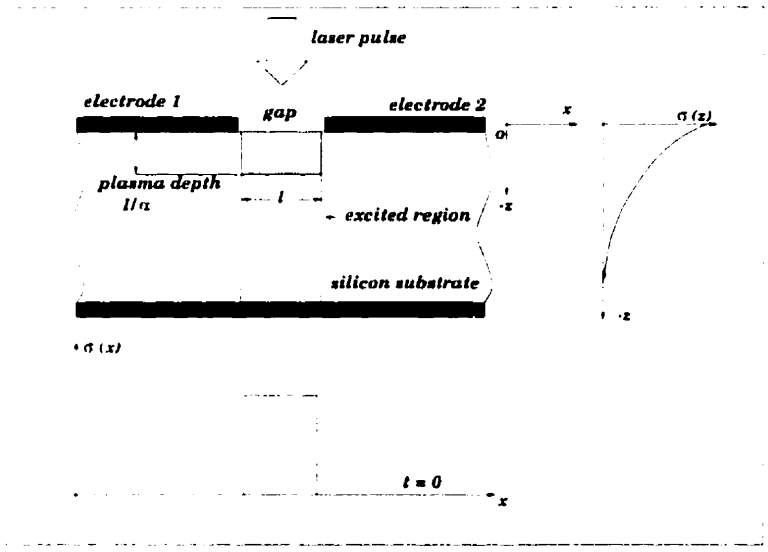

Figure 2.8: A cross sectional view of the gap configuration of an optically controlled microstrip switch

$$n(t=0^+) = p(0^+) \;=\; \frac{(1-R)\alpha\eta\mathcal{E}(x,y)e^{\alpha z}}{\frac{h}{2\pi}\omega}, \tag{2.10}$$

where n and p are the electron and hole densities respectively, R is the reflectivity of the surface given by 2.6, α is the absorption coefficient, described in section [2.2.1], η is the quantum efficiency, $\mathcal{E}(x,y)e^{\alpha z}$ is the energy distribution of the optical pulse in the gap region, and $\frac{h}{2\pi}\omega$ is the energy of one photon. The axes (x, y and z) are noted in Figure 2.6. The photon flux distribution for an externally illuminated microstrip circuit is an exponential decay function within the microstrip substrate, as shown in Figure 2.8. If pulsed optical radiation is considered, the diffusion effects can be neglected. Under this condition, the photo-excited carriers distribution assumes the same spatial distribution of the photon flux, as depicted in the above expression. Although the electron and hole densities are generated in equal numbers at the onset of the optical pulse, their time evolution may differ due to the different capture rates by different recombination sites, as well as their different drift behavior. For optical pulses with short durations, the initial carrier distribution described in the above expression is maintained for the duration of the switching action.

Based on the above assumptions, the change in conductivity due to illumination, $\delta\sigma$, is given by

$$\delta\sigma = \Delta\sigma e^{\alpha z} = (nq\mu_n + pq\mu_p) . \tag{2.11}$$

Hence,

$$g(t) = \frac{1}{V_g^2} \int_v (nq\mu_n + pq\mu_p)|\mathbf{E}|^2 dv , \tag{2.12}$$

where μ_n and μ_p are the electron and hole mobilities, respectively, and q is the electron charge. The carriers distribution is an exponential decay function. If diffusion effects are neglected as stated earlier, the photo-excited region is modeled as an equivalent semiconductor film of thickness $t = \frac{1}{\alpha}$ with a uniform photoconductivity $\Delta\sigma$ proportional to the photon density at the surface.

The electric field distribution in the gap, $\mathbf{E}(\mathbf{x})$ depends on the geometrical configuration of the photoconductor and the distribution of the photoexcited carriers. The later effect is particularly important in the high injection regime which is the typical operation regime for picosecond photoconductors. If the electric contacts are not ohmic contacts, they can influence the electric field distribution. However, as explained earlier, it is possible to obtain good ohmic contacts with relatively simple methods for radiation-damaged and amorphous semiconductors.

The photoexcited region of the series gap in a microstrip line can be modeled by equivalent lumped circuit elements provided that these conditions are met:

1. The operating microwave frequency is such that the microwave skin depth in the semiconductor $\delta = \frac{1}{\sqrt{\omega\mu\sigma}}$ is much bigger than $\frac{1}{\alpha}$ where α is the radiation absorption coefficient of the semiconductor. The quantity $\frac{1}{\alpha}$ represents the depth of the active photoexcited region.

2. The operating microwave frequency is such that the microwave signal's wavelength, λ_m, when propagating along the microstrip line is much bigger than the length and width of the light spot size.

3. The depth of the photoexcited region $\frac{1}{\alpha}$ is much smaller than the substrate width.

If the above conditions are met, the increase in the conductivity of the photoexcited region due to the incident light can be calculated from bulk lumped element approximations and the photo-excited region is modeled as an equivalent semiconductor film of thickness $t = \frac{1}{\alpha}$ with a uniform photoconductivity $\Delta\sigma$ proportional to the photon density at the surface. The conductance of this semiconductor film is given by

$$G_b \approx \gamma \Delta\sigma \frac{w}{\alpha l}, \tag{2.13}$$

where l and w are the length and width of the optical spot size respectively as noted in Figure 2.6, and γ is a reduction factor due shaded highly resistive semiconductor zones between the excited region and the conductor metalization [95]. These are otherwise assumed to be good ohmic contacts [92] [15]. The physical origin of this γ factor can be explained as follows. The conductivity $\sigma(x,y,z)$ is assumed constant along the gap length, b, i.e. along the x axis, i.e $\sigma(x,y,z) = \sigma(z)$. In reality, the finite aperture of the gap will impose an intensity profile on the optical beam penetrating through the gap. This profile is such that more light is concentrated in the middle of the gap, leaving the edges of the gap with very low light intensity. With such an intensity profile, there will be highly resistive areas around the metallic contacts on both sides of the gap. This will lead to a significant reduction in the conductivity compared to the analytically computed value. The reduction factor γ takes into account the effective decrease of the effective gap conductance, caused by these shaded highly resistive semiconductor zones between the excited region and the microstrip contacts [93], especially at low excitation levels. This γ factor was reported to be as low as 0.06 [95]. In should be noted here that the guided-wave approach, that will bring in the required illumination from below the aperture, will help

evade this situation. The effect of the finite aperture of the gap is illustrated schematically in Figure 2.9. As shown in that figure, the resistivity of the gap is very high at the two ends of the gap near the metallic contacts.

If the thickness of the substrate is such that the incident optical field penetrates into the substrate and reflects back from the ground plane, then the conductance, G_b, is given by

$$G_b = G_A + G_B + G_C, \tag{2.14}$$

where

$$G_A = \frac{l}{w} h \sigma_d \,, \tag{2.15}$$

$$G_B = \gamma \frac{l \Delta\sigma}{w\alpha} (1 - e^{-\alpha h}) \,, \tag{2.16}$$

$$G_C = \gamma \frac{l \Delta\sigma}{w\alpha} (e^{-\alpha h - 2\alpha h}) \,, \tag{2.17}$$

The third term on the RHS of equation 2.14 takes into account one optical reflection from the ground metal coating. This term should ideally be minimized for proper performance, as explained earlier. The term σ_d is the dark conductivity, which should be much smaller that $\Delta\sigma$ when the gap is illuminated.

In order to ensure good switching characteristics, the incident radiation must not penetrate through the substrate into the ground conducting plane, a condition that is satisfied if $G_B >> G_C$, which yields $\alpha h \geq 5$. This condition sets an minimum thickness limit or alternatively an upper limit on the wavelength to be used, governed by the variation of $\alpha(\lambda)$. For example, for a silicon substrate of thickness $h = 0.5$ mm, λ can be no longer than 1 μm.

Under the condition that $\alpha h \geq 5$, and that $G_B >>$ the dark conductance G_A, the conductance G_b reduces to

$$G_b \approx \gamma \, \Delta\sigma \, \frac{w}{\alpha l} \tag{2.18}$$

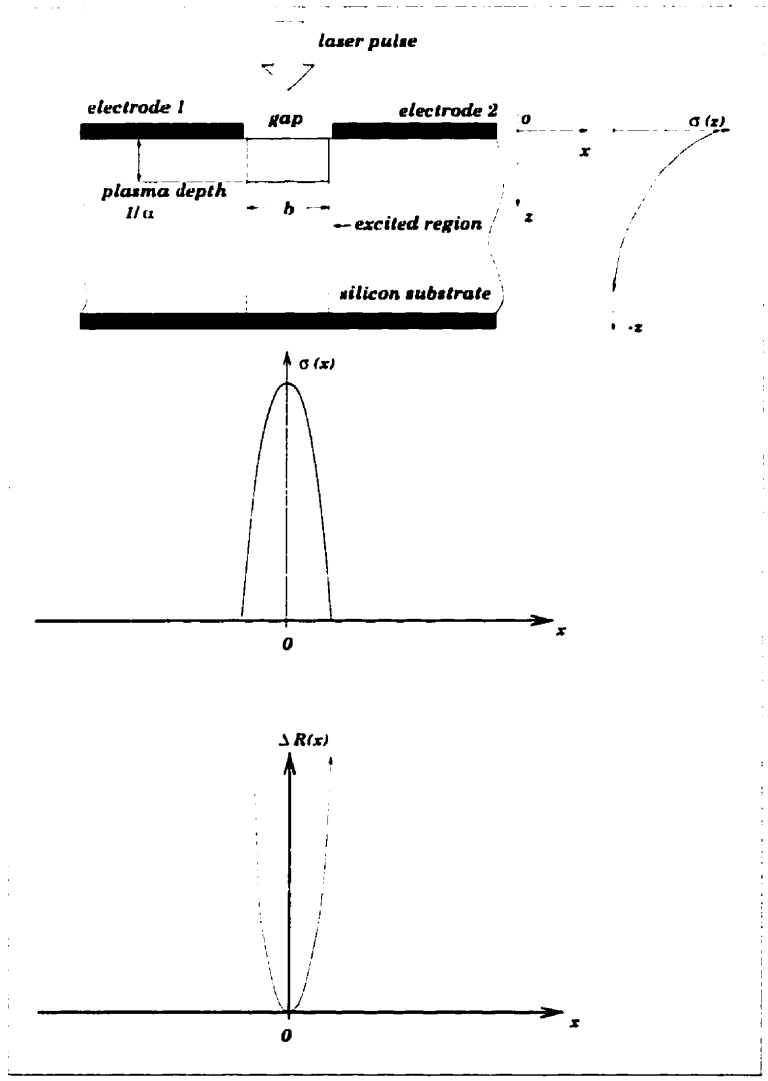

Figure 2.9: Effect of finite aperture on uniformity of the light distribution across the gap. The uneven distribution of carriers below the gap leads to shadowed areas near the metallic contacts with very high resistivity, as depicted in the sketch of $\Delta R(x)$

as deduced earlier. The photoconductivity $\Delta\sigma$ is given approximately by

$$\Delta\sigma \approx q\,(\mu_n' + \mu_p')\,\eta\,(1-R)\,\alpha\,Q_v\,\Delta t\,, \tag{2.19}$$

where Δt is the pulse duration, Q_v is the photon flux density in vacuum, and μ_n', μ_p' are the surface mobilities of the electrons and holes. These are normally one tenth of their bulk values when surface scattering and carrier-carrier scattering due to high injections are effective [92]. Q_v is given by

$$Q_v = \frac{H}{hf}\,\frac{\lambda H}{hc}\ \ [photons\ m^{-2}\ s^{-1}] \tag{2.20}$$

where λ is the optical wavelength and H is the irradiance (W/m^2) given by

$$H = \frac{P_l\,\eta_{lens}}{l * w}\,, \tag{2.21}$$

where P_l is laser peak output power and η_{lens} is the focusing lens efficiency. l and w are the spot length and width respectively. For a lens transmission loss of 10%, $\eta_{lens} = 0.9$.

As a numerical example, consider a GaAs diode with a peak output power of 40 W (Model RCA TA 7705) [95] operated at $\lambda = 0.906$ μm. Consider a Silicon substrate with a dark resistivity of 4000 Ωcm and height $h = 0.55$ mm. This yields $\alpha = 27{,}000$ m^{-1} or $t = 37.04$ μm. The depth $\frac{1}{\alpha}$ is much smaller than the substrate height, h. The surface mobilities $(\mu_n' + \mu_p') \approx 180$ $\frac{cm^2}{V.s}$ which is one tenth of their bulk values [95]. Using the above parameters, along with $l = 3$ mm, $w = 0.25$ mm, $\eta_{lens} = 0.9$, equation 2.21 yields $H = 4000 W/cm^2$. With $\eta \approx 1$, $R \approx 0.3$ (for Silicon-Air interface), $\Delta t = 100$ ns, $(\mu_n' + \mu_p') \approx 180$ $\frac{cm^2}{V.s}$, equation 2.19 yields a peak photoconductivity of $\Delta\sigma = 11.84$ $\Omega^{-1}m^{-1}$

From DC measurements, γ was found to be ≈ 0.06 [95]. Using the above data, equation 2.13 yields a conductivity, $G_b = 0.0316$ S or a resistance of 31.645 Ω which is

less than the characteristic Impedance of 50 Ω For comparison, the equivalent resistance in the dark state is 90 KΩ.

2.5.1 Circuit Analysis of photoexited Microstrip Lines with a Series Gap

The bias voltage of the photoconductor can be a fast varying signal and not necessarily a *DC* voltage. The effective load seen by the photoconductor is the line characteristic impedance, Z_o. To determine the response to an arbitrary incident electrical signal, $v_i(t)$, the voltage across the gap, $v_g(t)$ can be obtained using the laws of circuit theory,

$$Z_o C_b \frac{dv_g}{dt} + \frac{1}{2}[1 + 2Z_o G_b(t)]v_g(t) = v_i(t), \tag{2.22}$$

where the reflected wave, $v_r(t)$, and the transmitted wave, $v_t(t)$, from the transmission line are given by

$$v_r(t) = \frac{1}{2}v_g(t)\,, \tag{2.23}$$

$$v_t(t) = v_i(t) - \frac{1}{2}v_g(t)\,. \tag{2.24}$$

For the matched operating conditions, i.e., with signal source impedance and load impedance equal to the transmission line characteristic impedance, Z_o, it could be shown that the power transmission coefficient, based on the S parameter concepts, is given by

$$|S_{12}| = \frac{P_1}{P_2} = \frac{(2Z_o G_b)^2}{[(1 + Z_o G_a)(1 + Z_o G_a + 2Z_o G_b)]^2} \tag{2.25}$$

The above equation does not take into account the insertion losses due to the microstrip line. A low dark resistivity leads to a high value of G_b, and consequently S_{12}, in the OFF state (when no light is incident). As such, the discernment between the ON

and OFF states become less decisive. Further, the high dark conductivity, as well as the penetration of the incident light through the substrate to the ground plane, lead to a leakage conductance G_a of a considerable magnitude that again help minimize the difference between S_{12} in the OFF and ON states. Therefore, it is recommended to use materials that are semi-insulating in the absence of light, and to design the device parameters such that the incident light is mostly absorbed in a thin layer of the substrate close to the surface.

Consider a time harmonic microwave signal with radian frequency ω. The steady state expressions for v_g, v_t, and v_r for a constant $G(t) = G_b$ can be deduced by solving 2.22. These expressions are

$$\frac{V_g(\omega)}{V_i(\omega)} = \frac{1}{j\omega C_b + 0.5 * (1 + 2Z_o G_b)}, \tag{2.26}$$

$$V_r(\omega) = \frac{1}{2} V_g(\omega), \tag{2.27}$$

$$\frac{V_t(\omega)}{V_i(\omega)} = \frac{j\omega C_b + Z_o G_b}{j\omega C_b + 0.5 * (1 + 2Z_o G_b)}, \tag{2.28}$$

For very large values of $z_o G_b$, the ratio of the transmitted signal to the incident signal tends to unity as expected. The reflected signal is given by

$$V_r(\omega) = \frac{1}{Z_o G_b} \approx 0. \tag{2.29}$$

2.5.2 Step Response and Optical Generation of Electrical Pulses

Consider now an ideal photoconductor, with a step-function conductance and a *DC* bias, i.e.

$$G_b(t) = \begin{cases} 0; & \text{if} \quad t < 0 \\ G_1; & \text{if} \quad t > 0 \end{cases} \tag{2.30}$$

$$v_i(t) = \frac{1}{2}V_b = constant \tag{2.31}$$

Hence from equation 2.22, the transmitted signal, $v_t(t)$, is:

$$v_t(t) = \frac{V_b}{2}\left[\frac{2Z_oG_1}{1 + 2Z_oG_1}\right]\left[1 - e^{-\left(\frac{G_1}{C_b} + \frac{1}{2Z_oC_b}\right)t}\right] . \tag{2.32}$$

For small values of G_1, (i.e. low plasma densities), $v_t(t)$ will have the approximate form,

$$v_t(t) = Z_oG_1V_b\left[1 - e^{-\frac{1}{2Z_oC_b}t}\right] . \tag{2.33}$$

with a rise time = $2Z_oC_b$, and a steady state value of $Z_oG_1\ V_b$, which is linearly related to G_1, and hence to the incident light, a situation suitable for modulators,multipliers and like devices. This is called the linear regime of operation.

For large values of G_1, compared to Z_o, (i.e. $G_1Z_o >> 1$), the transmitted signal would be given approximately by

$$v_t(t) = \frac{v_b}{2}\left[1 - e^{-\frac{G_1}{C_b}t}\right] , \tag{2.34}$$

with a rise time given by $\frac{C_b}{G_1}$, which is much smaller compared to the earlier case, and a steady state value $\frac{V_b}{2}$ which is independent of the incident optical signal. This is called the saturated regime of operation, a regime that is suitable for the design of switches and gates where the optical signal plays the role of the gating signal [54]. For example, for medium values of G_1, say G_1Z_o =5, the rise time is less than 10% of the rise time in the small signal case, and the incident electric signal is transmitted with 91% efficiency.

2.5.3 Photoconducting Electronic Samplers

Picosecond photoconductors could be also deployed as electronic gates to measure the characteristics of high speed electrical waveforms. [89] [90] [97]. In this type of application,

the incident bias signal on the photoconductor is the pulsed waveform rather than a DC signal. The active photoconducting area is usually a gap between a main transmission line and a secondary line. When a light pulse strikes the sampling gap, a small sample of charge is transferred from the signal on the main transmission line to the sampling line. The response of this sampling gate can be analyzed in a manner similar to that of a single gap in a main line as explained in the previous section. Since the speed of the sampling gate is dictated by the response time of the photoconductor, it is sufficient to measure the total charge generated in the sampling transmission line without the necessity of time-resolving the sampled voltage waveform. This procedure also has to advantage that it does not contain a contribution from the signal which is capacitively coupled across the sampling gap. This can be written in the form of a convolution of a sampling function, $f_s(t)$ with the incident signal $v_i(t)$ as:

$$Q_s(\tau) = Q_o + \int_{-\infty}^{\infty} f_s(t' - \tau) v_i(t') dt' \ , \tag{2.35}$$

where

$$f_s(t) \ = \ \frac{\frac{2}{3Z_oC_s}}{\frac{1}{1 + \frac{1}{2}Z_oG_o}} \int_t^{\infty} g(t') e^{-\gamma(t'-t)} dt' \ , \tag{2.36}$$

and

$$\gamma \ = \ \frac{2}{3Z_oC_s} + \frac{G_o}{C_s} \ , \tag{2.37}$$

where C_s is the capacitance of the sampling gap.

The sensitivity and signal-to-noise ratio of photoconductive sampling is extremely good, permitting fast electrical signals having amplitudes of approximately 1 μ V to be measured with realistic integration times. The limiting noise properties of photoconductive sampling gates have not been studied in detail, nor have there been any studies with regards to their optimization. In the ideal case, the limiting noise level would be determined by generation-recombination noise and the Johnson noise, also known as the flicker

noise, or the $\frac{1}{f}$ noise [98]. For typical sampling gates this would predict a limiting sensitivity of a few tens of $nV/\sqrt{Hz}$. In practice, however, imperfect ohmic contacts give rise to a photovoltaic signal which tends to dominate the noise properties. This produces a noise background signal due to laser amplitude fluctuations. Although the quantum efficiency of the photovoltaic signal is extremely small, it is often sufficient to dominate the noise properties and results in sensitivity limits which are more typically a few $\mu V/\sqrt{Hz}$. Further work to make better ohmic contacts would greatly improve the minimum detectable signal that can be measured using this technique.

2.5.4 Autocorrelation Measurements

A simple and effective technique for evaluating the speed of response of photoconducting pulse generators and sampling gates is to directly connect them together so that the output of the optical pulse generator is the input to the sampling gate [89] [99]. This approach, which is termed "electronic autocorrelation measurement" gives an accurate measurement of the system response and has important applications for characterizing specific photoconducting materials, electrode geometries, transmission line structures, and mounting configurations. The system response is approximately equal to the convolution of the individual responses of the generator and sampling gate [100]. This approach has been used to measure the photocurrent decay rates in amorphous silicon, silicon-on-sapphire, radiation-damaged silicon-on-sapphire , radiation-damaged indium phosphide, gallium arsenide, radiation-damaged gallium arsenide and polycrystalline silicon among many others. In many cases, the capacitance of the electrode geometry limits the speed of response. For example, in microstrip structures having widths of 0.2 mm, gaps of 25 μm and substrate thicknesses of 0.25 mm, the limiting circuit response has a full-width at half-maximum (FWHM) of approximately 10 ps.

Recently, Ketchen and coworkers [101] have scaled down an autocorrelation circuit using 5 μm coplanar strip transmission lines and obtained a response with FWHM of only 1.6 ps, using a novel "sliding contact" technique which involved the illumination of regions

between the conductors. This technique was applied to the measurement of dispersion on coplanar transmission lines by sampling the generated electrical pulse further down the coplanar line. By using superconducting coplanar waveguides, the capability of observing the contribution to the propagation constant due the finite superconducting bandwidth was recently demonstrated [102].

2.5.5 Picosecond Photoconductivity Measurement Systems

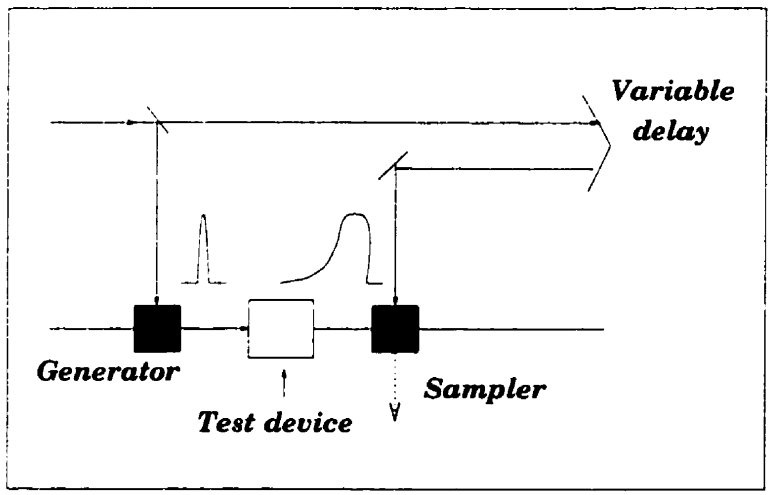

Figure 2.10: Optoelectronic measurement system that could be used for measuring the performance of high speed devices. Both the generator and sampler can be photoconducting devices. The measurement ia accomplished by varying the optical delay between the two optical pulses used to time the generator and sampler.

As mentioned earlier, the use of picosecond optical pulses for control and measurement of electronic devices and circuits can produce a substantial improvement in both performance and flexibility compared to conventional electronic measurement systems such as sampling oscilloscopes. In addition, an entirely new class of devices has evolved from the use of this approach having properties and applications that go beyond conventional electronic and microwave devices.

In the previous section, a number of devices using photoconducting materials have

been proposed. These are basically of two types: sources of electrical transients and electrical sampling gates. When one of these optoelectronic signal generators is combined with an optoelectronic sampling gate as illustrated in Fig 2.10, a flexible high speed measurement system results which can be used to measure a wide range of electronic devices and materials. An important feature of this system is the use of the same optical pulse for triggering both the optoelectronic pulse generator and sampling gate [103]. An optical beam splitter is used to split this pulse into two pulses, one of which goes to the generator and the other which goes to the sampling gate after passing through a variable path-length delay line. The variation of this delay permits accurate stroboscopic measurements with negligible jitter.

Clearly, speed is the single most important advantage of using optoelectronics, and it provides the main incentive for the extensive proliferation of activity in this field.

2.6 Typical Examples

2.6.1 Optoelectronic Switching of Microwave Signals Using Series Gaps

Consider the photoconductive microwave switch as shown in Figure 2.11. The effect of the light-generated conductivity on the microwave power transmission can be studied using the π equivalent circuit shown in Figure 2.7. The switch is built of a microstrip line of gold metalization of width 0.41 mm and film thickness of 7 μm, on a microstrip substrate of width 0.55 mm and resistivity of 4000 Ωcm. The above parameters yield a microstrip line of 50 Ω characteristic impedance. Referring to Figure 2.7, the power transmission through the laser excited plasma layer is described by the lumped conductance G_b, and shunting effects caused by greater absorption depths is taken into account through the shunt conductance G_a. To include the feature of the dark microstrip gap, the gap capacitance C_b and the shunt capacitance C_a are introduced [104] [105] [106]. In most

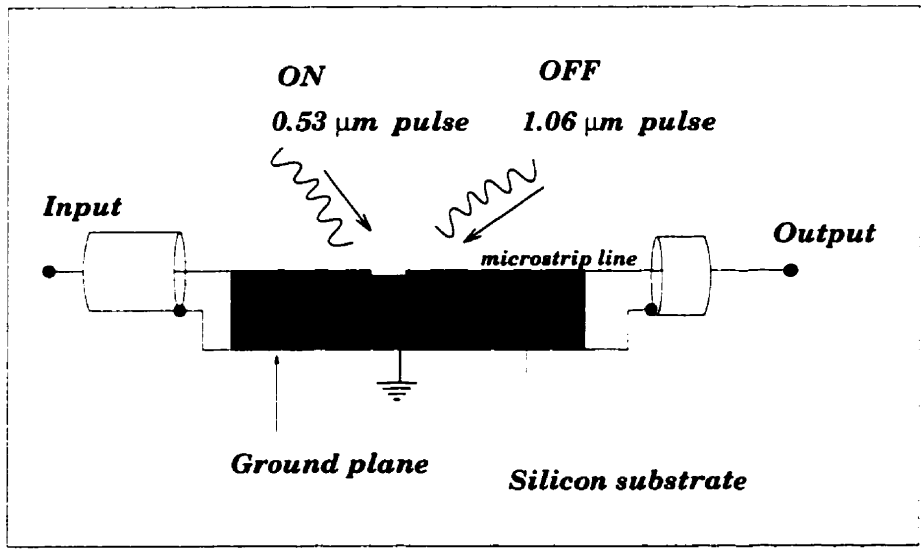

Figure 2.11: An optically controlled picosecond microstrip microwave switch. It uses a visible 0.53 μm picosecond pulse of approximately 5 μJ to initiate conduction and an infrared 1.06 μm pulse of approximately 5 μJ to terminate the conductance by introducing a short circuit between the top electrodes and ground plane.

cases, however, and using gap widths of 0.1 mm, C_a and C_b are in the order of 0.01 pF [104]. For signal frequencies of up to 10 GHz, these capacitances may be neglected [23]. This is always the case as long as the induced photoconductivity satisfies the conditions $G_b >> \omega C_b$ and $\omega C_a Z_o << 1$, where Z_o is the line characteristic impedance. The first condition ensures that the impedance level between the ON and OFF states are highly distinctive, which is a condition for achieving an effective switching. If this condition is not satisfied, the photo-excited microwave power transmission would barely exceed the residual "dark" power transmission through the gap capacitance. The second condition ensures that the shunt capacitive reactance is much higher than the transmission line impedance.

The picosecond photoconductor switch depicted in Figure 2.11 was first demonstrated experimentally by *Auston* [89] [13] in crystalline semiconductors. Optical pulses from a mode-locked Nd:glass laser were used to inject high densities of free carriers into a 50 ohm silicon microstrip photoconductor. One side of the line was connected to a microwave

source and the other to a load or a test instrument. The switching action was produced by an optical pulse of 5 μJ at $\lambda = 0.53\ \mu m$, which was obtained by second harmonic generation, and was used to turn the switch ON. Since the material used was a high quality crystalline material, the photocurrent produced persisted for a relatively long time, and hence, another pulse with $\lambda = 1.06\ \mu m$ was used to turn the switch OFF. For Silicon, at $\lambda = 0.53\ \mu m$, the absorption coefficient is $8x10^3\ cm^{-1}$ and consequently the effect of absorbing an optical pulse with this wavelength in the microstrip gap is to produce a thin surface layer of conductivity across the gap. If it is sufficiently intense, the optical control pulse at 0.53 μm wavelength can close the gap by generating a net resistance which is much less than the characteristic impedance of the microstrip line, thus permitting efficient transmission of the microwave signal across the device. To turn off the switch, the infra red pulse (the optical control pulse at 1.06 μm wavelength) is absorbed at the gap. In this case, however, the absorption depth is 1.4 mm, and consequently, the pulse penetrates through the substrate to the ground plane, producing a region of high conductivity between the lower and upper conductors. This shorts the transmission line, preventing further transmission by totally reflecting the incident microwave signal. By varying the delay between the two pulses, the duration of the pulse current could be continuously varied from approximately 15ps to several tens of nanoseconds. Unlike semiconductor junction devices, this switch does not depend on recombination or carrier sweep out to turn off. The optically generated electrons and holes remain; the volume conductivity in the second pulse has merely annulled the effect of the surface layer of conductivity produced by the first pulse. Consequently, the switching speed can be extremely fast being primarily limited by the durations of the optical pulses. Also the device is capable of handling moderately high microwave powers unlike conventional semiconductor switches which are limited by junction breakdown and thermal dissipation. Since the controlling signals are optical pulses, near-perfect isolation exists between the gated microwave signal and the gating optical signal [11]. A disadvantage of this technique is the repetition rate, since carriers must recombine or be swept out before the switch can be turned on again.

The same device can also function as a sampling gate if the DC bias voltage is replaced

by a microwave signal.

An alternate approach to turn the switch off is to direct the output to the ground plane through a parallel trapezoidal section similar to that of Figure 2.12. Another optical spot connects the parallel metalizations together [15]. The advantage of this approach is that the same optical wavelength can be used to turn the device on and off.

2.6.2 Optoelectronic Gating of Microwave Signals using Shunt Modulation

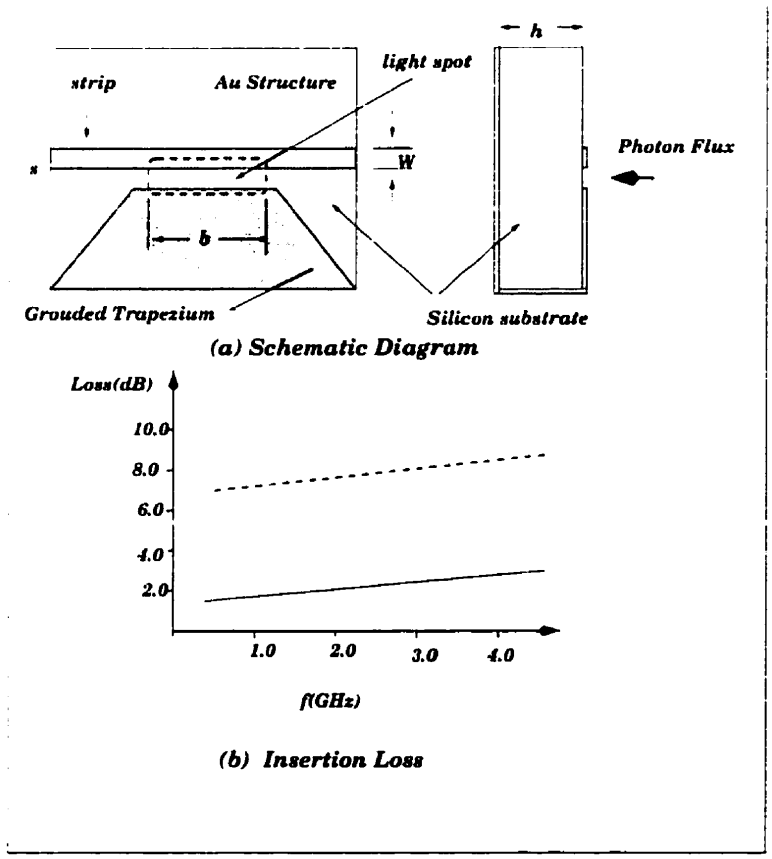

Figure 2.12: Optoelectronic gating of microwave signals using a shunt modulator. (a) a schematic diagram of the top and side view. (b) Insertion loss versus frequency for the dark state (solid line) and the illuminated state (dashed line)

Figure 2.12 shows a silicon microstrip modulator used for optoelectronic gating of microwave signals. The light induced insertion loss is the control element. Detailed investigations of similar modulators yields the following expression for the insertion loss, a. [95]

$$a = a_o + \Delta a \;=\; a_o + 20\ log(1 + \frac{G_b Z_o}{2} \text{x} 10^{\frac{a_o}{20}}) \;, \tag{2.38}$$

where a_o is the residual attenuation due to ohmic and dielectric losses and Z_o is the characteristic impedance of the line. It was shown that up to few GHz, the effect of the gap capacitances on a_o are negligible. G_b is given by the expression deduced above. As shown in Figure 2.12 the device exhibits a modulation depth of $\Delta a \approx 6$ dBs.

2.7 Picosecond Optoelectronic Transmission Lines

Picosecond optoelectronic pulse generators and switches require transmission lines which are extremely broad-band, have low dispersion and low loss, and which can be readily interconnected to optoelectronic and other devices. Unlike microwave and millimeter-wave signals, the frequency spectrum of the ultrafast optoelectronic pulse covers a range of frequencies from DC to many hundreds of GHz. For this reason, closed waveguides are unsuitable due to their large dispersion and low frequency cut-off. Some transmission line structures that have been used for ultrafast optoelectronics are the coaxial, microstrip, coplanar, and coplanar microstrip. Coaxial lines have good bandwidth and low loss and dispersion. They have been used extensively for high power optoelectronic switching with photoconductors mounted in a gap in the center conductor. They tend to be used less for high speed low power optoelectronic applications since they are difficult to interconnect to other structures such as microstrip lines and discrete devices, although schemes for accomplishing this have been developed. The microstrip, coplanar waveguide, and coplanar microstrip structures are all compatible with semiconductor microelectronic fabrication

technology. Consequently, optoelectronic devices such as photoconductors can be integrated into the transmission line being placed at a gap in an electrode or between two electrodes. The ability to use microelectronic processing technology also means that these structures can be scaled to extremely small sizes, thereby increasing the useful bandwidth. It also enables the future integration of these devices with other microelectronic components using same technology. In this thesis, these devices are proposed to be built in an integrated optical-microwave environment.

Dispersion is a major problem in transmission lines for picosecond opto-electrical pulses since it can easily produce a loss of speed due to pulse broadening. Theoretical calculations of the dispersive broadening of pulses on microstrip and coplanar lines have been made by Li et al. [107] and Hasnain et al. [108], which are in good agreement with experimental measurements of Mourou and Meyer [109]. Measurements of pulse dispersion on microstrip lines, however indicate that microstrip is much less dispersive than expected by theory [110]. Goosen and Hammond [111], have made time-domain calculations of the dispersion and loss of electrical pulses on microstrip lines on silicon substrates. Their results show the strong influence of substrate losses and demonstrate the need for high resistivity substrates. Mourou [112] has made extensive measurements on pulse dispersion on different lines. His results demonstrate that ultrashort pulses can propagate on suitably designed lines with relatively little broadening due to dispersion. In this thesis, the proposed devices do not require the entire substrate to be made of a semiconductor, as will be explained later. This enables the design of devices with better attenuation and dispersion performance.

The principal advantage of the coplanar geometries is that the size scale can be reduced to very small dimensions. Although microstrip can also be scaled down, it requires the use of very thin substrates which is often impractical. The geometrical properties of various transmission line structures have been exploited for pulse shaping applications. For example, Buck et al. [113] have shown how a stub microstrip transmission line can be used to shape the electrical pulse from a photoconductor. Margulis and Persson [114],

have used a coaxial differentiator to accomplish similar results. Chang et al. [115] have mounted a picosecond photoconductor in a coaxial Blumlein structure for pulse shaping applications. Li et al. [107] have reviewed the topic of pulse forming with optoelectronic switches.

The properties of nonlinear transmission lines have been examined theoretically by a number of workers. For example, Landauer [116] and Khokhlov [117] have shown that shock waves can be expected to develop for high voltage pulses propagating on transmission lines with nonlinear dielectrics. Paulus et al. [118] have suggested that soliton-like behavior should be possible in transmission lines having a quadratic nonlinearity and a cubic dispersion. The implementation of nonlinear transmission lines to the picosecond time domain could result in the development of electrical pulse compression techniques analogous to the soliton-like techniques that have been developed for optical pulses.

2.8 Concluding Remarks

It can be concluded from the diversity and volume of work in this area that picosecond photoconductivity is a well developed and rapidly growing field of research. The technology of using picosecond optical pulses to generate and detect picosecond microwave pulses is now relatively well developed. Substantial developments are still expected however with regards to speed, sensitivity and integration. There is also lots of potential for new device concepts and new applications.

The current approach of using free-space optical signaling is not suitable for the design of microwave devices requiring complex control mechanisms. These devices could be quite bulky as well as expensive if designed using free-space optical control. Moreover, the integration of these device could be linked to other advantages such as light weight, reliability, and cost which again are major decisive factors in some application such as space borne communication systems. In general, unless an integrated version of these devices is available, the commercialization of these devices will not be an easy task.

New materials for optoelectronics will also have an impact on what could be achieved in this area. So far, only better known semiconductors have served to establish the foundation for picosecond optoelectronics device concepts. New materials are required in order to go beyond what is available today. For example, semiconductors grown by molecular beam epitaxy (MBE) have proven to have valuable properties for optical modulators.

It is the area of applications that picosecond optoelectronics is now experiencing its most rapid growth. Current research papers report on advances that years ago were not considered possible. It is now expanded to include methods of testing high speed discrete devices and integrated circuits as well as measurement systems. For example, measurements of novel high speed electronics devices such as resonant tunneling transistors and "ballistic" transistors will be an important guide to research and development of new high speed technologies. In the very high speed area, the trend toward applications to materials characterization is expected to continue. For example, measurements of the detailed kinetics of electronic transport on the subpicosecond time scale over a wide range of density, electric field, and temperature are vitally important to the development and understanding of electronic and optical materials. Picosecond optoelectronic tools have recently been developed which will make this possible. The recent measurement of subpicosecond mobility transients by Nuss and Auston [119] is an example of what can be accomplished with these capabilities.

The continued development of techniques for generating and detecting large amplitude electrical pulses will have important applications for the study of the transient nonlinear response of materials and devices. For example, it is expected to observe electrical solitons on nonlinear transmission lines or in nonlinear dielectric materials, analogous to the optical solitons that have been produced in optical fibers. This could lead to pulse compression and result in even shorter electrical pulses than can be produced today.

In the next chapter the proposed contribution will be discussed. This contribution falls basically into two areas. One is enhancing the performance of the existing devices by addressing issues like integration and allowing for complex control objectives. The

other area is proposing new device concepts and ideas. Both of these objectives will be addressed by introducing the concept of guided wave optics to replace bulk illumination. The advantages, methodology and related issues will be addressed in that chapter.

The optically controlled microstrip switch has been traditionally treated in the literature with approximate formulas valid in the low-frequency quasi-static domain. This is done by representing the photoconductor by time-varying circuit elements obtained via a quasi-static analysis of the microstrip line, and proceeding to analyze the device using a lumped parameter circuit representation. In chapter 4, a more accurate analysis of the microwave component of the device is conducted.

Chapter 3

Integrated Optical Guided-wave controlled Microwave Switches

3.1 Introduction

This thesis envisions the future generation of optically controlled microwave structures to use guided optical wave excitation. The building block of these future devices is a microwave optically-controlled switch which is essentially a microstrip transmission line with a series gap. The optical signal is brought into the gap region using an optical waveguiding system buried in the semiconductor substrate of the microwave transmission line. Photo-generated carriers in the gap region produce a change in the transmission characteristics of the microstrip line.

One of the contributions of this PhD work is the study and development of a systematic knowledge base for the technology of guided wave optical control of microwave devices. The introduction of guided optical waves as a replacement of bulk optics creates an integrated version of these devices and enhances the fabrication yield. This also leads to the improvement in the overall performance of the device or system that is being optically controlled. More complex devices and systems and complicated control mechanisms could

be implemented using guided wave optics. These issues are discussed in this chapter.

In opting for guided waves as a mechanism that provides optical control signals for microwave devices and systems, the major advantage is in the area of integration. Further, the use of optical guided waves will provide opportunities for the design of microwave devices with complex optical control functionality such as optoelectronic logic elements. The current approach of free-space optical signaling is not suitable for the design of microwave devices requiring complex control mechanisms. These devices could be quite bulky as well as expensive if they were designed in the realm of free-space optical control.

Moreover, the integration of these device could be linked to other advantages such as light weight, reliability, and cost which again are major decisive factors in some applications such as space borne communication systems. In general, unless an integrated version of these devices is available, the commercialization of these devices will not be an easy task.

The efficiency of the devices designed using the proposed integrated optical guiding system is higher than that of current bulk-optics devices. Efficiency here is determined by comparing the amount of optical power or energy required to perform a certain control objective in a microwave structure controlled by guided optical signals relative to the one controlled by bulk optics, both of identical performance characteristics. This issue with be addressed in chapter 5.

The purpose of this PhD thesis is to study and provide an accurate model for the optical guided-wave controlled microwave switch, and to propose new devices whose building block is this optically controlled switch. The modeling task is comprised of two components: modeling the microwave device, for which a theory is developed and presented in the next chapter and modeling of the optical guided-wave control element, which is addressed in this chapter. Optical modeling is conducted using accurate numerical simulators such as Vector Finite Difference Time Domain (VFDTD) and Vector Beam Propagation Method (VBPM). These simulators, however, require an accurate launching (excitation) mode to avoid simulation errors arising from improper excitation of the opti-

cal system. This chapter presents an iterative electromagnetic algorithm that is used to compute the accurate optical field distributions required by these numerical simulators.

This chapter will also discuss how guided-wave optics could be utilized in designing different optically controlled microwave devices. This also includes novel device concepts where the guided wave control could be applied, with advantage.

3.2 Basic Device Configuration

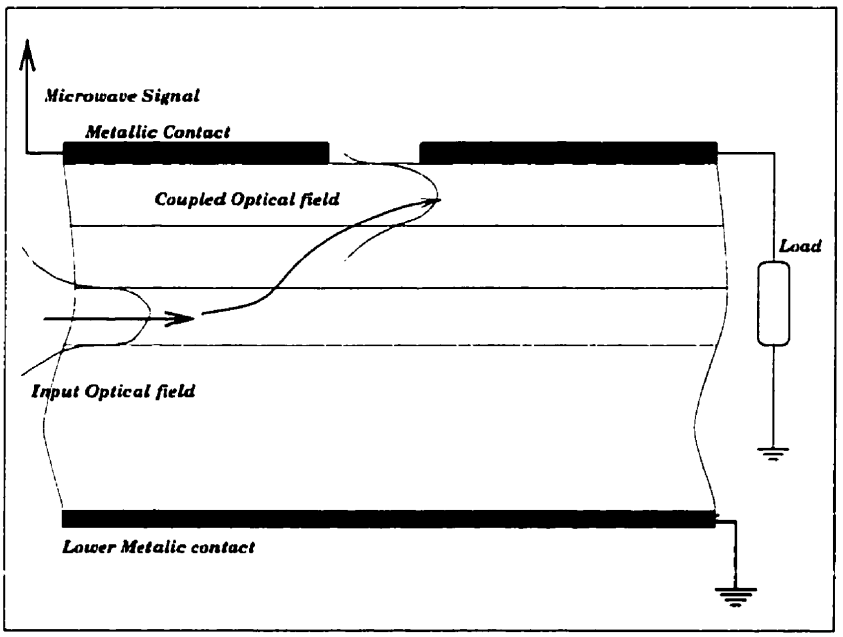

Figure 3.1: A schematic transverse cross-section in an optically controlled microstrip switch with optical energy being feed through a directional coupler.

Consider the configuration shown in Figure 3.1. The figure shows a microstrip transmission line with a series gap in its top metalization. The transmission line is connected to a microwave source on one side of the gap, and to a load or a detector on the other side. The substrate of the transmission line is used as a medium for optical guided-wave transmission. Light is guided through a waveguide situated in a low-loss dielectric region, where it couples into a parallel waveguide just below the gap in the microstrip metallic

line. The waveguide into which the optical energy couples is made of a photosensitive semiconductor material. Consequently, optical energy will be absorbed, and a plasma of electrical carriers will be generated.

The distribution profile of these electrical carriers below the gap is assumed to be the same as that of the optical-wave mode. This assumption is valid especially under optical short-pulse operation, where the effect of diffusion could be ignored, as discussed in the previous chapter. The capability of shaping the optical guided mode profile allows for a certain degree of freedom in profiling this plasma distribution, in order to best utilize the optical energy available. The merits of this guided wave approach, as far as efficiency of optical energy utilization is concerned, will be discussed in the following section.

Minimizing The Microwave Losses:

There are induced losses in the microwave energy carried in a microwave transmission line with a semiconductor substrate [120]. These losses are proportional to the area being illuminated and consequently occupied by light-generated carriers. By reducing the width of the semiconductor region, these losses could also be reduced. Platte [120] has proposed an approximate method to estimate these losses using conformal mapping and numerical calculations, which is a quasi-static analysis of photo-induced wave attenuation in a CW continuously illuminated transmission line. The present work employs a full-wave analysis of the microwave component of the device. This analysis provides accurate assessment of the microwave losses. Further, the present approach of using optical guided waves can reduce these microwave losses. In the devices studied in this thesis, only a thin layer of the substrate is made of lossy semiconductors, and hence substrate losses are minimized.

Dispersion is a major problem in transmission lines used in picosecond photoconductive switching since it can easily produce a loss of speed due to microwave pulse broadening. Experimental and theoretical calculations of the dispersion and attenuation of electrical pulses on microstrip lines show the strong influence of substrate losses and demonstrate the need for high resistivity substrates [111] [110] [109]. The proposed device structure allows for a low loss dielectric substrate, with just a thin semiconductor absorbing layer,

hence minimizing minimizing microwave dispersion and losses.

Minimizing The Optical Losses:

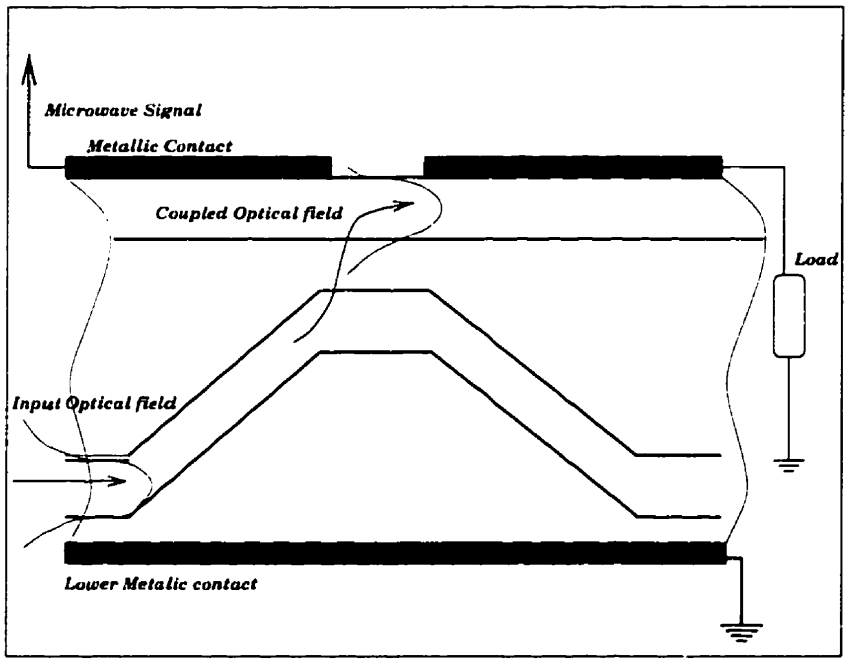

Figure 3.2: A schematic transverse cross-section in an optically controlled microstrip switch with optical energy fed through a directional coupler with an input curved guide. The effect of the curved guide is to reduce the optical losses due to the proximity of the metal layer.

Since there may be some optical attenuation due to the proximity of the optical guided mode to the surface of the metal, some techniques may be used to minimize this effect. For example, away from the gap region, the optical energy should be guided in the form of strongly-guided mode within a waveguide situated in the low-loss dielectric region. Also, TE modes are less sensitive to the existence of a metallic surface in their proximity, compared to TM modes, and hence, TE modes are preferred over TM modes. Further, the optical-energy could be made to approach the surface within the gap region only, using a bending waveguide structure for example, as shown in Figure 3.2. This approach may have its own limitations also, such as bending losses. Optical simulations conducted in this study utilize a vector finite difference time-domain (VFDTD) numerical algorithms with a boundary condition representing a perfect conducting plane. This boundary condition

bodes well with the actual physical boundary conditions encountered by the optical signal in the proposed device, with the existence of the microstrip line on top of the substrate and the perfect ground plane at the bottom. Hence, the optical simulations conducted implicitly takes into effect the metalization proximity, and the field profiles obtained are an accurate representation of those existing within the substrate.

Different topologies can also help reduce the microwave and optical losses. For example, the optical wave guides could be oriented in the direction normal to the cross section of the device, as shown in Figure 3.3. This layout minimizes the optical energy attenuation arising from the proximity of metallic surface. It also minimizes the microwave signal attenuation arising from microwave propagation in semiconductors. This architecture also allows for an added freedom of design where, for example, the optical propagation time delay could be used to synchronize a series of microwave gap switchings in a set of parallel microstrip lines.

In the following sections, these device layouts are utilized to suggests some functional complex device configurations.

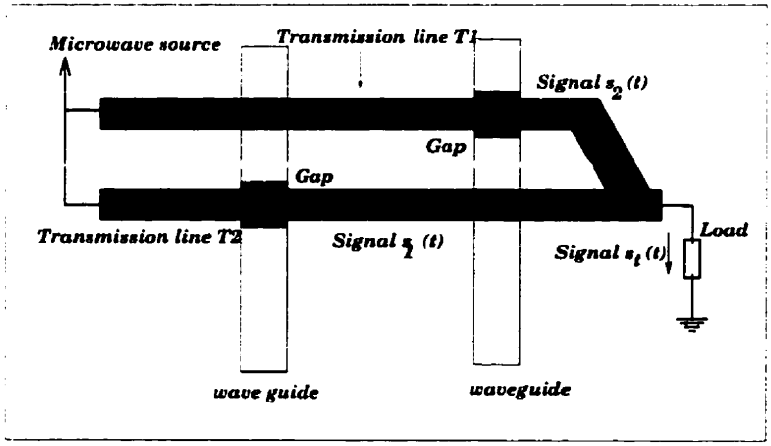

Figure 3.3: A top view of an optically controlled microwave switch. The optical guide is brought in a direction normal to the microwave strip line

3.3 Complex Device Configurations

3.3.1 Using Mach-Zehnder Interference for fast switching

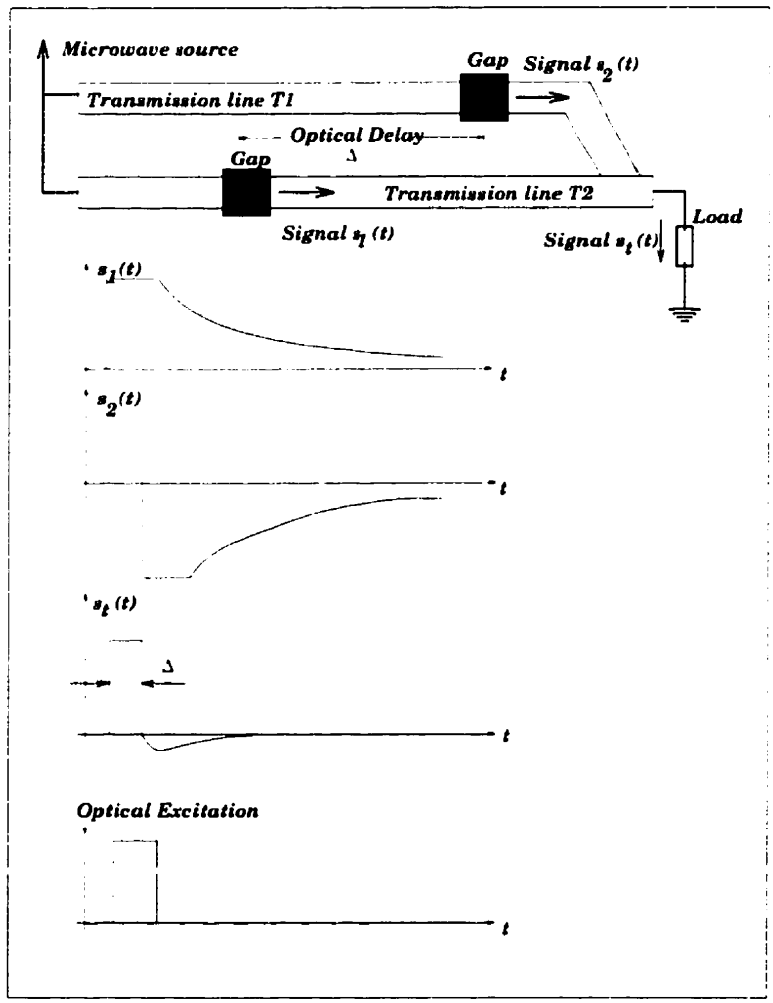

Figure 3.4: A schematic top view of an optically controlled microstrip switch with a Mach-Zehnder characteristic aimed at overcoming the recombination time limitation. Two signals with proper delay and phase are added such that the slow fall-tail is canceled out.

The use of guided optical waves allows for an increased freedom in the design of optically controlled microwave switching, and could be utilized to enhance the device performance characteristics. Consider for example the structure depicted in Figure 3.4. This structure is aimed at addressing the speed limitation problem.

As discussed in the previous chapter, the material's response to the optical excitation is quite fast, governed by the dielectric relaxation time, typically in the order of less than a picosecond. On the other hand, the switching-off of the device is limited by the carrier recombination and diffusion, which are rather slow phenomena, typically in the order of 10 picoseconds, and could even reach few milli-seconds in pure crystalline materials. Consequently, it is possible to generate microwave pulses with sharp rise edges, but with long fall tails. Since the fall-time is much longer than the rise-time, the device overall speed is limited and dictated by the fall-time.

Figure 3.4 depicts two parallel microstrip lines with series gaps, that could be optically excited. The microwave signals of the two lines, $s_1(t)$ and $s_2(t)$ are combined together coherently to give their sum $s_t(t)$. This configuration utilizes a "Mach-Zehnder"-type interferometry situation to achieve the required goal. If the propagation characteristics and relative lengths of the two transmission lines are designed in such a way as to produce identical microwave signals at π phase difference, the two fall-tails of the two pulses could cancel each other. Together with the phase difference of π, there could also be a delay, Δ, between the two signals that is equal to the required pulse width. This delay could be realized using the delay between the timing of the two optical excitations, as shown. Figure 3.4 also shows the time and phase relations between the signals $s_1(t)$, $s_2(t)$ and $s_t(t)$.

3.3.2 Optically Controlled Microwave Logic Devices

Combining the signals of one or more microstrip lines, and utilizing the effects of one or more gaps could be used to enhance the device performance with designs as the previous one. It could be also used to design new devices such as optoelectronic logic devices. For example, Figure 3.5 depicts a logic AND. With careful design of the coupling characteristics of the optical energy with two different optical wavelengths λ_1 and λ_2, the optical energy with the first wavelength will be made to couple to the surface just below the first gap, and the optical energy at the second wavelength will be made to couple to the region

just below the second gap. Figure 3.5 depicts the device performance by showing sample random sequences of optical pulses at wavelengths λ_1 and λ_2 and the resultant microwave output signal $s(t)$ as a result of the combined effect of these pulses.

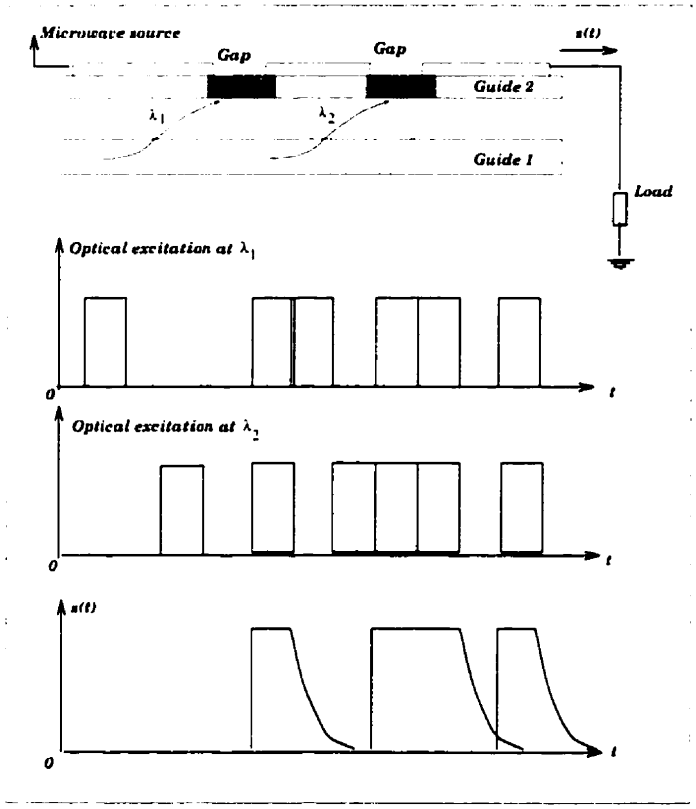

Figure 3.5: A schematic transverse cross section in an optically controlled microwave AND Gate. Only when both optical signals with wavelengths λ_1 and λ_2 are present, the device will be ON, as shown.

The two optical signals at λ_1 and λ_2 could couple back and forth between the two guides. However, they will only be absorbed in the designated locations where photosensitive materials are located. This could be realized by carefully designing the two different coupling lengths, or using optical signals with different phase matching conditions. This situation is depicted in Figure 3.6. Only when both wavelengths are present will the microwave line be conducting. This realizes an AND optoelectronic logic. This topology could also be extended for more than two wavelengths, or in other words, a multi-input

opto-electronic AND logic could be realized. Another approach to design the coupling locations of the two optical signals is to use step changes in the optical waveguide width as shown in Figure 3.7. The change in the width of the optical waveguide allows one of the signals to couple to the other guide at a specific location, if the change in guide dimensions leads to a matching condition between the two optical waveguide modes of the two guides. The other optical signal will not couple at the same location as the phase matching condition will not be satisfied for that wavelength.

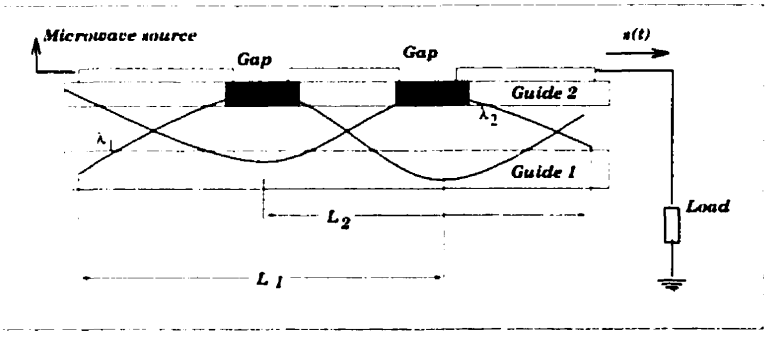

Figure 3.6: A schematic transverse cross section in an optically controlled microwave AND Gate. Due to different coupling lengths at the two wavelengths λ_1 and λ_2, the optical energy of each wavelength couples to one given gap only.

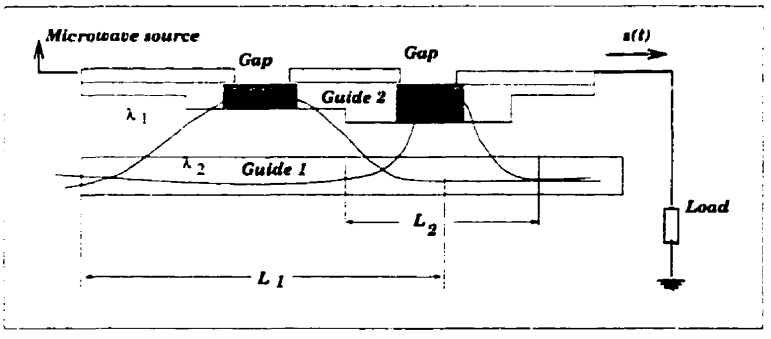

Figure 3.7: A schematic transverse cross section in an optically controlled microwave AND Gate. Due to the step change in the width of one of the optical waveguides, the two optical signals with wavelengths λ_1 and λ_2 will couple at different locations where the phase matching condition for only one specific wavelength is satisfied.

Consider two parallel microstrip lines, with a gap in each line, joined together at the

end. This configuration could serve as an OR logic, since if only one of the gaps is excited, the microwave signal path will be connected. Figure 3.8 shows a schematic diagram of this setup as well as sketches of the different signals. If the phase difference between the two line is π, then this configuration could work as a logic XOR logic, as depicted in Figure 3.9. The configuration of an OR logic could be extended to design a multi-input OR logic using multiple parallel lines. Figures 3.10 describes this multi-input OR logic, together with sketches of the signals involved.

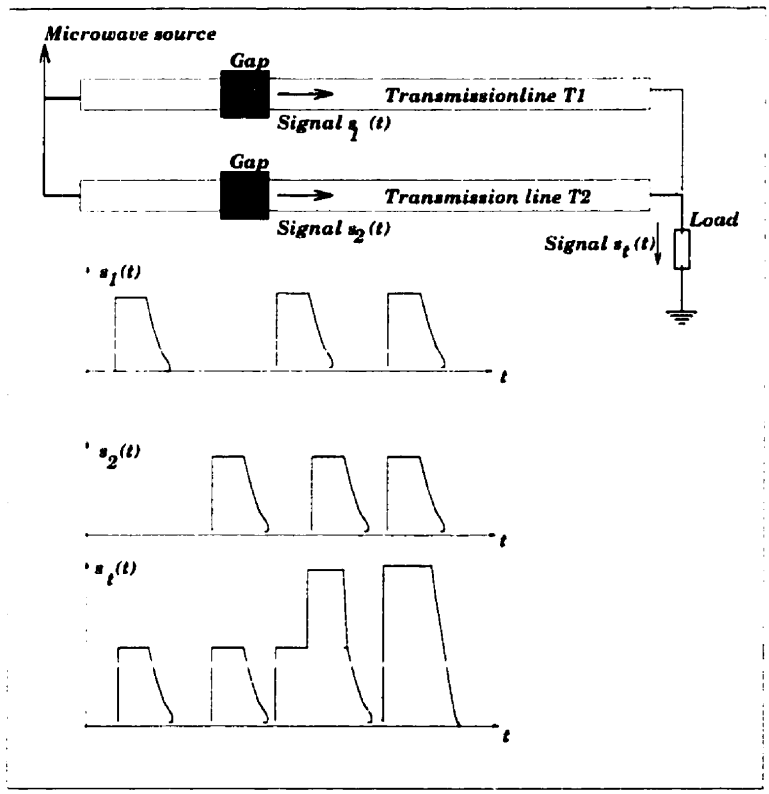

Figure 3.8: A schematic top view of an optically controlled OR Gate. When either one or both of the optical signals with wavelengths λ_1 and λ_2 are present, the device will be ON, as shown.

Consider two parallel microstrip lines with a photoconductive gap in one of the lines, joined together at the end. The signals on the two lines are again designed in such a way so as to add with a π phase difference. This configuration could serve as a NOT (inverter) , since if the gaps is excited, the microwave signal path will be connected, and the two

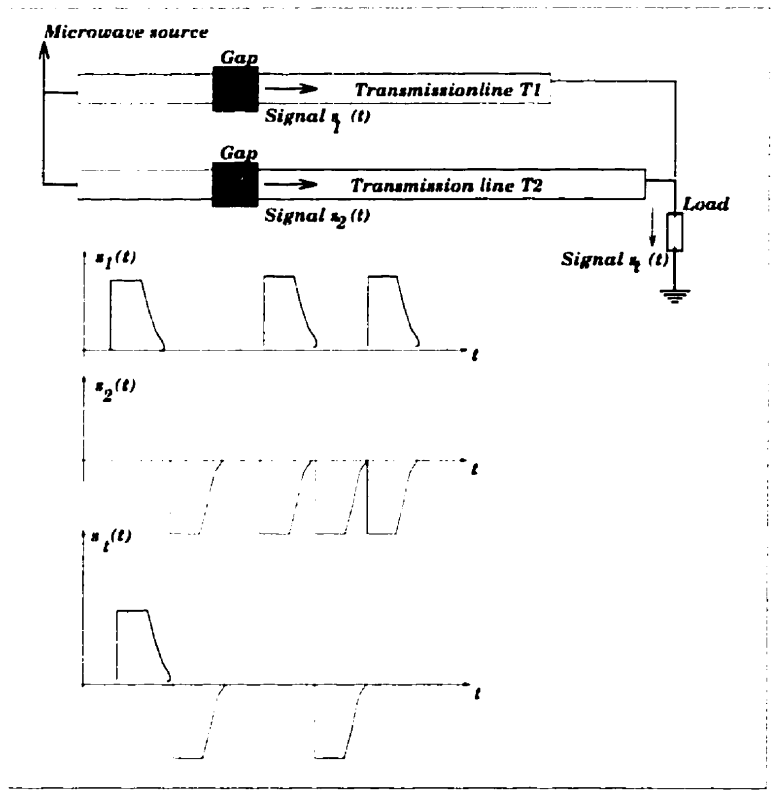

Figure 3.9: An schematic top view of an optically controlled XOR Gate. Only when either of the optical signals with wavelengths λ_1 and λ_2 are present, the device will be ON. If both signals are there, the device will be OFF, since the two microwave signals will cancel each other, as shown.

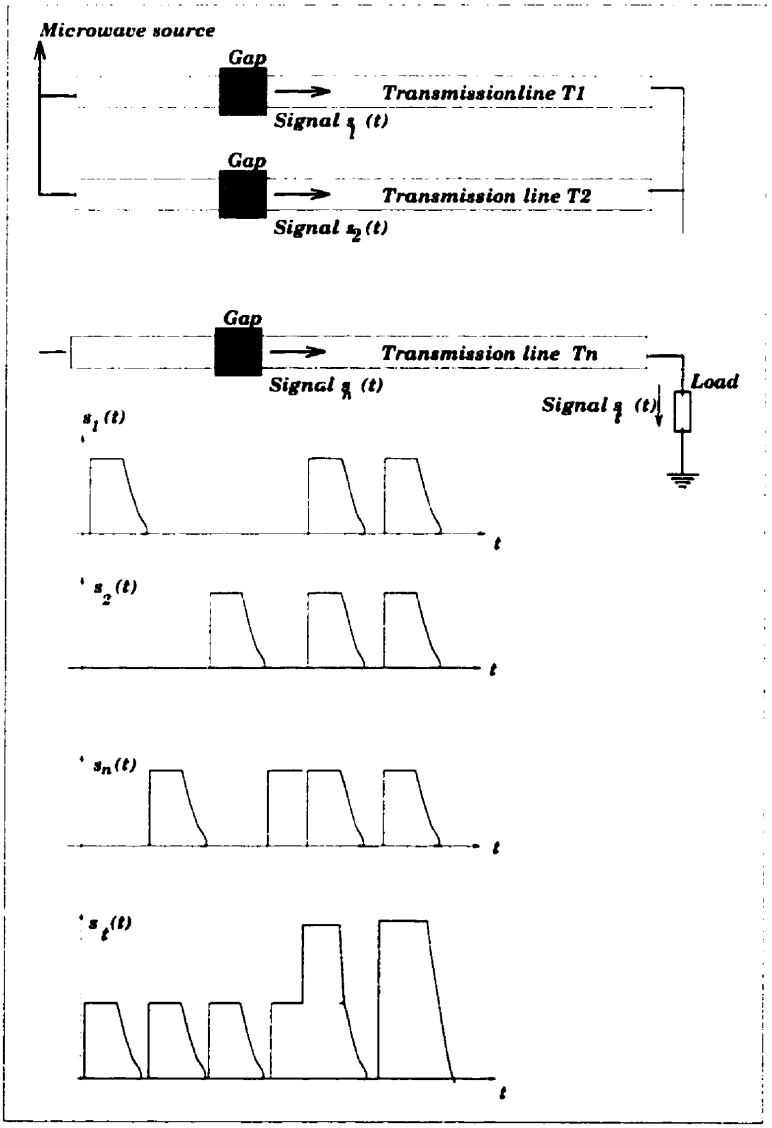

Figure 3.10: A schematic top view of an optically controlled OR Gate with multiple inputs. When either one or more of the optical signals with wavelengths λ_1 ,λ_2,... λ_n are present, the device will be ON, as shown.

signals will cancel each other. Figure 3.11 describe this situation and shows the different signals.

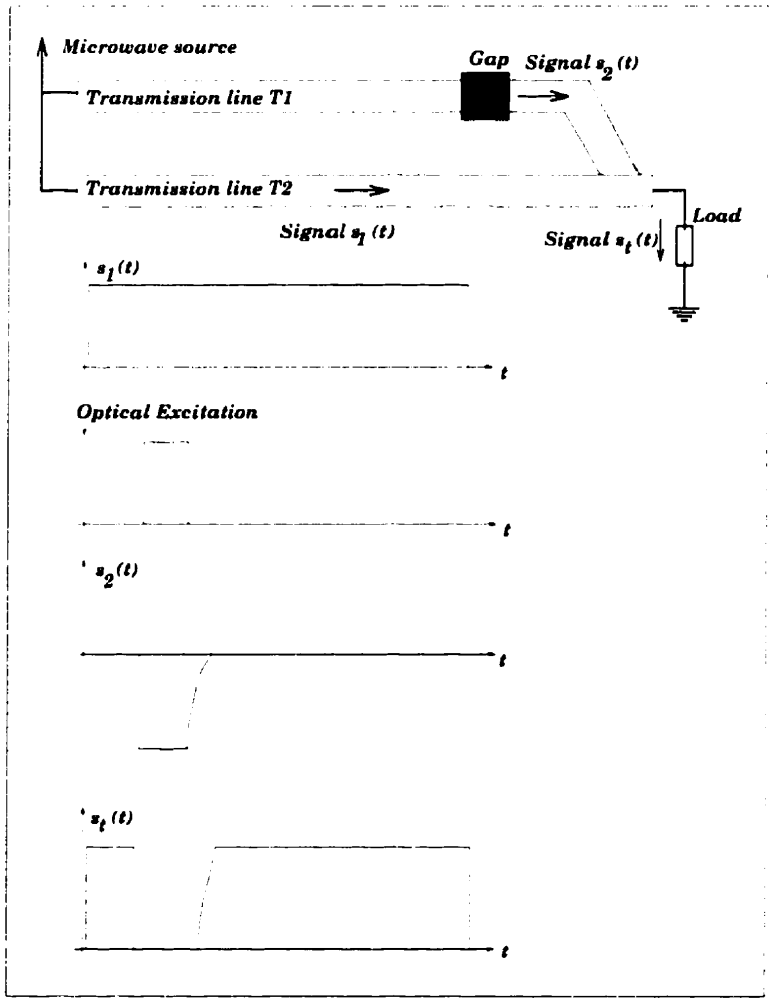

Figure 3.11: A top view of an optically controlled NOT (inverter) logic. When the gap is excited, the two microwave signals add destructively, due to phase cancellation, as shown.

For each of these devices, the complete design would include addressing issues like the study of the suitable model to analyze the optical energy coupling and how to optimize this process in order to achieve both efficiency and uniform distribution of carriers.

In the following section, an algorithm for computing the optical signal propagation characteristics in highly lossy guiding systems is presented. This algorithm provides the complex propagation constant and optical transverse distribution for a multi-layered

guiding system. This information is essential in computing the optical signal absorption, and providing the input excitation for numerical simulators such as the vector finite difference time domain and the vector beam propagation method. These simulators are used in this thesis to design the optimum optical guiding system.

3.4 Modeling of Highly Lossy Optical Guiding Structures

This section presents the electromagnetic model that is used to model the optical component of the proposed optical guided-wave controlled microwave switch. Using this model, the optical power distribution within the microstrip gap region is accurately computed. The optical guiding system proposed for the optical control element is a directional coupler, which is essentially a multi-layered optical waveguide with one or more lossy layers. The width of the microstrip transmission line is typically several hundreds of optical wavelengths wide. Thus the optical waveguide problem reduces to a two-dimensional problem.

This section presents an algorithm that computes the propagation characteristics and fields distribution in a highly lossy multi-layered optical slab waveguide using a simple exact iterative method. Starting with the solution for the equivalent lossless structure, the algorithm goes through several iterations for computing the complex effective refractive index of the lossy guiding system. This analysis was developed by Sharma and Singh [121] [122]. A brief summary of the analysis is presented next. A computer code based on this analysis was developed and used in the present research.

Obtaining the propagation characteristics of lossy structures normally require scanning the complex domain. This is potentially a computationally expensive step. In order to avoid this procedure, several first order approximation techniques have been proposed [123] [124] [125] [126]. These techniques are restricted to low-loss structures and most of them still require considerable numerical effort.

The algorithm presented here is simple and exact. It is also perfectly suited for highly lossy structures, which is the situation at hand. For a given lossy structure, the eigenvalues for the lossless similar structure are computed first. Utilizing those, the complex propagation characteristics are computed via simple algebraic expressions.

3.4.1 Theory

Consider a slab waveguide structure comprised of N layers of lossy dielectrics. Each layer is characterized by a refractive index n_m given by

$$n_m = n_m{}' + jn_m{}'' \,, \tag{3.1}$$

and a relative permittivity ϵ_{rm} given by

$$\epsilon_{rm} = \epsilon_{rm}{}' + j\epsilon_{rm}{}'' \;=\; (n_m{}')^2 - (n_m{}'')^2 + j(2n_m{}'n_m{}'') \,. \tag{3.2}$$

The solution of the scalar wave equation for the discrete bound modes of the structure can be written as

$$\Psi_1 = A_1 e^{\gamma_1 x} \,, \tag{3.3}$$

$$\Psi_2 = A_2 \cos\left[\gamma_2(x - x_1)\right] \;+\; B_2 \sin\left[\gamma_2(x - x_1)\right], \tag{3.4}$$

$$\Psi_N = A_N \cos\left[\gamma_N(x - x_{N-1})\right] \;+\; B_N \sin\left[\gamma_N(x - x_{N-1})\right], \tag{3.5}$$

where Ψ_i represents E_y for TE modes or H_y for TM modes in the layer m. A_m and B_m are complex constants. For layer 1, which is the top layer, γ_1 is given by

$$\gamma_1 = k_o\sqrt{\epsilon_{eff} - \epsilon_1} \,, \tag{3.6}$$

whereas for any other layer, γ_m is given by

$$\gamma_m = k_o\sqrt{\epsilon_m - \epsilon_{eff}} \,, \tag{3.7}$$

where ϵ_{eff} is given by

$$\epsilon_{eff} = \epsilon_{eff}{}' + j\epsilon_{eff}{}'' = n_{eff}{}^2 == \left(\frac{\beta}{k_o}\right)^2 \;=\; (n_{eff}{}' + jn_{eff}{}'')^2 \tag{3.8}$$

Applying the well known boundary conditions at each interface, and simplifying, one arrives at the following recurrence relations [121]:

$$A_2 = A_1 , \tag{3.9}$$

$$B_2 = G_1 A_1 , \tag{3.10}$$

$$A_{m+1} = A_m \cos(\gamma_m d_m) + B_m \sin(\gamma_m d_m) , \tag{3.11}$$

$$B_{m+1} = G_m[-A_m \cos(\gamma_m d_m) + B_m \sin(\gamma_m d_m)] , \tag{3.12}$$

where d_m is the layer thickness and is given by $(x_{m+1} - x_m)$ and

$$G_m = \begin{cases} \frac{\gamma_m}{\gamma_{m+1}} & \text{for TE modes ,} \\ \frac{\gamma_m}{\gamma_{m+1}} \frac{\epsilon_{m+1}}{\epsilon_m} & \text{for TM modes .} \end{cases} \tag{3.13}$$

For bound modes with exponentially decaying functions in the top and bottom layers, an eigenvalue equation $F(n_{eff})$ can be defined as

$$F(n_{eff}) = A_N \pm jB_N , \tag{3.14}$$

where the layer N is the bottom layer. The $\pm$ signs correspond to the cases where $Im\gamma_N$ is positive or negative respectively. The quantity $F(n_{eff})$ represents the amplitude of the exponential growth term in the substrate. An exact eigenvalue for n_{eff} should lead to $F(n_{eff})$=0. For a given n_{eff}, the derivative of $F(n_{eff})$ is given by

$$F(n_{eff})' = A_N' \pm jB_N' , \tag{3.15}$$

where

$$A_2' = A_1' = 0 , \tag{3.16}$$

$$B_2' = n_{eff} k_o^2 \left(\frac{1}{\gamma_1^2} + \frac{1}{\gamma_2^2} \right) B_2 , \tag{3.17}$$

$$A_{m+1}' = A_m' \cos(\gamma_m d_m) + B_m \sin(\gamma_m d_m) - B_{m+1} n_{eff} k_o^2 \frac{d_m}{G_m \gamma_m} , \tag{3.18}$$

$$B_{m+1}' = G_m[B_m' \cos(\gamma_m d_m) - A_m' \sin(\gamma_m d_m)] + B_{m+1} \left(\frac{1}{\gamma_1^2} + \frac{1}{\gamma_2^2} \right) + A_{m+1} n_{eff} k_o^2 \frac{d_m}{G_m \gamma_m} , \tag{3.19}$$

where all derivatives are with respect to n_{eff}.

The algorithm to solve the complex eigenvalue problem proceeds as follows: First, a first-order solution is obtained starting by solving the real eigenvalue problem, then a refinement to this solution is computed using Newton-Raphson method. The function to which the Newton-Raphson method is applied is $F(n_{eff})$.

First Order Solution

The real eigenvalue problem is solved first. The imaginary part of ϵ_m is set to zero in all layers. A corresponding solution for the effective index n_{eff} is obtained. For this case, n_{eff} and F are real. This solution gives a first order estimate for the real part of n_{eff}, denoted as $n_{eff}^{(0)'}$. The corresponding A_m, B_m and γ_m can be obtained analytically utilizing 3.9 - 3.13. Once the problem of the lossless structure is solved, all subsequent calculations utilize analytical expressions.

The imaginary part of the effective index n_{eff}'' is related to the signal attenuation due to ohmic loss in the absorbing layers. This can be expressed in terms of the fields as [127]:

$$n_{eff}'' = \begin{cases} \dfrac{\int_{-\infty}^{\infty} \epsilon' |E_y|^2 dx}{2Re\left(\int_{-\infty}^{\infty} n_{eff}^* |E_y|^2 dx\right)} & \text{for TE modes ,} \\ \dfrac{(n_{eff})^2 \int_{-\infty}^{\infty} \epsilon' |\frac{H_y}{\epsilon}|^2 dx + \frac{1}{k_0^2} \int_{-\infty}^{\infty} \epsilon' |\frac{H_y'}{\epsilon}|^2 dx}{2Re\left(n_{eff} \int_{-\infty}^{\infty} \frac{1}{\epsilon} |H_y|^2 dx\right)} & \text{for TM modes ,} \end{cases} \tag{3.20}$$

where E_y and H_y are the $y-$components of the exact fields of the absorbing structure. Using the solution obtained for E_y or H_y of the lossless structure instead of the exact solution, a first order estimate for n_{eff}'' given by $n_{eff}^{(0)''}$ can be obtained. Evaluating the above integrals using the fields description given 3.3- 3.5 yields the following analytical

expressions for ${n^{(0)}_{eff}}''$:

$$ {n^{(0)}_{eff}}'' = \begin{cases} \left(\sum_{m=1}^{N} p_m {\epsilon_m}''\right) / \left(2{n^{(0)}_{eff}}' \sum_{m=1}^{N} p_m\right) & \text{for TE modes ,} \\ \left({n^{(0)}_{eff}}' \sum_{m=1}^{N} \frac{q_m}{\epsilon_m{}^2}\right) / \left(2\sum_{m=1}^{N} \frac{p_m}{\epsilon_m}\right) & \text{for TM modes .} \end{cases} \tag{3.21} $$

where

$$ p_1 = \frac{{A_1}^2}{2\gamma_1} , \tag{3.22} $$

$$ p_N = \frac{j(A_N - jB_N)^2}{8\gamma_N} , \tag{3.23} $$

$$ p_m = \frac{({A_m}^2 + {B_m}^2)d_m}{2} + \frac{({A_m}^2 - {B_m}^2)\sin(2\gamma_m d_m)}{4\gamma_m} + A_m B_m \frac{\sin^2(\gamma_m d_m)}{\gamma_m} \quad 1 < m < N, \tag{3.24} $$

$$ q_1 = p_1(2 - \Delta_1), \tag{3.25} $$

$$ q_N = p_N \Delta_N , \tag{3.26} $$

$$ q_N = p_N \Delta_N , \tag{3.27} $$

$$ q_m = p_m(2 - \Delta_m) - (1 - \Delta_m)({A_m}^2 + {B_m}^2)d_m , \tag{3.28} $$

where

$$ \Delta_m = \frac{{\epsilon_m}'}{{n_{eff}}^2} \tag{3.29} $$

Once ${n^{(0)}_{eff}}$ is evaluated, a first order approximation for the complex effective index, and subsequently the fields, is obtained. In some cases, this first order approximation is sufficiently accurate.

Exact Solution

To obtain a more accurate solution, Newton-Raphson method is deployed to evaluate a more accurate root of the equation $F(n_{eff}) = 0$, Hence

$$ {n^{(1)}_{eff}} = {n^{(0)}_{eff}} - \frac{F({n^{(0)}_{eff}})}{F'({n^{(0)}_{eff}})} , \tag{3.30} $$

Mode	Lossless	$n_{eff}{}^{(0)}$	$n_{eff}{}^{(2)}$	$n_{eff}{}^{(4)}$	$\alpha(\frac{dB}{mm})$
TM_0	3.45707 -j0	3.45380 -j0.06901	3.45366 -j0.07014	3.45366 -j0.07014	2469.50
TM_1	3.31650 -j0	3.31213 -j0.02435	3.31205 -j0.02356	3.31205 -j0.02356	829.51

Table 3.1: Convergence of the results for the detector-loaded waveguide of Figure 3.12.

with subsequent roots given by

$$n^{(p+1)}{}_{eff} = n^{(p)}{}_{eff} - \frac{F(n^{(p)}{}_{eff})}{F'(n^{(p)}{}_{eff})} . \tag{3.31}$$

In most calculations, $n^{(2)}{}_{eff}$ is the converged value.

Example

This algorithm is applied to the problem of the detector loaded waveguide whose configuration is shown in figure 3.12. This configuration is a standard testing configuration for numerical algorithms [128]. It also closely resembles the type of application considered in this thesis, where optical energy is propagated in a low loss region then coupled into an absorbing layer where optical energy is used to excite electrical carriers. Table 3.1 show the computed complex propagation constant for the first two TM modes of this eight-layer structure. Even for the extremely high attenuation of $\approx$ 2500 dB/mm experienced by the TM_0 mode, only two iterations are required for a convergent result of less than 0.1% variation.

The transverse distribution of the scalar field for the TM_0 and TM_1 modes of the lossless and lossy cases of the structure depicted in Figure 3.12 are shown in Figure 3.13. The transverse distribution of the field magnitudes for these modes are depicted in Figure 3.14.

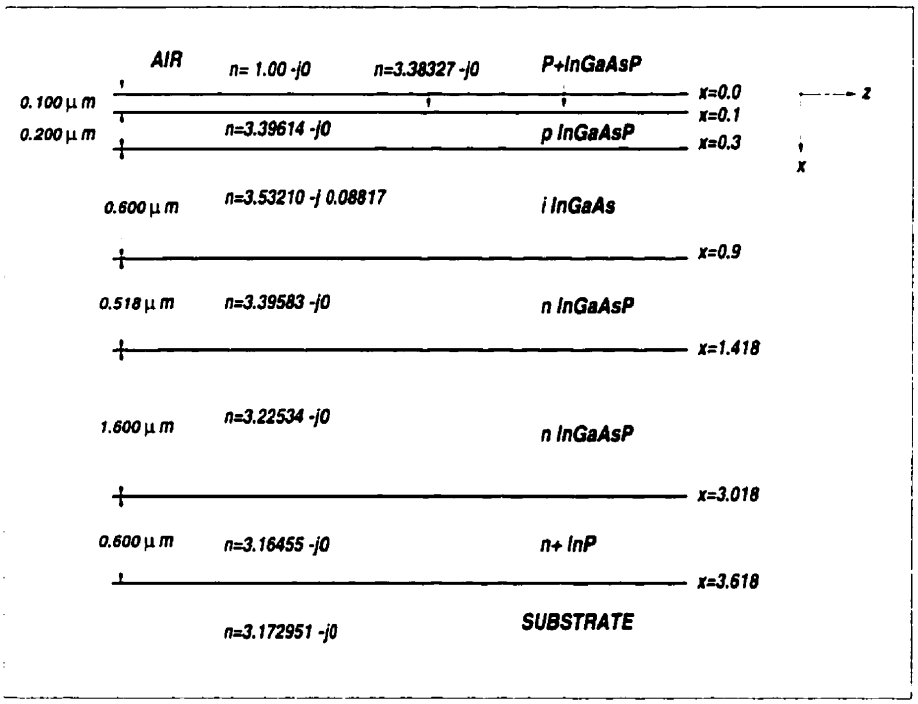

Figure 3.12: A schematic cross-section of a detector-loaded optical waveguide. The figure shows the width and the complex refractive index of each layer. This guiding structure is used as an example to demonstrate the algorithm presented in this chapter.

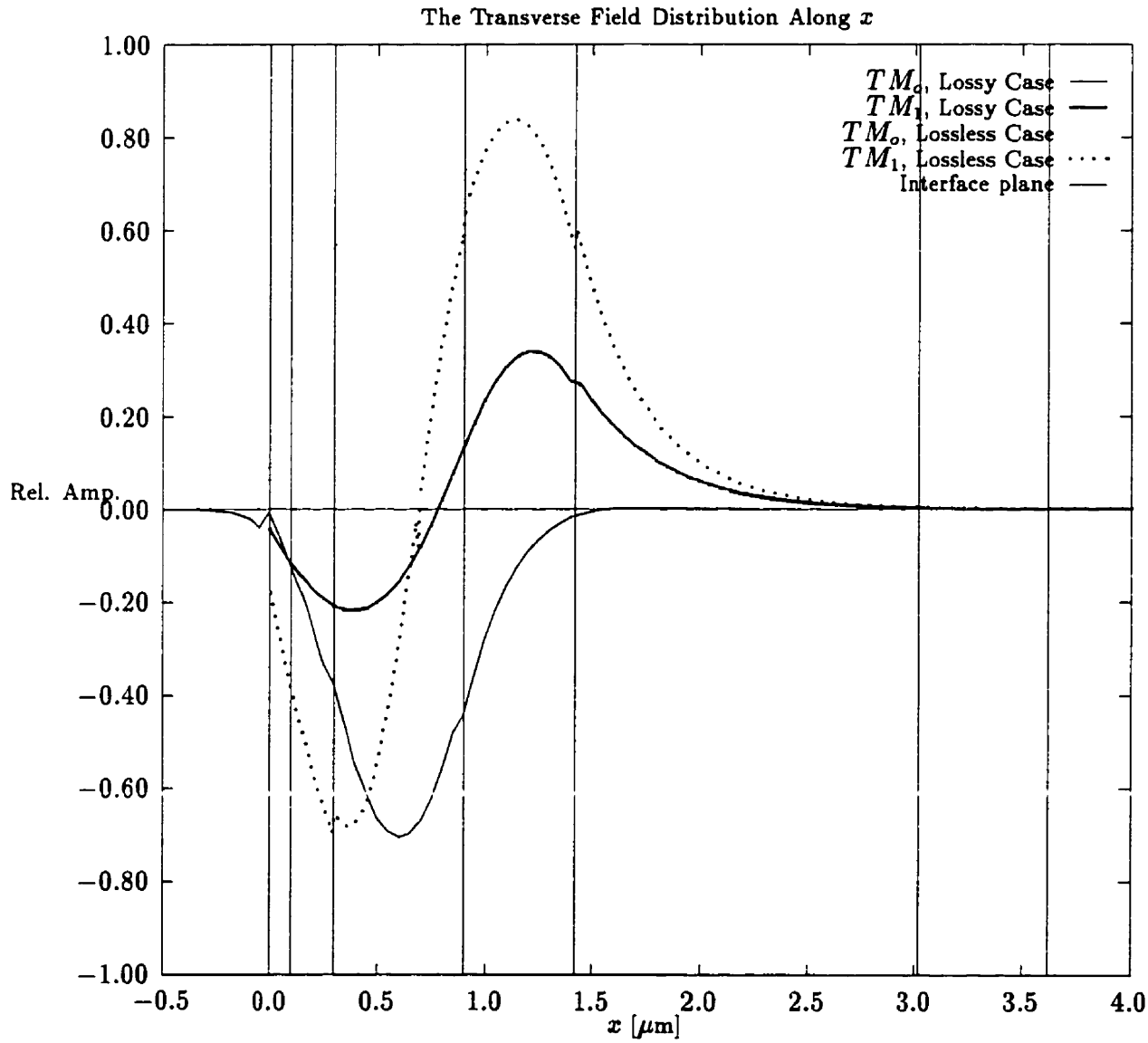

Figure 3.13: The transverse distribution of the scalar field for the lossless and lossy cases of the structure depicted in Figure 3.12.

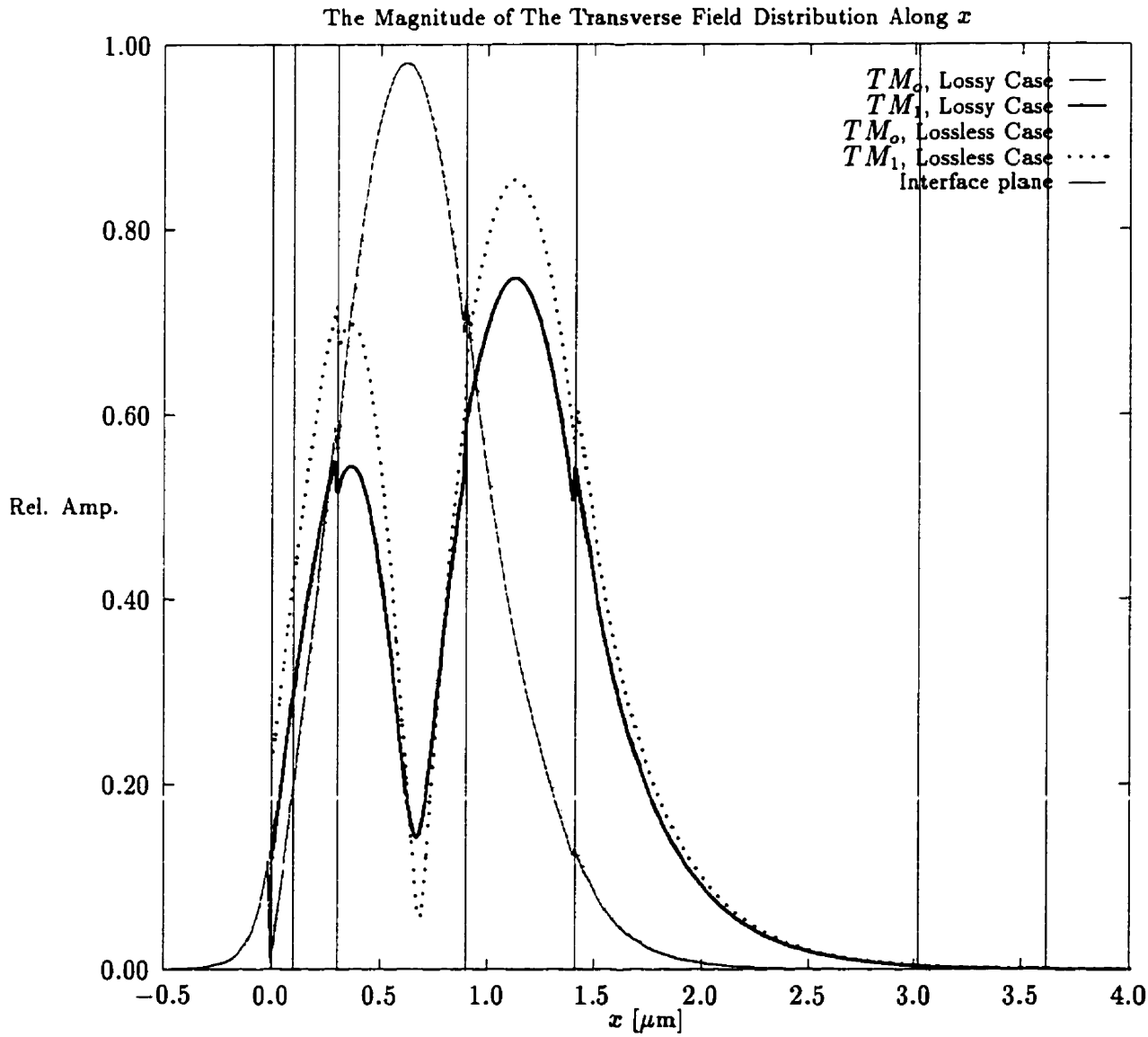

Figure 3.14: **The transverse distribution of the field magnitude for the lossless and lossy cases of the structure depicted in Figure 3.12.**

3.4.2 Effect of High Loss on the Modal Nature of the fields

A mode is an eigensolution of the wave equation. It describes the fields distribution as a function of the transverse coordinates. The modal field expression is a multiplying term to the fast-varying phase term $e^{j\beta z}$ where z is the axial propagation direction and β is the phase constant. The product of these two terms is what defines the field everywhere. Hence, the mode describes a field whose amplitude is independent of the axial propagation direction z, and whose phase increases linearily with z.

For a lossy structure, there is no theoretically valid definition of the mode. As a perturbation to the lossless case, the multiplying "phase" term is modified to be $e^{j\beta z - \alpha z}$, where α is the attenuation constant. The above algorithm attempts to calculate the complex effective index $n_{eff} = \frac{\beta + j\alpha}{k_o}$. Perturbation assumes that the "mode" of a lossy structure keeps its transverse distribution as it propagates along the axial direction z, and the only amplitude variation it endures is an exponential decay $e^{-\alpha z}$. While this is a very good approximation in most practical cases, it is not always valid for a number of reasons. First, the effective index concept, from its definition, is an averaged quantity. It does not represent the exact amount of loss in each layer of the structure. This is of an increasing importance when the various layers have different loss tangents, like the above given example, where one layer is highly lossy and the others are lossless. Secondly, when the the loss is quite high in one of the layers, the field distribution (shape) varies at different axial locations. Thirdly, because of the above effects, the scalar nature of the modes cannot be maintained, and a vector analysis become more proper. It may also mean, depending on the level of loss, that the fields cannot be separated into TE and TM polarizations.

To demonstrate this, the following study was conducted using a vector finite difference time domain two dimensional (VFDTD-2D) simulation [129] [130] [131]. The detector loaded waveguide problem of 3.12 is studied again. A simulation window in the x direction of width 5.62 μm is considered. This includes the layers shown in Figure 3.12 plus a 1 μm wide air region on top and a 1 μm wide substrate region at the bottom. The $x = 0$

coordinate is situated at the bottom of the substrate. A mesh discretization of 100 points per micrometer is considered. This translates to more than 44 points per wavelength which satisfies the accuracy criteria given in [131]. A propagation length of 4.00 μm for the lossy cases is studied, again using a mesh discretization of 100 points per micrometer.

Figure 3.15 depicts the transverse field profile of the TE_0 mode for the lossless case (i.e. with the third layer having n_3= 3.5321 -j0), at different points along a 100 μm propagation distance. The shown attenuation is a numerical attenuation due to the nature of the absorbing boundary conditions at the simulation window's extremities.

Figure 3.16 depicts the transverse field profile of the TE_0 mode for the case where σ = 2500 $\mho$/m (i.e. with the *InGaAs* layer having n_3= 3.5321 -j0.033), at distances z= 0.0, 0.1,1.0,2.0 and 3.9 μm. In this case, while the attenuation is relatively high (α = 730 dB/mm), the perturbation assumption still holds. The same is true for Figure 3.17 which depicts the transverse field profile of the TE_0 mode for the case where σ = 8400 $\mho$/m (i.e. with the *InGaAs* layer having n_3= 3.5321 -j0.11), at distances z= 0.0, 0.1,1.0,2.0 and 3.9 μm. In this case, for an attenuation α = 2430 dB/mm, the perturbation theory again still holds.

For much higher conductivities, where the semiconductor assumes quasi-metallic properties, the above analysis fails. This is shown in Figures 3.18, 3.19 and 3.20 where σ = 2.5x10^4$\mho$/m, 2.5x10^5$\mho$/m and 2.5x10^6$\mho$/m respectively. These cases correspond to a reflective index n_3 = 3.5321 -j0.33, 3.5321 -j3.31, and 3.5321 -j33.1 respectively. As shown, the mode concept is no longer valid, with the transverse field distribution varying along the propagation axis.

For the research conducted in this thesis, simulations using Vector Finite Difference time-domain (VFDTD) and the Vector Beam Propagation Method (VBPM) numerical algorithms are utilized to model the optical component of the device, since it represents a much more accurate approach over modal analysis. These numerical simulators however, require an accurate launching mode at the onset of the simulation, to avoid errors due to exciting the guiding system with an inaccurate optical mode. The algorithm developed

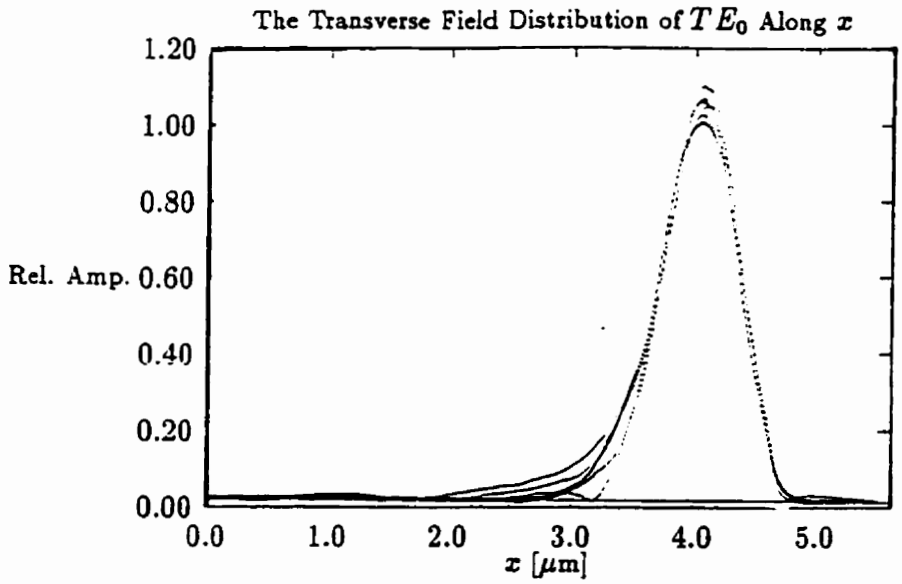

Figure 3.15: The transverse field profile of the TE_0 mode for the lossless case (i.e. n_3= 3.5321 -j0), at different points along a 100 μm propagation distance. The shown attenuation is a numerical attenuation due to the absorbing boundary conditions.

above is used to supply this launching optical field.

3.5 Optical System Design Case Study

In this section, an optical guiding system for the optical control element of the proposed devices is suggested and studied. This guiding system is built into the substrate of the microstrip line.

Consider an optical directional coupler as that shown in Figure 3.21. The directional coupler is comprised of five parallel layers: a substrate whose refractive index is $\bar{n}_s$, a cover of index $\bar{n}_c$, and two waveguides of core indices $\bar{n}_1$ and $\bar{n}_3$ with a separating cladding of index $\bar{n}_2$. These refractive indices are complex numbers in general. As a numerical example, consider the following parameters: The input waveguide, into which the optical energy is launched has a core of thickness $2d_1 = 1$ μm and refractive index $\bar{n}_1$

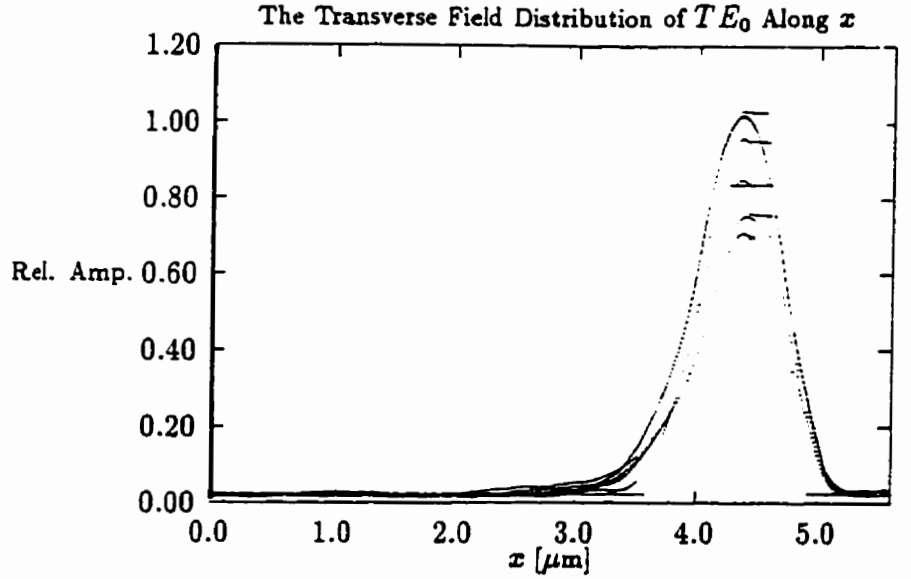

Figure 3.16: The transverse field profile of the TE_0 mode for the case where σ = 2500 $\mho$/m (i.e. n_3= 3.5321 -j0.033), at distances z= 0.0, 0.1,1.0,2.0 and 3.9 μm. α = 730 dB/mm.

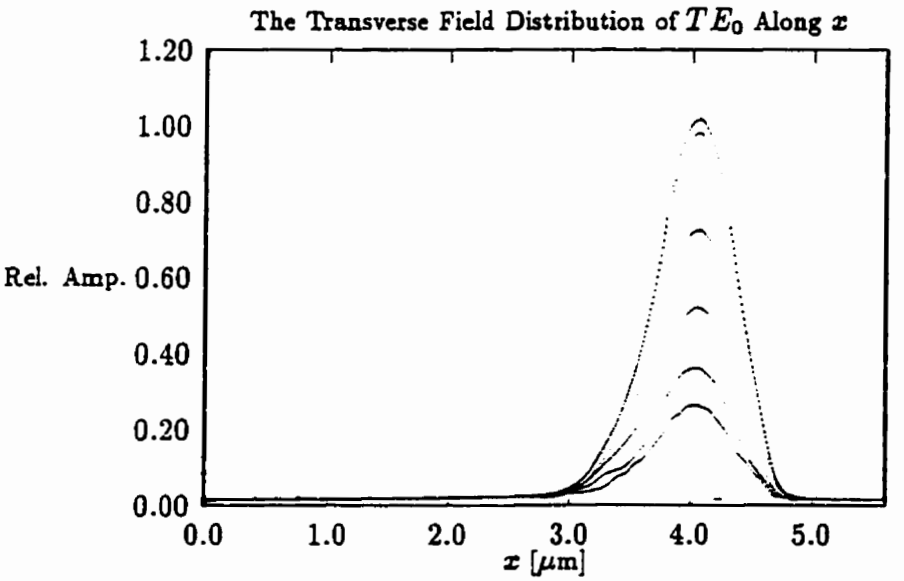

Figure 3.17: The transverse field profile of the TE_0 mode for the case where σ = 8400 $\mho$/m (i.e. n_3= 3.5321 -j0.11), at distances z= 0.0, 0.1,1.0,2.0 and 3.9 μm. α = 2430 dB/mm.

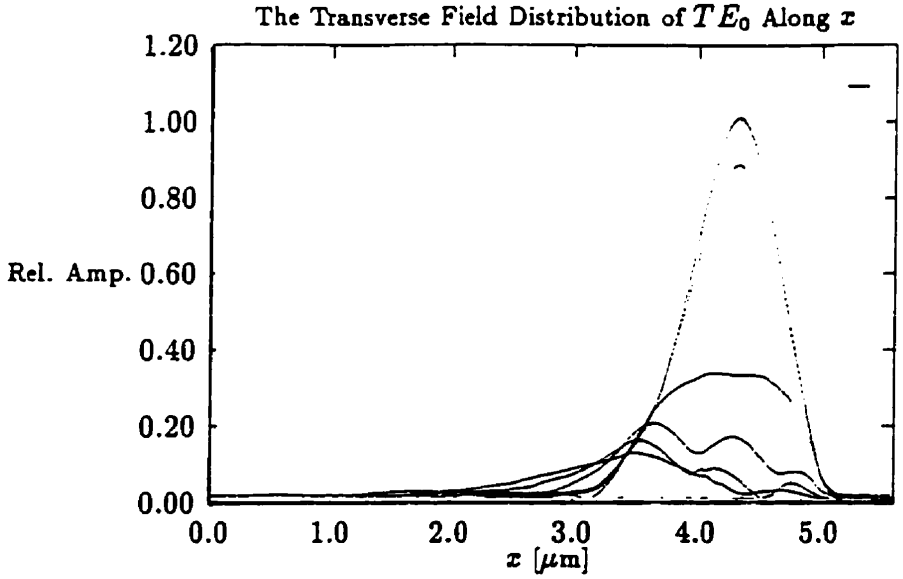

Figure 3.18: The transverse field profile of the TE_0 mode for the case where σ = 2.5x10^4℧/m (i.e. n_3= 3.5321 -j0.33), at distances z= 0.0, 0.1,1.0,2.0 and 3.9 μm. α = 2430 dB/mm.

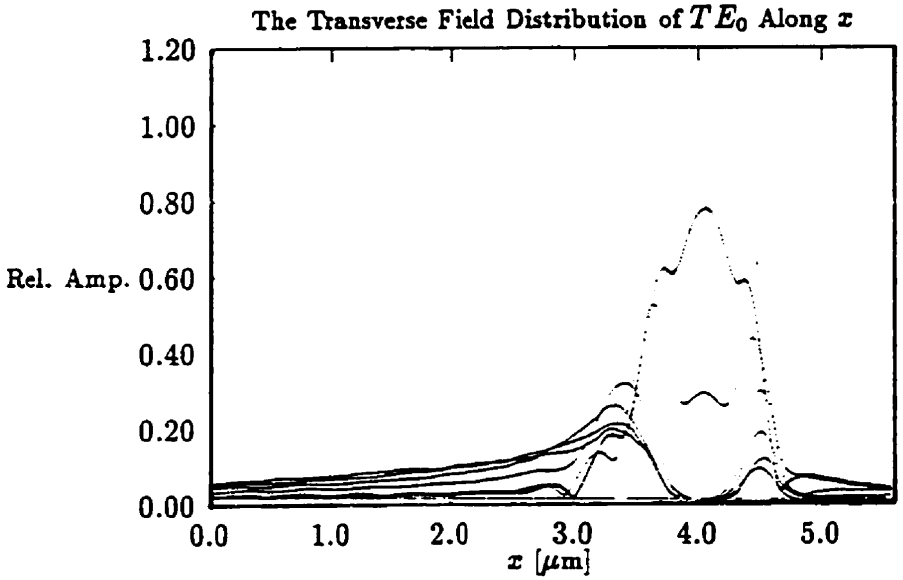

Figure 3.19: The transverse field profile of the TE_0 mode for the case where σ = 2.5x10^5℧/m (i.e. n_3= 3.5321 -j3.31), at distances z= 0.0, 0.1,1.0,2.0 and 3.9 μm. α = 2430 dB/mm.

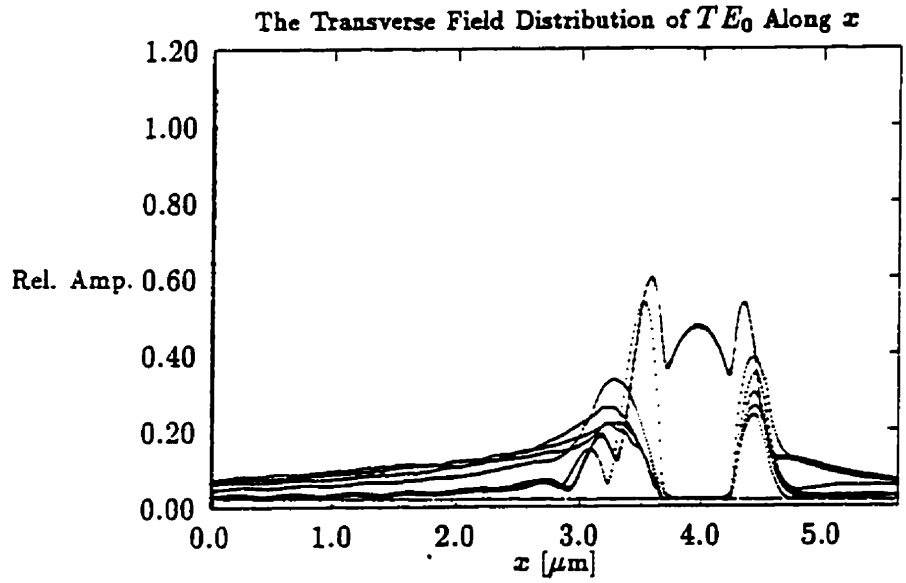

Figure 3.20: The transverse field profile of the TE_0 mode for the case where σ = 2.5x10^6℧/m (i.e. n_3= 3.5321 -j33.1), at distances z= 0.0, 0.1,1.0,2.0 and 3.9 μm. α = 2430 dB/mm.

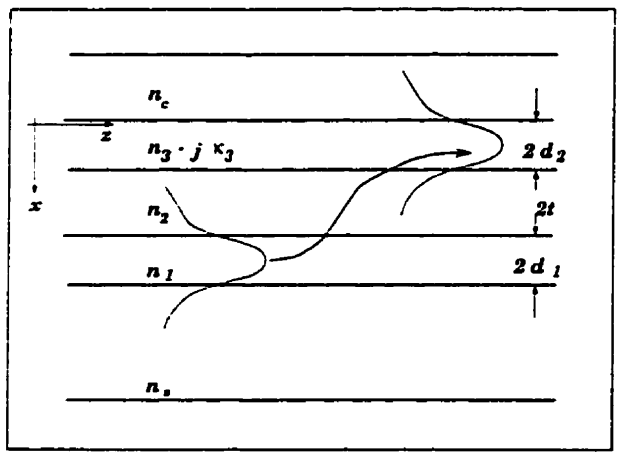

Figure 3.21: A cross-sectional view in a directional coupler with an absorbing layer

$= n_1 - j\kappa_1 = 3.65 - j0$. This guide is parallel to another waveguide, into which the optical energy couples, that has a thickness of $2d_2 = 1$ μm and a refractive index $n_3 - j\kappa_3 = 3.65 - j$ 0.0684, i.e. the core of the second guide is optically lossy or in other words absorbs optical energy. This is the active region where optical energy is absorbed and electrical carriers are released. The separating cladding is comprised of a material of refractive index n_2 =3.63. The width of the separation layer between the two guides, $2t$, a parameter that is varied in the following study.

For simplicity, the two dimensional case is considered. However, This is a quite valid approximation of the proposed structure. The microstrip line width is typically a fraction of a millimeter, which is a hundred or more optical wavelengths. The optical waveguide underneath the transmission line would have a comparable width. Hence, this width, in terms of optical wavelength is practically infinite, and the optical model is reduced to the two dimensional model depicted in Figure 3.21.

Assume that the incident optical light has a wavelength of 0.83 μm and consider the TE wave propagating down the input wave guide. The numbers given above are typical values of double heterostructure with GaAs/AlGaAs MQW materials. Refractive index values between 3.66 and 3.15 can be obtained by varying the Al composition in $AlGa_{1-x}As$ from x =0.0 to x=0.7 at a wavelength of $\approx$ 826 nm [132]. The layer of index $n_3 - j\kappa_3$ = 3.65 - j 0.0684 is a GaAs absorption layer at λ_o = 830 nm. At this wavelength, GaAs has an $n(\lambda_o)$ characteristic described by

$$n(\lambda_o) = [3.65 - 0.0005\ \delta\lambda] - j\ [0.0684 - 0.000434\ \delta\lambda] \qquad (3.32)$$

where $\delta\lambda = (\lambda - \lambda_o)$ is in nanometers.

Using the above parameters, the input field into the launching guide can be computed using the algorithm presented earlier and supplied to the Vector Beam Propagation Method (VBPM) numerical simulator [133] [134] [135] . The above parameters restrict the modal propagation of the input guide to single-mode propagation where only TE_o and TM_o modes can propagate.

In what follows, results for simulations done for different separations, $2t$, are presented. Figure 3.22 depicts the case where the guides separation is 0.6 μm. Figure 3.23 depicts the case where the guides separation is 0.5 μm. Figures 3.24 and3.25 are for the cases of $2t$ = 0.4 and 0.3 μm respectively. For comparison, the case of weak coupling in the same structure is depicted in Figure 3.26. For this case, $2t$ was chosen to be 1.5 μm. A narrow separation between the guides leads to a stronger interaction between the optical guides, and subsequently, shorter coupling lengths.

3.5.1 Conductivity and Conductance Model

From the above simulations, it is possible to estimate the rate at which optical energy is being coupled and absorbed in the GaAs layer, which in turn would give an estimate of the conductivity, $\sigma(x,z)$, and the photogenerated conductance, G_b; here x is the transverse direction and z is the axial propagation direction. Based on the simulation results, it was possible to numerically calculate the amount of power absorbed in the $GaAs$ layer along the gap length. This is depicted in Figure 3.27. The rate of absorption of optical power $\frac{\Delta P_a}{\Delta z}$ is proportional to the conductivity $\sigma(z)$ at each point along the gap. The linear portion of the curves depicted in Figure 3.27 are the regions where the plasma is evenly distributed, and hence the conductance is relatively constant. The portion at which the curve's slope is almost zero indicates dark regions with high resistivity. By numerically calculating the quantity $\frac{\Delta P_a}{\Delta z} \propto \Delta G_b$, as depicted in Figure 3.28, it is possible to investigate the way conductance changes along the gap.

If within a small length segment Δz along the gap width, a certain amount of optical power, ΔP_a is absorbed, the conductivity of this segment can be expressed as,

$$\Delta G_b(z) = \frac{\sigma(z)A}{\Delta z} \tag{3.33}$$

where A is the area normal to the propagation direction. The conductivity of the gap region is determined by a series of these segments. By adding up these series conductances,

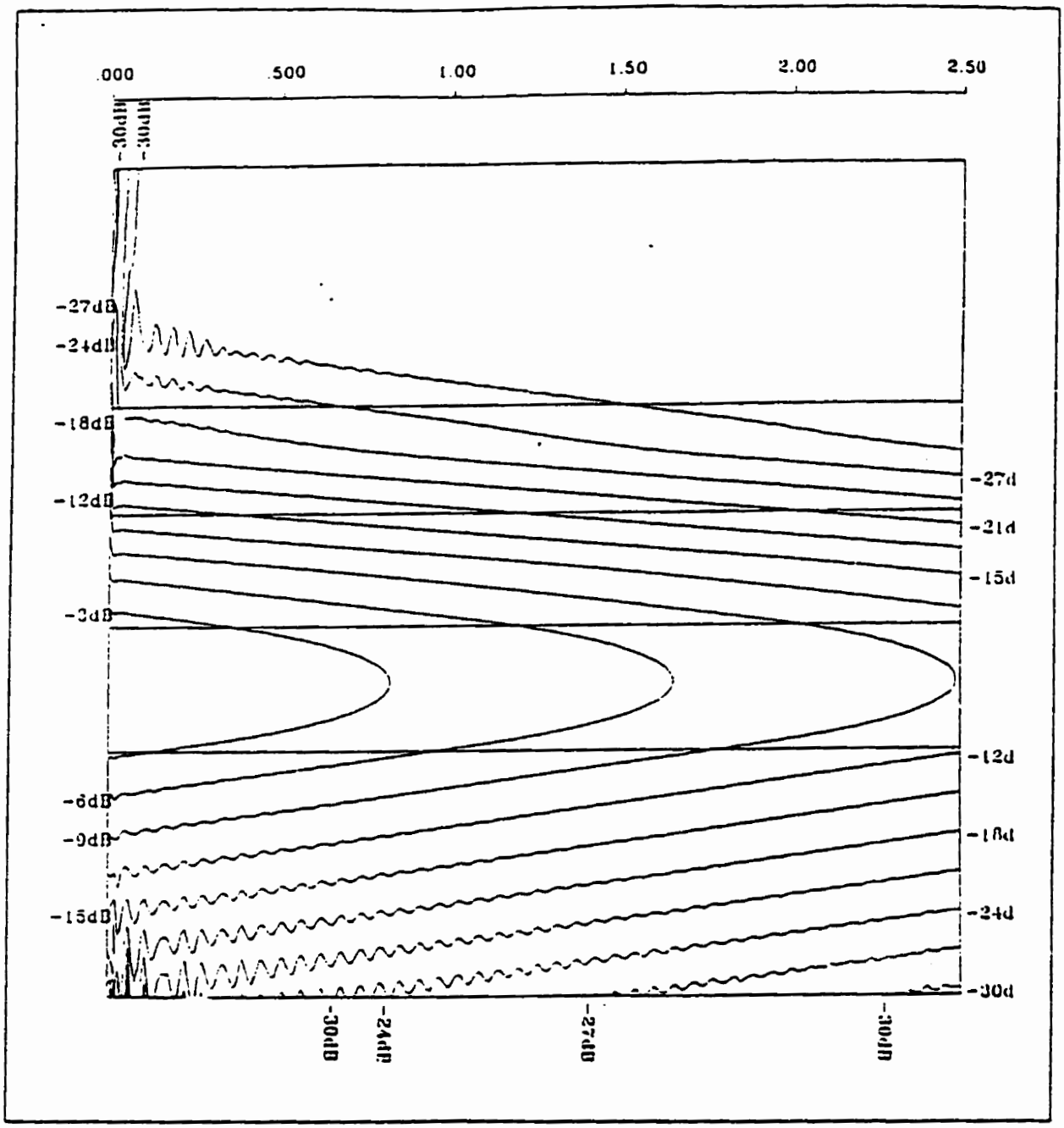

Figure 3.22: A contour plot for the E_y field amplitude in a directional coupler with one of the waveguides (the top guide) being an absorbing layer. The two waveguide thicknesses are 1 μm each and the separation between the guides is 0.6 μm. Optical power is launched into the lower guide, and is being absorbed while being coupled into the upper guide. The entire simulation length is 2.5 mm.

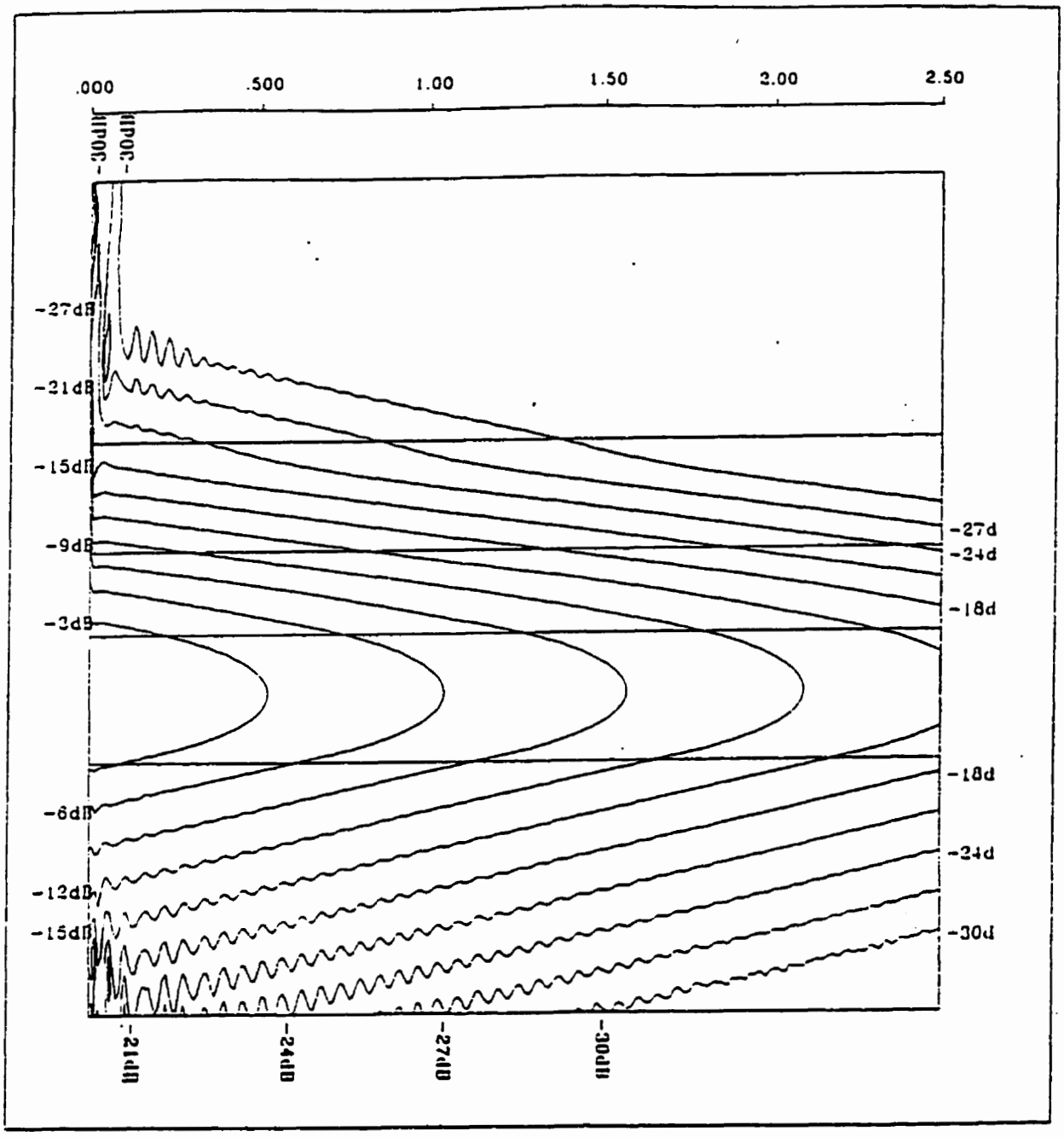

Figure 3.23: A contour plot for the E_y field amplitude in a directional coupler with one of the waveguides (the top guide) being an absorbing layer. The two waveguide thicknesses are 1 μm each and the separation between the guides is 0.5 μm. Optical power is launched into the lower guide, and is being absorbed while being coupled into the upper guide. The entire simulation length is 2.5 mm.

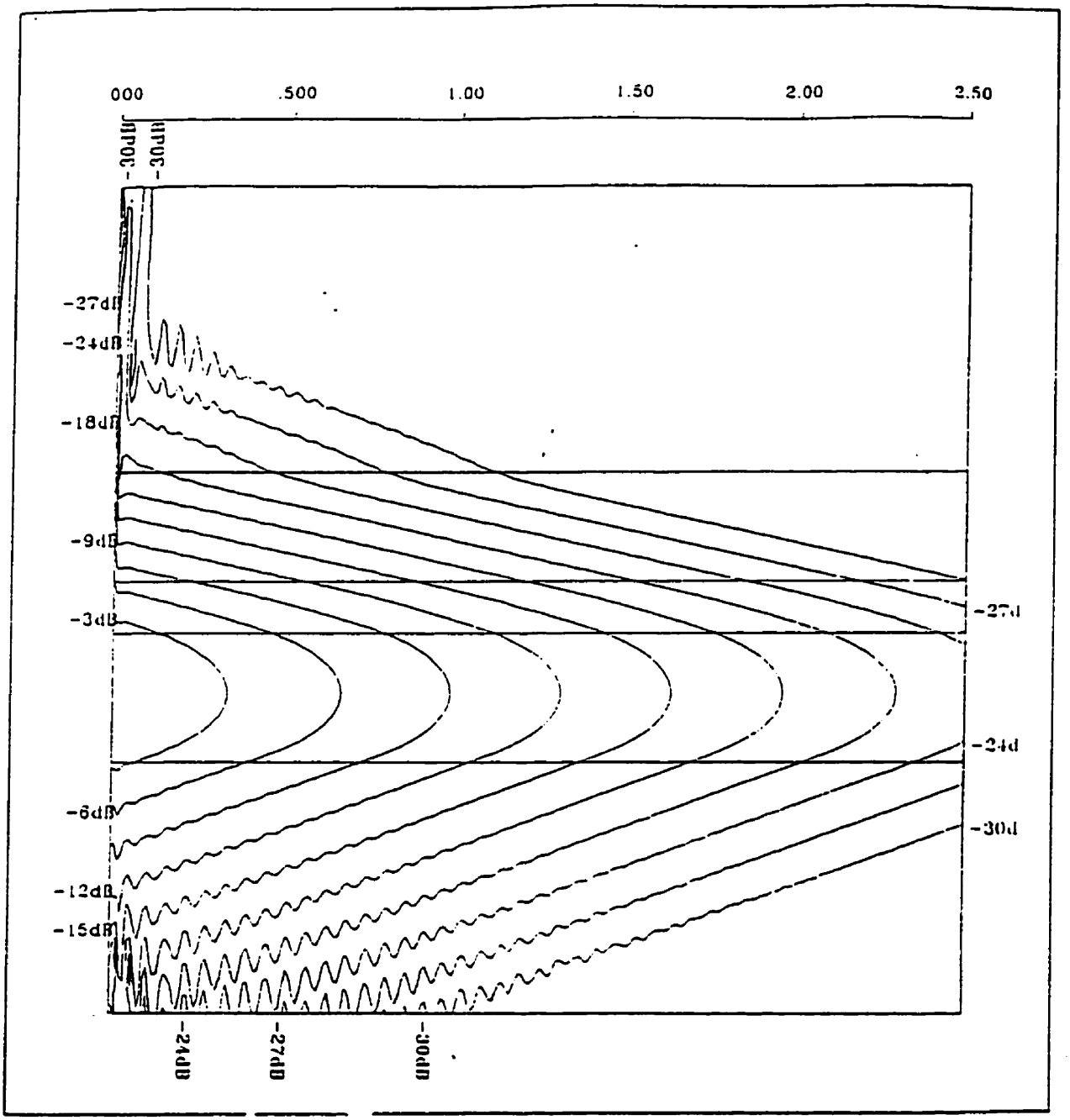

Figure 3.24: A contour plot for the E_y field amplitude in a directional coupler with one of the waveguides (the top guide) being an absorbing layer. The two waveguide thicknesses are 1 μm each and the separation between the guides is 0.4 μm. Optical power is launched into the lower guide, and is being absorbed while being coupled into the upper guide. The entire simulation length is 2.5 mm.

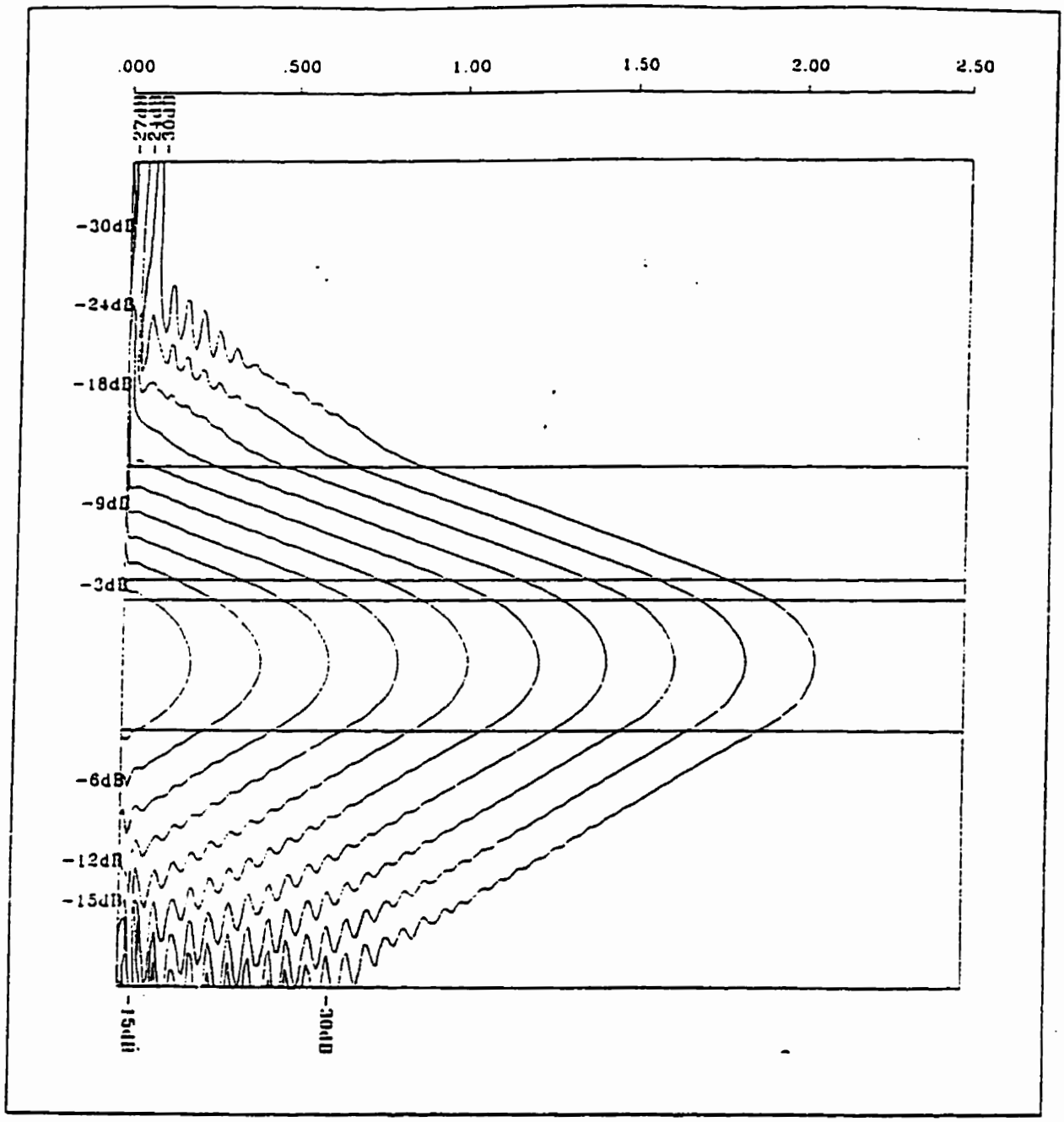

Figure 3.25: A contour plot for the E_y field amplitude in a directional coupler with one of the waveguides (the top guide) being an absorbing layer. The two waveguide thicknesses are 1 μm each and the separation between the guides is 0.3 μm. Optical power is launched into the lower guide, and is being absorbed while being coupled into the upper guide. The entire simulation length is 2.5 mm.

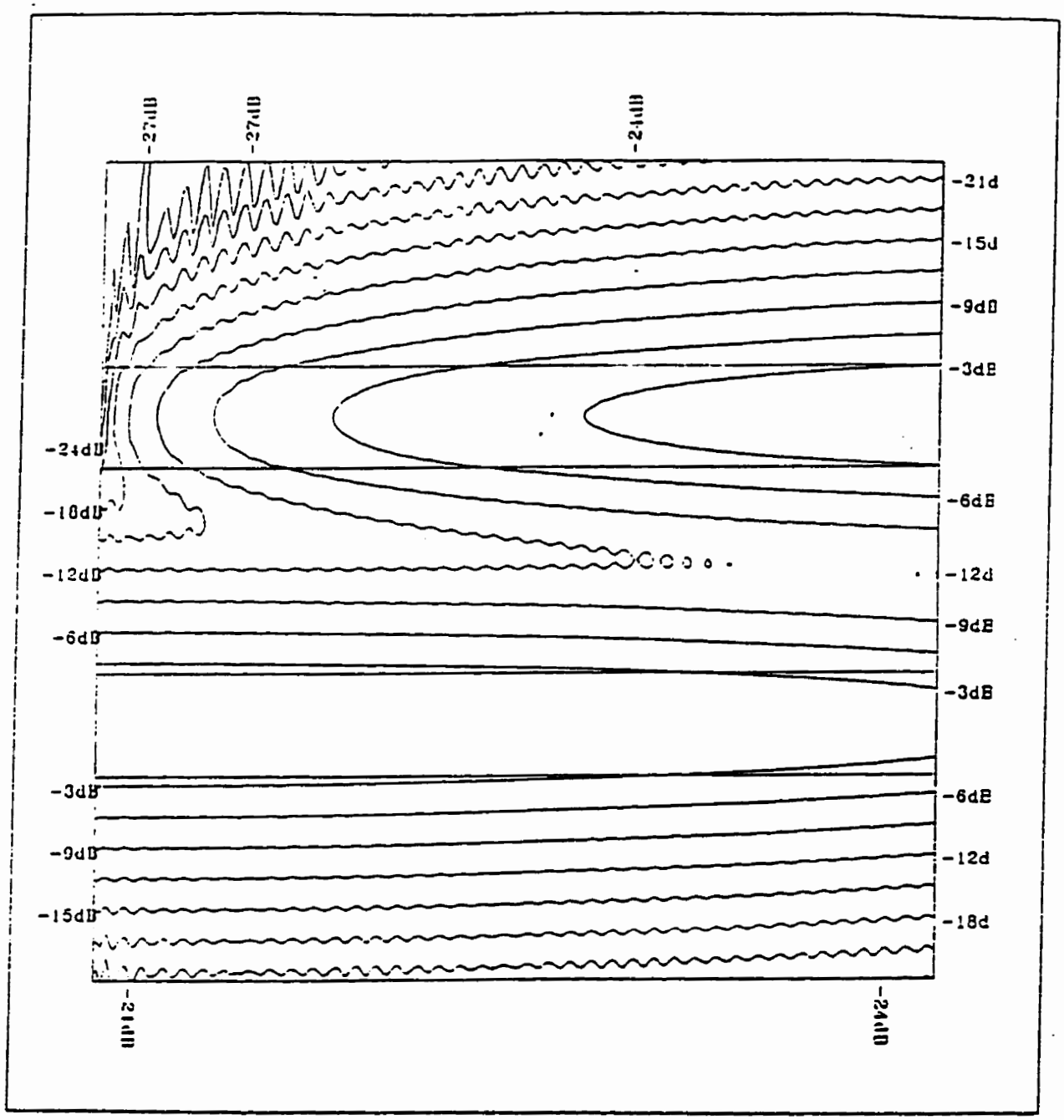

Figure 3.26: A contour plot for the E_y field amplitude in a directional coupler with one of the waveguides (the top guide) being an absorbing layer. The two waveguide thicknesses are 1 μm each and the separation between the guides is 1.5 μm. Optical power is launched into the lower guide, and is being absorbed while being coupled into the upper guide. The entire simulation length is 2.5 mm.

we get the total gap conductance, G_b.

$$\frac{1}{G_b} = \sum_{i=1}^{n} \frac{1}{\Delta G_b} = \int_0^b \frac{dz}{\sigma(z)A} \tag{3.34}$$

where b is the length of the gap.

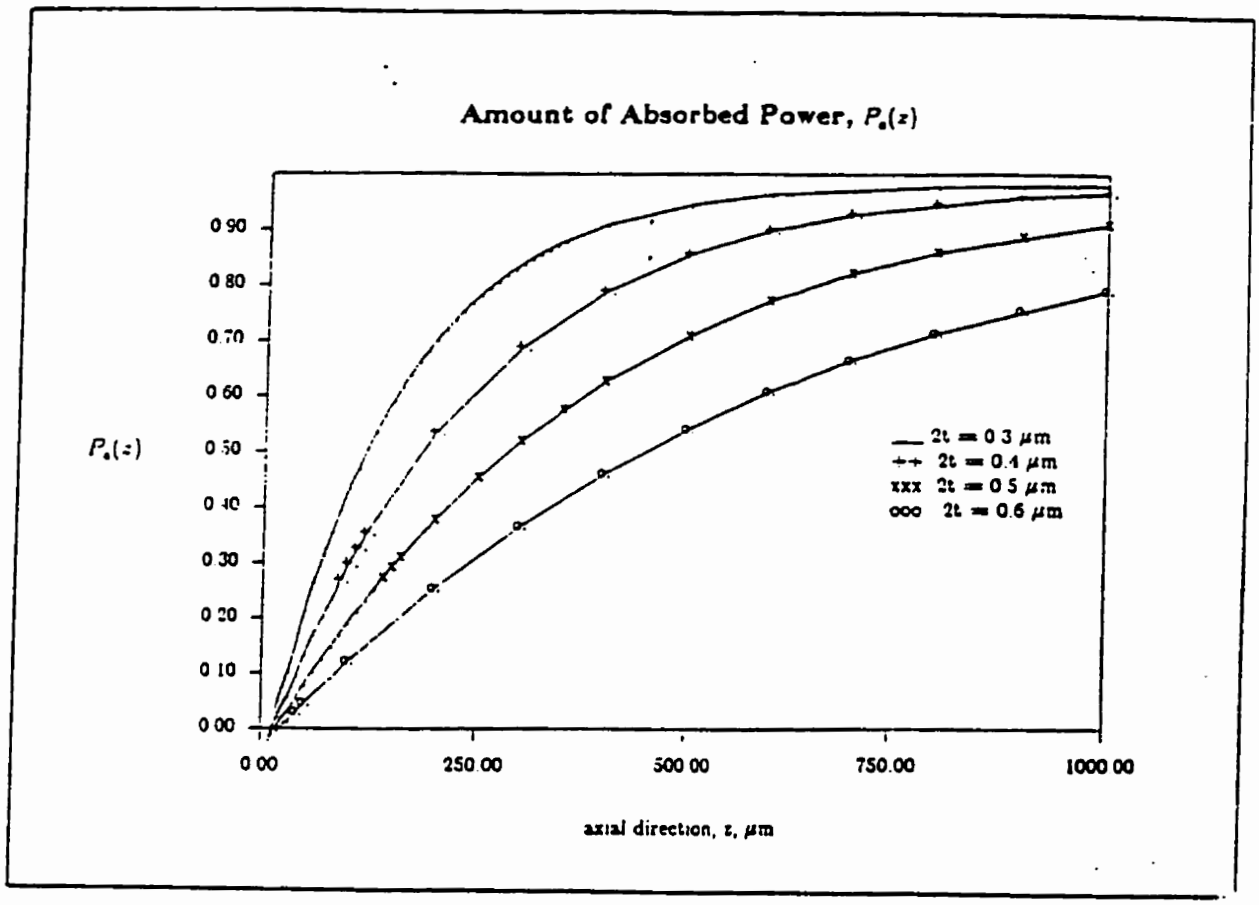

Figure 3.27: The amount of power absorbed along the gap length. The linear portion of the curves are the regions where the plasma is evenly distributed, and hence the conductance is relatively constant. The portion at which the curve's slope is almost zero indicates dark regions with high resistivity.

From Figures 3.27 and 3.28, it is evident that coupling strength affects the carriers distribution along the gap, and hence it could be used to design an evenly distributed plasma across the gap. Depending on the gap length, the coupling strength could be adjusted

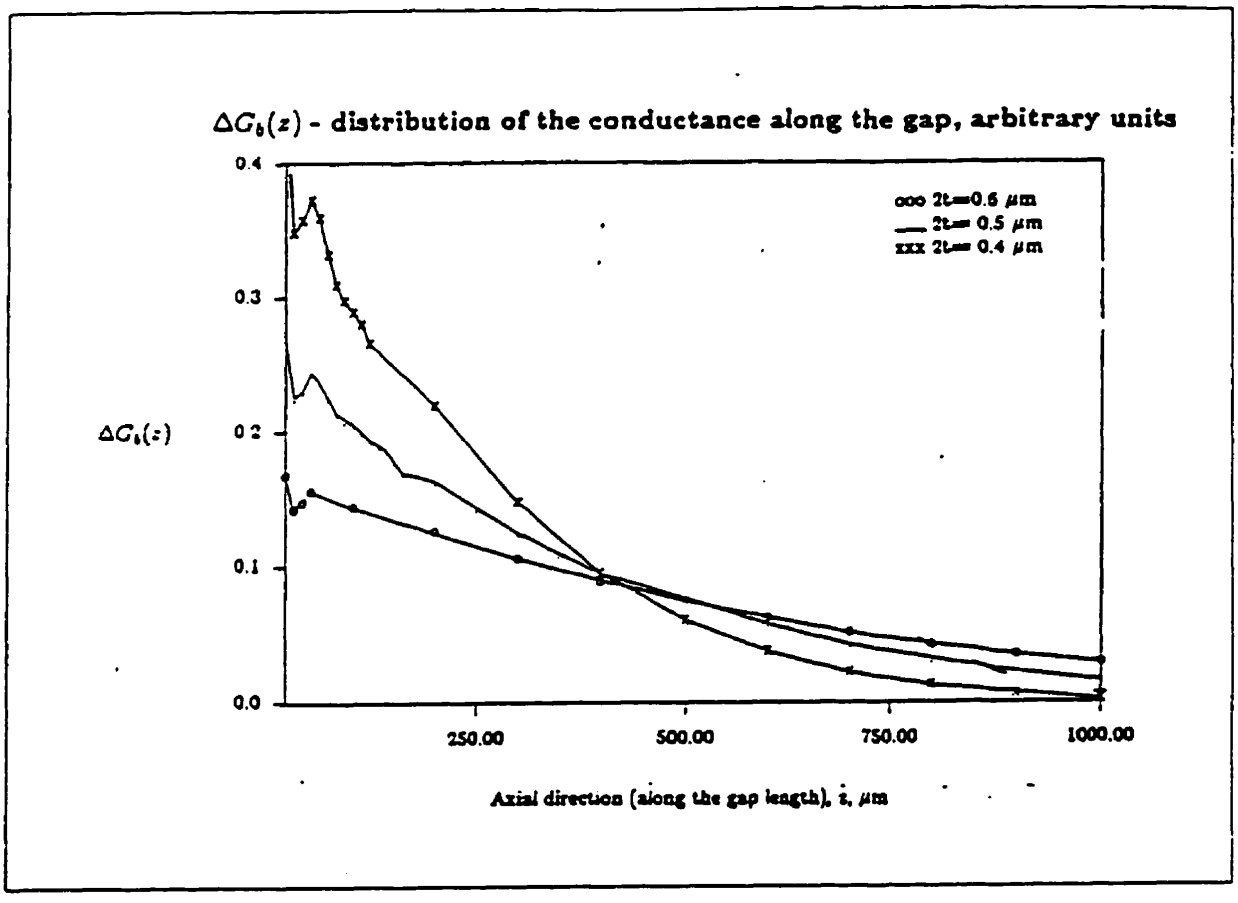

Figure 3.28: The variation of photo-induced conductance $G_b(z)$ along the axial direction, z. The coupling strength affects the carriers distribution along the gap, and hence could be used to design an evenly distributed plasma across the gap. Depending on the gap length, the coupling strength could be adjusted accordingly .

accordingly. The even distribution of carriers leads to an overall higher conductivity, as explained in the following section.

It should be noted that the capability to produce an even distribution of photogenerated carriers along the gap is an advantage over bulk illumination. As discussed in the previous chapter, the external bulk illumination of the aperture of the gap creates shadowed high-resistive regions near the metallic contacts, which reduces the effective conductivity.

3.6 Advantages of Optical Guided-wave Control of Microwaves

The proposed approach of using guided waves for the control element of microwave switches have numerous advantages over free-space optics. These advantages can be summarized as follows:

1. By using guided waves, it is possible to confine a high intensity of light into a thin layer, near the substrate surface, whose thickness is carefully chosen. This thin layer is nominally the effective waveguide thickness. It is important to achieve a high-density plasma at the surface, that can short circuit the gap. By confining this high-density plasma into a thin layer near the substrate surface, using guided wave optics, the same effective conductivity could be obtained with less optical power than that required in the case of conventional free-space illumination. It should be noted that from the point of view of efficient optical energy utilization, the depth of the photoexcited region should be approximately equal to the microwave skin depth. If the photoexcited region extends into the substrate for a depth larger than the microwave length, the carriers situated in the region beyond the skin depth will not contribute to effective conductivity sensed by the microwave signal. Further reduction in the optical power requirement is achieved through utilizing a mode of

propagation for the microwave signal which is spatially limited. For this purpose, the skin-effect mode of microwave propagation is considered. The optimum design of the microwave transmission line is discussed in detail in chapter 5.

2. The condition that the absorption depth for bulk illumination, $\frac{1}{\alpha}$, should be much smaller than the microwave skin depth sets an upper limit on the microwave frequency that could be used in conjunction with a given optical wavelength in a given material. For the guided-wave optics case, the thickness of the photoexcited region is dictated by the optical guiding system. This allows for designing the microwave switch to operate at a much higher frequency without being limited by the choice of material or optical wavelength.

3. The penetration of the incident light through the substrate to the ground plane leads to a leakage conductance G_a of a considerable magnitude that would minimize the difference between the OFF and ON states as sensed by the microwave signal [refer to equation 2.25]. Therefore, it is recommended to use materials that are semi-insulating in the absence of light, and to design the device parameters such that the incident light is mostly absorbed in a thin layer of the substrate close to the surface. This can be easily achieved using guided waves compared to bulk illumination. The choice of strongly guided modes will confine the light to the thin core of the guide.

4. As discussed earlier, the guided-wave approach will further reduce the optical power requirement by providing a more even distribution of the light intensity across the gap, leading to a higher overall conductivity. Further, bringing in the light from within the substrate, rather than illuminating the gap from the top, will help evade the shadowing pattern created by the aperture nature of the gap [see Figure 2.9]. This will effectively eliminate the γ factor discussed in the previous chapter [refer to equation 2.13]. The plasma distribution and consequently the conductivity distribution for the guided-wave approach for a typical case are depicted in Figure 3.28. In these figures, the carriers distribution profile is controlled by adjusting the coupling strength of the optical directional coupler.

5. More savings in the optical power requirements can be achieved through the miniaturization of the device. The sensitivity of the device increases with reducing the gap size. From equations 2.13 and 2.25, the power sensitivity will increase with $\frac{1}{l^2}$, where l is the length of the gap. Using bulk optics excitation techniques, however, poses limitation on the extent of the miniaturization of the gap size. The proposed guided-wave technique allows for much smaller devices. It should be noted that reducing the gap length will lead to an increase in the gap capacitance [104] [105] [106]. However, the dependence of the gap capacitance on the gap length is logarithmic [15]. Hence, it is possible to minimize the gap length and increase the sensitivity of the device, without much sacrifice of the speed. In devices where much higher speeds is required, guided-wave optics can also out-perform bulk optics. In bulk optics illumination, a longer gap translates directly to a much higher optical power requirement. In the guide-wave approach, profiling and confining the optical energy will help reduce the amount of optical energy required.

6. The use of optical guided waves provide opportunities for profiling the carrier distribution and adjusting the carrier densities to meet the requirements of more complex device designs.

7. The amount of microwave signal attenuation can be reduced by minimizing the semiconductor areas to which the microwave signals are exposed. In the previous section, topologies to minimize the semiconductor areas to which the microwave signals are exposed were presented.

8. The introduction of guided optical waves creates an integrated version of these devices. This leads to a better fabrication yield, lower cost, smaller size and a lighter weight. The integrated guided-wave device design will have an on-chip laser as an integral part of the device. Current bulk optics devices use external lasers with an expensive and lossy lens system to direct the light [95].

3.7 Assessment and Comparison of Optical Power Requirement for the Proposed Devices

In what follows, an analysis of the amount of guided optical power required to achieve the same conductivity G_b as that in the case of free-space illumination will be conducted. The optical power is propagated in a waveguide made of a low loss dielectric material. At the gap, this optical power is coupled into another waveguide whose core is the semiconductor absorbing layer.

Assume the case where the plasma distribution is designed to be held constant along the axial direction z. Referring to Figure 3.21, the conductivity G_b is given by

$$G_b = \frac{w}{l}\int_{-\infty}^{\infty}\sigma(x)dx \tag{3.35}$$

Here w is the width of the gap and l is the length of the gap designed to be half the coupling length of the coupler L_c. If the gap is situated in the middle of the coupling length profile of the optical directional coupler, and has a length of approximately $\frac{L_c}{2}$, the carriers distribution will be almost constant along the axial direction. Throughout the length L_c, optical energy is completely coupled from the lossless dielectric waveguide to the surface semiconductor waveguide. The plasma distribution could be made almost constant along the axial direction by adjusting the rate at which the optical energy is being coupled into the absorbing layer, to be approximately equal to the absorption rate of this optical energy. This is done by the proper choice of the coupling strength of the coupler in conjunction with the absorbing characteristics of the semiconductor material at the operating wavelength.

The even carrier distribution is important in order to ensure that the entire length of the gap will be illuminated with an approximately uniform intensity, so as to avoid a situation where strong absorption leads to a poorly illuminated region near one of the contacts. This dark region would decrease the effectiveness of the incident light in the

same way as the small aperture shadowing affects the conductivity in the case of bulk illumination.

In the above equation, $\sigma(x)$ could be assumed to have the same spatial distribution as the guided optical modal power. This assumption is equivalent to that which was assumed for the case of free-space optical illumination in earlier works by Platte and others [23] [95] and was verified experimentally [93]. It is specifically valid for short-duration switching pulses where diffusion could be ignored. For a TE mode, the optical power distribution will be proportional to ${E_y}^2$, where E_y is the $y-$component of the electric field. Consequently, $\sigma(x)$ could be assumed to have a distribution in the form:

$$\sigma(x) = \begin{cases} \Delta\sigma_s cos^2(\kappa d) e^{2p(x+d)}; & \text{if} \quad x < -d \\ \Delta\sigma_s cos^2(\kappa x); & \text{if} \quad -d < x < d \\ \Delta\sigma_s cos^2(\kappa d) e^{-2p(x-d)}; & \text{if} \quad x > d \end{cases} \tag{3.36}$$

In the above expression, κ, p, and d are related through the well known expressions for the slab waveguide propagation model:

$$(\kappa^2 + p^2)d^2 = {k_o}^2 d^2 ({n_1}^2 - {n_2}^2) = V^2 , \tag{3.37}$$

$$\beta^2 = {k_o}^2 {n_1}^2 - \kappa^2 = {k_o}^2 {n_2}^2 + p^2 , \text{and} \tag{3.38}$$

$$\kappa\, tan(\kappa d) = p \quad , \qquad \text{for TE even modes} \tag{3.39}$$

where β is the axial propagation constant, $2d$ is the guide thickness, V is the numerical aperture, and n_1 and n_2 are the core and cladding refractive indices respectively. Substituting equation 3.36 in equation 3.35, one arrives at

$$G_b \approx \frac{w}{\frac{L_c}{2}} \Delta\sigma_s [d_{eff}] \approx \frac{w}{\frac{L_c}{2}} \Delta\sigma_s (d + \frac{1}{p}) \tag{3.40}$$

where $2d_{eff}$ is the effective guide thickness. By comparing this formula to the one obtained for the case of bulk illumination [equation 2.13], one concludes that in order

to obtain equal conductances for the guided-wave illumination and the bulk illumination cases, for a gap of the same length, $l = \frac{L_c}{2}$, and same width w, the ratio of required plasma density, or alternatively the ratio of required conductivities, is given by

$$\frac{\Delta\sigma_{guided}}{\Delta\sigma_{non-guided}} \approx \frac{\gamma}{\alpha(d + \frac{1}{p})} \tag{3.41}$$

The expression obtained for G_b for bulk illumination assumes that the absorption depth, $\frac{1}{\alpha}$, is much smaller than the microwave skin depth. Similarly, the expression obtained for G_b for guide-wave illumination assumes that the effective guide thickness, d_{eff} is again much smaller than the microwave skin depth. This assumption means that the entire photoexcited region will contribute to the microwave conduction.

As a practical case study, consider the directional coupler described earlier made of $GaAs/Al_xGa_{1-x}As$ double heterostructure MQW materials. Consider cores of refractive indices of 3.65, and surrounding layers of indices of 3.647. One of the cores is a GaAs absorbing layer of index $n_r - j\,n_i$ = 3.65-j0.0684 (at $\lambda = 0.83\ \mu$m) and the thicknesses of both guides is 1.5 μm and the separation between them is 0.4 μm.

For this case, analysis yields a coupling length of L_c = 0.78 mm, and an effective guide thickness $2d_{eff}$ = 3.83 μm. The power absorption coefficient $\alpha = \frac{4\pi}{\lambda}n_i = 1.035\text{x}10^6\ m^{-1}$. Substituting these numbers in the above expression, yields

$$\frac{\Delta\sigma_{guided}}{\Delta\sigma_{non-guided}} \approx \frac{\gamma}{2} \tag{3.42}$$

For γ =0.06 [95], the above ratio is equal to -15.23 dBs, and for the extreme case of γ =1, the above ratio is = -3 dBs.

This means that the guided-wave approach reduces the amount of optical power requirement by 50-97%. In other words, the guided-wave approach can tolerate 3-15 dBs of insertion and propagation losses and still be equally efficient to the free-space conventional devices with the added advantages explained earlier.

3.8 Conclusion

In this chapter, an approach whereby optical guided waves can be used to realize an integrated architecture of optically controlled microwave devices was presented. This new architecture was utilized to propose some composite devices such as the optical-microwave logic devices described above. These devices would be very complicated to implement otherwise, as they require complex optical control signaling. Using free-space illumination, an equivalent system will require a complex, bulky, lossy and expensive lens system to direct the optical signals to their appropriate destinations, and the device will not be practical to implement.

This chapter also proposed a model for the guided optical energy conversion into electronic plasma. The plasma distribution in space and its relation to the optical field distribution would lead to suggesting specific guiding characteristics and optimized optical field distribution patterns that can be more effective in achieving the control function and hence enhancing the device performance. The optical energy should be coupled into the region of interest in such a way that a uniform plasma distribution across the gap is realized. Further, through the guiding of the optical energy, profiling of both the optical beam and the resulting plasma distribution is possible, which would reduce optical losses, reduce the optical energy requirement, among other advantages.

Modeling the optical component of the proposed optically controlled microwave switch was presented. For this purpose, accurate numerical simulators such as VFDTD and BPM are used. These numerial simulators require an input field excitation that is the eigensolution of fields for the structure to be simulated. This minimizes simulation errors due to incorrect launching fields. An algorithm to compute the field profiles and the complex propagation constant for multi-layered highly lossy optical guiding systems is presented in this chapter. Using this algorithm, the optical power distribution within the microstrip gap region is accurately modeled. This algorithm is an iterative exact solution for the fields and the effective index of the propagating optical power within the structure. This modeling tool is best suited for highly lossy structures, and yields fast

accurate results.

The performance of the proposed guided-wave device was compared versus an equivalent bulk optics device. It was shown that the proposed architecture was more efficient in terms of the optical energy requirements. From point of view of integrability, efficiency, capability of more complex integration and more complex structure, as well as fabrication yield, cost, and size, the proposed structure outperforms the bulk optics one.

As noted in Chapter 2, the optically controlled microstrip switch has been treated in the literature with approximate formulas valid in the low-frequency quasi-static domain. This was traditionally done using the simple approach of representing the photoconductor by time-varying circuit elements obtained via a quasi-static analysis of the microstrip line. Using these circuit elements, the device is analyzed using a lumped parameter circuit representation.

The following chapter is dedicated to developing an accurate model of the microwave component of the switch. To model the propagation characteristics and the microwave discontinuity, an analysis that utilizes spatial Green's functions formulations is developed. This analysis is capable of modeling continuous and discontinuous shielded microstrip multi-conductor transmission lines with lossy multi-layer substrates. The formulation utilizes the concepts of the Green's function in the space domain and the principle of scattering superposition to obtain the propagation characteristics. The analysis is kept broad enough to allow for multi-layered substrates in which one or more of the layers are lossy. Using the developed accurate model, the proposed device is subjected to much more accurate design methodology than the currently in use equivalent circuit models based on quasi-TEM assumptions.

Chapter 4

Analysis of Shielded Lossy Multi-Layered-Substrate Microstrip Structures

4.1 Introduction

Planar structures such as striplines and microstrips were introduced in the early 1950's. These guiding systems have come to be of considerable importance because they offer the advantages of low loss as well as ease of fabrication with technologies similar to those of the well established semiconductor technology. Since then, planar transmission lines have become the chief guiding mechanism for microwaves. In pursuit of better performance, in terms of compactness, losses and reproducibility, the range of basic guides has grown. This also led to the realization of more flexible structures that allowed for a wide variety of components and convenient interconnections. From microstrip, has grown the coplanar waveguide, the inverted microstrip, the suspended microstrip, the slot-line, the finline and a lot of variations thereof. A schematic diagram of a planar structure is shown in Figure 4.1.

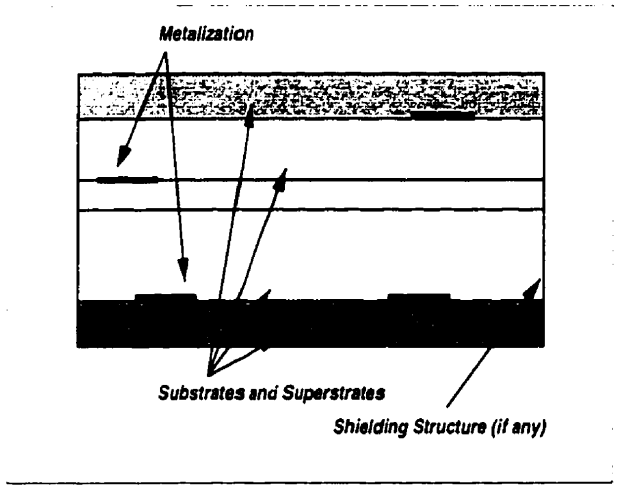

Figure 4.1: A schematic cross-section of a planar guiding structure. The substrates and the superstrates can be dielectrics, semiconductors, ferrites etc. depending on the circuit design.

Each of these guides offer its own desirable features. For example, the suspended substrate stripline offers low attenuation, extreme broad-band and low dispersion characteristics, attributed to the quasi-TEM mode of propagation. Suspended substrate stripline is a desirable medium for IF filters and matching networks used in millimeter-wave mixers. Coplanar waveguides and finlines have the added advantage of compatibility with microwave semiconductor devices. Finline, due to its favorable characteristics, has proven to be one of the most used media for millimeter-wave Microwave Integrates Circuits (MICs) [139]. In many cases, systems are designed to combine different media to increase design flexibility and to exploit the unique advantages of each of these media. For example, unilateral finlines and coplanar lines are often combined to achieve very broad-band hybrid junctions for millimeter-wave mixer designs. Attempts to further increase the design flexibility of MICs have bean made by introducing additional conductors and multiple dielectric layers [140]. Aikawa [141] and Itoh [142], [143] have demonstrated the usefulness of this technique in the design of high directivity couplers by using coupled suspended substrate stripline with tuned septums.

Further, these guides became a building block in a larger MIC. An MIC is a collection of active and passive microwave devices interconnected on a common substrate. The two

possible types of MICs are the monolithic MIC (MMIC) or hybrid MIC. In MMICs, all active and passive devices and their connecting lines are fabricated on the same substrate using epitaxial and photolithographic technologies, as shown in Figure 4.2. Active device implementation require the substrate to be a semiconductor, mostly $GaAs$ or Si. Hybrid MICs are usually made of a low-loss dielectric substrates. Passive components and interconnects are made by deposition techniques. Active devices are mounted on the substrate after being manufactured separately.

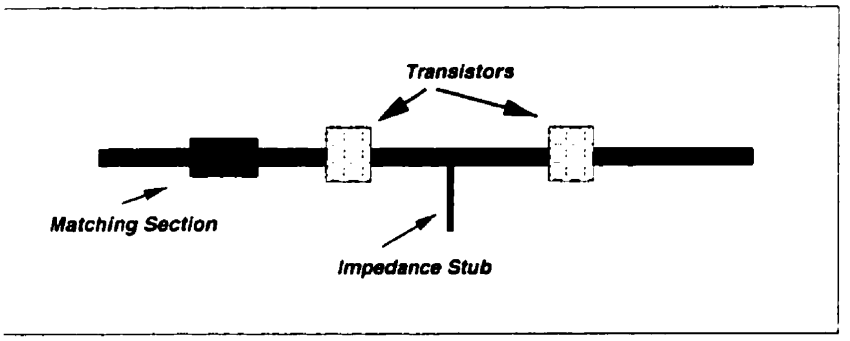

Figure 4.2: A Monolithic Microwave Integrated Circuit (MMIC). All active and passive devices and their connecting lines are fabricated on the same substrate using epitaxial and photolithographic technologies.

There is a strong interest in the monolithic integration of microwave and radio frequency (RF) circuits because of the growing market of wireless communications. In particular, integration of active and passive components on a silicon wafer is of great interest because the silicon technology is a mature technology that allows much higher integration density [144]. There is also a very strong interest in the monolithic integration of optical and microwave components. The focus of future developments is directed towards MMIC, which provide possibilities of integrating entire microwave, electrical and optical systems on the same chip.

4.2 Modeling Techniques of Planar Structures

Hybrid and Monolithic MICs are both quite costly to design through engineering iteration processes. Further, once fabricated, their performance cannot be appreciably changed but for fine tuning. For this reason, the initial MIC theoretical designs should be as accurate as possible in order to minimize the number of engineering iterations. For example, the electromagnetic coupling between adjacent devices on the same MIC are significant enough to warrant including them in the analysis in order to get the best possible initial design. Microstrip circuits often include discontinuities such as impedance stubs, matching sections and series and end gaps. The accurate prediction of electromagnetic coupling and scattering from these components is important in order to minimize the number of design iterations. Accurate calculation of the propagation constant and the characteristic impedance of the interconnects leads to an accurate prediction of the interaction between various circuit components.

For this reason, in tandem with the progress in the design of various planar transmission line structures, a variety of theoretical methods were developed to analyze these planar structures. The problem of electromagnetic propagation in stratified isotropic and anisotropic media have been studied extensively [145] [146]. This effort has been devoted to the task of being able to design MMICs for the use in the high frequency ($f > 20$ GHz) region. Accurate theoretical modeling of MMICs, microstrip transmission lines of various types, and their discontinuities are essential so that the device performance can be predicted confidently, thus avoiding a time consuming and costly production and testing cycle [147] [148].

Due to the inherent complex nature of the electromagnetic fields in MIC structures, almost invariably all the mathematical techniques capable of rigorously predicting the basic parameters of the guiding system are either numerical or semi-analytical. The quality of these techniques can be assessed by means of comparing their computing efficiency, their ease of use, generality and reliability. The main problem in accurate analysis of planar transmission line lies in the fact that these structures involve mixed boundaries. Hence,

all the six components of the field must be taken into account. Also, the final equations have to be solved numerically, being of a rather complicated nature, and almost always not in a closed form.

Computer-aided design (CAD) tools such as TouchStone, Supercompact [149], and Libra [150] often adequately characterize many basic microstrip configurations and discontinuities. The models used in these tools, however, are approximate and do not allow for complex multi-layer geometries, highly dissipative substrates or shielding considerations. IE3D [151] by Zeland, Inc. is a powerful simulation tool that utilizes the Method of Moment. Zelad has developed another software, FIDELITY, that is bsed on a finite difference scheme (FDTD) to solve a generalized electrical field integral equation (EFIE) associated with microstrips in three dimensions. A generalized computer code, however, is quite expensive in terms of computational efforts.

Some modeling approaches utilize dispersion models based on empirical formulae derived from experimental data [152],[153]. Apart from those, analysis techniques can be categorized into three main categories:

1. Quasi-static Analysis Techniques.
2. Full-Wave Semi-Analytical Techniques.
3. Numerical Techniques.

In what follows, a brief review of the various analysis techniques used in microstrip modeling is presented.

4.2.1 Quasi-static Analysis Techniques

Initially, theoretical work on microstrip was primarily based on quasi-TEM analysis. With these techniques, equivalent circuits are derived in terms of static capacitances and low frequency impedances. The static capacitance is calculated and used to determine the

characteristic impedance and the propagation constant of the transmission line. Wheeler [154] [155] was the first to evaluate the static capacitance through conformal mapping and effective dielectric constant approach. Other works for the static analysis of gaps in microstrips [104], gaps and steps [105], and other microstrip discontinuities [106] followed. More recently, the quasi-static conformal mapping approach was used to characterize coplanar transmission lines on multilayer substrates [156] [157].

Other approaches include the Green's function formulation by Silvester [158], application of the variational technique in the Fourier domain by Yamashita and Mittra [159] and the quasi-TEM spectral domain analysis by Itoh and Hebert [142] and Itoh [143]. The latter approach has the flexibility of analyzing multi-conductor multi-layered substrate lines. The limitation of quasi-TEM approximation, however, is that it cannot be applied to compute the electromagnetic characteristics at higher frequencies, given the dispersive nature of microstrips, and hence the technique is limited to a range of frequencies up to few GHz. Also, most existing models ignore the shielding effects.

Generally, quasi-static approximation methods sacrifice accuracy for sake of fast and less computationally expensive formulations. They generally yield good results at the lower end of frequency range of interest, although some quasi-static have been proven to be useful for characterizing microstrip lines for up to 10 GHz [144]. The quasi-TEM spectral domain technique [142] is a numerically-efficient approximate modeling tool. These quasi-static approaches often lead to a simple equivalent circuit representation that models the transmission line or the discontinuity. An example of this is depicted in Figure 4.3. This feature gives them the added strength of being easy to integrate with other efficient circuit simulators.

4.2.2 Full-Wave Semi-Analytical Techniques

A mathematically rigorous full-wave solution for the fields in a particular structure requires the knowledge of an accurate Green's function for that family of structures. A

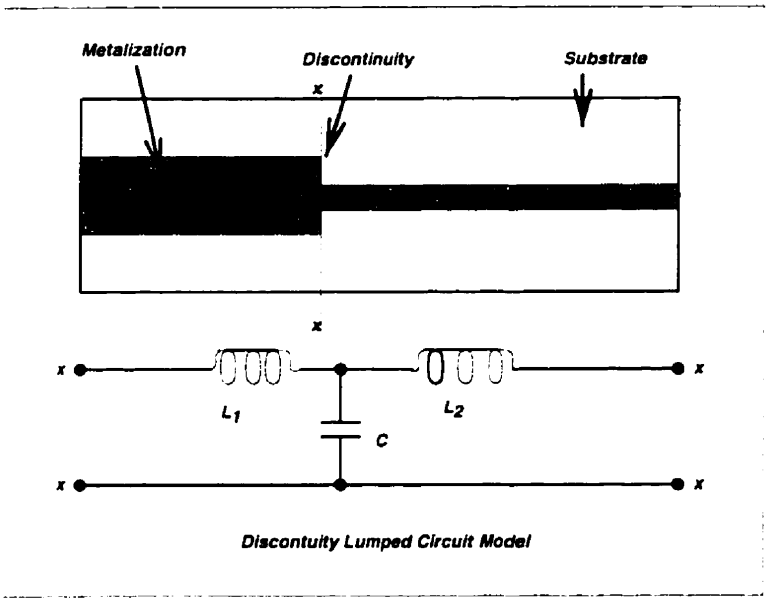

Figure 4.3: An equivalent circuit representation that models a step discontinuity.

short review of the relevant methods for obtaining such Green's function can be found in the introductions of several papers on that topic [160] [162] [163].

The Green's function is obtained either in the spatial domain or in the spectral domain. Generalized techniques for deriving the spectral-domain Green's function for multilayered substrates have been given in [160] [161] [163] [164] Examples of full-wave analysis methods that starts from the spatial Fourier domain are [165] [166] [167] [168] [169].

The quasi-static approximation is compared to the results of full-wave analysis in [162]. For this purpose, an approach based on a vector potential and a scalar potential is used to obtain the Green's function. A mixed-potential integral equation is stated to be superior in [170]

A rigorous formulation for shielded microstrip via an integral equation was introduced by Mittra and Itoh [171]. The solution for open microstrip was presented by Denlinger [172] where a coupled integral equation in the spectral domain was utilized. These tools were simplified by introducing the numerically efficient Galerkin's technique for the solution of the spectral domain problem. A variational technique for modeling step dis-

continuities was presented in [173] and an iterative approach was reported in [174]. A CAD-suitable approach was reported in [175].

Full-Wave Spectral Domain Analysis Techniques

Some of the theoretical models are geared more towards a special geometry, and hence they are inherently computationally efficient. Of these, the spectral domain methods is the most commonly used. The Spectral Domain Technique (SDT) is an efficient semi-analytical method that was applied extensively to problems covering the analysis of planar couplers, filters, antenna arrays and lossy planar structures [139]. Spectral domain methods range from those providing a quick and approximate results to those which are most accurate but more computationally expensive. The variety of these methods allows for a trade off between accuracy and computing time. The quasi-TEM spectral domain technique is an example of the former [142]. The hybrid spectral domain approach is a more elaborate and accurate technique that is also more computationally expensive [176], [177], [178], [179]

The Spectral Domain method is an integral transformation method: the differential equations governing the electromagnetic system are transformed from the space domain into the spectral domain, via a Fourier transform, where they are easy to solve. The actual solution is then obtained by inverse transformation. In boundary value problems, the above process results in one or more integral equations in the original space domain. The solution can then be obtained by using a standard numerical technique. The numerical efficiency of the solution depends on the choice of the technique for converting the integral equation into the final set of linear equations. Methods of solution of the final equations that are most commonly used include the Point Matching (Point Collocation) method, and more importantly the Galerkin technique. The aim of these methods is to convert the integral equations into a homogeneous system of linear equations. When the determinant of this system is equated to zero, the characteristic equation of the transmission line is obtained. This equation yields the complex propagation constant of the transmission line

modes. Substituting back with the complex propagation constant, the current distribution on the strip, and the field patterns can be computed. The Galerkin's technique and the point matching technique have the same philosophical base in the numerical analysis and are both categorized as the moment method. Unlike the point matching method, the Galerkin's technique can be applied both to the spectral domain and to the spatial domain analysis, and in both cases they finally yield the same set of linear equations which is solved to obtain the dispersion characteristics. However, the combination of Galerkin's technique and Parseval's identity to generate a set of linear equations has now become a specific feature in the spectral domain solution of planar structures.

For a uniform microstrip line, it is possible to predict the general shape of the current distribution, and deploy it to obtain the dispersion equation. In doing so, the computationally expensive step of using the Method of Moments (MOM) can be avoided altogether. This can be done with both the space domain and the spectral domain Green's function formulations.

When a discontinuity occurs along a planar transmission line, some of the energy propagated on the line is reflected. Characterization of microstrip discontinuities is a major task, even to arrive to a representative approximate lumped parameter model.

Radiation from open planar structures involving discontinuities is another major task. An accurate assessment of the radiation from a planar structure depends on the accuracy of the solution of the associated electromagnetic problem.

The spectral domain technique for the analysis of planar microstrip lines was first introduced by T. Itoh and R. Mittra [180] in 1973. Between 1973-1976, basic applications for the SDT were reported by Jansen [181] [182], Rahmat-Samii [183], Itoh [184] among others. These basic applications included planar resonators, coupled microstrip lines and microstrip discontinuities. In 1977, a generalized form for the SDT for the application to multiconductor multilayer planar transmission lines was proposed by Davies [185]. The technique employs a transfer matrix method to account for multilayers of dielectrics. In 1980, Itoh [186] introduced the immittance approach for the SDT of multilayer multicon-

ductor transmission line. Since then, various refinements have been made to the SDT in order to increase its numerical efficiency and capabilities [187] [188] [189] [190]. For example, [191] proposes a non-uniform discretization scheme of the integral equation. This technique was also extended to model anisotropic substrates [192].

Some FFT methods such as [161] are not suitable for calculations if the observation point, (x, y, z), and the source point, (x', y', z'), coincide. The method proposed in [163] circumvents this problem. This is essential if the Green's function must serve as the basis for solving an integral equation for the current on a microstrip patch. Apart from that, the approaches of [161] and [163] are basically similar.

The Green's function for layered lossy media reported in [163] is intended for special application to microstrip antennas. In this paper, Suitable Green's dyadics for the fields generated by a surface current density in a plane parallel to the interface of a layered isotropic structure are determined. Special care is taken to ensure that the Green's function can still be calculated in the source region by circumventing the numerical problem by analytical techniques. This method is intended for modeling devices in highly lossy media. An analytical method is developed to avoid numerical problems arising from the exponential decay of the fields due to these losses.

A standard spectral domain analysis assumes the microstrip line to be enclosed in a shielding cavity. This model is more general, as it can model shielded structures, as well as open structures (by letting the shielding cavity's dimensions tend to infinity). Hence it can model open structures, laterally open structures, and shielded structures. However, since modes associated with closed structures are discrete, the SDT will only render the discrete modes of open microstrip lines. Shielded microstrips are the most common for practical applications.

The major shortcoming of the spectral domain method is its inability to model thick conductors. Therefore, for very high frequencies, when the wavelength is comparable to the metalization thickness, the results of spectral domain analysis depart from accuracy. Also, for very high losses, the SDT yields inaccurate results.

For a closed structure, there is essentially no big difference between the spectral domain and the space domain Green's function approach. In the spectral domain, Fourier transform will be applied to the field expressions in the direction parallel to the layered structure discontinuity interface. Since the field is bounded by the shielding cavity, the Fourier transform reduces to a Fourier series with a set of sinusoidal functions which are more or less the functional expressions of the modes sustained by the shielding cavity in the absence of the microstrip metalization. In the space domain analysis, the spatial functional expression for the fields is the summation of sinusoidal functions, with a set of unknown amplitudes. These sinusoidal functions are the modal representations of the modes sustained by the enclosing cavity. Using the boundary conditions along the discontinuity boundaries, the relation between these unknown amplitudes is established. It is obvious that the Fourier series representation in the spectral domain is the modal summation representation in the space domain.

Full-Wave Spatial Domain Analysis Techniques

Full-wave spatial domain analysis was first introduced by Itoh [165]. Since then, several versions of that approach were proposed [166] [168] [169] [193] [194] [167] [195]. For example, in [193], the Green's function for a rectangular waveguide filled with two dielectrics is given. The inhomogeneous system of equations encountered in [193] increases substantially with the number of layers. It is hence not suitable for the treatment of multilayered structures. Some techniques for deriving the spectral or space domain Green's function for multilayered substrates for open and closed geometries [160] [163] [164] require that the current in the circuit be parallel to the layers' interfaces. A significant reduction in the algebraic complexity of the analysis is achieved by choosing a set of vector potentials, such as Hertz vectors, that is oriented in the direction normal to the layer interfaces. These vectors are then used to compute the electromagnetic fields.

An efficient generalized technique for deriving the space-domain Green's function due to an arbitrarily oriented current in a shielded two-layer isotropic substrate structure is

presented in [169] [196] [197]. In this chapter, an extension of this method for the case of multilayered lossy substrates is conducted.

Another approache that can be included under this category of techniques is the mode matching technique [198] [199], which is a method for analyzing microstrip discontinuities. In this method, the modal expansions on both sides of the discontinuity are evaluated and equated at an appropriate reference plane. The resulting system of equations are solved yielding the amplitude of the scattered mode of interest. A closed-form spatial Green's function for thick microstrip substrate is presented in [200]. The technique of complex images and quasi-dynamic images is utilized to arrive at these formulas.

4.2.3 Full-Wave Numerical Methods

Full-wave three-dimensional-discretization numerical methods are considered the most versatile, as they are applicable to geometrically more complex structures than those which can be solved analytically or semi-analytically using quasi-static or full-wave spectral/spatial domain techniques. These analytical and semi-analytical tools take advantage of the special geometry of a class of devices to model their performance. Further, the numerical methods can be made increasingly accurate by minimizing the mesh discretization, assuming that the computation resources are available.

Some of these numerical methods are the method of lines [201] [202] [203], the finite difference time domain (FDTD) approach [204] [205] [206] [207] [208] [209], and the transmission line matrix method [210].

In the method of lines and the FDTD, the microstrip circuit is discretized into a three dimensional grid. By imposing the appropriate boundary conditions within the structure, Maxwell's equations are solved at each point.

In the transmission line matrix (TLM) method [210], the structure is discretized into a three dimensional grid of points interconnected by ideal transmission lines. The distributed parameters of these transmission lines can be obtained by enforcing the EM field

boundary conditions [189].

A commercially available software, IE3D [151], utilizes the finite difference scheme to solve a generalized electrical field integral equation (EFIE) in three dimensions.

It should be noted, however, that solving the system of equations resulting from the formulations based on a three dimensional grid, such as the transmission line matrix (TLM) method or the finite element approach, may require detrimental computation time and resources.

4.3 Shielded Metal-Insulator-Semiconductor Planar Structures

In most cases, MMICs with semiconductor substrates are shielded in a metallic rectangular cavity, given the brittle nature of semiconductors, and in order to isolate the circuit from interaction with the surrounding environment. For this reason, shielded metal-insulator-semiconductor (MIS) microstrip structures are often found in MMICs, as they provide a variety of desired features. MIS technology is used for the design of phase shifters, attenuators and tunable filters [60] [211] [212] as well as modeling very high speed VLSI circuit interconnects [213] [214]. The basic MIS geometry consists of a semiconductor substrate with a very thin layer of an insulating material on top of it. In many cases, that insulating layer is the oxide layer of the semiconductor material that forms on the surface.

MIS structures are particularly attractive for applications in the area of optical control of microwaves. A large variation in attenuation and phase properties of the propagating signal can be achieved by changing the resistivity of the substrate, which can be achieved optically. These changes arise from the change in the spatial distribution of the stored electrical and magnetic energies during device operation as explained later in this chapter. Experimental results for the propagation constant and characteristic Impedance of MIS

structures [60] [215] [216] confirm these properties. This makes the MIS geometry attractive for such applications as optically tuned delay lines and attenuators. The proposed integrated optically controlled microwave switch of this research utilizes a shielded MIS geometry. Understanding the operation principles of the MIS geometry is key to accurate design of the optically controlled microwave switch. This is one of the objectives of this chapter.

Several full wave analysis techniques have been utilized to analyze MIS structures and their discontinuities such as finite element analysis [211] [217], spectral domain analysis [218] [219], and spatial domain analysis [168] [169]. Full-wave finite element analysis often requires three dimensional discretization of the discontinuity region, and hence is computationally intensive and requires a large amount of computer memory and time.

The effect of shielding on discontinuity characteristics can be significant and requires accurate modeling at higher frequencies [220]. Cases of significant effect of the shielding structure include those when the circuit is operated at a frequency close to or above the cut-off frequency of the higher order modes of the microstrip, which are essentially the rectangular waveguide modes of the shielding structure [168]. Also, when the shielding structure is close to the circuitry, significant shielding effects are observed. Such effects are not accounted for in most commercial CAD packages.

The method proposed in [169] is an efficient generalized technique for deriving the space-domain Green's function due to an arbitrarily oriented current in a shielded two-layer isotropic substrate MIS structure. The derived Green's function is then used to find the dispersion characteristics of single and symmetric coupled MIS slow-wave transmission line structures. The approach given is based on the principle of scattering superposition combined with appropriately chosen magnetic and electric vector potentials.

The treatment proposed in [168] [221] [220] is intended primarily for discontinuities of thin width in thin lines, as it assumes only the axial component for the current. This method uses magnetic frill current excitation of the discontinuity. The treatment in [169] [196] [197] [222] assumes the two components for the current, the axial current I_z and

the transverse current I_x, and hence it is suitable for the treatment of discontinuities in wider lines. This analysis uses gap generator excitation of the discontinuity rather than frill current.

4.4 The Present Analysis

In this chapter, the analysis presented in [197] is extended for the case of multilayered lossy substrates. The obtained semi-analytical expressions are developed into a set of computer codes. The validity of this method was established earlier through comparison with measured data for highly lossy substrates and low loss substrates, published data obtained experimentally or using other methods, and Libra CAD simulations [169]. The major advantages of this method are:

1. It can accommodate arbitrarily oriented current densities.

2. It is a spatial domain analysis that is particularly suitable for highly lossy substrates. This is important to model the optically excited semiconductor substrates required in this research.

3. As opposed to the SDT approach, the spatial dependence of the fields of the structure under consideration are directly observable.

4. This method expresses all the unknown field amplitude coefficients in terms of the amplitude coefficients of one layer only. Hence, regardless of the number of substrate layers, all the unknown amplitude coefficients can be evaluated by solving a 2x2 system of equations. This provides an immense reduction in the mathematical manipulation compared to other approaches [223]. This feature makes it preferable over other approaches.

Using this method, theoretical formulations for a multilayered lossy inhomogeneously filled rectangular waveguide and cavity are conducted. These are used to obtain the

electric Green's function for each of these structures. Using the Green's function for the rectangular waveguide, an integral equation that models a uniform transmission line is formulated. Using the electric Green's function for the rectangular cavity, an integral equation that models a discontinuity in the transmission line is formulated. Both of these are known as the electric field integral equation (EFIE). The sequence of this derivation is shown in Figure 4.4.

For a uniform microstrip line with no discontinuity, the general shape of the current distribution is known, and is deployed in the EFIE to obtain the dispersion equation. In doing so, the computationally expensive step of using the Method of Moments (MOM) is avoided. The dispersion relation is a complex equation with complex roots. Complex root searching is conducted using *Müller* method and the roots of the dispersion equation are obtained. These are the complex propagation constants for the microstrip propagating modes. Once the propagation constant is known, the fields of the transmission line propagating mode are obtained, and are used to compute the line characteristic impedance through a power/current relationship.

To analyze a discontinuity, the unknown surface current maintained on the microstrip discontinuity is expanded in terms of certain basis functions. The electric field components in the plane of the discontinuity region are then written in terms of the current. Imposing the condition that the component of the electric fields tangential to the metalization is zero, (E_{tan}=0), yields an integral equation known as the electric field integral equation (EFIE). The moment method is applied to the EFIE to obtain a a system of linear equations. An LU-Decomposition routine is deployed in order to obtain the matrix inverse. The elements of this matrix are complex in general. For a given voltage excitation of the discontinuity, a current distribution profile can be obtained. To obtain the discontinuity characteristics, this current distribution profile is fitted to transmission line current model. This curve fitting is used for the extraction of the incident and reflected current amplitudes at the discontinuity, as well as the complex propagation constant. The computer optimization code L-BFGS-B is used for this purpose[224]. Using a two port

network representation, the incident and reflected currents are used to compute the scattering matrix and the impedance matrix representing the discontinuity. This technique for extracting the scattering parameters from the discontinuity feed line current distribution does not require prior knowledge of the feed line propagation constant, an advantage over other methods [197].

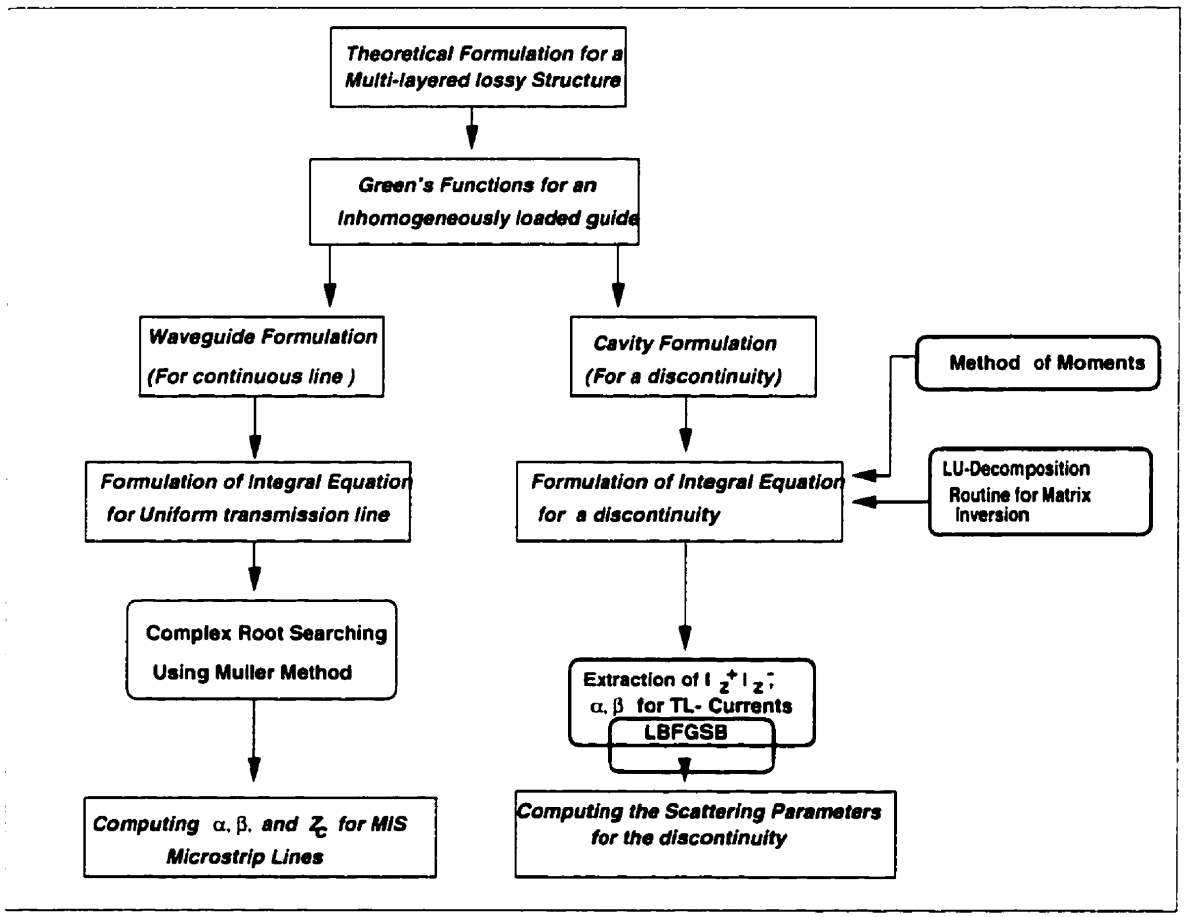

Figure 4.4: A chart showing the sequence of the derivation conducted for modeling uniform multilayered lossy transmission lines and their discontinuities.

Two basic assumptions are made in the forthcoming analysis.

1. All conductor losses are ignored, i.e. perfect conductors with $\sigma = \infty$ are assumed.

2. The thickness of the microstrip metalization is assumed to be zero.

For microstrip lines, most of the fields are concentrated under the center conductor, and fringe fields attenuate rapidly away from it. Hence, losses in the shielding walls can be ignored. Microstrip metalizations are mostly made of gold, which is a very good conductor. Conductor losses are skin-effect losses that are most significant at lower frequencies ($f \leq$ 2 GHz. Gold microstrip conductor losses for a line of width 500 μm is 0.01 dB/mm at 1 GHz [225]. For MIS structures, this is a negligible quantity compared to the propagation losses due to the semiconductor substrates. Hence, the perfect conductor assumption is justified.

For an operating frequency of 20 GHz, and for a typical semiconductor substrate permittivity of 12 (for Si), the microwave wavelength is a few mm. A typical microstrip line thickness is 5 μm [169]. Hence, the operating wavelength is at least 1000 times bigger than the conductor thickness . Hence, the zero conductor thickness is justified.

Normally at the interface between the insulator (dielectric) layer and the semiconductor layer of an MIS geometry, a depletion layer forms and extends into the semiconductor. This depletion region can be modeled as an insulating layer whose permittivity is the semiconductor permittivity, but with infinite resistivity (because this region is depleted of carriers). For a typical MIS geometry, the width of this depletion region is about 10-30 μm depending on the microwave voltage and substrate conductivity [24] [226] [169]. The MIS analysis reported in [169] ignores the effect of this depletion region because the analysis is limited to the case of two layers of materials; one is the insulator and the other is the semiconductor. The present analysis can take this depletion region into account. An argument is presented in [169] in an attempt to justify ignoring the depletion region. Studies conducted here show that ignoring the depletion region lead to an erroneous result. For example, ignoring the effect of the depletion region leads to errors in computing the propagation constant. For the quasi-TEM mode of operation, The imaginary part of the propagation constant (attenuation constant) is off by up to 15%, and the phase constant is off by up to 3%. Moreover, for the slow-wave mode of operation, ignoring the depletion region leads to totally erroneous results, with errors of 50%-90%. This issue is

addressed later in this chapter.

To accommodate the dissipative nature of the MIS geometry, the conduction current in the semiconductor, J_c, is taken into account in the form of a complex permittivity $\epsilon_r \equiv \epsilon_r' - j\epsilon_r''$. This complex permittivity is derived from Ampere's law. For a linear time-independent non-dispersive isotropic material of a real relative permittivity ϵ_r' and resistivity ρ, Ampere's law for time harmonic fields is given by

$$\vec{\nabla} \mathrm{x} \vec{H} = j\omega\epsilon_r'\epsilon_o\vec{E} + \vec{J}_c = j\omega\epsilon_r'\epsilon_o\vec{E} + \frac{1}{\rho}\vec{E} = j\omega\epsilon_r'\epsilon_o\left[1 + \frac{1}{j\omega\epsilon_r'\epsilon_o\rho}\right]\vec{E}, \qquad (4.1)$$

from which it is deduced

$$\epsilon_r \boxminus \epsilon_r' - j\epsilon_r'' \equiv \epsilon_r'(1 - j\tan\delta) = \epsilon_r'\left[1 - \frac{j}{\omega\epsilon_r'\epsilon_o\rho}\right] . \qquad (4.2)$$

Here $\tan\delta$ is the loss tangent where δ is the phase angle between the displacement current $\frac{\partial \mathcal{D}}{\partial t}$ and the conduction current J_c, where $\mathcal{D}$ is the displacement vector.

In what follows, a systematic procedure for deriving the electrical Green's function, $G(\vec{r}, r')$, for a multilayer structure is presented. This general procedure could be applied to a wide range of structures. An example of such an application is an inhomogeneous dielectric-loaded rectangular waveguide. This configuration is depicted in Fig. 4.5.

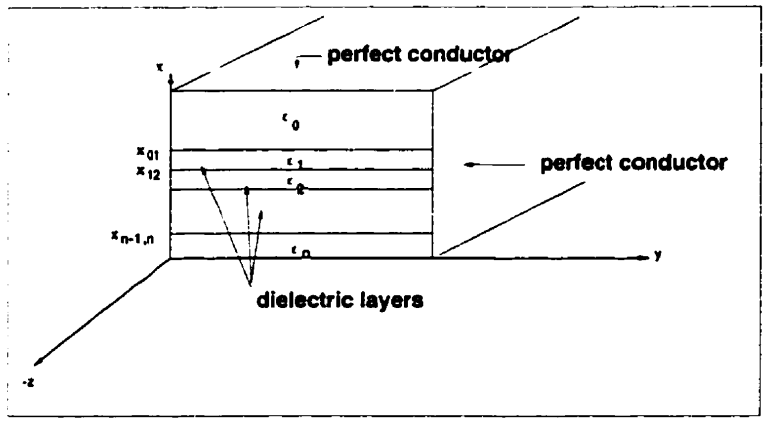

Figure 4.5: An inhomogeneously loaded rectangular waveguide

The electric Green's function, $G(\vec{r}, r')$, relates the electric field anywhere within the given waveguide to an arbitrary surface current on the metalization region, $\vec{J}_s(r')$, through

the relation,

$$\vec{E}(\vec{r}) = -j\omega\mu_o \int\int \vec{G}(\vec{r},\vec{r}') \cdot \vec{J}_s(\vec{r}')ds', \tag{4.3}$$

where s' is the area of the surface where $\vec{J}_s(\vec{r}')ds'$ exists. All fields and sources are assumed to be time harmonic with a time dependence $e^{j\omega t}$. $\vec{G}(\vec{r},\vec{r}')$ is the dyadic Green's function.

The analysis is carried out by employing the principle of scattering superposition. The field of a given inhomogeneously dielectric loaded rectangular waveguide is represented as a superposition of the primary fields of parallel plate structures and the scattered fields of another parallel plate structure, as depicted in Figure 4.6. The primary fields which satisfy the boundary conditions at the source are derived first. The scattered fields' Eigenfunctions are then deduced and the boundary condition of the continuity of the tangential components of the fields is enforced at all the dielectric layer interfaces.

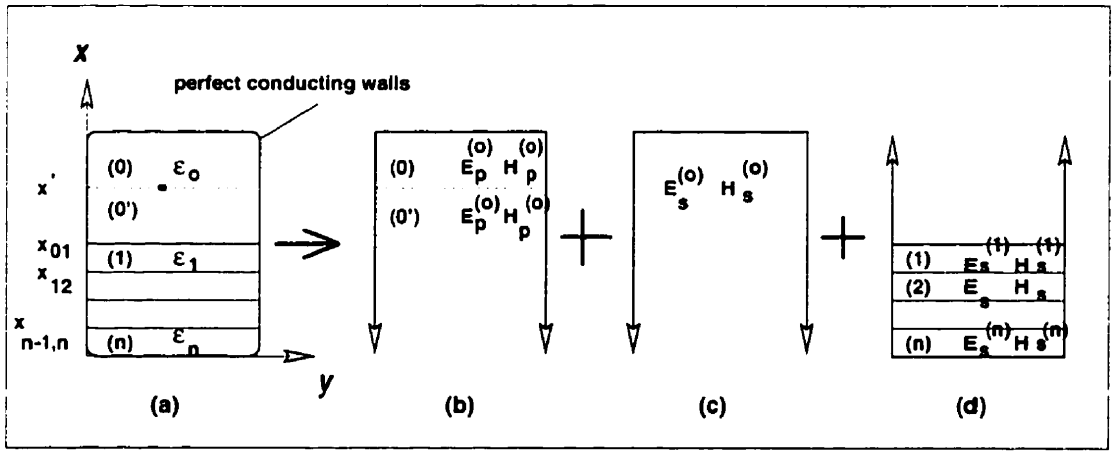

Figure 4.6: An equivalent waveguide system that models an inhomogeneously loaded rectangular waveguide. The analysis uses a superposition of an equivalent set of parallel plate structures.

The above approach yields the fields excited in the complex structure by the infinitesimal source. The electric field due an infinitesimal source is the Green's function as per 4.3. By employing 4.3, the electric field due to a complex distribution of currents is then computed.

4.4.1 The Hertz Vectors and their relation to the EM fields

For a multi-layered substrate, a significant reduction in the algebraic complexity of the analysis is achieved by choosing a set of Hertz vector potentials that are oriented in the direction normal to the layers' interfaces. These vectors are then used to compute the electromagnetic fields. The electric and magnetic Hertz vectors, given by $\vec{\Pi}_e$ and $\vec{\Pi}_h$ respectively, can be used to derive the electromagnetic fields in any canonical system using

$$\vec{E} = \vec{\nabla}\vec{\nabla}\cdot\vec{\Pi}_e + k^2\vec{\Pi}_e - j\omega\mu_o\vec{\nabla}\times\vec{\Pi}_h \ , \tag{4.4}$$

and

$$\vec{H} = \vec{\nabla}\vec{\nabla}\cdot\vec{\Pi}_h + k^2\vec{\Pi}_h + j\omega\epsilon\vec{\nabla}\times\vec{\Pi}_e. \tag{4.5}$$

Chosing Hertz potentials that are directed normal to the layers' interfaces (along the x-axis of Figure 4.6), i.e.,

$$\vec{\Pi}_e = \hat{x}\psi_e, \tag{4.6}$$

and

$$\vec{\Pi}_h = \hat{x}\psi_h, \tag{4.7}$$

and substituting in the above expressions for $\vec{E}$ and $\vec{H}$, yields the following equations for the six field components in Cartesian coordinates:

$$E_x = \frac{\partial^2\psi_e}{\partial x^2} + k^2\psi_e, \tag{4.8}$$

$$H_x = \frac{\partial^2\psi_h}{\partial x^2} + k^2\psi_h, \tag{4.9}$$

$$E_y = \frac{\partial^2\psi_e}{\partial y\partial x} - j\omega\mu_o\frac{\partial\psi_h}{\partial z}, \tag{4.10}$$

$$H_y = \frac{\partial^2\psi_h}{\partial y\partial x} + j\omega\epsilon\frac{\partial\psi_e}{\partial z}, \tag{4.11}$$

$$E_z = \frac{\partial^2\psi_e}{\partial z\partial x} + j\omega\mu_o\frac{\partial\psi_h}{\partial y}, \tag{4.12}$$

and

$$H_z = \frac{\partial^2\psi_h}{\partial z\partial x} - j\omega\epsilon\frac{\partial\psi_e}{\partial y} \ . \tag{4.13}$$

where the medium is assumed as a non-magnetic, isotropic, lossy dielectric. Away from the sources, the Hertz potentials satisfy the homogeneous partial differential wave equations

$$\vec{\nabla}^2\psi_e + k^2\psi_e = 0 \ , \tag{4.14}$$

and

$$\vec{\nabla}^2\psi_h + k^2\psi_h = 0 \ . \tag{4.15}$$

In general, both electric and magnetic current sources can be represented in this formulation. For the analysis of microstrip structures, however, only an infinitesimal electric current source is required. The source boundary conditions can be expressed in terms of the electromagnetic fields directly.

The choice of the above Hertz vectors allows for the decoupling of two sets of solutions (modes):

1. Longitudinal Section Magnetic (LSM) fields: Those having $H_x = 0$, and are derived from an x-directed electric Hertz vector, $\vec{\Pi}_e = \hat{x}\psi_e$.

2. Longitudinal Section Electric (LSE) fields: Those having $E_x = 0$, and are derived from an x-directed magnetic Hertz vector, $\vec{\Pi}_h = \hat{x}\psi_h$.

This choice of the orientation of the Hertz vector potentials allow for the simplification of the analysis. The LSM and LSE electromagnetic fields are orthogonal to each other. Thus, during the solution for the respective amplitude coefficients, the boundary condition equations decouple which leads to a significant reduction in the required algebra.

4.4.2 The Principle of Scattering superposition

Assume that the electromagnetic fields or potentials for a given boundary value problem is known. If the boundary conditions change, the EM fields for the new structure is obtained by a superposition of the original known fields and a scattered one, which has the same spatial dependence but with an unknown amplitudes. Imposing the new boundary

conditions yields these unknown amplitudes. The resulting superposition of functions yields a solution that satisfies all the boundary conditions within the modified structure, and hence, it is the eigensolution for the overall structure. This is called the principle of scattering superposition. In Figure 4.6, It is assumed that we have a certain boundary value problem depicted in Fig. 4.6(b). The solution to this problem is given by the primary fields E_p and H_p. The boundary conditions are then changed by adding a set of N layers of dielectrics and a bottom conducting wall (Fig. 4.6(d)). As a result, the fields in the overall guide change. This change is represented by a set of added fields E_s and H_s. The principle of scattering superposition is discussed in [227] and was previously applied to problems such as deriving the space domain Green's function for a waveguide inhomogeneously filled with two different dielectrics [193]. It was also applied to other problems involving rectangular waveguides and cavities [196] [169] [228]. The uniqueness of the solution of the electromagnetic boundary value problem in the presence of a partly lossy dielectric region was considered in [229].

4.4.3 The Green's Function for A Rectangular Waveguide Partially Filled With Multiple Layers of Lossy Dielectrics

The Primary Fields of An Inhomogeneously Filled Rectangular waveguide

Figure 4.6(a) shows an infinitesimal current source, $\vec{J}_s(r')$, located within the air-filled region of a rectangular waveguide that is also filled with a set of N parallel layers of dielectrics. The air-filled region above the current source is denoted by region 0. The air-filled region bellow the current source is denoted by region $0'$. This waveguide is analyzed using the superposition of the set of three parallel plate structures as shown. A primary ("original") structure [shown in Fig. 4.6(b)] is analyzed first, and the primary fields are obtained. Then, a set of scattered fields are added when the boundary conditions change through adding the set of dielectric layers and bottom conducting wall of Figs 4.6(c)-(d).

In what follows, the general eigenfunction expansions for the primary fields are being

deduced from the primary Hertz vectors. Consider the Hertz vectors of the primary fields to be directed along the x-direction, and are given by:

$$\vec{\Pi}_{e_p}{}^{i} = \hat{x}\psi_{e_p}{}^{i}, \tag{4.16}$$

and

$$\vec{\Pi}_{h_p}{}^{i} = \hat{x}\psi_{h_p}{}^{i}, \tag{4.17}$$

where $i = 0$ and $0'$. These fields need to satisfy only the boundary condition imposed by the equivalent shorted parallel-plate waveguide of figure 4.6(b), which contains the infinitesimal current source. The primary fields exist only in the region where the infinitesimal electric source is non-zero. Scattered fields exist in all the layers as shown in figures 4.6(c)-(d). For the primary structure, the following boundary conditions apply:

$$E_{zp} = 0 \quad \text{at } y = 0\,, \tag{4.18}$$

$$E_{zp} = 0 \quad \text{at } y = \mathrm{b}\,, \tag{4.19}$$

$$E_{zp}{}^{(0)} = 0 \quad \text{at } x = \mathrm{a}\,, \tag{4.20}$$

and

$$E_{y_p}{}^{(0)} = 0 \quad \text{at } x = \mathrm{a}\,. \tag{4.21}$$

Also, for $x < x'$, all fields must satisfy the radiation condition, where x' is the location of plane of the current source.

Employing the above boundary conditions with equations 4.10 and 4.12, the proper eigenfunction expansions for $\psi_{e_p}{}^{(0)}$ and $\psi_{h_p}{}^{(0)}$ **for region 0** are given by,

$$\psi_{e_p}{}^{(0)} = \frac{1}{2\pi}\int_{-\infty}^{\infty} dk_z \sum_m A_{m_p}{}^{(0)} \cos k_x{}^{(0)}(a-x)\sin(\frac{m\pi y}{b})e^{-jk_z z}\,, \tag{4.22}$$

and

$$\psi_{h_p}{}^{(0)} = \frac{1}{2\pi}\int_{-\infty}^{\infty} dk_z \sum_m B_{m_p}{}^{(0)} \sin k_x{}^{(0)}(a-x)\cos(\frac{m\pi y}{b})e^{-jk_z z}\,. \tag{4.23}$$

Whereas **for region** $0'$, $\psi_{e_p}{}^{(0')}$ and $\psi_{h_p}{}^{(0')}$ are given by

$$\psi_{e_p}{}^{(0')} = \frac{1}{2\pi}\int_{-\infty}^{\infty} dk_z \sum_m A_{m_p}{}^{(0')} e^{jk_x{}^{(0)}x}\sin(\frac{m\pi y}{b})e^{-jk_z z}\,, \tag{4.24}$$

and

$$\psi_{h_p}{}^{(0')} = \frac{1}{2\pi}\int_{-\infty}^{\infty} dk_z \sum_m B_{m_p}{}^{(0')} e^{jk_x{}^{(0)}x} \cos(\frac{m\pi y}{b}) e^{-jk_z z} , \tag{4.25}$$

where

$$k_i{}^2 = [k_x{}^{(i)}]^2 + [\frac{m\pi}{b}]^2 + k_z{}^2 = \omega^2 \epsilon_i \mu_o \qquad i = 0, 1, ..., N . \tag{4.26}$$

Here k_i is the wave number for the i-th layer, $k_x{}^i$ is the eigenvalue in the x direction, $\frac{m\pi}{b}$ is the eigenvalue in the y direction, and k_z is the Fourier transform variable. In these expressions, all the boundary values stated in 4.18,4.19,4.20 and 4.21 have been satisfied. Deploying the boundary condition at the source yields expressions for the unknown coefficients $A_{m_p}{}^{(0)}$, $B_{m_p}{}^{(0)}$, $A_{m_p}{}^{(0')}$, and $B_{m_p}{}^{(0')}$. The integration over k_z in the above expressions implies the inclusion of all the "modes" scattered by the point source. Away from the source, the above integration yields the discrete propagating modes of a source-free inhomogeneously filled rectangular waveguide. This has been verified numerically. For example, the x component of the magnetic field as a function of x, $H_x(x)$, at a frequency f= 10 GHz in an air-filled rectangular waveguide is shown in Figures 4.7 and 4.8. The guide dimensions are a = 23 mm and b= 11 mm, the longer dimension being along the x-axis. A point current source $J_y = \delta$ and $J_z = \delta$ is located at ($x = \frac{a}{2}$, $y = \frac{b}{2}$, $z = 0$). Figure 4.7 displays the field at the source, z=0.0. Figure 4.8 displays the field away from the source at a distance z = 0.01 λ, 0.1 λ and 0.5 λ. The plots show the evolution of the fundamental mode of the rectangular waveguide away from the source location.

For a current source $\vec{J}_s(r')$, located at $x = x'$ and defined as,

$$\vec{J}_s(r') = \hat{y}J_y + \hat{z}J_z , \tag{4.27}$$

the boundary conditions at the source are given by,

$$H_{y_p}{}^{(0)} - H_{y_p}{}^{(0')} = J_z , \tag{4.28}$$

$$H_{z_p}{}^{(0)} - H_{z_p}{}^{(0')} = -J_y , \tag{4.29}$$

$$E_{y_p}{}^{(0)} = E_{y_p}{}^{(0')} , \tag{4.30}$$

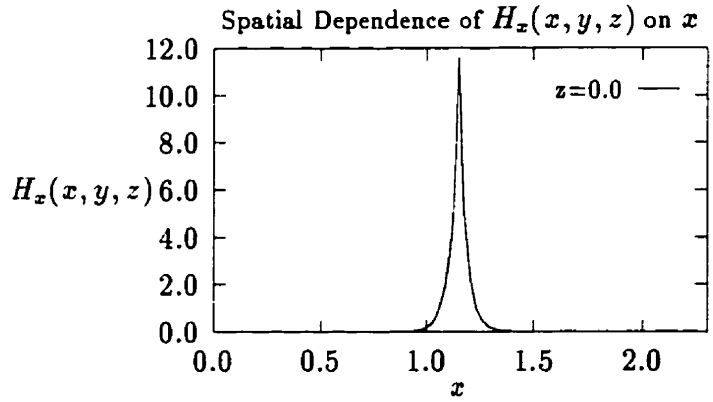

Figure 4.7: The x component of the magnetic field as a function of x (in cms), $H_x(x)$, at a frequency f= 10 GHz in an air-filled rectangular waveguide of dimensions a = 2.3 cms and b= 1.1 cms, the longer dimension being along the x-axis. A point current source $J_y = \delta$ and $J_z = \delta$ is located at $(x = \frac{a}{2},\ y = \frac{b}{2})$. The plot displays the field at the source. M=10.

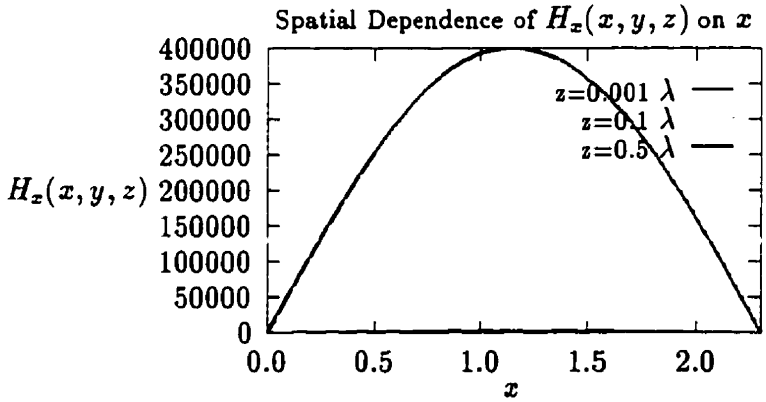

Figure 4.8: The x component of the magnetic field as a function of x, $H_x(x)$, at a frequency f= 10 GHz in an air-filled rectangular waveguide of dimensions a = 23 mm and b= 11 mm, the longer dimension being along the x-axis. A point current source $J_y = \delta$ and $J_z = \delta$ is located at $(x = \frac{a}{2},\ y = \frac{b}{2})$. The plot displays the field at the distance z = 0.001 λ, 0.1 λ and 0.5 λ from the source. The magnitude of the field very close to the source (at z= 0.001 *lambda*) is very small due to destructive interference of the modes. M=10.

and

$$E_{zp}^{(0)} = E_{zp}^{(0')} . \tag{4.31}$$

For the purpose of analyzing a planar geometry, the current flow is restricted to the plane of metalization. This analysis, however, can be extended to model an arbitrarily oriented current by including the third component of the current, J_x. For planar geometries, the infinitesimal current source is given by

$$J_y = \delta(y - y')\delta(z - z') , \tag{4.32}$$

and

$$J_z = \delta(y - y')\delta(z - z') . \tag{4.33}$$

The electric Green's function is related to the electric field as described in equation 4.3. Since the infinitesimal electric surface current source has only two components to it, namely a $y-$directed component and a $z-$directed component, the dyadic electric Green's function will only have six components to it, as opposed to the general form that has nine components. This is due to the fact that there are no components of the dyadic electric Green's function that give rise to an electric field due to a $x-$directed current source. The Green's function for this case is cast as:

$$\begin{aligned}\vec{G}^i(\vec{r},\vec{r}') = {} & \hat{x}\hat{y}\vec{G}^i_{xy}(\vec{r},\vec{r}') + \hat{x}\hat{z}\vec{G}^i_{xz}(\vec{r},\vec{r}') + \hat{y}\hat{y}\vec{G}^i_{yy}(\vec{r},\vec{r}') \\ & + \hat{y}\hat{z}\vec{G}^i_{yz}(\vec{r},\vec{r}') + \hat{z}\hat{y}\vec{G}^i_{zy}(\vec{r},\vec{r}') + \hat{z}\hat{z}\vec{G}^i_{zz}(\vec{r},\vec{r}') .\end{aligned} \tag{4.34}$$

The term $\vec{G}^i_{xy}(\vec{r},\vec{r}')$ is the component of the electric Green's function associated with the $\hat{x}$ component of the electric field in region i due to the $\hat{y}$-directed component of the infinitesimal electric surface current source located at $x' = x_{01}$. The rest of the terms are defined similarly.

In what follows, we proceed to apply the boundary conditions specified in equations 4.28-4.31. This yields the unknown amplitude coefficients for the Hertz vectors. Once the Hertz vectors are fully specified, the six components of the EM fields are deduced from their relations to the Hertz vectors. The boundary condition for H_y of equation 4.28, combined with equations 4.11, 4.22- 4.25 yields

$$\frac{1}{2\pi}\int_{-\infty}^{\infty}\sum_m\Big[\ B_{m_p}{}^{(0)}k_x{}^{(0)}\tfrac{m\pi}{b}\cos k_x{}^{(0)}(a-x')\sin(\tfrac{m\pi y}{b})$$

$$+j\omega\epsilon_o(-jk_z)A_{m_p}{}^{(0)}\cos k_x{}^{(0)}(a-x')\sin(\tfrac{m\pi y}{b})+B_{m_p}{}^{(0')}jk_x{}^{(0)}\tfrac{m\pi}{b}e^{jk_x{}^{(0)}x'}\sin(\tfrac{m\pi y}{b})$$

$$-j\omega\epsilon_o(-jk_z)A_{m_p}{}^{(0')}e^{jk_x{}^{(0)}x'}\sin(\frac{m\pi y}{b})\ \Big]e^{-jk_zz}\ =\ \delta(y-y')\delta(z-z')\ . \qquad (4.35)$$

Since the Dirac delta is defined as

$$\delta(z-z')\ =\ \frac{1}{2\pi}\int_{-\infty}^{\infty}dk_ze^{-jk_z(z-z')}, \qquad (4.36)$$

the integration in 4.35 can be eliminated and equation 4.35 reduces to

$$\sum_m\Big\{\Big[\ B_{m_p}{}^{(0)}k_x{}^{(0)}(\tfrac{m\pi}{b})+A_{m_p}{}^{(0)}\omega\epsilon_ok_z\Big]\cos k_x{}^{(0)}(a-x')$$

$$+\Big[B_{m_p}{}^{(0')}jk_x{}^{(0)}(\frac{m\pi}{b})-A_{m_p}{}^{(0')}\omega\epsilon_ok_z\Big]e^{jk_x{}^{(0)}x'}\Big\}\sin(\frac{m\pi y}{b})\ =\ \delta(y-y')e^{jk_zz'}\ . \qquad (4.37)$$

Multiplying both sides of 4.37 by $\sin(\frac{m\pi y'}{b})$ and utilizing the orthogonality property of sine functions,

$$\int_0^b\sin(\frac{p\pi}{b})\sin(\frac{m\pi}{b})dy\ =\ \begin{cases}0 & \text{if } p\neq m\\ \frac{b}{2} & \text{if } p=m\neq 0\ ,\end{cases} \qquad (4.38)$$

yields

$$\Big[B_{m_p}{}^{(0)}k_x{}^{(0)}(\tfrac{m\pi}{b})+A_{m_p}{}^{(0)}\omega\epsilon_ok_z\Big]\cos k_x{}^{(0)}(a-x')$$

$$+\Big[B_{m_p}{}^{(0')}jk_x{}^{(0)}(\frac{m\pi}{b})-A_{m_p}{}^{(0')}\omega\epsilon_ok_z\Big]e^{jk_x{}^{(0)}x'}\ =\ \frac{2}{b}\sin(\frac{m\pi y'}{b})e^{jk_zz'}\ . \qquad (4.39)$$

Similarly, utilizing the boundary condition for H_z of equation 4.29, and using an analogous procedure, one arrives at

$$\Big[B_{m_p}{}^{(0)}jk_x{}^{(0)}k_z-A_{m_p}{}^{(0)}j\omega\epsilon_o(\tfrac{m\pi}{b})\Big]\cos k_x{}^{(0)}(a-x')$$

$$-\Big[B_{m_p}{}^{(0')}k_x{}^{(0)}k_z-A_{m_p}{}^{(0')}j\omega\epsilon_o(\frac{m\pi}{b})\Big]e^{jk_x{}^{(0)}x'}\ =\ \frac{-\varepsilon_{om}}{b}\cos(\frac{m\pi y'}{b})e^{jk_zz'}\ , \qquad (4.40)$$

where,

$$\varepsilon_{o\nu}\ =\ \begin{cases}1 & \text{if } \nu=0\\ 2 & \text{if } \nu\geq 1\ ,\end{cases} \qquad (4.41)$$

and where the orthogonality condition for the cosine functions,

$$\int_0^b \cos(\frac{p\pi y}{b})\cos(\frac{m\pi y}{b})dy \;=\; \begin{cases} 0 & \text{if } p \neq m \\ \frac{b}{2} & \text{if } p = m \neq 0 \\ b & \text{if } p = m = 0 \;, \end{cases} \tag{4.42}$$

have been utilized. Similarly, from the continuity condition of E_y of equation 4.30, the following expression is derived:

$$[B_{m_p}{}^{(0)}\omega\mu_o k_z - A_{m_p}{}^{(0)}k_x{}^{(0)}(\tfrac{m\pi}{b})]\sin k_x{}^{(0)}(a-x') - [B_{m_p}{}^{(0')}\omega\mu_o k_z - A_{m_p}{}^{(0')}k_x{}^{(0)}(\frac{m\pi}{b})]e^{jk_x{}^{(0)}x'} \;=\; 0\;. \tag{4.43}$$

And from the continuity condition of E_z of equation 4.31, one arrives at

$$[B_{m_p}{}^{(0)}j\omega\mu_o(\tfrac{m\pi}{b}) + A_{m_p}{}^{(0)}jk_x{}^{(0)}k_z)]\sin k_x{}^{(0)}(a-x') - [B_{m_p}{}^{(0')}j\omega\mu_o(\frac{m\pi}{b}) + A_{m_p}{}^{(0')}k_x{}^{(0)}k_z]e^{jk_x{}^{(0)}x'} \;=\; 0\;. \tag{4.44}$$

Multiplying equation 4.40 by $j\frac{(\frac{m\pi}{b})}{k_z}$ and adding to equation 4.39 yields,

$$A_{m_p}{}^{(0)}\cos k_x{}^{(0)}(a-x') - A_{m_p}{}^{(0')}e^{jk_x{}^{(0)}x'} \;=\; \frac{e^{jk_z z'}}{\omega\epsilon_o b[(\frac{m\pi}{b})^2 + k_z{}^2]}\left\{-j\varepsilon_{om}\frac{m\pi}{b})\cos(\frac{m\pi y'}{b}) + 2k_z\sin(\frac{m\pi y'}{b})]\right\}\;. \tag{4.45}$$

Multiplying equation 4.43 by $\frac{(\frac{m\pi}{b})}{jk_z}$ and adding to equation 4.44 yields,

$$A_{m_p}{}^{(0)}\sin k_x{}^{(0)}(a-x') - A_{m_p}{}^{(0')}je^{jk_x{}^{(0)}x'} \;=\; 0\;. \tag{4.46}$$

In equations 4.45 and 4.46, $B_{m_p}{}^{(0)}$ and $B_{m_p}{}^{(0')}$ have been eliminated. By eliminating $A_{m_p}{}^{(0)}$ and $A_{m_p}{}^{(0')}$ instead of $B_{m_p}{}^{(0)}$ and $B_{m_p}{}^{(0')}$ using an analogous procedure, one arrives at

$$B_{m_p}{}^{(0)}\cos k_x{}^{(0)}(a-x') \;-\; B_{m_p}{}^{(0')}e^{jk_x{}^{(0)}x'} \;=\; \frac{e^{jk_z z'}}{k_x{}^{(0)}b[(\frac{m\pi}{b})^2 + k_z{}^2]}\left\{-\varepsilon_{om}k_z\cos(\frac{m\pi y'}{b}) + j2(\frac{m\pi}{b})\sin(\frac{m\pi y'}{b})\right\}\;, \tag{4.47}$$

and

$$B_{m_p}{}^{(0)} \sin k_x{}^{(0)}(a - x') - B_{m_p}{}^{(0')} e^{jk_x{}^{(0)}x'} = 0 . \tag{4.48}$$

Solving the above four equations for $A_{m_p}{}^{(0)}$,$A_{m_p}{}^{(0')}$,$B_{m_p}{}^{(0)}$ and $B_{m_p}{}^{(0')}$ using direct substitution yields:

$$A_{m_p}{}^{(0)} = \frac{e^{jk_z z'} e^{-jk_x{}^{(0)}(a-x')}}{\omega\epsilon_o b[(\frac{m\pi}{b})^2 + k_z{}^2]} \left\{ 2k_z \sin(\frac{m\pi y'}{b}) - j\varepsilon_{om}(\frac{m\pi}{b}) \cos(\frac{m\pi y'}{b}) \right\}, \tag{4.49}$$

$$A_{m_p}{}^{(0)'} = \frac{-je^{jk_z z'} e^{-jk_x{}^{(0)}a} \sin k_x{}^{(0)}(a - x')}{\omega\epsilon_o b[(\frac{m\pi}{b})^2 + k_z{}^2]} \left\{ 2k_z \sin(\frac{m\pi y'}{b}) - j\varepsilon_{om}(\frac{m\pi}{b}) \cos(\frac{m\pi y'}{b}) \right\}, \tag{4.50}$$

$$B_{m_p}{}^{(0)} = \frac{je^{jk_z z'} e^{-jk_x{}^{(0)}(a-x')}}{k_x{}^{(0)} b[(\frac{m\pi}{b})^2 + k_z{}^2]} \left\{ \varepsilon_{om} k_z \cos(\frac{m\pi y'}{b}) - j2(\frac{m\pi}{b}) \sin(\frac{m\pi y'}{b}) \right\}, \tag{4.51}$$

and

$$B_{m_p}{}^{(0)'} = \frac{je^{jk_z z'} e^{-jk_x{}^{(0)}a} \sin k_x{}^{(0)}(a - x')}{k_x{}^{(0)} b[(\frac{m\pi}{b})^2 + k_z{}^2]} \left\{ \varepsilon_{om} k_z \cos(\frac{m\pi y'}{b}) - j2(\frac{m\pi}{b}) \sin(\frac{m\pi y'}{b}) \right\}. \tag{4.52}$$

Here $A_{m_p}{}^{(0)}$,$A_{m_p}{}^{(0')}$ are the coefficients of the electric Hertz vectors $\psi_{e_p}{}^0$ and $\psi_{e_p}{}^{0'}$ which, for the case of $H_x = 0$, correspond to the LSM modes. $B_{m_p}{}^{(0)}$ and $B_{m_p}{}^{(0')}$ are the coefficients of the magnetic Hertz vectors $\psi_{e_p}{}^0$ and $\psi_{e_p}{}^{0'}$ which, for the case of $E_x = 0$, correspond to the LSE modes. The LSM and LSE modes are orthogonal to each others, and can exist independently. This property will be utilized to simplify the extraction of various coefficients in the analysis.

The amplitude coefficients for the various primary Hertz vectors have been obtained. With these coefficients, expressions for the various fields due to the point source surface current could be obtained in a straightforward manner from the expressions 4.8-4.13.

The Scattered Fields of An Inhomogeneously Filled Rectangular waveguide

In what follows, the general eigenfunction expansions will be deduced for the Hertz vectors of the scattered fields. This is achieved by considering the electromagnetic boundary

conditions at the various dielectric interfaces in the dielectric-filled shorted parallel plate waveguides depicted in Fig. 4.6(c)-(d).

The appropriate expansions for scattered Hertz potentials that are directed along the x-axis, i.e.,

$$\vec{\Pi}_{e_s}^{\,l} = \hat{x}\psi_{e_s}^{\,l}, \tag{4.53}$$

and

$$\vec{\Pi}_{h_s}^{\,l} = \hat{x}\psi_{h_s}^{\,l}, \tag{4.54}$$

are given by the following expressions for various regions $l = 0, 1, ..., N$.

For region 0:

$$\psi_{e_s}^{(0)} = \frac{1}{2\pi}\int_{-\infty}^{\infty} dk_z \sum_m A_{m_s}^{(0)} \cos k_x^{(0)}(a-x)\sin(\frac{m\pi y}{b})e^{-jk_z z}\ . \tag{4.55}$$

$$\psi_{h_s}^{(0)} = \frac{1}{2\pi}\int_{-\infty}^{\infty} dk_z \sum_m B_{m_s}^{(0)} \sin k_x^{(0)}(a-x)\cos(\frac{m\pi y}{b})e^{-jk_z z}\ . \tag{4.56}$$

For region 1:

$$\psi_{e_s}^{(1)} = \tfrac{1}{2\pi}\textstyle\int_{-\infty}^{\infty} dk_z \sum_m A_{m_s}^{(N)}[K_{1_s}\sin(k_x^{(1)}(x-x_{12})) + K_{1c}\cos(k_x^{(1)}(x-x_{12}))]$$

$$\sin(\frac{m\pi y}{b})e^{-jk_z z}\ . \tag{4.57}$$

$$\psi_{h_s}^{(1)} = \tfrac{1}{2\pi}\textstyle\int_{-\infty}^{\infty} dk_z \sum_m B_{m_s}^{(N)}[R_{1_s}\sin(k_x^{(1)}(x-x_{12})) + R_{1c}\cos(k_x^{(1)}(x-x_{12}))]$$

$$\cos(\frac{m\pi y}{b})e^{-jk_z z}\ . \tag{4.58}$$

For region 2:

$$\psi_{e_s}^{(2)} = \tfrac{1}{2\pi}\textstyle\int_{-\infty}^{\infty} dk_z \sum_m A_{m_s}^{(N)}[K_{2_s}\sin(k_x^{(2)}(x-x_{23})) + K_{2c}\cos(k_x^{(2)}(x-x_{23}))]$$

$$\sin(\frac{m\pi y}{b})e^{-jk_z z}\ . \tag{4.59}$$

$$\psi_{h_s}^{(2)} = \tfrac{1}{2\pi}\textstyle\int_{-\infty}^{\infty} dk_z \sum_m B_{m_s}^{(N)}[R_{1_s}\sin(k_x^{(2)}(x-x_{23})) + R_{1c}\cos(k_x^{(2)}(x-x_{23}))]$$

$$\cos(\frac{m\pi y}{b})e^{-jk_z z}\ . \tag{4.60}$$

For region i:

$$\psi_{e_s}{}^{(i)} = \frac{1}{2\pi}\int_{-\infty}^{\infty} dk_z \sum_m A_{m_s}{}^{(N)}[K_{i_s}\sin(k_x{}^{(i)}(x - x_{i,i+1})) + K_{i_c}\cos(k_x{}^{(i)}(x - x_{i,i+1}))]$$

$$\sin(\frac{m\pi y}{b})e^{-jk_z z} \ . \tag{4.61}$$

$$\psi_{h_s}{}^{(i)} = \frac{1}{2\pi}\int_{-\infty}^{\infty} dk_z \sum_m B_{m_s}{}^{(N)}[R_{i_s}\sin(k_x{}^{(i)}(x - x_{i,i+1})) + R_{i_c}\cos(k_x{}^{(i)}(x - x_{i,i+1}))]$$

$$\cos(\frac{m\pi y}{b})e^{-jk_z z} \ . \tag{4.62}$$

For region N-1:

$$\psi_{e_s}{}^{(N-1)} = \frac{1}{2\pi}\int_{-\infty}^{\infty} dk_z \sum_m A_{m_s}{}^{(N)}$$

$$[K_{N-1_s}\sin(k_x{}^{(N-1)}(x - x_{N-1,N})) + K_{N-1_c}\cos(k_x{}^{(N-1)}(x - x_{N-1,N}))]\sin(\frac{m\pi y}{b})e^{-jk_z z} \ . \tag{4.63}$$

$$\psi_{h_s}{}^{(N-1)} = \frac{1}{2\pi}\int_{-\infty}^{\infty} dk_z \sum_m B_{m_s}{}^{(N)}$$

$$[R_{N-1_s}\sin(k_x{}^{(N-1)}(x - x_{N-1,N})) + R_{N-1_c}\cos(k_x{}^{(N-1)}(x - x_{N-1,N}))]\cos(\frac{m\pi y}{b})e^{-jk_z z} \ . \tag{4.64}$$

and finally, for region N:

$$\psi_{e_s}{}^{(N)} = \frac{1}{2\pi}\int_{-\infty}^{\infty} dk_z \sum_m A_{m_s}{}^{(N)}\cos k_x{}^{(N)}(x)\sin(\frac{m\pi y}{b})e^{-jk_z z} \ . \tag{4.65}$$

$$\psi_{h_s}{}^{(N)} = \frac{1}{2\pi}\int_{-\infty}^{\infty} dk_z \sum_m B_{m_s}{}^{(N)}\sin k_x{}^{(N)}(x)\cos(\frac{m\pi y}{b})e^{-jk_z z} \ . \tag{4.66}$$

Note that the Hertz potentials $\psi_{e_s}{}^{(i)}$ and $\psi_{h_s}{}^{(i)}$, $i > 0$ are all expressed in terms of $A_{m_s}{}^{(N)}$ and $B_{m_s}{}^{(N)}$ respectively. The multiplying coefficients K_{i_s},K_{i_c},R_{i_s}, R_{i_c} can be evaluated using the boundary conditions for the continuity of the tangential fields at all the boundaries $x_{i,i+1}$, in succession, starting by the interface $x_{N-1,N}$. Regardless of the number of dielectric layers, there will always be a set of 2x2 equations with four unknowns $A_{m_s}{}^{(0)}$, $B_{m_s}{}^{(0)}$, $A_{m_s}{}^{(N)}$ and $B_{m_s}{}^{(N)}$. This important feature of the analysis greatly reduces the amount of mathematical manipulations compared to other methods.

The Boundary conditions for the Scattered Fields:

In this section, evaluation of the coefficients K_{i_s},K_{i_c},R_{i_s}, R_{i_c} included in the above expression are conducted. This is accomplished by enforcing the continuity boundary conditions for E_z, and H_y (or alternatively E_y, and H_z) at all the boundaries $x_{i,i+1}$, starting by the interface $x_{N-1,N}$. Once K_{N-1_s},K_{N-1_c},R_{N-1_s} and R_{N-1_c} are evaluated for region $N-1$, those for region $N-2$ can then be evaluated, and so on.

Enforcing the Boundary Conditions at the Interface $x_{N-1,N}$:

Using equations 4.63- 4.66 with equation 4.12 yields the following boundary condition for the continuity of E_z at the interface point $x_{N-1,N}$.

$$
\begin{aligned}
&k_z A_{m_s}{}^N [k_x{}^{(N-1)}(K_{N-1_s}\cos(k_x{}^{(N-1)}(x-x_{N-1,N}))\\
&-K_{N-1_c}\sin(k_x{}^{(N-1)}(x-x_{N-1,N}))) - k_x{}^{(N)}\sin(k_x{}^{(N)}x)]\\
&+j\omega\mu_o\tfrac{m\pi}{b}B_{m_s}{}^N[k_x{}^{(N-1)}(R_{N-1_s}\sin(k_x{}^{(N-1)}(x-x_{N-1,N}))\\
&+R_{N-1_c}\cos(k_x{}^{(N-1)}(x-x_{N-1,N})) - \sin(k_x{}^{(N)}x)] = 0, \qquad \text{for } x = x_{N-1,N}, \qquad (4.67)
\end{aligned}
$$

which yields,

$$
\begin{aligned}
&k_z A_{m_s}{}^N [k_x{}^{(N-1)}K_{N-1_s} - k_x{}^{(N)}\sin(k_x{}^{(N)}x_{N-1,N})]\\
&+ j\omega\mu_o\frac{m\pi}{b}B_{m_s}{}^N[R_{N-1_c} - \sin(k_x{}^{(N)}x_{N-1,N})] = 0\ , \qquad (4.68)
\end{aligned}
$$

and for this equation to hold, independent of $A_{m_s}{}^N$ and $B_{m_s}{}^N$, the following conditions are deduced;

$$K_{N-1_s} = \frac{k_x{}^{(N)}}{k_x{}^{(N-1)}}\sin(k_x{}^{(N)}x_{N-1,N}), \qquad (4.69)$$

and

$$R_{N-1_c} = \sin(k_x{}^{(N)}x_{N-1,N}) \qquad (4.70)$$

The independency of $A_{m_s}{}^N$ and $B_{m_s}{}^N$ is a direct consequence of them being the amplitude coefficients of the LSM and LSE modes respectively. The LSM and LSE mode are orthogonal modes of the structure that can exist independently. Similarly, using

equations 4.63- 4.66 with equation 4.10 yields the following boundary condition for the continuity of H_y at the interface point $x_{N-1,N}$.

$$-\omega k_z A_{m_s}{}^N[\epsilon_N \cos(k_x{}^{(N)}(x_{N-1,N})) - \epsilon_{N-1} K_{N-1_c}]$$

$$+ \frac{m\pi}{b} B_{m_s}{}^N[k_x{}^{(N-1)} R_{N-1_s} - k_x{}^N \cos(k_x{}^{(N)}(x_{N-1,N}))] = 0. \tag{4.71}$$

For this equation to hold, independent of $A_{m_s}{}^N$ and $B_{m_s}{}^N$,

$$R_{N-1_s} = \frac{k_x{}^{(N)}}{k_x{}^{(N-1)}} \cos(k_x{}^{(N)} x_{N-1,N}), \tag{4.72}$$

and

$$K_{N-1_c} = \frac{\epsilon_N}{\epsilon_{N-1}} \cos(k_x{}^{(N)} x_{N-1,N}) \, . \tag{4.73}$$

Enforcing the Boundary Conditions at the Interfaces $x_{i-1,i}$:

Enforcing the condition

$$E_z{}^{i-1} = E_z{}^i \tag{4.74}$$

yields

$$k_z A_{m_s}{}^N k_x{}^{(i)}[K_{i_s} \cos(k_x{}^{(i)} d_i) - K_{i_c} \sin(k_x{}^{(i)} d_i)]$$

$$-\omega\mu_o \tfrac{m\pi}{b} B_{m_s}{}^N[R_{i_s} \sin(k_x{}^{(i)} d_i) + R_{i_c} \cos(k_x{}^{(i)} d_i)]$$

$$- k_z A_{m_s}{}^N[k_x{}^{(i-1)} K_{i-1_s}] + \omega\mu_o \frac{m\pi}{b} B_{m_s}{}^N[R_{i-1_c}] \, , = 0 \tag{4.75}$$

where

$$d_i = x_{i,i+1} - x_{i-1,i} \, , \tag{4.76}$$

and

$$d_0 = a - x_{01} \, . \tag{4.77}$$

Since $A_{m_s}{}^N$ and $B_{m_s}{}^N$ are independent, the following two conditions hold simultaneously:

$$K_{i-1_s} = \frac{k_x{}^{(i)}}{k_x{}^{(i-1)}}[K_{i_s} \cos(k_x{}^{(i)} d_i) - K_{i_c} \sin(k_x{}^{(i)} d_i)] \, , \tag{4.78}$$

and

$$R_{i-1_c} = [R_{i_s} \sin(k_x{}^{(i)} d_i) + R_{i_c} \cos(k_x{}^{(i)} d_i)] \, . \tag{4.79}$$

Similarly, enforcing the boundary condition

$$H_y{}^{i-1} = H_y{}^{i} \tag{4.80}$$

yields

$$\begin{aligned}
&\omega\epsilon_i k_z A_{m_s}{}^{N}[K_{i_s}\sin(k_x{}^{(i)}d_i) + K_{i_c}\cos(k_x{}^{(i)}d_i)] \\
&+\tfrac{m\pi}{b}B_{m_s}{}^{N}k_x{}^{(i)}[R_{i_s}\cos(k_x{}^{(i)}d_i) \;+\; R_{i_c}\sin(k_x{}^{(i)}d_i)] \\
&\qquad - \omega\epsilon_{i-1}k_z A_{m_s}{}^{N}[K_{i-1_c}] - \frac{m\pi}{b}B_{m_s}{}^{N}k_x{}^{(i-1)}[R_{i-1_s}] \;=\; 0\ ,
\end{aligned} \tag{4.81}$$

which again leads to,

$$K_{i-1_c} = \frac{\epsilon_i}{\epsilon_{i-1}}[K_{i_s}\sin(k_x{}^{(i)}d_i) + K_{i_c}\cos(k_x{}^{(i)}d_i)]\ , \tag{4.82}$$

and

$$R_{i-1_s} \;=\; \frac{k_x{}^{(i)}}{k_x{}^{(i-1)}}[R_{i_s}\cos(k_x{}^{(i)}d_i) \;-\; R_{i_c}\sin(k_x{}^{(i)}d_i)]\ . \tag{4.83}$$

The expressions for K_{i-1_s}, K_{i-1_c}, R_{i-1_s}, and R_{i-1_c} are recursive. All these terms are implicitly functions of K_{N-1_s}, K_{N-1_c}, R_{N-1_s}, and R_{N-1_c}.

Enforcing the Boundary Conditions of The Total Fields at the Interface $x_{0,1}$:

The boundary conditions for all the three equivalent parallel plate guides have been satisfied. All the equivalent guides are combined to model the actual rectangular wave guide with its filling dielectrics. This requires that the boundary condition at $x = x_{01}$ be enforced. The scattered tangential fields in region 1 must match the corresponding fields (which are the superposition of scattered and primary fields) in region $0'$, at the interface. These boundary conditions are

$$E_{y_p}{}^{0'} + E_{y_s}{}^{0} = E_{y_s}{}^{1} \qquad \text{at } x = x_{01}\ , \tag{4.84}$$

$$E_{z_p}{}^{0'} + E_{z_s}{}^{0} = E_{z_s}{}^{1} \qquad \text{at } x = x_{01}\ , \tag{4.85}$$

$$H_{y_p}{}^{0'} + H_{y_s}{}^{0} = H_{y_s}{}^{1} \qquad \text{at } x = x_{01}\ , \tag{4.86}$$

and

$$H_{zp}{}^{0'} + H_{zs}{}^{0} = H_{zs}{}^{1} \qquad \text{at } x = x_{01} \; . \tag{4.87}$$

Deploying equation 4.84 yields,

$$\begin{aligned}
&A_{m_p}{}^{(0')} e^{jk_x{}^{(0)}x_{0,1}} jk_x{}^{(0)} (\tfrac{m\pi}{b}) - B_{m_p}{}^{(0')} e^{jk_x{}^{(0)}x_{0,1}} (\omega\mu_o k_z) \\
&- A_{m_s}{}^{(0)} k_x{}^{(0)} (\tfrac{m\pi}{b}) \sin k_x{}^{(0)}(a - x_{0,1}) - B_{m_s}{}^{(0)} \sin k_x{}^{(0)}(a - x_{0,1})(\omega\mu_o k_z) \; = \\
&A_{m_s}{}^{(N)} k_x{}^{(1)} (\tfrac{m\pi}{b}) [K_{1_s} \cos k_x{}^{(0)}(x_{0,1} - x_{1,2}) - K_{1_c} \sin k_x{}^{(0)}(x_{0,1} - x_{1,2})] \\
&- B_{m_s}{}^{(N)} (\omega\mu_o k_z) [R_{1_s} \sin k_x{}^{(0)}(x_{0,1} - x_{1,2}) + R_{1_c} \cos k_x{}^{(0)}(x_{0,1} - x_{1,2})] \; .
\end{aligned} \tag{4.88}$$

and similarly for the three other equations. The above 4x4 system of equations decouples into a set of two 2x2 equations, one for the LSE coefficients, B_{m_s}, and the other for the LSM coefficients, A_{m_s}. With some algebraic manipulations, the following equations are deduced:

$$\begin{pmatrix} k_x{}^{(0)} \sin k_x{}^{(0)}(a - x_{0,1}) & -k_x{}^{(1)} [K_{1_s} \cos k_x{}^{(1)}(x_{0,1} - x_{1,2}) - K_{1_c} \sin k_x{}^{(0)}(x_{0,1} - x_{1,2})] \\ \cos k_x{}^{(0)}(a - x_{0,1}) & -\epsilon_{r1} [K_{1_s} \sin k_x{}^{(1)}(x_{0,1} - x_{1,2}) + K_{1_c} \cos k_x{}^{(1)}(x_{0,1} - x_{1,2})] \end{pmatrix}$$

$$\begin{pmatrix} A_{m_s}{}^{(0)} \\ A_{m_s}{}^{(N)} \end{pmatrix} = \begin{pmatrix} -A_{m_p}{}^{(0')} e^{jk_x{}^{(0)}x_{0,1}} jk_x{}^{(0)} \\ -A_{m_p}{}^{(0')} e^{jk_x{}^{(0)}x_{0,1}} \end{pmatrix} \tag{4.89}$$

for the LSM coefficients and

$$\begin{pmatrix} -\sin k_x{}^{(0)}(a - x_{0,1}) & R_{1_s} \sin k_x{}^{(1)}(x_{0,1} - x_{1,2}) + R_{1_c} \cos k_x{}^{(1)}(x_{0,1} - x_{1,2})] \\ k_x{}^{(0)} \cos k_x{}^{(0)}(a - x_{0,1}) & k_x{}^{(1)} [R_{1_s} \cos k_x{}^{(1)}(x_{0,1} - x_{1,2}) - R_{1_c} \sin k_x{}^{(1)}(x_{0,1} - x_{1,2})] \end{pmatrix}$$

$$\begin{pmatrix} B_{m_s}{}^{(0)} \\ B_{m_s}{}^{(N)} \end{pmatrix} = \begin{pmatrix} B_{m_p}{}^{(0')} e^{jk_x{}^{(0)}x_{0,1}} \\ B_{m_p}{}^{(0')} e^{jk_x{}^{(0)}x_{0,1}} jk_x{}^{(0)} \end{pmatrix} \tag{4.90}$$

for the LSE coefficients. Solving for $A_{m_s}{}^{(N)}$ and $A_{m_s}{}^{(0)}$ in 4.89 yields

$$\begin{aligned}
A_{m_s}{}^{(N)} &= \frac{k_x{}^{(0)} e^{jk_x{}^{(0)}x_{0,1}} [\sin k_x{}^{(0)}(a - x_{0,1}) - j \cos k_x{}^{(0)}(a - x_{0,1})]}{k_x{}^{(0)} \sin k_x{}^{(0)}(a - x_{0,1}) \Re - \cos k_x{}^{(0)}(a - x_{0,1}) \Im} A_{m_s}{}^{(0')} \\
&= \frac{-jk_x{}^{(0)} e^{jk_x{}^{(0)}a}}{k_x{}^{(0)} \sin k_x{}^{(0)}(a - x_{0,1}) \Re - \cos k_x{}^{(0)}(a - x_{0,1}) \Im} A_{m_p}{}^{(0')} \; ,
\end{aligned} \tag{4.91}$$

and

$$A_{m_s}^{(0)} = \frac{e^{jk_x^{(0)}x_{0,1}}[\Re - jk_x^{(0)}\Im]}{k_x^{(0)}\sin k_x^{(0)}(a-x_{0,1})\Re - \cos k_x^{(0)}(a-x_{0,1})\Im} A_{m_p}^{(0')} , \tag{4.92}$$

where

$$\Re = \epsilon_{r1}[K_{1_s}\sin k_x^{(1)}(x_{0,1}-x_{1,2}) + K_{1_c}\cos k_x^{(1)}(x_{0,1}-x_{1,2})] , \tag{4.93}$$

and

$$\Im = k_x^{(1)}[K_{1_s}\cos k_x^{(1)}(x_{0,1}-x_{1,2}) - K_{1_c}\sin k_x^{(0)}(x_{0,1}-x_{1,2})] . \tag{4.94}$$

Similarly, solving for $B_{m_s}^{(N)}$ and $B_{m_s}^{(0)}$ in 4.90 yields

$$B_{m_s}^{(N)} = \frac{k_x^{(0)}e^{jk_x^{(0)}x_{0,1}}[j\sin k_x^{(0)}(a-x_{0,1})+\cos k_x^{(0)}(a-x_{0,1})]}{\sin k_x^{(0)}(a-x_{0,1})\aleph + k_x^{(0)}\cos k_x^{(0)}(a-x_{0,1})\wp} B_{m_p}^{(0')}$$

$$= \frac{k_x^{(0)}e^{jk_x^{(0)}a}}{\sin k_x^{(0)}(a-x_{0,1})\aleph + k_x^{(0)}\cos k_x^{(0)}(a-x_{0,1})\wp} B_{m_p}^{(0')} , \tag{4.95}$$

and

$$B_{m_s}^{(0)} = \frac{-k_x^{(0)}e^{jk_x^{(0)}x_{0,1}}[\aleph - jk_x^{(0)}\wp]}{\sin k_x^{(0)}(a-x_{0,1})\aleph + k_x^{(0)}\cos k_x^{(0)}(a-x_{0,1})\wp} B_{m_p}^{(0')} , \tag{4.96}$$

where

$$\aleph = k_x^{(1)}[R_{1_s}\cos k_x^{(1)}(x_{0,1}-x_{1,2}) - R_{1_c}\sin k_x^{(1)}(x_{0,1}-x_{1,2})] , \tag{4.97}$$

and

$$\wp = R_{1_s}\sin k_x^{(1)}(x_{0,1}-x_{1,2}) + R_{1_c}\cos k_x^{(1)}(x_{0,1}-x_{1,2})] . \tag{4.98}$$

The relations for $\Re$, $\Im$, $\aleph$, $\wp$ are all implicitly functions of K_{N-1_s}, K_{N-1_c}, R_{N-1_s}, and R_{N-1_c}. Since the metallization of the MIS microstrip circuit rests on top of the dielectric layers, i.e. at $x = x_{01}$, the point current source studied so far will be actually located at that plane, i.e., in the previous analysis $x' = x_{01}$. It follows that region $0'$ no longer exists. The total EM fields in region 0 are the superposition of the primary and scattered fields. From equations 4.22, 4.23, 4.55 and 4.56, we notice that these fields have the same functional form but with different amplitude coefficients. Hence, the total LSM field in region 0, obtained by adding the primary and scattered fields, will have the same functional form with an amplitude coefficient, $A_m^{(0)}$ that is the sum of $A_{m_p}^{(0)}$ and $A_{m_s}^{(0)}$, i.e.

$$A_m^{(0)} = A_{m_p}^{(0)} + A_{m_s}^{(0)}, \tag{4.99}$$

and similarly,

$$B_m^{(0)} = B_{m_p}^{(0)} + B_{m_s}^{(0)}, \tag{4.100}$$

and similarly, for consistency,

$$A_m^{(N)} = A_{m_s}^{(N)}\,, \tag{4.101}$$

$$B_m^{(N)} = B_{m_s}^{(N)}\,. \tag{4.102}$$

The electric Green's function in region 0 will be used in the next section to conduct a theoretical dispersion analysis for shielded MIS lines. Hence, evaluating the amplitude coefficient $A_m^{(0)}$ and $B_m^{(0)}$ is of particular importance. After some algebraic manipulations of the expressions 4.99 and 4.100, $A_m^{(0)}$ and $B_m^{(0)}$ can be cast in the following explicit form:

$$A_m^{(0)} = \frac{e^{jk_z z'}}{\omega\epsilon_o b[(\frac{m\pi}{b})^2+k_z{}^2]\cos k_x^{(0)}d_0}\left[-j\varepsilon_{om}\frac{m\pi}{b}\cos\left(\frac{m\pi y'}{b}\right)+2k_z\sin\left(\frac{m\pi y'}{b}\right)\right]$$

$$\frac{1}{\left[1-k_x^{(0)}\tan k_x^{(0)}d_0\frac{a_{22}}{a_{12}}\right]} \tag{4.103}$$

and

$$B_m^{(0)} = \frac{je^{jk_z z'}}{b[(\frac{m\pi}{b})^2+k_z{}^2]\cos k_x^{(0)}d_0}\left[\varepsilon_{om}k_z\cos\left(\frac{m\pi}{b}\right)-j2\frac{m\pi y'}{b}\sin\left(\frac{m\pi y'}{b}\right)\right]$$

$$\frac{1}{\left[k_x^{(0)}+\tan k_x^{(0)}d_0\frac{b_{22}}{b_{12}}\right]} \tag{4.104}$$

where

$$a_{12} = k_x^{(1)}(\,K_{1c}\sin k_x^{(1)}d_1 - K_{1_s}\cos k_x^{(1)}d_1\,) \tag{4.105}$$

$$a_{22} = \epsilon_{r1}(\,K_{1c}\cos k_x^{(1)}d_1 + K_{1_s}\sin k_x^{(1)}d_1\,) \tag{4.106}$$

$$b_{12} = (\,R_{1_s}\sin k_x^{(1)}d_1 + R_{1c}\cos k_x^{(1)}d_1\,) \tag{4.107}$$

$$b_{22} = k_x^{(0)}(\,R_{1_s}\cos k_x^{(1)}d_1 - R_{1c}\sin k_x^{(1)}d_1\,) \tag{4.108}$$

The multiplying factor ε_{om} is defined in 4.41. The terms R_{1_s}, R_{1c}, K_{1_s}, and K_{1c} are related recursively to R_{N-1_s}, R_{N-1_c}, K_{N-1_s}, and K_{N-1_c} through equations 4.83, 4.79, 4.78, and 4.82 respectively, with the values R_{N-1_s}, R_{N-1_c}, K_{N-1_s}, and K_{N-1_c} given in 4.72, 4.70, 4.69, and 4.73 respectively.

In the above analysis, the Hertz vectors excited by an infinitesimal electric surface current in an inhomogeneously loaded waveguide have been derived. The electric and magnetic fields in all the layers are related to the Hertz vectors as described in equations 4.8-4.13. The electric Green's function is related to the electric field as described in equations 4.3 and 4.34. From these, all fields become readily available. For example, in region N (the bottom dielectric layer), the components of the electric and magnetic fields are given by

$$E_x^{(N)} = \frac{1}{2\pi}\int_{-\infty}^{\infty} dk_z \sum_m [k^2 - (k_x^{(N)})^2] A_m^{(N)} \cos k_x^{(N)} x \sin(\frac{m\pi y}{b})\, e^{-jk_z z}\ , \tag{4.109}$$

$$H_x^{(N)} = \frac{1}{2\pi}\int_{-\infty}^{\infty} dk_z \sum_m [k^2 - (k_x^{(N)})^2] B_m^{(N)} \sin k_x^{(N)} x \cos(\frac{m\pi y}{b})\, e^{-jk_z z}\ , \tag{4.110}$$

$$E_y^{(N)} = \tfrac{1}{2\pi}\textstyle\int_{-\infty}^{\infty} dk_z \sum_m [-k_x^{(N)}(\frac{m\pi}{b}) A_m^{(N)} - k_z \omega \mu_o B_m^{(N)}]$$
$$\sin k_x^{(N)} x \cos(\frac{m\pi y}{b})\, e^{-jk_z z}\ , \tag{4.111}$$

$$H_y^{(N)} = \tfrac{1}{2\pi}\textstyle\int_{-\infty}^{\infty} dk_z \sum_m [-k_x^{(N)}(\frac{m\pi}{b}) B_m^{(N)} - k_z \omega \epsilon_N A_m^{(N)}]$$
$$\cos k_x^{(N)} x \sin(\frac{m\pi y}{b})\, e^{-jk_z z}\ , \tag{4.112}$$

$$E_z^{(N)} = \tfrac{1}{2\pi}\textstyle\int_{-\infty}^{\infty} dk_z \sum_m [jk_z k_x^{(N)} A_m^{(N)} - j\omega \mu_o(\frac{m\pi}{b}) B_m^{(N)}]$$
$$\sin k_x^{(N)} x \sin(\frac{m\pi y}{b})\, e^{-jk_z z}\ , \tag{4.113}$$

$$H_z^{(N)} = \tfrac{1}{2\pi}\textstyle\int_{-\infty}^{\infty} dk_z \sum_m [jk_z k_x^{(N)} B_m^{(N)} - j\omega \epsilon_N(\frac{m\pi}{b}) A_m^{(N)}]$$
$$\cos k_x^{(N)} x \cos(\frac{m\pi y}{b})\, e^{-jk_z z}\ , \tag{4.114}$$

where $A_m^{(N)}$ and $B_m^{(N)}$ have been derived in 4.91 and 4.95. The above electric field expressions are directly proportional to the electric Green's function as defined in 4.3 and 4.34. Using this definition, the components of the Green's function can be easily extracted. For example, the components of the electric field in region N are given by

$$E_x^{(N)} = -j\omega\mu_o \left\{ \left[G^N{}_{xz}(\vec{r}, \vec{r}') \right] + \left[G^N{}_{xy}(\vec{r}, \vec{r}') \right] \right\}\ , \tag{4.115}$$

$$E_y^{(N)} = -j\omega\mu_o \left\{ \left[G^N{}_{yz}(\vec{r},\vec{r}') \right] + \left[G^N{}_{yy}(\vec{r},\vec{r}') \right] \right\} , \tag{4.116}$$

and

$$E_z^{(N)} = -j\omega\mu_o \left\{ \left[G^N{}_{zz}(\vec{r},\vec{r}') \right] + \left[G^N{}_{zy}(\vec{r},\vec{r}') \right] \right\} . \tag{4.117}$$

As noted earlier, the fields generated from the $z-$component of the point current source are proportional to $\sin(\frac{m\pi y'}{b})$, whereas the fields generated from the $y-$component of the point current source are proportional to $\cos(\frac{m\pi y'}{b})$. Hence $G^N{}_{xz}$, $G^N{}_{yz}$, and $G^N{}_{zz}$ are proportional to $\sin(\frac{m\pi y'}{b})$ whereas $G^N{}_{xy}$, $G^N{}_{yy}$, and $G^N{}_{zy}$ are proportional to $\cos(\frac{m\pi y'}{b})$. Analogous expressions can be cast for the Green's function all other layers.

In the next section, the derived Green's functions will be used to conduct a dispersion analysis for shielded lossy MIS transmission lines. Evaluating the Green's function for only region (0) is sufficient to achieve this task, as will be explained later. Furthermore, the Green's function will be used to establish the continuity of the electric fields tangential to the plane of metalization. Hence, the evaluation of $G_{xy}{}^{(0)}$ and $G_{xz}{}^{(0)}$ is unnecessary. The mathematical task reduces to obtaining the remaining four components of the Green's function dyad: $G_{yy}{}^{(0)}$, $G_{yz}{}^{(0)}$, $G_{zy}{}^{(0)}$, and $G_{zz}{}^{(0)}$. These are readily available from the previous analysis, and are given explicitly as:

$$G_{yy}{}^{(0)} = \frac{1}{2\pi}\int_{-\infty}^{\infty} dk_z \sum_m g^{(0)}{}_{yy_m}(x) \cos\left(\frac{m\pi y}{b}\right) \cos\left(\frac{m\pi y'}{b}\right) e^{-jk_z(z-z')} , \tag{4.118}$$

$$G_{yz}{}^{(0)} = \frac{1}{2\pi}\int_{-\infty}^{\infty} dk_z \sum_m g^{(0)}{}_{yz_m}(x) \cos\left(\frac{m\pi y}{b}\right) \sin\left(\frac{m\pi y'}{b}\right) e^{-jk_z(z-z')} , \tag{4.119}$$

$$G_{zy}{}^{(0)} = \frac{1}{2\pi}\int_{-\infty}^{\infty} dk_z \sum_m g^{(0)}{}_{zz_m}(x) \sin\left(\frac{m\pi y}{b}\right) \cos\left(\frac{m\pi y'}{b}\right) e^{-jk_z(z-z')} , \tag{4.120}$$

and

$$G_{zz}{}^{(0)} = \frac{1}{2\pi}\int_{-\infty}^{\infty} dk_z \sum_m g^{(0)}{}_{zz_m}(x) \sin\left(\frac{m\pi y}{b}\right) \sin\left(\frac{m\pi y'}{b}\right) e^{-jk_z(z-z')} , \tag{4.121}$$

where

$$g^{(0)}{}_{yy_m}(x) = \varepsilon_{om} \left[\left(\frac{m\pi}{b}\right)^2 T_1 - k_z{}^2 T_{LSE}(x_{01}) \right] C(x) , \tag{4.122}$$

$$g^{(0)}{}_{yz_m}(x) = 2\left(\frac{m\pi}{b}\right) k_z \left[T_1 + T_{LSE}(x_{01}) \right] C(x) , \tag{4.123}$$

$$g^{(0)}{}_{zy_m}(x) = g^{(0)}{}_{yz_m}(x) , \tag{4.124}$$

and

$$g^{(0)}{}_{zz_m}(x) = \left[k_z{}^2 T_1 - (\frac{m\pi}{b})^2 T_{LSE}(x_{01})\right] C(x) , \tag{4.125}$$

and where

$$T_1 = \frac{1}{k_o{}^2}[k_x{}^{(0)} k_x{}^{(1)} T_{LSM}(x_{01})] , \tag{4.126}$$

and

$$C(x) = \frac{1}{b[(\frac{m\pi}{2})^2 + k_z{}^2]} \frac{\sin k_x{}^{(0)}(a-x)}{\cos k_x{}^{(0)}(a-x_{01})} , \tag{4.127}$$

with T_{LSM} and T_{LSE} given by

$$T_{LSM}(x_{01}) = \frac{-1}{k_x{}^{(1)}(1 - \frac{a_{22}}{a_{12}} k_x{}^{(0)} \tan k_x{}^{(0)} d_0)} \tag{4.128}$$

and

$$T_{LSE}(x_{01}) = \frac{1}{k_x{}^{(0)} + \frac{b_{22}}{b_{12}} \tan k_x{}^{(0)} d_0} \tag{4.129}$$

Case of Two Dielectric Layers

Consider the case of two dielectric layers, i.e $N = 2$. By arranging the terms and re-writing equations 4.91 and 4.95 for $N = 2$, one arrives at

$$A_m{}^{(2)} = \frac{-\epsilon_{r1} k_x{}^{(0)} k_x{}^{(1)} \tan k_x{}^{(0)}(a-x_{0,1})[-j\varepsilon_{om} \frac{m\pi}{b} \cos \frac{m\pi y'}{b} + 2k_z \sin \frac{m\pi y'}{b}]}{\omega \epsilon_o b [(\frac{m\pi}{b})^2 + (k_z)^2] [\cos k_x{}^{(2)} x_{12} \cos k_x{}^{(1)}(x_{01} - x_{12})]}$$

$$\frac{e^{jk_z z'}}{d_{LSM}}, \tag{4.130}$$

and

$$B_m{}^{(2)} = \frac{-jk_x{}^{(1)} \tan k_x{}^{(0)}(a - x_{0,1})[-\varepsilon_{om} k_z \cos \frac{m\pi y'}{b} + 2j \frac{m\pi}{b} \sin \frac{m\pi y'}{b}]}{b [(\frac{m\pi}{b})^2 + (k_z)^2] [\cos k_x{}^{(2)} x_{12} \cos k_x{}^{(1)}(x_{01} - x_{12})]} \frac{e^{jk_z z'}}{d_{LSE}}. \tag{4.131}$$

For $A_m{}^{(0)}$ and $B_m{}^{(0)}$,

$$A_m{}^{(0)} = \frac{k_x{}^{(1)} [\epsilon_{r1} k_x{}^{(2)} \tan k_x{}^{(2)} x_{12} + \epsilon_{r2} k_x{}^{(1)} \tan k_x{}^{(1)}(x_{01} - x_{12})]}{\omega \epsilon_o b [(\frac{m\pi}{b})^2 + (k_z)^2] \cos k_x{}^{(0)}(a - x_{01})}$$

$$[-j\varepsilon_{om}(\frac{m\pi}{b}) \cos(\frac{m\pi y'}{b}) + 2k_z \sin(\frac{m\pi y'}{b})] \frac{e^{jk_z z'}}{d_{LSM}} \tag{4.132}$$

and

$$B_m^{(0)} = \frac{-j\,[k_x^{(2)}\,\tan k_x^{(1)}(x_{01}-x_{12}) + k_x^{(1)}\,\tan k_x^{(2)}x_{12}]}{b\,[(\frac{m\pi}{b})^2+(k_z)^2]\,\cos k_x^{(0)}(a-x_{01})}$$

$$[-\varepsilon_{om}k_z\,\cos(\frac{m\pi y'}{b}) + 2j(\frac{m\pi}{b})\,\sin(\frac{m\pi y'}{b})]\,\frac{e^{jk_z z'}}{d_{LSE}}\,. \qquad (4.133)$$

where d_{LSM} and d_{LSE} are given by

$$d_{LSM} = \epsilon_{r1}k_x^{(0)}\tan k_x^{(0)}(a-x_{01})[\epsilon_{r2}k_x^{(1)} - \epsilon_{r1}k_x^{(2)}\tan k_x^{(2)}x_{12}\tan k_x^{(1)}(x_{01}-x_{12})]$$

$$+\ k_x^{(1)}\,[\epsilon_{r1}\,k_x^{(2)}\,\tan k_x^{(2)}x_{12} + \epsilon_{r2}\,k_x^{(1)}\,\tan k_x^{(1)}(x_{01}-x_{12})\,, \qquad (4.134)$$

and

$$d_{LSE} = k_x^{(0)}\,[k_x^{(2)}\,\tan k_x^{(1)}(x_{01}-x_{12}) + k_x^{(1)}\tan k_x^{(2)}x_{12}]$$

$$+\ k_x^{(1)}\,\tan k_x^{(0)}(a-x_{01})[k_x^{(2)} - k_x^{(1)}\,\tan k_x^{(2)}x_{12}\tan k_x^{(1)}(x_{01}-x_{12})] \qquad (4.135)$$

For example, the $\hat{z}$ component of the electric field, after some algebra, could be cast as

$$E_z^{(2)} = \frac{1}{2\pi}\int_{-\infty}^{\infty}dk_z\,\sum_m \frac{-j\omega\mu_o\tan k_x^{(0)}(a-x_{0,1})[\sin k_x^{(2)}x\ \sin(\frac{m\pi y}{b})]}{b\,[(\frac{m\pi}{b})^2+(k_z)^2]\,[\cos k_x^{(2)}x_{12}\ \cos k_x^{(1)}(x_{01}-x_{12})]}$$

$$\left\{\varepsilon_{om}\cos(\frac{m\pi y'}{b})\left[\frac{-j\epsilon_{r1}k_x^{(0)}k_x^{(1)}k_x^{(2)}(\frac{m\pi}{b})k_z}{k_o{}^2 d_{LSM}} + \frac{jk_x^{(1)}(\frac{m\pi}{b})k_z}{d_{LSE}}\right]\right.$$

$$\left. +2\sin(\frac{m\pi y'}{b})\left[\frac{\epsilon_{r1}k_x^{(0)}k_x^{(1)}k_x^{(2)}k_z{}^2}{k_o{}^2 d_{LSM}} + \frac{k_x^{(1)}(\frac{m\pi}{b})^2}{d_{LSE}}\right]\right\} e^{-jk_z(z-z')}\,. \qquad (4.136)$$

with d_{LSM} and d_{LSE} defined in 4.134 and 4.135 respectively. The above equation could be written as

$$E_z^{(2)} = -j\omega\mu_o\left\{\left[\vec{G}_{zz}^2(\vec{r},\vec{r}')\right] + \left[\vec{G}_{zy}^2(\vec{r},\vec{r}')\right]\right\}\,, \qquad (4.137)$$

where

$$\vec{G}_{zz}^2 = \frac{1}{2\pi}\int_{-\infty}^{\infty}dk_z\,\sum_m \frac{2k_x^{(1)}\tan k_x^{(0)}(a-x_{0,1})[\sin k_x^{(2)}x\ \sin(\frac{m\pi y}{b})\ \sin(\frac{m\pi y'}{b})]}{b\,[(\frac{m\pi}{b})^2+(k_z)^2]\,[\cos k_x^{(2)}x_{12}\ \cos k_x^{(1)}(x_{01}-x_{12})]}$$

$$\left[\frac{\epsilon_{r1}k_x^{(0)}k_x^{(2)}k_z{}^2}{k_o{}^2 d_{LSM}} + \frac{(\frac{m\pi}{b})^2}{d_{LSE}}\right] e^{-jk_z(z-z')}\,, \qquad (4.138)$$

and

$$\vec{G}^2_{zy} = \frac{1}{2\pi}\int_{-\infty}^{\infty} dk_z \sum_m \frac{-j\epsilon_{om}(\frac{m\pi}{b})k_x^{(1)}k_z \tan k_x^{(0)}(a-x_{0,1})[\sin k_x^{(2)}x \;\; \sin(\frac{m\pi y}{b})\cos(\frac{m\pi y'}{b})]}{b\;[(\frac{m\pi}{b})^2+(k_z)^2]\;[\cos k_x^{(2)}x_{12} \;\; \cos k_x^{(1)}(x_{01}-x_{12})]}$$

$$\left[\frac{\epsilon_{r1}k_x^{(0)}k_x^{(2)}}{{k_o}^2 d_{LSM}} - \frac{1}{d_{LSE}}\right] e^{-jk_z(z-z')} \; . \tag{4.139}$$

Similarly, all the field components in all the layers can be obtained in the same systematic approach.

Case of Three Dielectric Layers

In what follows, the recursive relations for K_{i_s}, K_{i_c}, R_{i_s}, and R_{i_c} are evaluated for the case of three layers of dielectrics. Substituting for N=3 in equations 4.69, 4.73, 4.72, 4.70, 4.78, 4.82, 4.83 and 4.79, one arrives at,

$$K_{2_s} = \frac{k_x^{(3)}}{k_x^{(2)}}\sin(k_x^{(3)}x_{2,3}), \tag{4.140}$$

$$K_{2_c} = \frac{\epsilon_3}{\epsilon_2}\cos(k_x^{(3)}x_{2,3}), \tag{4.141}$$

$$R_{2_s} = \frac{k_x^{(3)}}{k_x^{(2)}}\cos(k_x^{(3)}x_{2,3}), \tag{4.142}$$

$$R_{2_c} = \sin(k_x^{(3)}x_{2,3}), \tag{4.143}$$

$$K_{1_s} = \frac{k_x^{(2)}}{k_x^{(1)}}[K_{2_s}\cos(k_x^{(2)}d_2) - K_{2_c}\sin(k_x^{(2)}d_2)]$$

$$= \frac{k_x^{(2)}}{k_x^{(1)}}[\frac{k_x^{(3)}}{k_x^{(2)}}\sin(k_x^{(3)}x_{2,3})\cos(k_x^{(2)}d_2) - \frac{\epsilon_3}{\epsilon_2}\cos(k_x^{(3)}x_{2,3})\sin(k_x^{(2)}d_2)], \tag{4.144}$$

$$K_{1_c} = \frac{\epsilon_2}{\epsilon_1}[K_{2_s}\sin(k_x^{(2)}d_2) + K_{2_c}\cos(k_x^{(2)}d_2)]$$

$$= \frac{\epsilon_2}{\epsilon_1}[\frac{k_x^{(3)}}{k_x^{(2)}}\sin(k_x^{(3)}x_{2,3})\sin(k_x^{(2)}d_2) + \frac{\epsilon_3}{\epsilon_2}\cos(k_x^{(3)}x_{2,3})\cos(k_x^{(2)}d_2)], \tag{4.145}$$

$$R_{1_s} = [R_{2_s}\sin(k_x^{(2)}d_2) + R_{2_c}\cos(k_x^{(2)}d_2)]$$

$$= [\frac{k_x^{(3)}}{k_x^{(2)}}\cos(k_x^{(3)}x_{2,3})\sin(k_x^{(2)}d_2) + \sin(k_x^{(3)}x_{2,3})\cos(k_x^{(2)}d_2)], \tag{4.146}$$

and

$$R_{1c} = \frac{k_x^{(2)}}{k_x^{(1)}}[R_{2s}\cos(k_x^{(2)}d_2) - R_{2c}\sin(k_x^{(2)}d_2)] =$$

$$= \frac{k_x^{(2)}}{k_x^{(1)}}[\frac{k_x^{(3)}}{k_x^{(2)}}\cos(k_x^{(3)}x_{2,3})\cos(k_x^{(2)}d_2) - \sin(k_x^{(3)}x_{2,3})\sin(k_x^{(2)}d_2)], \quad (4.147)$$

where

$$d_2 = x_{1,2} - x_{2,3}\ . \quad (4.148)$$

Using these terms and substituting back into the recurrence relations for $\Re$, $\Im$, $\aleph$, $\wp$, the amplitude coefficients $A_m^{(0)}$, $A_m^{(N)}$, $B_m^{(0)}$ and $B_m^{(N)}$ become readily available. These are then used to evaluate the six components of the EM fields in all the layers.

4.4.4 Theoretical Study of Uniform Shielded Multi-layered Microstrip Structures

Dispersion Analysis:

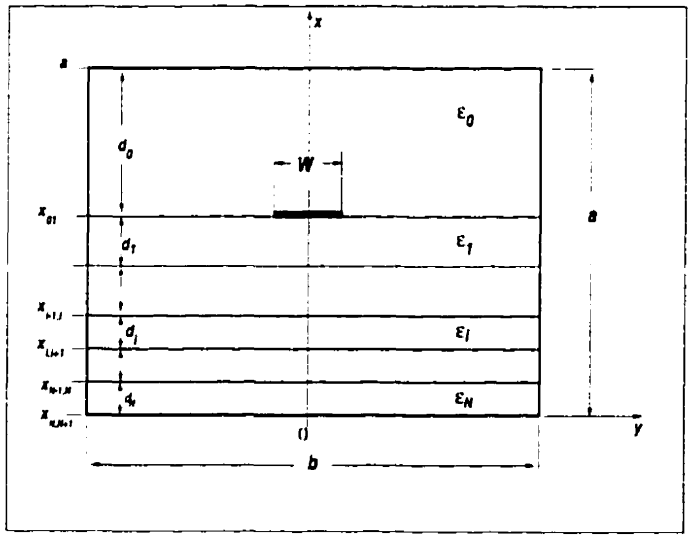

Figure 4.9: A schematic cross-section of a perfectly conducting stripline of negligible thickness and width W situated in a shielded rectangular guide of dimensions a and b, filled with N layers of dielectrics.

Consider now a strip of metalization of width W and negligible thickness situated on top of the N layers of dielectrics of the previous analysis. This transmission line is assumed to

be made of a perfect conducting material. This geometry is depicted in Figure 4.9. As a result of adding this conducting strip, the boundary conditions of the problem will change. Using the Green's functions obtained earlier for a rectangular waveguide and using the current distribution on the metalization, the electric field is recalculated from equation 4.3 subject to a new boundary condition: the tangential component of the electric field must vanish on the metallic strip.

The current distribution on the metalization is cast in the form

$$J_y(y',z') = \sum_i I_{y_i} J_{y_i}(y') e^{-jK_z z'} , \tag{4.149}$$

and

$$J_z(y',z') = \sum_i I_{z_i} J_{z_i}(y') e^{-jK_z z'} , \tag{4.150}$$

where $J_{y_i}(y')$ and $J_{z_i}(z')$ are basis function expansions with I_{y_i} and I_{z_i} being their respective amplitudes. K_z is the complex propagation constant of the microstrip transmission line. A minimal number of terms in the above expansion is sufficient if the basis functions are carefully chosen. In particular, if the basis functions are chosen to satisfy the surface current edge conditions at the strip edges (at $|y| = \frac{W}{2}$), then keeping only one term in the expansions 4.149 and 4.150 is sufficiently accurate. These edge conditions are $J_{y_i}(y') = 0$ and $J_{z_i}(z') \rightarrow \infty$ at the edge of the strip ($|y| = \frac{W}{2}$). Thus, $J_y(y',z')$ and $J_z(y',z')$ are expressed as [189]

$$J_y(y',z') = jI_y \left[\frac{1}{\pi W} \sin\left(\frac{2\pi(y' - \frac{b}{2})}{W} \right) \right] e^{-jK_z z'} , \tag{4.151}$$

and

$$J_z(y',z') = I_z \left[\frac{2}{\pi W} \frac{1}{\sqrt{1 - \left[\frac{2(y' - \frac{b}{2})}{W}\right]^2}} \right] e^{-jK_z z'} , \tag{4.152}$$

Substituting 4.151 and 4.152 in 4.3 results in expressions for the electric field due to the specified surface current density distribution. Enforcing the boundary condition $\vec{E}_{tan} = 0$ on the metalization yields the only remaining unknown in these fields, namely K_z. Since only the tangential component of the electric field is of interest at this point, only this

component of the field will be evaluated in the forthcoming analysis. The components of the electric field tangential to the metalization are the E_y and E_z components, which can be expressed in the form of a set of two equations that can be written in the following short form:

$$E_y^{(0)} = E_{yy}^{(0)} + E_{yz}^{(0)}, \tag{4.153}$$

$$E_z^{(0)} = E_{yz}^{(0)} + E_{zz}^{(0)}, \tag{4.154}$$

where

$$E_{yy}^{(0)} = -j\omega\mu_o \int_{-\infty}^{\infty} \int_{\frac{b}{2}-\frac{W}{2}}^{\frac{b}{2}+\frac{W}{2}} G_{yy}^{(0)} J_y(y', z') dy' dz', \tag{4.155}$$

$$E_{yz}^{(0)} = -j\omega\mu_o \int_{-\infty}^{\infty} \int_{\frac{b}{2}-\frac{W}{2}}^{\frac{b}{2}+\frac{W}{2}} G_{yz}^{(0)} J_z(y', z') dy' dz', \tag{4.156}$$

$$E_{zy}^{(0)} = -j\omega\mu_o \int_{-\infty}^{\infty} \int_{\frac{b}{2}-\frac{W}{2}}^{\frac{b}{2}+\frac{W}{2}} G_{zy}^{(0)} J_z(y', z') dy' dz', \tag{4.157}$$

$$E_{zz}^{(0)} = -j\omega\mu_o \int_{-\infty}^{\infty} \int_{\frac{b}{2}-\frac{W}{2}}^{\frac{b}{2}+\frac{W}{2}} G_{zz}^{(0)} J_z(y', z') dy' dz', \tag{4.158}$$

The superscript (0) denotes the air-filled region of width d_0 above the microstrip line as shown in Figure 4.9. It should be noted that evaluating the Green's function for only region (0) or region (1) is sufficient to compute the propagation constant. Expressions for $G_{yy}^{(0)}$, $G_{yz}^{(0)}$, $G_{zy}^{(0)}$, and $G_{zz}^{(0)}$ are given in 4.118-4.121. $J_y(y', z')$ and $J_z(y', z')$ are given in 4.151 and 4.152 respectively. This yields the following expressions for $E_{yy}^{(0)}$, $E_{yz}^{(0)}$, $E_{zy}^{(0)}$, and $E_{zz}^{(0)}$:

$$E_{yy}^{(0)} = \frac{-j\omega\mu_o}{2\pi} \int_{-\infty}^{\infty} dk_z \sum_m I_y g^{(0)}{}_{yy_m}(x) \cos\left(\frac{m\pi y}{b}\right) \cos\left(\frac{m\pi y'}{b}\right) Int_{I_y}(m) Int_z(K_z) e^{-jk_z z}, \tag{4.159}$$

$$E_{yz}^{(0)} = \frac{-j\omega\mu_o}{2\pi} \int_{-\infty}^{\infty} dk_z \sum_m I_z g^{(0)}{}_{yz_m}(x) \cos\left(\frac{m\pi y}{b}\right) \sin\left(\frac{m\pi y'}{b}\right) Int_{I_z}(m) Int_z(K_z) e^{-jk_z z}, \tag{4.160}$$

$$E_{zy}^{(0)} = \frac{-j\omega\mu_o}{2\pi} \int_{-\infty}^{\infty} dk_z \sum_m I_y g^{(0)}{}_{zy_m}(x) \sin\left(\frac{m\pi y}{b}\right) \cos\left(\frac{m\pi y'}{b}\right) Int_{I_y}(m) Int_z(K_z) e^{-jk_z z}, \tag{4.161}$$

$$E_{zz}^{(0)} = \frac{-j\omega\mu_o}{2\pi} \int_{-\infty}^{\infty} dk_z \sum_m I_z g^{(0)}{}_{zz_m}(x) \sin\left(\frac{m\pi y}{b}\right) \sin\left(\frac{m\pi y'}{b}\right) Int_{I_z}(m) Int_z(K_z) e^{-jk_z z}, \tag{4.162}$$

where

$$Int_{I_y}(m) = \int_{\frac{b}{2}-\frac{W}{2}}^{\frac{b}{2}+\frac{W}{2}} j\left[\frac{1}{\pi W}\sin\left(\frac{2\pi(y'-\frac{b}{2})}{W}\right)\right]\cos\left(\frac{m\pi y'}{b}\right)dy' = j\sin\left(\frac{m\pi}{2}\right)\frac{\sin\left(\frac{m\pi W}{2b}\right)}{\left(\frac{m\pi W}{2b}\right)^2-\pi^2}, \tag{4.163}$$

$$Int_{I_z}(m) = \int_{\frac{b}{2}-\frac{W}{2}}^{\frac{b}{2}+\frac{W}{2}}\left[\frac{2}{\pi W}\frac{1}{\sqrt{1-\left[\frac{2(y'-\frac{b}{2})}{W}\right]^2}}\right]\sin\left(\frac{m\pi y'}{b}\right)dy' = \sin\left(\frac{m\pi}{2}\right)J_0\left(\frac{m\pi W}{2b}\right), \tag{4.164}$$

and

$$Int_z(K_z) = \int_{-\infty}^{\infty} e^{jk_z z'}e^{-jK_z z'}\,dz' = 2\pi\delta(k_z-K_z)\,. \tag{4.165}$$

where $J_0\left(\frac{m\pi W}{2b}\right)$ is the cylindrical Bessel function of the first kind and zeroth order, and $\delta(k_z-K_z)$ is the Dirac delta. ${g^{(0)}}_{yy_m}(x)$, ${g^{(0)}}_{yy_m}(x)$, ${g^{(0)}}_{yy_m}(x)$, ${g^{(0)}}_{yy_m}(x)$ are given in 4.122-4.125. After some algebraic straightforward manipulations, the following expressions for ${E_{yy}}^{(0)}$, ${E_{yz}}^{(0)}$, ${E_{zy}}^{(0)}$, and ${E_{zz}}^{(0)}$ are deduced:

$${E_{yy}}^{(0)} = I_y\omega\mu_o e^{-jK_z z}\sum_m {g^{(0)}}_{yy_m}(x)\cos\left(\frac{m\pi y}{b}\right)\sin\left(\frac{m\pi}{2}\right)\frac{\sin\left(\frac{m\pi W}{2b}\right)}{\left(\frac{m\pi W}{2b}\right)^2-\pi^2}, \tag{4.166}$$

$${E_{yz}}^{(0)} = -I_z\omega\mu_o e^{-jK_z z}\sum_m {g^{(0)}}_{yz_m}(x)\cos\left(\frac{m\pi y}{b}\right)\sin\left(\frac{m\pi}{2}\right)J_0\left(\frac{m\pi W}{2b}\right), \tag{4.167}$$

$${E_{zy}}^{(0)} = jI_y\omega\mu_o e^{-jK_z z}\sum_m {g^{(0)}}_{zy_m}(x)\sin\left(\frac{m\pi y}{b}\right)\sin\left(\frac{m\pi}{2}\right)\frac{\sin\left(\frac{m\pi W}{2b}\right)}{\left(\frac{m\pi W}{2b}\right)^2-\pi^2}, \tag{4.168}$$

$${E_{zz}}^{(0)} = jI_z\omega\mu_o e^{-jK_z z}\sum_m {g^{(0)}}_{zz_m}(x)\sin\left(\frac{m\pi y}{b}\right)\sin\left(\frac{m\pi}{2}\right)J_0\left(\frac{m\pi W}{2b}\right)\,. \tag{4.169}$$

The z and y components of the electric field due to the given surface current density distribution of 4.151 and 4.152 have been found. Enforcing the boundary condition $\vec{E_{tan}} = 0$ on the perfectly conducting metal strip yields the remaining unknown , K_z. An equivalent boundary condition is that the conduction current and the tangential electric field are complementary (mutually exclusive) quantities. Conduction current exists on a perfectly conducting metalization where there is no tangential electric field. Away from the metalization, it is vice versa. Hence, this condition is cast as

$$\int_{\frac{b}{2}-\frac{W}{2}}^{\frac{b}{2}+\frac{W}{2}} {E_y}^{(0)}J_y dy|_{x=x_{01}} = \int_{\frac{b}{2}-\frac{W}{2}}^{\frac{b}{2}+\frac{W}{2}} {E_z}^{(0)}J_z dy|_{x=x_{01}} = 0\,. \tag{4.170}$$

This is an implicit application of Galerkin's technique. A minimization of the inner product of the tangential component of the electric field and the surface current density is enforced [230] [231]. The two equations in 4.170 can be written in the following matrix form:

$$\begin{pmatrix} \sum_{m,odd}^{M} Z_{yy_m}(k_z) & \sum_{m,odd}^{M} Z_{yz_m}(k_z) \\ \sum_{m,odd}^{M} Z_{zz_m}(k_z) & \sum_{m,odd}^{M} Z_{zz_m}(k_z) \end{pmatrix} \begin{pmatrix} I_y \\ I_z \end{pmatrix} = \begin{pmatrix} 0 \\ 0 \end{pmatrix} \tag{4.171}$$

Here I_y and I_z are the amplitude coefficients of the current components J_y and J_z respectively. The summation over m is truncated at $m = M < \infty$ and only includes the odd ordered terms. Even-order terms are equal to zero because of the factor $\sin \frac{m\pi}{b}$ in equations 4.166-4.169. For an infinitely long transmission line, the quantities $\sum_{m,odd}^{M} Z_{yy_m}(k_z)$, $\sum_{m,odd}^{M} Z_{yz_m}(k_z)$, $\sum_{m,odd}^{M} Z_{zy_m}(k_z)$, and $\sum_{m,odd}^{M} Z_{zz_m}(k_z)$ are independent of z. Evaluating these elements at $z = 0$ yield

$$Z_{yy_m}(k_z) = -j\omega\mu_o {g^{(0)}}_{yy_m}(x_{01}) \left[\frac{\sin(\frac{m\pi W}{2b})}{(\frac{m\pi W}{2b})^2 - \pi^2} \right]^2 \mathcal{F} , \tag{4.172}$$

$$Z_{yz_m}(k_z) = -j\omega\mu_o {g^{(0)}}_{yz_m}(x_{01}) \left[\frac{\sin(\frac{m\pi W}{2b})}{(\frac{m\pi W}{2b})^2 - \pi^2} \right] J_0(\frac{m\pi W}{2b}) \mathcal{F} , \tag{4.173}$$

$$Z_{zy_m}(k_z) = j\omega\mu_o {g^{(0)}}_{zy_m}(x_{01}) \left[\frac{\sin(\frac{m\pi W}{2b})}{(\frac{m\pi W}{2b})^2 - \pi^2} \right] J_0(\frac{m\pi W}{2b}) \mathcal{F} = -Z_{yz_m}(k_z) , \tag{4.174}$$

and

$$Z_{zz_m}(k_z) = j\omega\mu_o {g^{(0)}}_{zy_m}(x_{01}) \left[J_0(\frac{m\pi W}{2b}) \right]^2 \mathcal{F} . \tag{4.175}$$

where ${g^{(0)}}_{yy_m}$, ${g^{(0)}}_{yz_m}$, ${g^{(0)}}_{zy_m}$, and ${g^{(0)}}_{zz_m}$ are given by 4.122-4.125 respectively. The unknowns in these equations are k_z and k_x which are interrelated through 4.26. The factor $\mathcal{F}$ assumes the following values:

$$\mathcal{F} = \begin{cases} 1 & \text{for a single stripline,} \\ \left[\cos(\frac{m\pi(S+W)}{2b})\right]^2 & \text{for the symmetric mode of a coupled stripline ,} \\ \left[\sin(\frac{m\pi(S+W)}{2b})\right]^2 & \text{for the anti-symmetric mode of a coupled stripline ,} \end{cases} \tag{4.176}$$

where S is the separating distance between the coupled two parallel striplines as shown in Figure 4.10

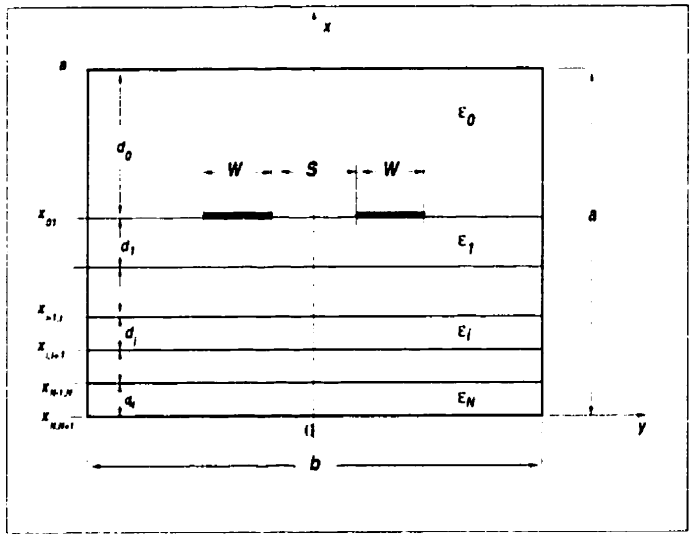

Figure 4.10: A schematic cross-section of two parallel coupled striplines separated by a distance S and each is of width W situated in a shielded rectangular guide of dimensions a and b, inhomogeneously filled with N layers of dielectrics.

Complex Root Searching Using Muller's Method:

The system of linear equations 4.171 is a homogeneous one. A non-trivial solution of 4.171 requires that the determinant of the Z coefficients matrix be zero. The determinant equation is a complex analytic function of the complex variable k_z. The roots of this equation are the complex propagation constants of the propagating modes of the microstrip transmission line. In general, a microstrip transmission line has an infinite number of modes propagating at a given frequency, each with its own propagation constant and characteristic impedance and each has its own cut-off frequency. The dominant propagating mode of a transmission line have a zero cut-off frequency. Other propagation constant for higher order microstrip modes in shielded structures are essentially the propagating modes of the enclosing shielding rectangular waveguide [168]. The roots of the determinant equation are obtained using the well known *Müller* method with deflation [232]. A computationally efficient computer code that computes the complex propagation constant of single and coupled striplines in a shielded multi-layered lossy environment was developed and used the produce the results reported in this thesis. This code is written

in C-language and employs the theory developed and explained above.

For example, Figure 4.11 show the normalized propagation constant (effective index) $n_{eff} = \frac{\beta}{k_o}$, versus frequency, f, for a transmission line of width $W = 50\ \mu m$, having a three layer silica-silicon-silica substrate of thickness 40 μm, with $d_1 = 1\ \mu m$, $d_2 = 5\mu m$, $d_3 = 34\mu$m, ϵ_1=4, ϵ_2=12, ϵ_3=4, with $\rho_2 = 0.12\ \Omega-$m, and $\rho_1 = \rho_2 = \infty$. Shielding structure dimensions are $a = 0.6\ mm$ and b= 0.65 mm (see Fig. 4.9). Computation was conducted using M= 201. The dependence of the attenuation constant, α in $[\frac{dB}{mm}]$, on frequency for the same transmission line is depicted in Figure 4.12.

Figures 4.13 and 4.15 show the dependence of the normalized propagation constant (effective index) $n_{eff} = \frac{\beta}{k_o}$ on frequency for a transmission line of width $W = 500\ \mu m$, having a three layer silica-silicon-silica substrate of thickness 391.4 μm, with $d_1 = 1.4\ \mu m$ and ϵ_1=4, ϵ_2=12, ϵ_3=4, with $\rho_2 = 0.12\ \Omega-$m and $\rho_1 = \rho_2 = \infty$. A lossy layer d_2 is varied in thickness such that $d_2 + d_3 = 390\ \mu m$. Results show the effect of varying the width of the lossy layer, d_2. The shielding structure dimensions are $a = 6\ mm$ and b= 6.5 mm. Computation was conducted using M= 201. The dependence of the attenuation constant, α in $[\frac{dB}{mm}]$, on frequency for the same transmission line is depicted in Figures 4.14 and 4.16.

Notice that towards the higher end of the frequency range depicted in these figures, the effective index n_{eff} settles to a value $\approx sqrt\epsilon_1$. This is known as the quasi-TEM mode, as explained later. Towards the lower end of the frequency range, the effective index n_{eff} reaches values that are even higher than the semiconductor refractive index $\sqrt{\epsilon_2}$. This is known as the slow-wave mode of operation as will be explained later. In this mode of operation, n_{eff} could reach as high as $sqrt\epsilon_1 \frac{d_2}{d_1}$. This is why when the width of the semiconductor region d_2 is much bigger than d_1, as in Figure 4.13, n_{eff} reaches very high values at lower frequencies. When d_2 is of a magnitude comparable to d_1, n_{eff} does not go through these wide variations in magnitude as shown in Figure 4.15.

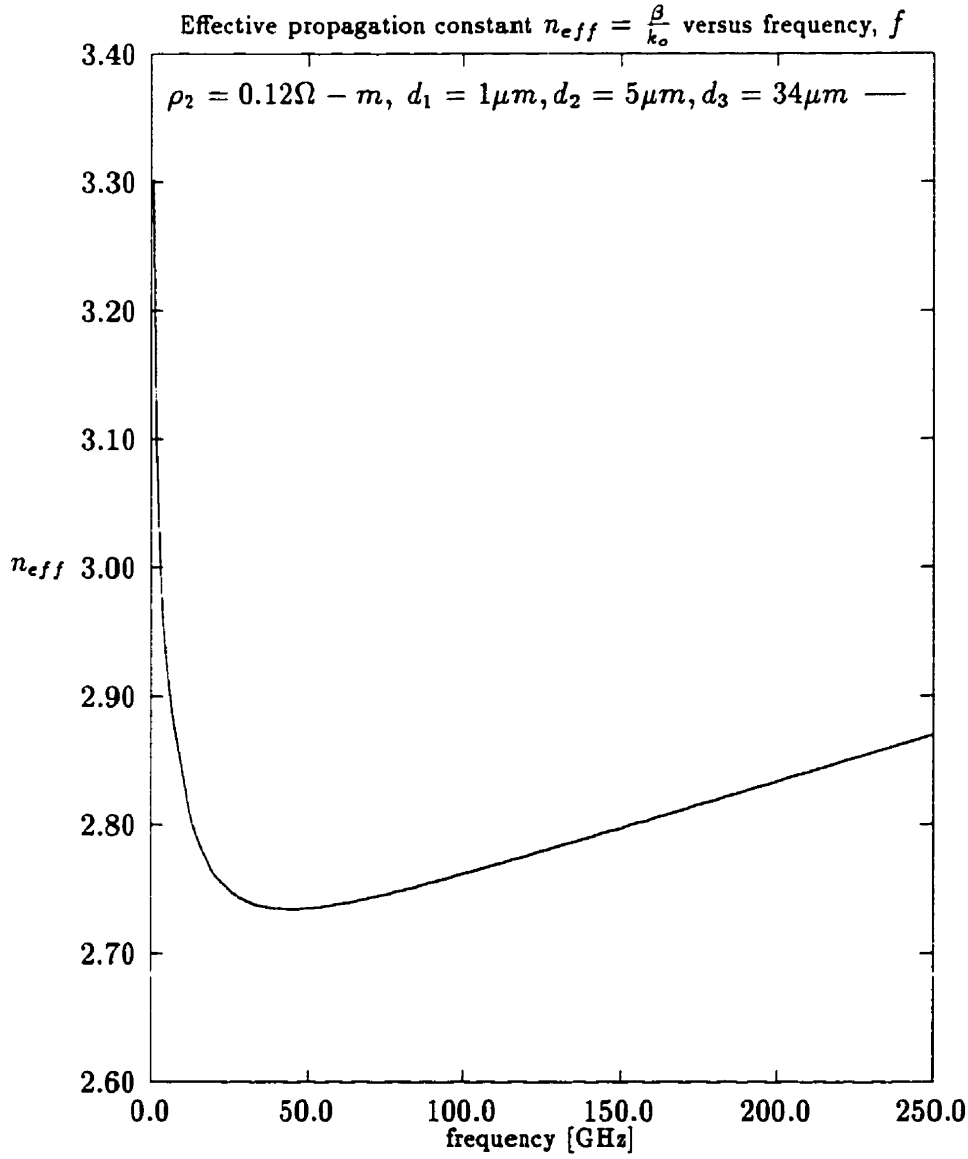

Figure 4.11: The normalized propagation constant (effective index) $n_{eff} = \frac{\beta}{k_o}$, versus frequency, f [GHz], for a transmission line of width W= 50 μm, having a three layer silica-silicon-silica substrate of thickness 40 μm, with d_1 =1 μm, d_2 = 5μm, d_3= 34μm, ϵ_1=4, ϵ_2=12, ϵ_3=4, with ρ_2 = 0.12 Ω−m. Shield dimensions: a = 0.6 mm and b= 0.65 mm. Computation conducted using M= 201.

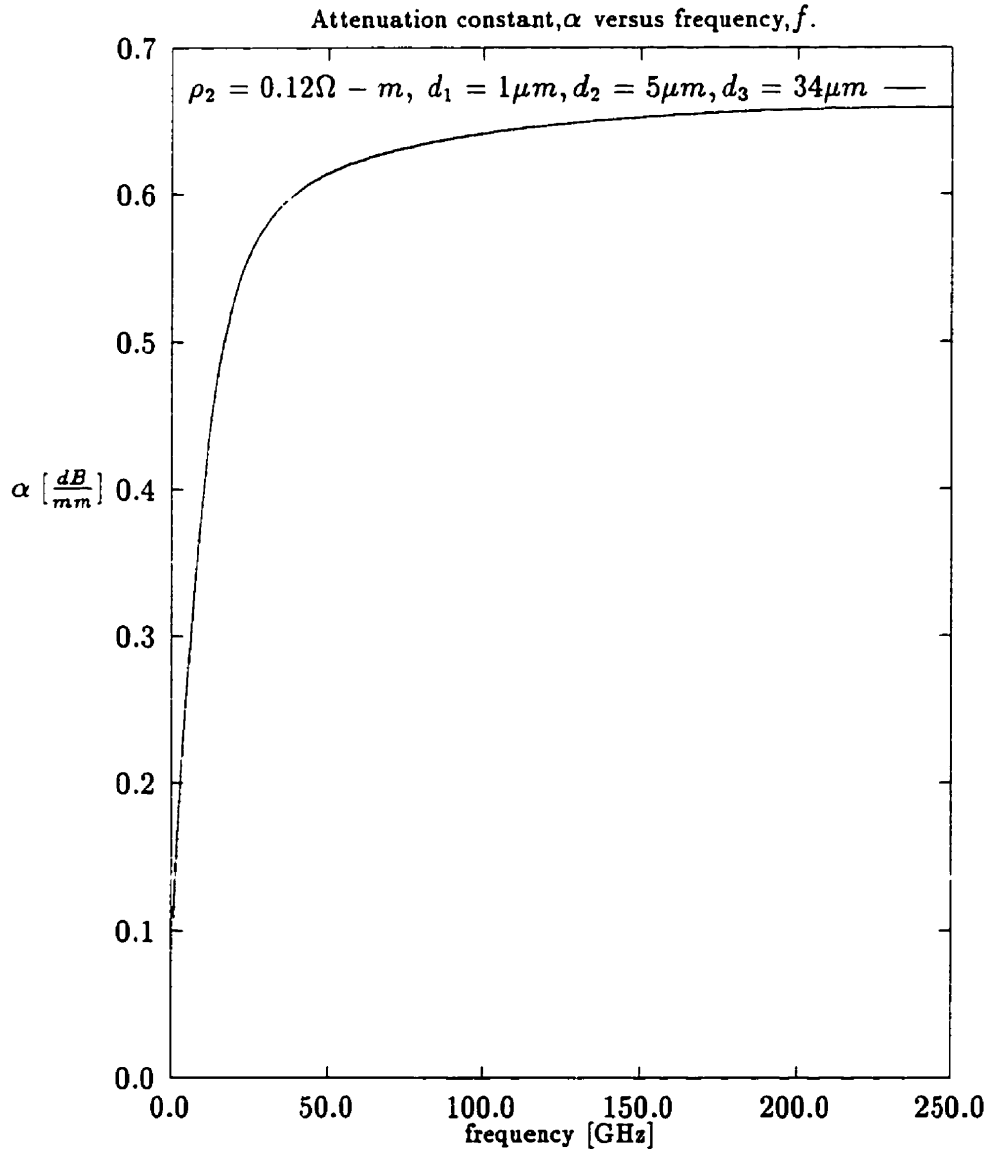

Figure 4.12: The attenuation constant, $\alpha\ [\frac{dB}{mm}]$, versus frequency, f [GHz], for a transmission line of width $W = 50\ \mu m$. All parameters are as noted in the previous figure.

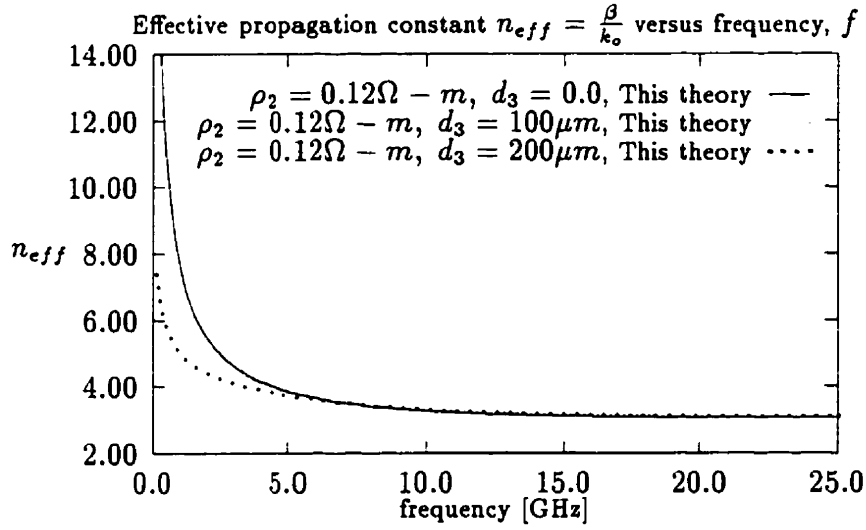

Figure 4.13: The normalized propagation constant (effective index) $n_{eff} = \frac{\beta}{k_o}$, versus frequency, f [GHz], for a transmission line of width W= 500 μm, having a three layer silica-silicon-silica substrate of thickness 391.4 μm, with d_1 =1.4 μm and ϵ_1=4. $d_2 + d_3$ = 390 μm, ϵ_2=12, ϵ_3=4, with ρ_2 = 0.12 Ω−m. Results show the effect of varying the width of the lossy layer, d_2. Shield dimensions: a = 6 mm and b= 6.5 mm. Computation was conducted using M= 201.

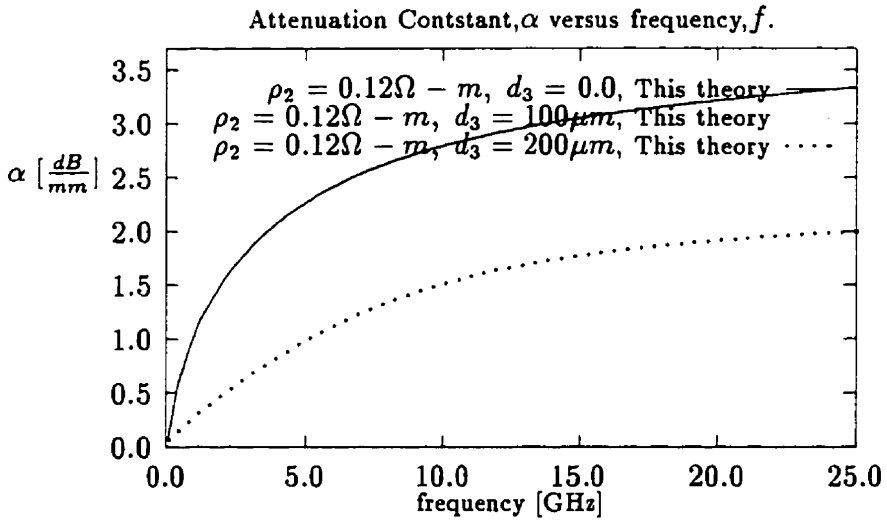

Figure 4.14: The attenuation constant, α $[\frac{dB}{mm}]$, versus frequency, f [GHz], for a transmission line of width W= 500 μm. All parameters are as noted in the previous figure.

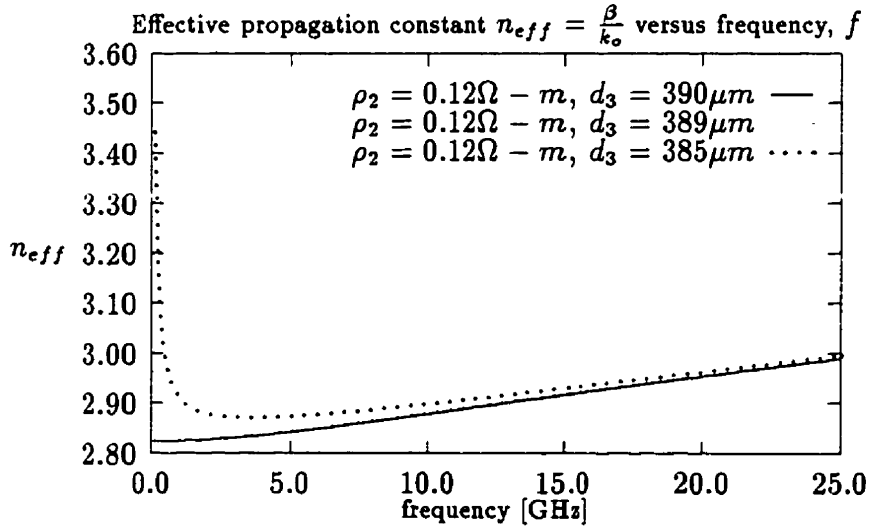

Figure 4.15: The normalized propagation constant (effective index) $n_{eff} = \frac{\beta}{k_o}$, versus frequency, f [GHz], for a transmission line of width W= 500 μm. All parameters are as noted in the previous figure.

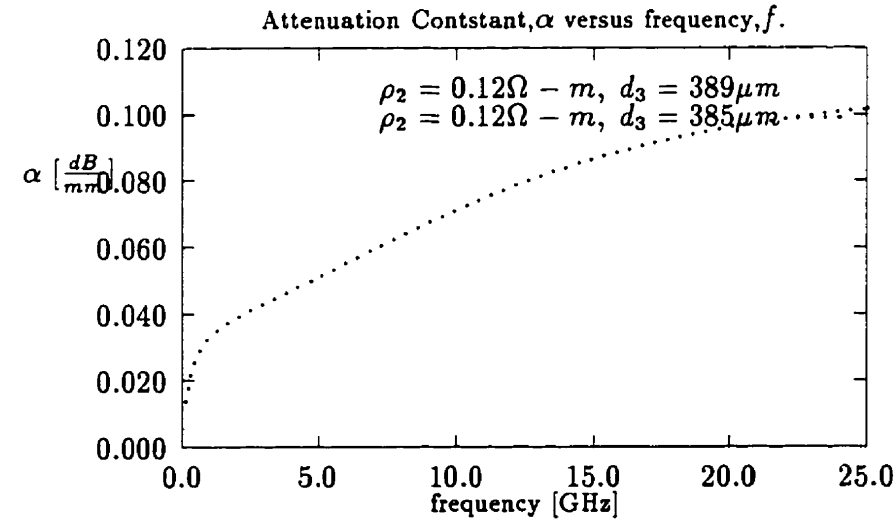

Figure 4.16: The attenuation constant, α [$\frac{dB}{mm}$], versus frequency, f [GHz], for a transmission line of width W= 500 μm. All parameters are as noted in the previous figure.

Field Patterns and Characteristic Impedances:

All the unknowns of the problem at hand have been evaluated. Using these quantities, the EM fields and the microstrip characteristic impedance, Z_o, can be derived. For structures with mixed boundaries, where a propagating mode has all the six components of the EM fields, several definitions of the characteristic impedance exist [189]. The most common definition for Z_o is the power-current relationship:

$$Z_o = \frac{P_z}{I_z^2} = \frac{\int\int \vec{E} \times \vec{H}^*.z \; dx \; dy}{\left[\int_{-\frac{W}{2}}^{\frac{b}{2}+\frac{W}{2}} J_z dy'\right]^2} , \tag{4.177}$$

where $\vec{E}$ and $\vec{H}$ are the EM fields excited by the stripline surface current whose longitudinal component is J_z. Primed coordinates denote a source point. Unprimed ones denote a field point. In the previous analysis, the Green's functions, the surface current basis functions expansion, and the propagation constant have been evaluated. Using Maxwell's equation for time harmonic fields,

$$\nabla \times \vec{E} = -\frac{\partial \vec{B}}{\partial t} = -j\omega\mu_o \vec{H} , \tag{4.178}$$

the magnetic fields can be derived as well. Substituting these expressions in equation 4.177 yields Z_o. The current amplitude coefficients I_y and I_z are inter-related through the system of two homogeneous linear equations 4.171. This allows for the freedom to choose one of them. Choosing $I_z = 1$ makes the denominator of the expression in 4.177 equal to one, since

$$\int_{\frac{b}{2}-\frac{W}{2}}^{\frac{b}{2}+\frac{W}{2}} J_z dy' = I_z \int_{\frac{b}{2}-\frac{W}{2}}^{\frac{b}{2}+\frac{W}{2}} \left[\frac{2}{\pi W} \frac{1}{\sqrt{1-\left[\frac{2(y'-\frac{b}{2})}{W}\right]^2}} \right] dy' = I_z = 1. \tag{4.179}$$

This can be easily proven using the change of variable $\sin u = [\frac{2(y'-\frac{b}{2})}{W}]$. Using this simplification, the expression for Z_o reduces to

$$Z_o = \int\int \vec{E} \times \vec{H}^*.z \; dx \; dy = P_z = \sum_{n=0}^{n=N} P_z^{(i)} , \tag{4.180}$$

where $P_z^{(i)}$ is the portion of the power propagating along z in the $i-$th region.

The electric and magnetic fields are derived in a systematic format analogous to that used above. Subsequently, their cross-product is evaluated and expression 4.180 yields an expression for Z_o. This analysis was developed into a computer code using C-language. This code is capable of computing the characteristic impedance for a shielded microstrip line situated on top of N layers of lossy dielectrics.

As an example, the characteristic impedance of a 500 μm-wide microstrip line is computed using the codes. Results showing the dependence of the real part of the characteristic impedance on frequency are shown in Figure 4.17. The dependence of the imaginary part of the characteristic impedance on frequency for the same line is shown in Figure 4.18. Substrate resistivity $\rho = 1.2$ and $0.12\ \Omega - m$ were assumed. Other parameters are as follows: substrate permittivity ϵ_r=12 and substrate height = 390 μm, with 1.4 μm of silica (ϵ_r=4) on top. The shielding structure dimensions are a= 6mm and b= 6.5 mm. The total number of modes used in the computation, $M = 500$. This is slightly more than the minimum number of modes required for convergent results as explained later.

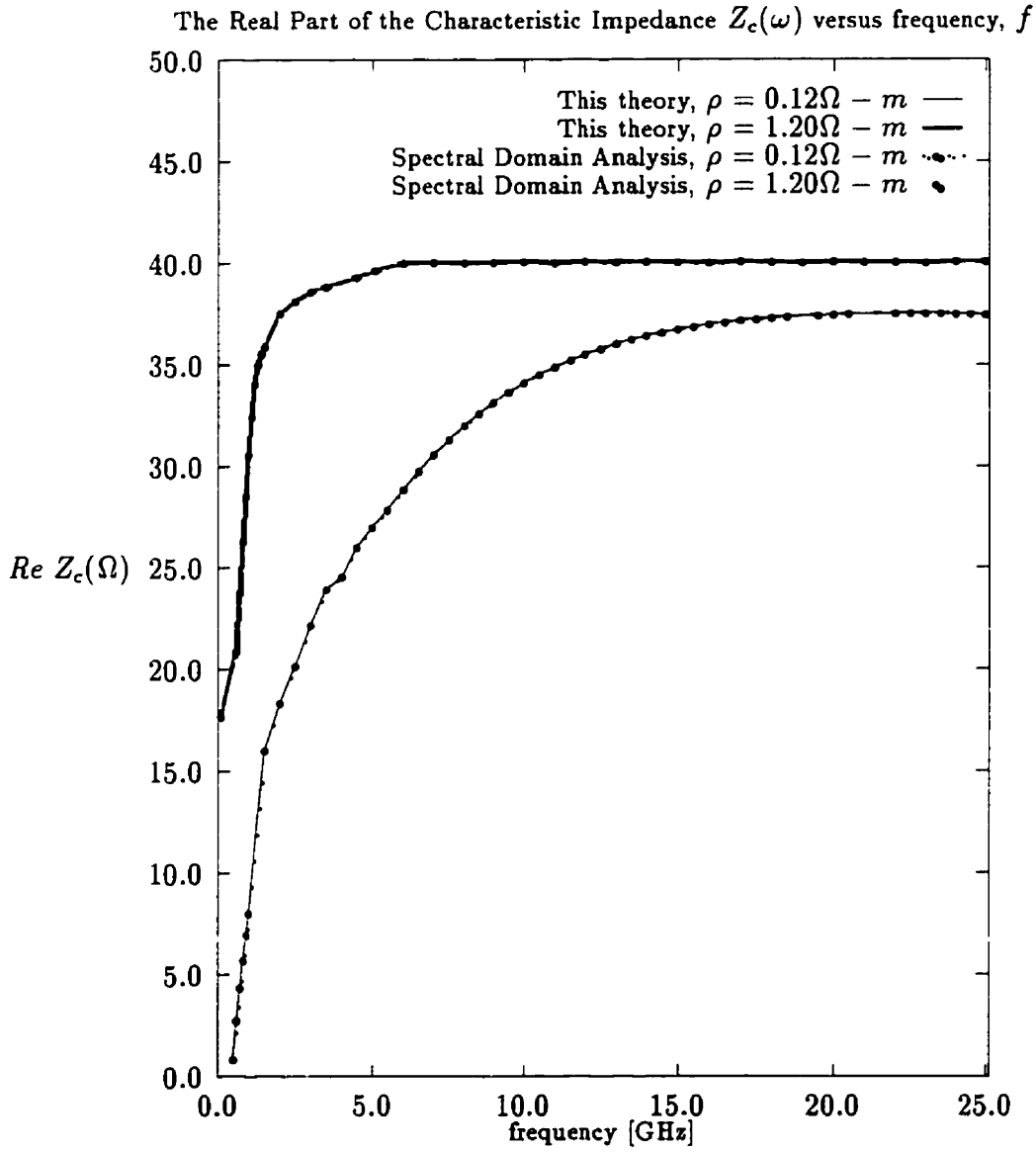

Figure 4.17: The Real part of the characteristic impedance $Z_c(\Omega)$, versus frequency, f [GHz], for a transmission line of width W= 500 μm, and a silicon substrate (ϵ_r=12) of thickness 390 μm, with 1.4 μm of silica (ϵ_r=4) on top of it. Substrate resistivity of ρ = 1.2 and 0.12 $\Omega - m$ is assumed. The shielding structure dimensions are a= 6mm and b= 6.5 mm. M=500.

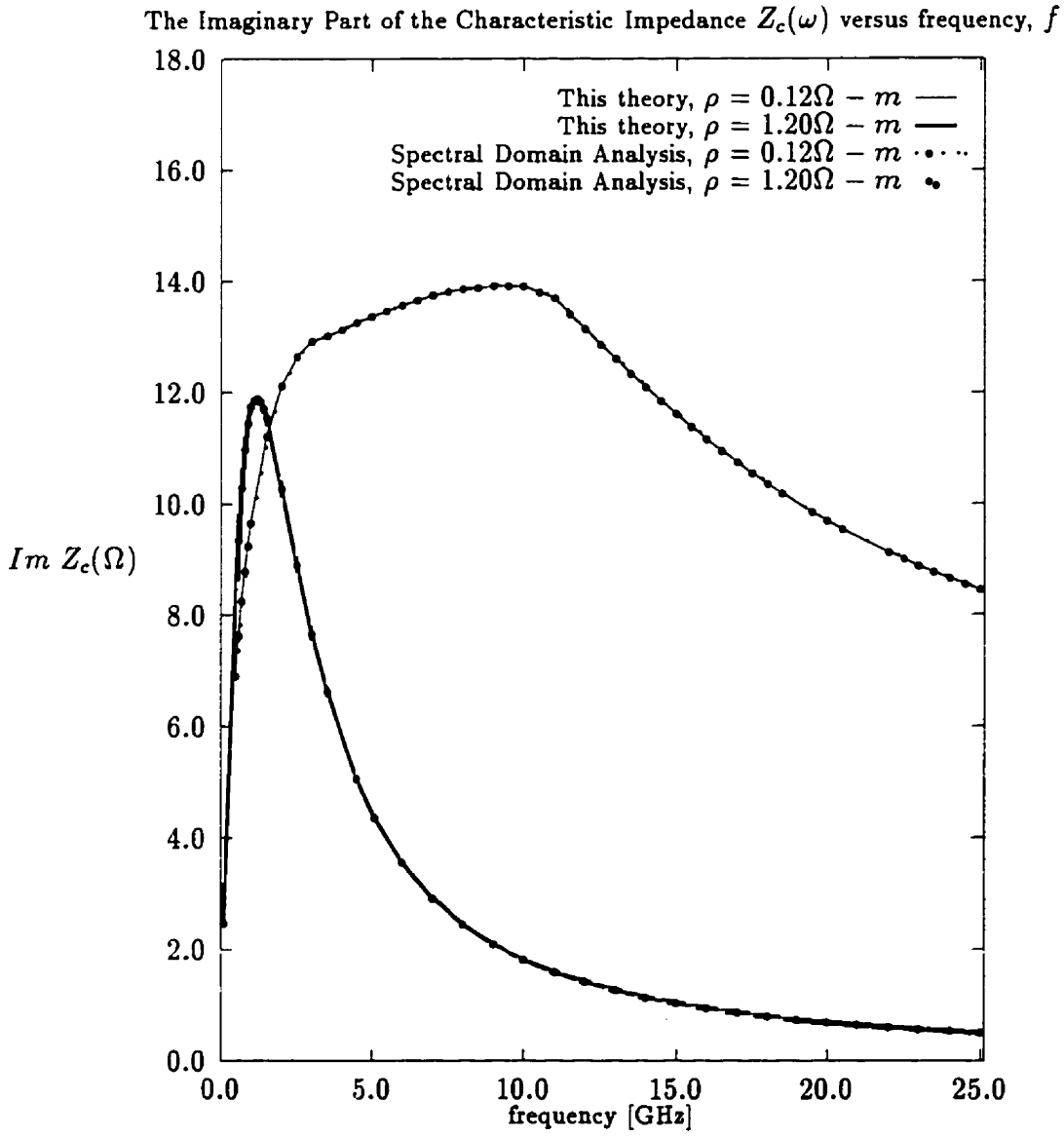

Figure 4.18: The imaginary part of the characteristic impedance $Z_c(\Omega)$, versus frequency, f [GHz], for a transmission line of width W= 500 μm, and a silicon substrate (ϵ_r=12) of thickness 390 μm, with 1.4 μm of silica (ϵ_r=4) on top of it. Substrate resistivity of ρ = 1.2 and 0.12 $\Omega - m$ is assumed. The shielding structure dimensions are a= 6mm and b= 6.5 mm. M=500.

Different Propagating Modes in Shielded MIS Structures:

Hasegawa *et al.* [215] demonstrated that there are three different fundmental modes of wave propagation in metal-insulator-semiconductor (MIS) microstrip structures. The propagation characteristics of each mode and the condition for its excitation are described in references such as [60] [215] [233]. These three modes are the quasi-TEM mode, the skin-effect mode and the slow-wave mode.

In a typical MIS structure, the substrate is comprised of two layers: a semiconductor layer of thickness d_2 and resistivity ρ and on top of it a thin dielectric layer of thickness d_1 and infinite resistivity, where $d_2 >> d_1$. When the frequency-resistivity product $(f\rho)$ is large, i.e., when the conductivity of the semiconductor layer is small, the semiconductor substrate may be treated as a low-loss dielectric, and the transverse EM fields extend through the entire substrate leading to a *quasi-TEM mode of operation* [144].

When the frequency-resistivity product $(f\rho)$ is small, i.e., when the conductivity of the semiconductor layer is large, the semiconductor may be treated as an imperfect ground plane. The transverse EM fields are primarily concentrated in the thin dielectric layer, leading to a *skin-effect mode of operation.* This occurs when the frequency of operation and the substrate resistivity assume values in such a way that the substrate width is about 2 skin-depths thick or more, i.e $d_2 \geq 2\sqrt{\frac{\rho}{\pi\mu_o f}}$.

When the frequency-resistivity product $(f\rho)$ is such that the magnetic fields penetrate into the substrate, whereas the electric field doesn't, a *slow-wave mode of operation* exists. The electric and magnetic fields are spatially separated. The line capacitance is largely increased compared to the quasi-TEM mode, whereas the line inductance changes a little. This leads to an extremely low phase velocity (and conversely an extremely high effective index) whereas the propagation losses remain relatively low. This mode of operation occurs towards the lower end of the frequency range in which the MIS is typically operated.

To illustrate this mode of operation, a parallel plate MIS transmission line and its

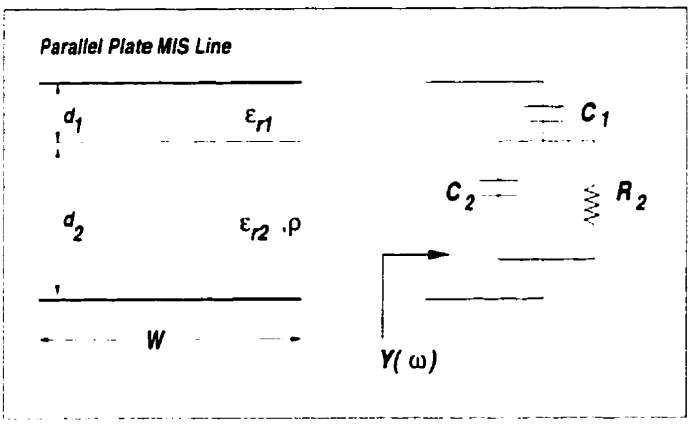

Figure 4.19: A transverse-section in a parallel-plate transmission line and its equivalent circuit representation.

equivalent circuit representation is considered as shown in Figure 4.19. The input admittance as per the equivalent circuit representation of the parallel plate MIS transmission line can be readily derived as [169]:

$$Y(\omega) = \frac{j\omega C_1(j\omega C_2 + G_2)}{j\omega(C_1 + C_2) + G2} = j\omega\epsilon_{eff}C_o \tag{4.181}$$

where

$$C_1 = \frac{\epsilon_{r1}\epsilon_o W}{d_1}\,, \tag{4.182}$$

$$C_2 = \frac{\epsilon_{r2}\epsilon_o W}{d_2}\,, \tag{4.183}$$

$$C_2 = \frac{\epsilon_o W}{d_1 + d_2}\,, \tag{4.184}$$

and

$$G_2 = \frac{W}{\rho d_2}\,. \tag{4.185}$$

These quantities are per unit length in the longitudinal direction. C_o in expression 4.181 is the line capacitance of a line with equivalent paramenters but with an "air" substrate. ϵ_{eff} is the effective permittivity of a propagating mode whose propagation constant is K_z, i.e $K_z = \sqrt{\epsilon_{eff}}k_o$. From the above basic circuit analysis, ϵ_{eff} can be cast as,

$$\epsilon_{eff} = \frac{C_1}{C_o}\frac{(j\omega C_2 + G_2)}{j\omega(C_1 + C_2) + G2} = \frac{\epsilon_{r1}(1 + j\omega\epsilon_{r2}\epsilon_o\rho)(d_1 + d_2)}{\left[1 + j\omega\epsilon_o\rho\left(\epsilon_{r1}\frac{d_2}{d_1} + \epsilon_{r2}\right)\right]}. \tag{4.186}$$

At very high frequencies, and for $d_2 >> d_1$, ϵ_{eff} reduces to

$$\lim_{\omega \to \infty} \epsilon_{eff} = \epsilon_{r2} , \tag{4.187}$$

which means that ϵ_{eff} is frequency independent, and is equal to the relative dielectric permittivity of the thin dielectric layer. This result has been born-out by numerical testing of the code developed. At low frequencies, and for $d_2 >> d_1$, ϵ_{eff} reduces to

$$\lim_{\omega \to 0} \epsilon_{eff} = \epsilon_{r1} \frac{d_2}{d_1} . \tag{4.188}$$

In essence, this means that the effective index of the transmission line can assume values that are even higher than the semiconductor refractive index. This is the "slow-wave" domain of operation. The line capacitance is very high, and subsequently, the phase velocity is decreased. These results can be seen in the numerical examples provided such as those depicted in Figs. 4.13 and 4.15.

Hasegawa *et al.* [215] derive the upper limit of the frequency at which the slow-wave phenomena starts to occur. This is done by considering the relaxation of charge in the semiconductor layer at its interface with the dielectric region. The first order differential equation describing the relaxation of charge is derived as

$$\frac{\partial \rho_v(t)}{\partial t} + \frac{\rho_v(t)}{\rho \epsilon_{eff} \epsilon_o} = 0 , \tag{4.189}$$

where $\rho_v(t)$ is the volume charge density and ϵ_{eff} is the effective permittivity. The solution of this equation is straightforward:

$$\rho_v(t) = A e^{-\rho \epsilon_{eff} \epsilon_o t} . \tag{4.190}$$

Hence, $\rho \epsilon_{eff} \epsilon_o$ is the relaxation time constant. When the operating frequency is reduced to reach the inverse of the relaxation time constant (i.e. $f = f_s = \frac{d_1}{2\pi d_2 \epsilon_{r1} \epsilon_o \rho}$), the polarization current begins to lag the applied signal. The electric field is concentrated in the thin dielectric layer, whereas the magnetic field is extending into the substrate. References [60] [215] provides explicit expressions for defining the three different modes of MIS operation that are tabulated in table 4.1. These expressions are derived for the

f Description	f range	Mode of Operation
Low Frequency	$f \leq 0.3 f_o$	Slow-Wave Mode
Medium Frequency	$1.5 f_e \leq f \leq f_d$	quasi-TEM Mode
High Frequency	$f \geq 4 f_d$	Skin-effect Mode

Table 4.1: Frequency ranges for various modes of operation of MIS lines

parallel plate MIS structure of figure 4.19 and are valid for wide microstrip lines, i.e. those satisfying the condition $W > d_1 + d_2$. The general sense of these regions remain valid for thin lines. As apparent from this table, the boundaries of operation do not coincide. However, the transition from one mode of operation to the other is gradual.

In table 4.1, f_o is the slow wave characteristic frequency given by

$$f_o = \frac{1}{\frac{1}{f_s} + \frac{2}{3 f_d}} \tag{4.191}$$

where f_d is the skin-effect characteristic frequency and f_s is the relaxation frequency of the charge at the interface. Those are given by

$$f_d = \frac{\rho}{\pi \mu_o {d_2}^2} , \tag{4.192}$$

and

$$f_s = \frac{d_1}{2\pi \epsilon_o \epsilon_{r1} \rho d_2} , \tag{4.193}$$

respectively. Finally, f_e is the relaxation frequency of the semiconductor

$$f_e = \frac{1}{2\pi \epsilon_o \epsilon_{r2} \rho} . \tag{4.194}$$

Convergence Considerations

The analysis presented thus far is an exact analysis of shielded multi-layered lossy stripline structures. All computations are evaluated in terms of an infinite summation over the index m of modal expansions. Theoretically, the obtained formulae would be exact in

the limit should the infinite series be evaluated. In practice, this series is truncated at $m = M$. The choice of M is such that the retained terms provide sufficiently accurate results. Extensive case studies conducted in [169], for the case of a two-layer substrate, resulted in the following convergence condition

$$M \geq Integer\left[\frac{25b}{\pi W}\right] \tag{4.195}$$

This condition ensures that the term $x = (\frac{m\pi W}{2b})$ is large enough to guarantee that the quantities $J_o(x)$ and $(\frac{\sin x}{x^2-\pi^2})$ for $m > M$ are of negligible magnitude. Hence, quantities like the propagation constant (equation 4.171) and the characteristic impedance (equation 4.177) are evaluated accurately. As it is obvious, the above criterion equally applies to the case of N-layered substrate. Testing of the developed codes confirms this.

The following case study is presented to demonstrate the effect of changing the value of M on the convergence of the results. Fig. 4.20 shows the normalized wave length, $\frac{\lambda}{\lambda_o}$, versus frequency for a transmission line of width W= 600 μm, and a lossy semiconductor silicon substrate of permittivity ϵ_r=12 and height 250 μm, with 1 μm of silica (ϵ_r=4) on top of it. Results are obtained for different substrate conductivities. The shielding structure dimensions are a = 1.5 mm and b= 10 mm. Computation is conducted using M=25000 and M= 121. Fig. 4.21 show the attenuation constant, α (in $[\frac{dB}{mm}]$), for the same structure.

This is the case of a wide transmission line, where convergence could be achieved for a relatively small value for M. Based on the convergence criterion 4.195, convergent results for this structure can be obtained for $M \geq$133. As shown, there is a considerable difference in the values of $\frac{\lambda}{\lambda_o}$ and α for the non-convergent case (M = 121) compared to the convergent case (M = 25000). Studies comparing the cases for M=500 and M=25000 show almost identical results. These are shown in Figs. 4.22 and 4.23. Once the condition given in 4.195 is satisfied, the computed values for the propagation constant stabilize rapidly and become almost independent of further increase in the value of M. This is borne out by the results shown in Figs 4.22 and 4.23 which compare the cases of M=500

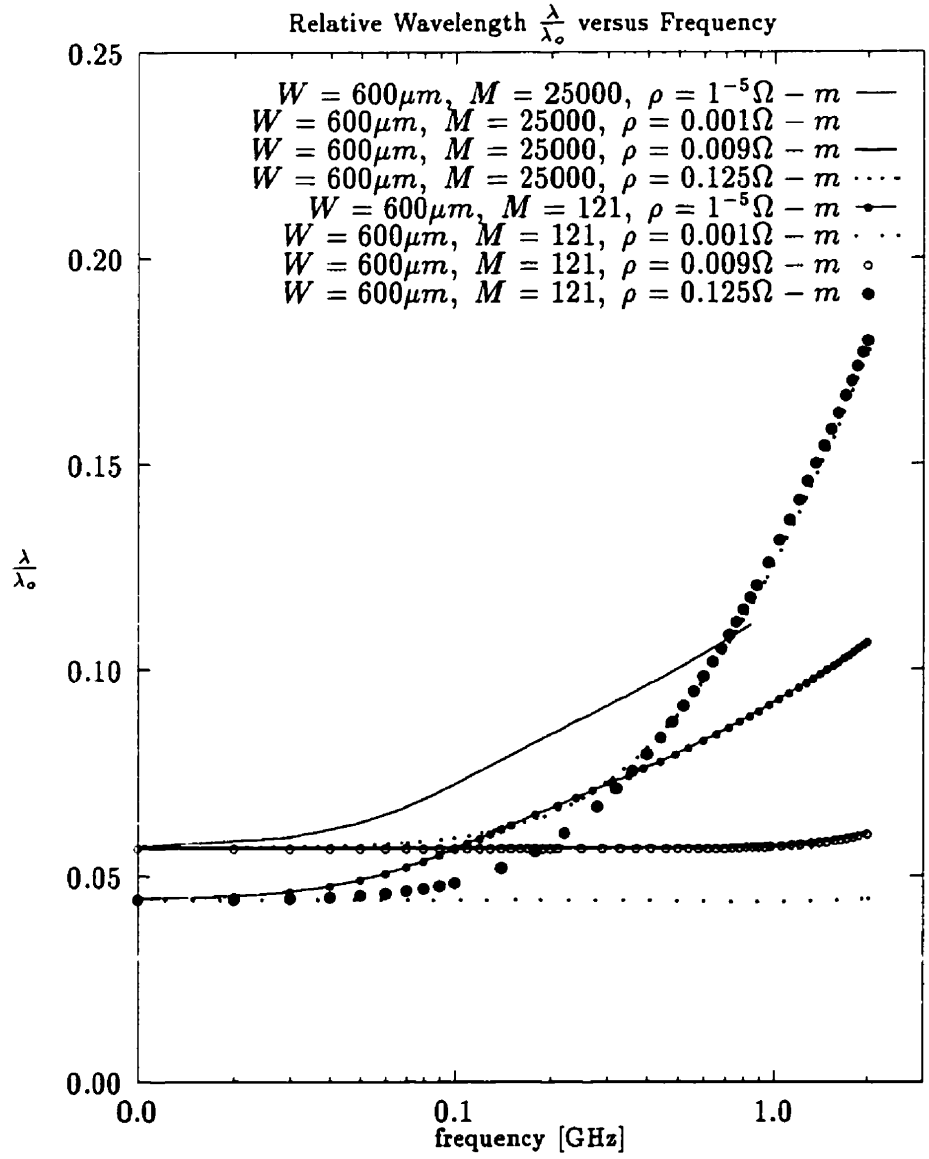

Figure 4.20: The normalized wave length, $\frac{\lambda}{\lambda_o}$, versus frequency, f [GHz], for a transmission line of width W= 600 μm, and a silicon (ϵ_r=12) substrate of thickness 250 μm, with 1 μm of silica (ϵ_r=4) on top of it. Results are obtained for different substrate conductivities. Shield dimensions: a = 1.5 mm and b= 10 mm. Computation conducted using M=25000 and 121.

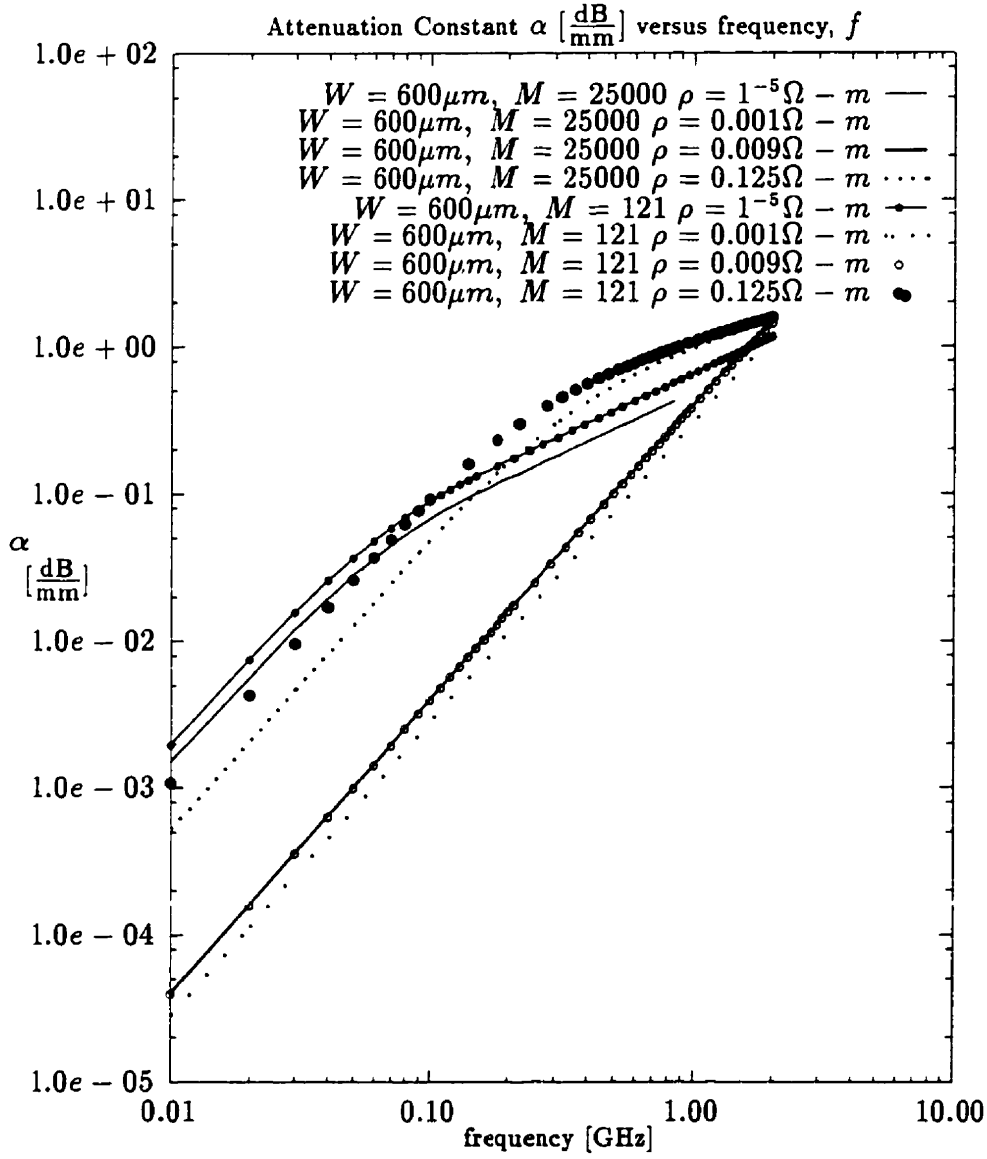

Figure 4.21: The attenuation constant, α [$\frac{dB}{mm}$], versus frequency, f [GHz], for a transmission line of width W= 600 μm. All parameters are as noted in the previous figure.

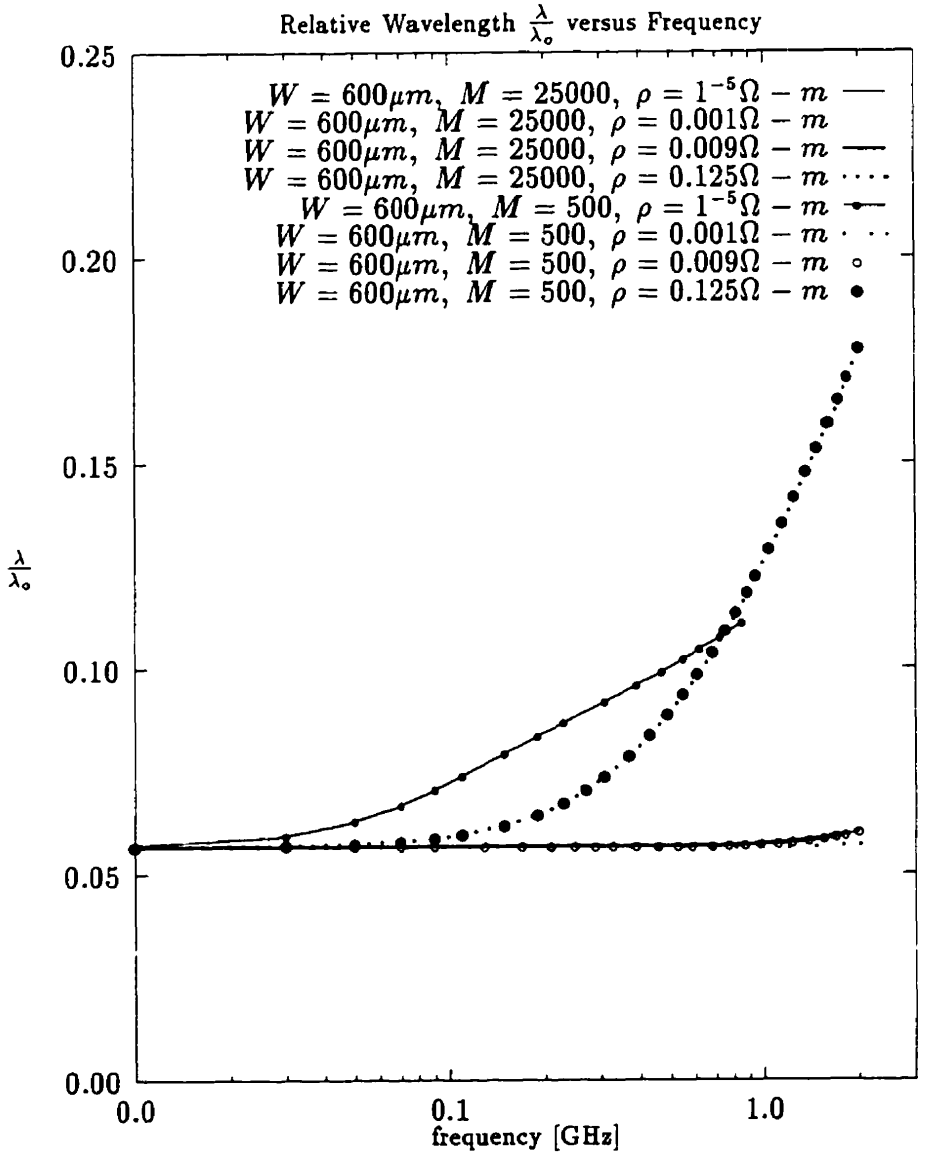

Figure 4.22: The normalized wave length, $\frac{\lambda}{\lambda_o}$, versus frequency, f [GHz], for a transmission line of width W= 600 μm, and a silicon substrate (ϵ_r=12) of thickness 250 μm, with 1 μm of silica (ϵ_r=4) on top of it. Results are obtained for different substrate conductivities. Shield dimensions: a = 1.5 mm and b= 10 mm. Computation conducted using M=25000 and 500.

and M=25000. Further studies using other values of M, and other structures confirmed this observation.

Figure 4.24 show the rapid convergence of the effective index n_{eff} as M is increased. The figure shows the effective index, at a frequency of 2.9 GHz, for the even mode of a pair of coupled striplines as that of Figure 4.10. The width of the striplines W = 1 mm, and separation S= 1 mm on a gallium arsenide substrate with a dielectric constant of 12.9 and thickness = 1 mm. The cover plate is at a height a= 1.5 mm above the ground plane, and the side wall spacing is b = 60 mm. These numerical values stipulate that convergent results can be obtained for $M \geq 478$, as per equation 4.195. As shown in the figure, accurate results are yielded at about that value for M and higher. For higher values of M, no further changes in the value of the effective index is recorded. The obtained result converge rapidly once the minimum value of M stipulated by 4.195 is achieved.

Verification of the Present Analysis

In this section, a sample of the results that could be obtained using the developed codes is provided. These are compared to other methods and experimental results reported in the literature, with the intent of verifying the present analysis, and establishing its domain of accuracy.

An example for the dispersion curves of shielded transmission line is given in Fig. 4.25 ([189], p. 425). The comparison curves were computed via the mode matching technique (MMT) [234] and the Method of Lines (MOL) [235]. In Fig. 4.25, the effective Index, ϵ_{eff} is plotted versus normalized substrate height, $\frac{h}{\lambda_o}$, for a transmission line of width to substrate height ratio $\frac{W}{d}$= 1.0 and 3.0. Substrate permittivity ϵ_r=9.7 and shielding structure dimensions are $\frac{a}{d}$ = 16 and $\frac{b}{d}$ =8. Computations based on this theory were conducted using M= 500. As shown, an excellent agreement between the three methods is evident.

In Fig. 4.26, some typical computed results for the effective dielectric constant ϵ_{eff} for a coupled microstrip line on a gallium arsenide, $GaAs$, substrate with a dielectric constant

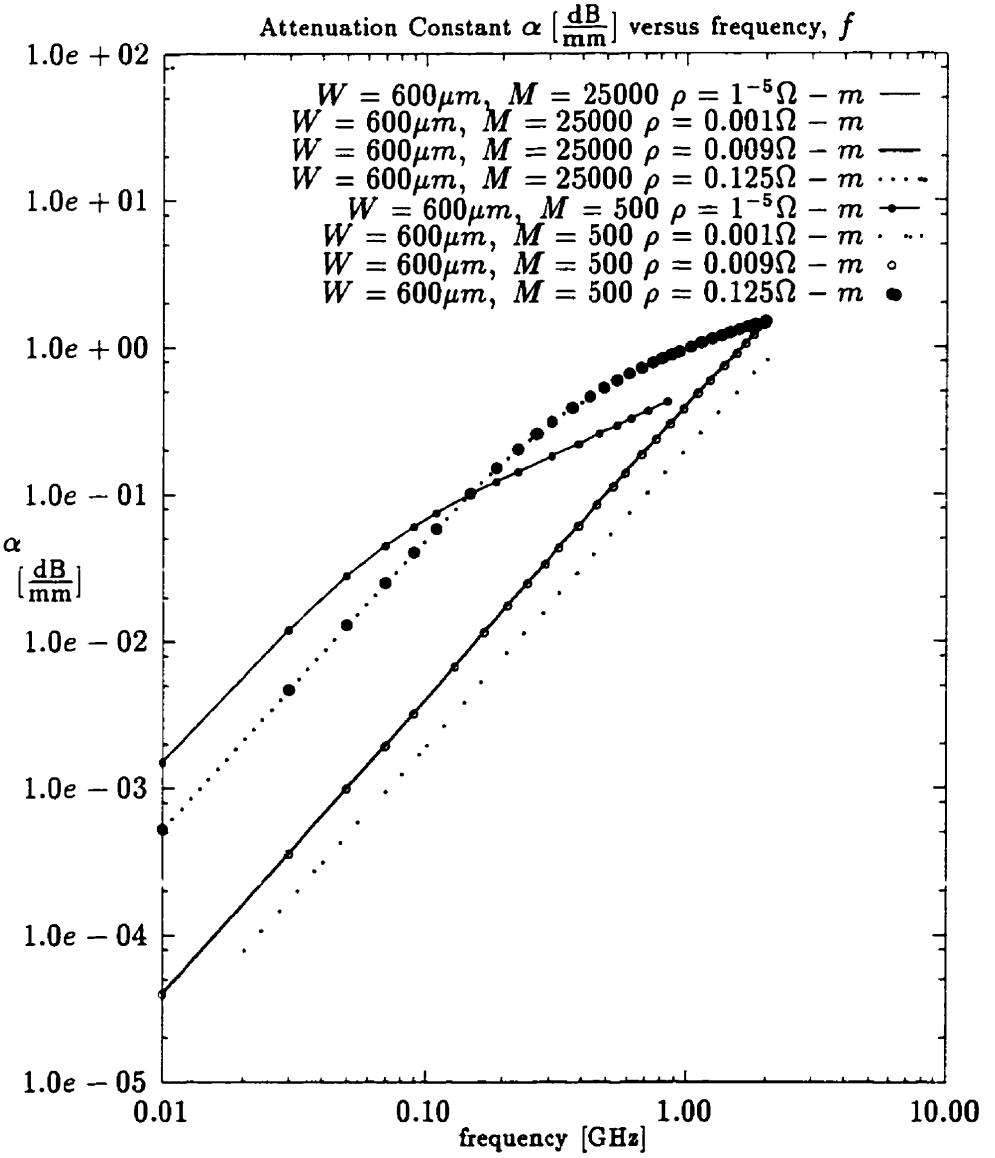

Figure 4.23: The attenuation constant, α [$\frac{dB}{mm}$], versus frequency, f [GHz], for a transmission line of width W= 600 μm. All parameters are as noted in the previous figure.

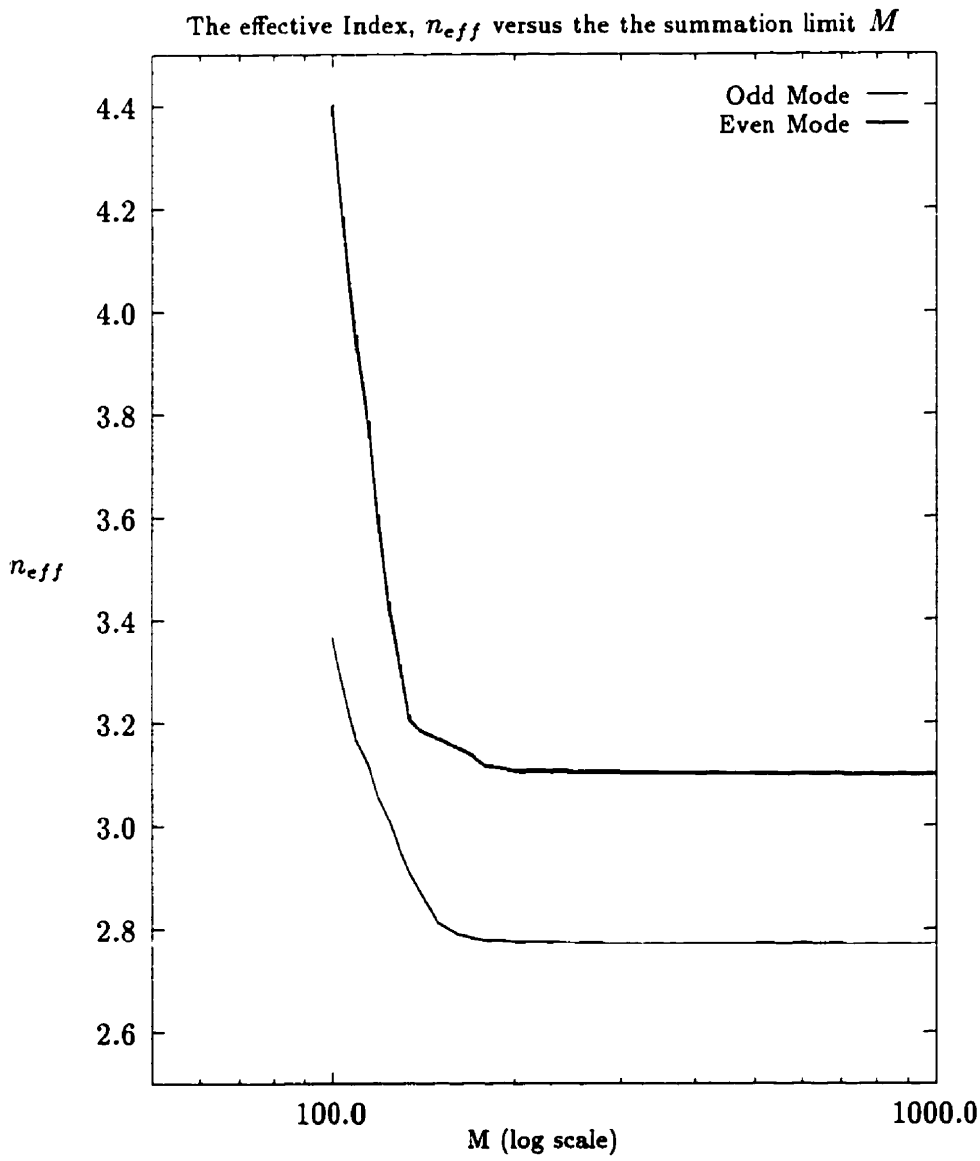

Figure 4.24: The effective index n_{eff}, versus the summation limit M, for the even and odd modes of a coupled transmission line of width W= 1 mm and separation S = 1 mm situated over a $GaAs$ substrate of thickness H= 1 mm and a permittivity ϵ_r=12.9. Shield dimensions: a = 8 mm and b= 60 mm. Computation conducted for a frequency f = 2.9 GHz.

of 12.9. These results were obtained by Morich [236] and were reported in ([237], p. 322). The curves supplied by Morich were obtained by a perturbation-iteration approach. As shown, they are almost identical to those obtained via this theory. Specific parameters are as follows: side wall separation b = 60 mm, cover plate height a above the ground plane is varied as shown in the figure, substrate thickness x_{01} = 1mm, strip width W = 1mm, strips separation S = 1 mm (see Fig.4.10). The results shown can be scaled to apply to a different frequency range. A notable feature of the transmission line in this example is that the effective dielectric constant for the even mode excitation is significantly larger than that for the odd mode at high frequencies. It can also be seen that the top shield has relatively little effect on the magnitude of the effective index if placed a distance equal to four or more times the substrate thickness above the ground plane. This observation confirms the earlier stipulations that the developed analysis can equally be applied to open structures by making the dimensions of the shielding structure wide enough.

4.4.5 Effect of the Depletion Region on the Propagation Characteristics of MIS Structures

Previous analyses of MIS structures such as [169] ignore considering the effect of the depletion region that exist in these MIS lines. During the course of this research, it was observed that this depletion layer may have a considerable effect on the propagation characteristics of these transmission lines. This issue is addressed in this section.

At the interface between the insulator layer and the semiconductor layer of an MIS geometry, a depletion layer forms and extends into the semiconductor layer. This depletion region can be modeled as an insulating layer whose permittivity is the semiconductor permittivity, but with infinite resistivity since this region is depleted of carriers. The depth of this depletion region, h, is given by [24]:

$$h = \sqrt{\frac{2\epsilon_s(V_{bi} - V)}{qN_D}} \tag{4.196}$$

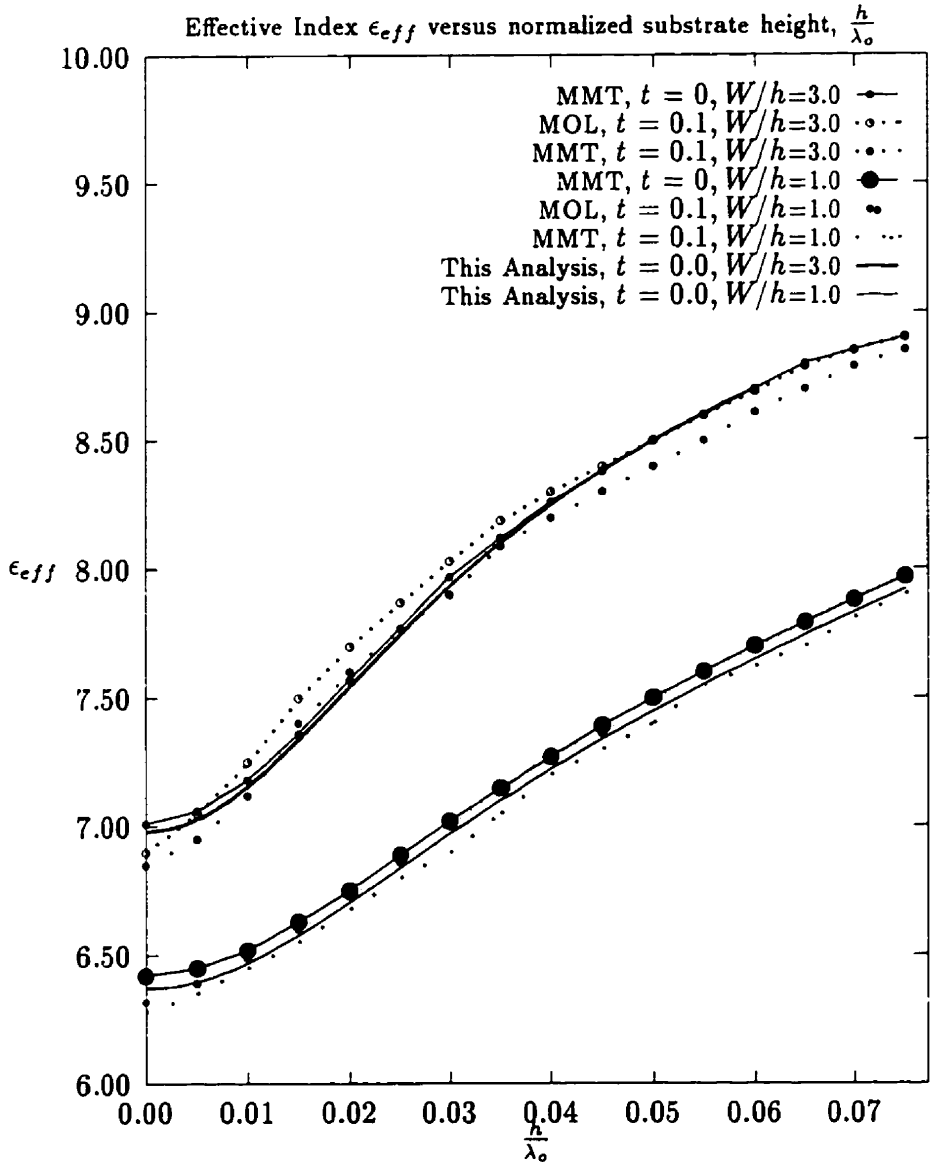

Figure 4.25: The effective Index, ϵ_{eff}, versus normalized substrate height, $\frac{h}{\lambda_o}$, for a transmission line of width to substrate height ratio $\frac{W}{d}$= 1.0 and 3.0. Substrate permittivity ϵ_r=9.7. Results obtained by this theory are compared to those obtained by the Method of Lines (MOL) and the mode matching technique (MMT) for metalization thickness of zero and 0.1 W. Shield dimensions: $\frac{a}{d}$ = 16 and $\frac{b}{d}$ =8. Computations based on this theory are conducted using M= 500.

where ϵ_s is the semiconductor permittivity, V_{bi} is the break-in potential, V is the applied voltage and N_D is the donners carrier density for n-type semiconductors, and q is the electron charge. Alternatively, N_D is replaced by N_A for p-type semiconductors. The electron and hole carrier density, N_D and N_A respectively, are related to conductivity, σ through

$$\sigma = q(\mu_n N_D + \mu_p N_A) = q(mu_n N_D + \mu_p \frac{{n_i}^2}{N_A}) \approx q\mu_n N_D \qquad (4.197)$$

where n_i is the intrinsic carrier concentration, μ_n and μ_p are the electron and hole mobilities respectively. For Silicon, $\mu_n = 1450\ \frac{cm^2}{V.sec}$ and $\mu_p = 505\ \frac{cm^2}{V.sec}$. For a typical MIS geometry, and using the above expression, the width of this depletion region is about 10 μm for an applied microwave voltage = 1 V, and a substrate resistivity $\rho \approx 10\ \Omega-$cm. The MIS analysis reported in [169] ignores the effect of this depletion region because the analysis can only model the case of two layers of substrate materials, one is the dielectric and the other is the semiconductor. It is shown here that ignoring the depletion region may lead to inaccurate and sometimes erroneous results. The present analysis takes this depletion region into account, given its general nature.

For example, consider a typical MIS structure where the transmission line width is W= 500 μm with a silicon substrate (ϵ_r=12) of thickness 390 μm and resistivity $\rho = 0.12$ $\Omega-$m, with 1.4 μm of silica (ϵ_r=4) on top of it. The shielding structure dimensions are a = 6 mm and b= 6.5 mm. These parameters were obtained from [169]. Figure 4.27 depict the normalized propagation constant $n_{eff} = \frac{\beta}{k_o}$ for the case of different depletion region widths. Those are also compared with the case where $\frac{\beta}{k_o}$ is computed ignoring the depletion region. Figure 4.28 show the attenuation constant for the same structure. The effect of the depletion region is more pronounced in the case of the slow-wave mode of operation, which occur at a lower frequency range. Figs 4.29 and 4.30 show the dependence of the normalized propagation constant and the attenuation constant on the depletion region width for that frequency range. All computations were conducted using M= 2000. Using 4.197 and 4.196, the depletion region width is calculated to be 10.7 μm for an applied voltage of 1 V, for this particular structure. Similarly, an applied voltage of 2 V

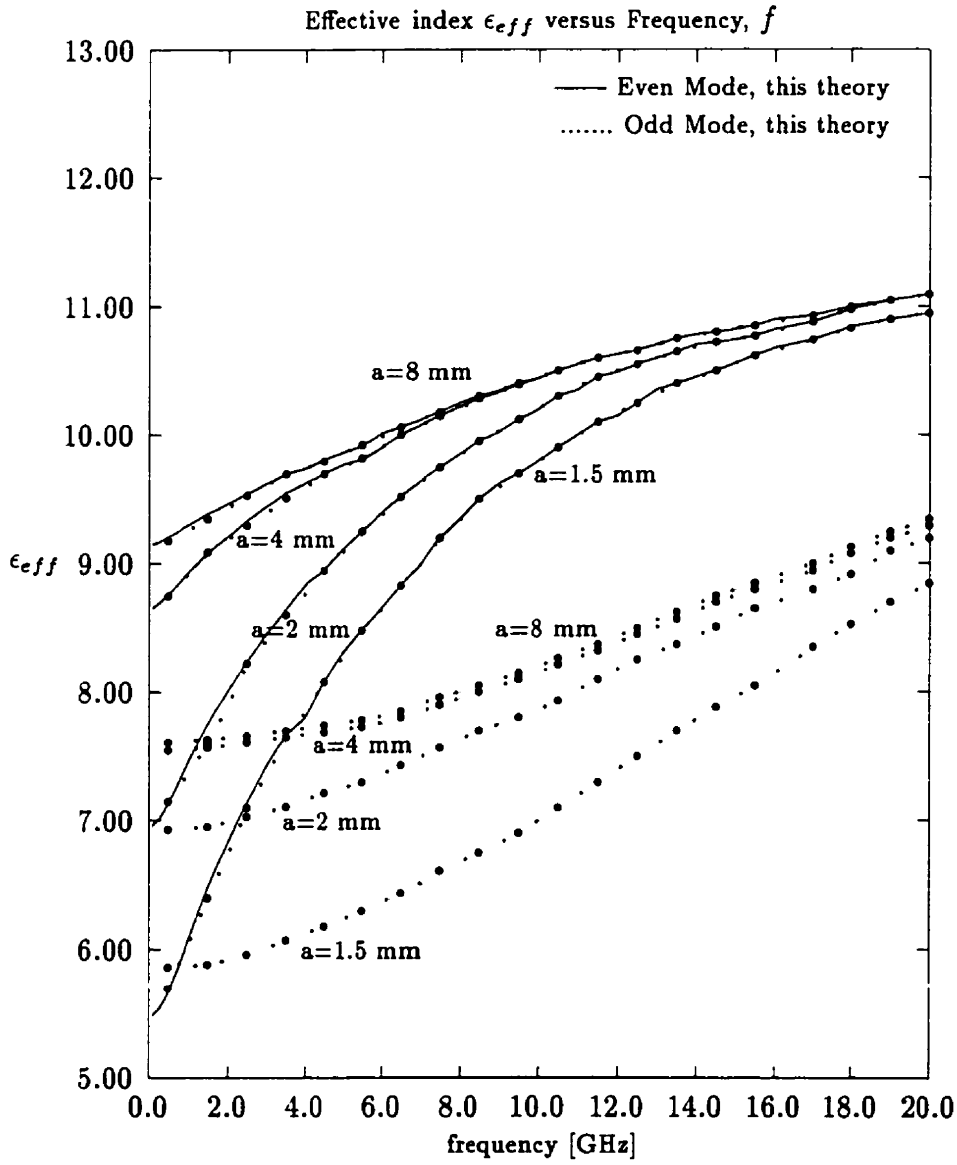

Figure 4.26: The effective index ϵ_{eff}, versus frequency, f [GHz], for a coupled stripline of width $W = 1$ mm and separation $S = 1$ mm. The substrate is a single $GaAs$ layer of permittivity $\epsilon_r = 12$. Shield dimensions are b=60 mm, and a is varied. M=1001. The results obtained using this theory is compared to those obtained by Morich [226] using a perturbation iteration technique. Morich's results are shown here by dots.

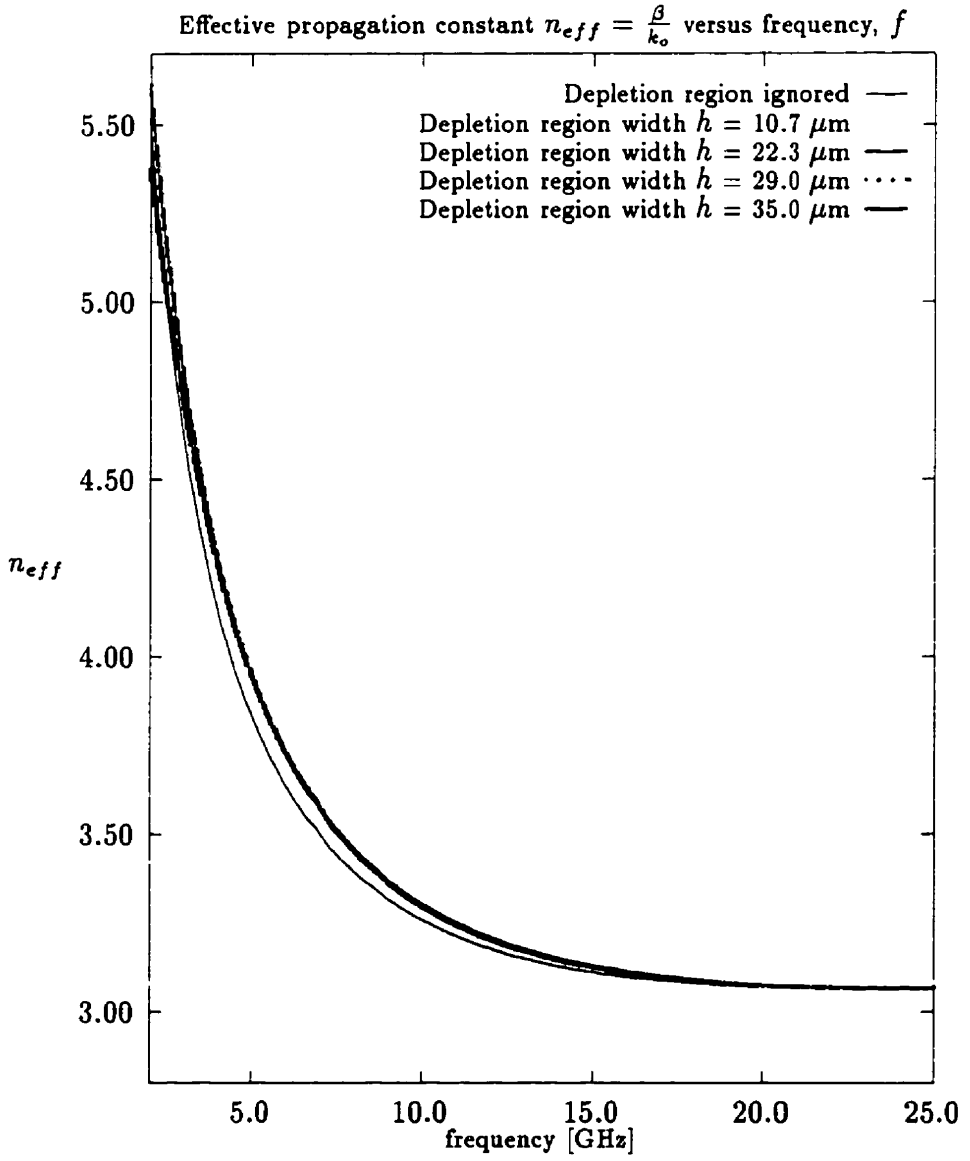

Figure 4.27: The normalized propagation constant (effective index) $n_{eff} = \frac{\beta}{k_o}$, versus frequency, f [GHz], for a transmission line of width W= 500 μm, and a silicon (ϵ_r=12) substrate of thickness 390 μm, with 1.4 μm of silica (ϵ_r=4) on top of it. Results show the effect of considering the depletion region in the analysis. Shield dimensions: a = 6 mm and b= 6.5 mm. Computation conducted using M= 2000.

leads to a depletion region of width 22.3 μm, with 3 V and 4 V leading to widths of 29.0 μm and 35.0 μm respectively.

From these figures, it can be concluded that the depletion region has little effect on the magnitude of the propagation constant at higher frequencies, where the mode of propagation is considered a quasi-TEM mode. This is evident from Figure 4.27. Further, the propagation constant settles to the same value for higher frequencies regardless of the width of the depletion layer. Difference in computed β among all cases is less than 0.1% for the higher frequencies. The percentage difference in the magnitude of β for the case of a depletion region of depth 35.0 μm and that with no depletion region is less than 0.01% at 25 GHz. At high frequencies, the skin depth is small, and the EM fields are more confined to the dielectric region, and they are less affected by both the depletion region and the semiconductor region.

The depletion region does, however, greatly affect the propagation characteristics at lower frequencies where the mode of operation of the transmission line is a slow-wave mode. This is evident from Figure 4.29. The differences in the values of $\frac{\beta}{k_o}$ are in the excess of 85% between the case of no depletion region and the case of a depletion region of width 10.7 μm at very low frequencies. At 1 GHz, the percentage difference is 2%, and it goes to 20% if the case of a depletion region of height 35.0 μm is compared to the no-depletion layer case. It can be concluded that the presence of the depletion region helps to suppress the slow-wave effect. This is expected, as the existence of the depletion layer acts as a buffer between the insulator layer and the semiconductor layer. The slow-wave mode, as discussed earlier, occurs when the electric field is shielded from the semiconductor lossy layer, whereas the magnetic field extends deep into that region. That spatial separation of the fields leads to a larger line capacitance and smaller line inductance. With the existence of the depletion region, both the magnetic and electric fields will coexist in the insulator region and the depletion region, with much less portion of the magnetic field extending alone into the semiconductor region. This becomes more evident by re-examining the heuristic representation of figure 4.19 in the presence of a depletion region.

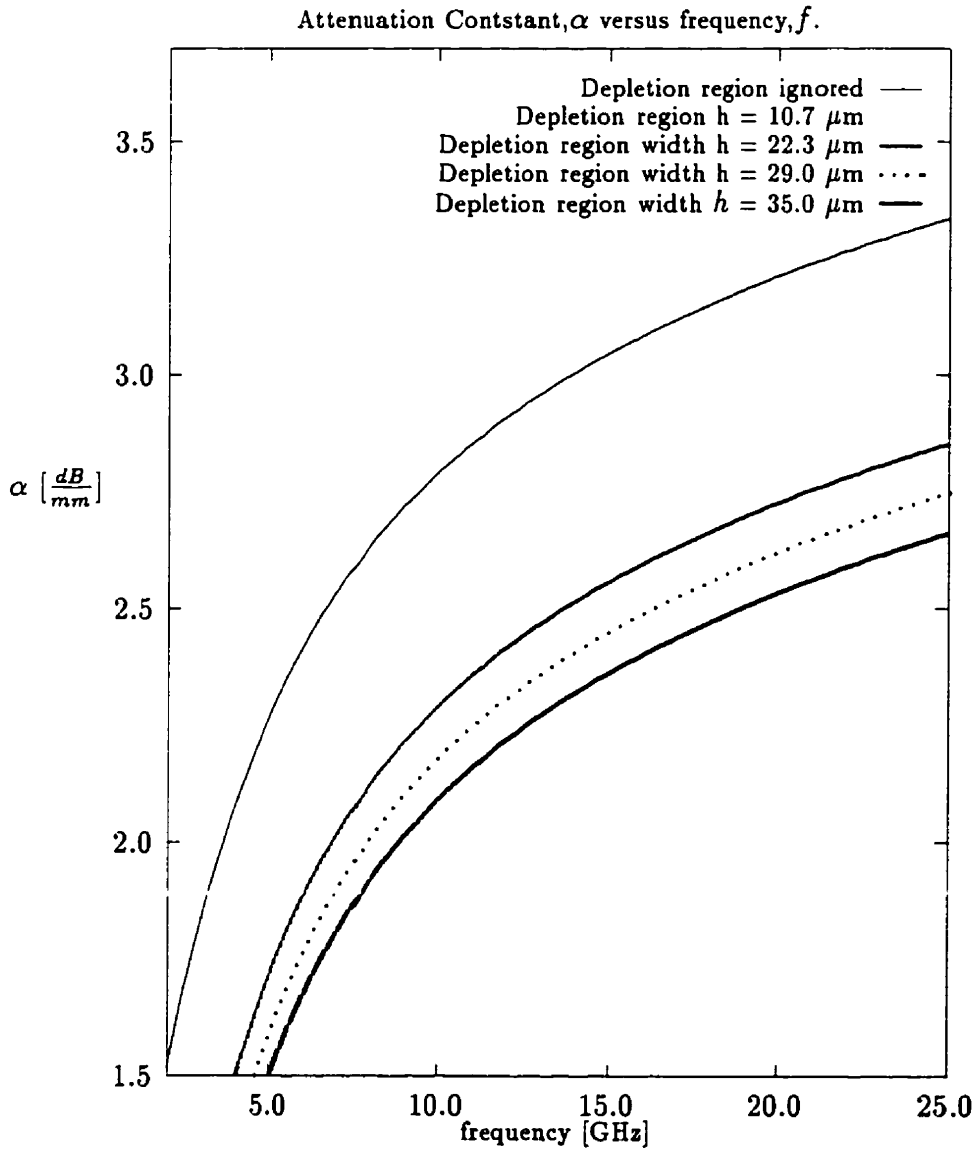

Figure 4.28: The attenuation constant, α [$\frac{dB}{mm}$], versus frequency, f [GHz], for a transmission line of width W= 500 μm. All parameters are as noted in the previous figure.

As for the attenuation constant, α, it is affected by the depletion region at both higher and lower frequencies. This is evident since the microwave signal is made to propagate in less-lossy media in the presence of the depletion region. The percentage error is more pronounced in the lower frequency range, with a 27% difference between the computation conducted with no depletion region considered and with a 10.7 μm depletion region at 2 GHz. The percentage error is less, but remains considerable, at higher frequencies since at these frequencies, the skin depth is smaller, and the EM fields are confined to a smaller depth near the metalization. At 25 GHz, the percentage difference in the magnitude of α for the cases h= 0 and h= 10.7 μm is 8.5%, and it goes to 20% if the case of h = 35.0 μm is considered.

Figure 4.31 depicts the characteristic impedance $Z_{in}(\omega)$, versus frequency, f [GHz], for the same transmission line. The effect of a depletion region of width 10 μ is considered and is compared to the results obtained by neglecting its existence. As shown, an error of about 10% in estimating the real part of the characteristic impedance is encountered when the depletion region effect is ignored. The effect of the depletion region on the imaginary component of the characteristic impedance is even more prominent, leading to errors of almost 100%.

The effect of the depletion region on the imaginary components of the propagation constant and the characteristic impedance is quite substantial as it is directly related to the attenuation of the signal. The existence of the depletion region effectively displaces the lossy segment of the substrate away from the microstrip line by a distance equal to the depletion region width. Hence, a major portion of the microwave signal spatial distribution is propagated in an effectively lossless substrate.

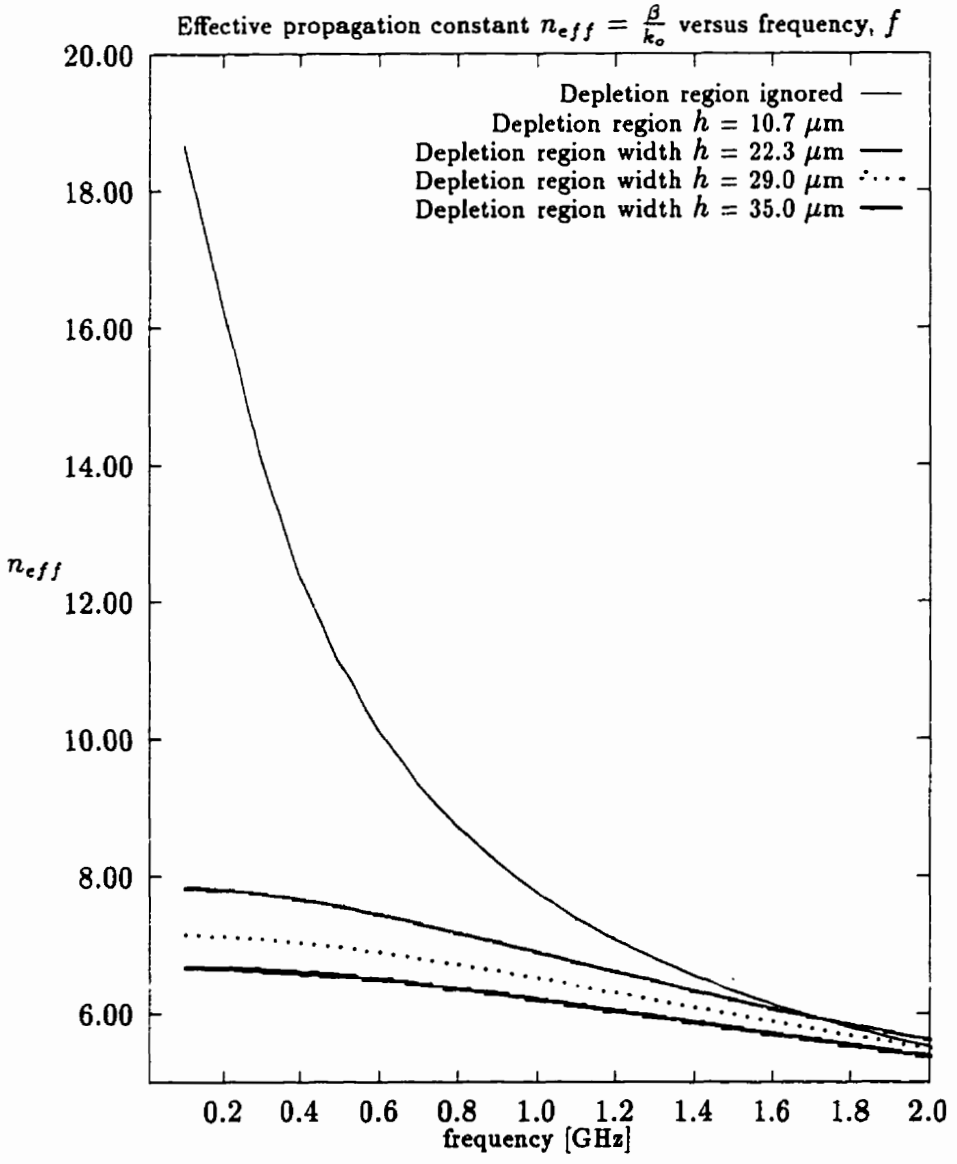

Figure 4.29: The normalized propagation constant (effective index) $n_{eff} = \frac{\beta}{k_o}$, versus frequency f [GHz] in the frequency range of the slow-wave mode, for a transmission line of width W= 500 μm, and a silicon (ϵ_r=12) substrate of thickness 390 μm, with 1.4 μm of silica (ϵ_r=4) on top of it. Results show the effect of considering the depletion region in the analysis. Shield dimensions: a = 6 mm and b= 6.5 mm. Computation conducted using M= 2000.

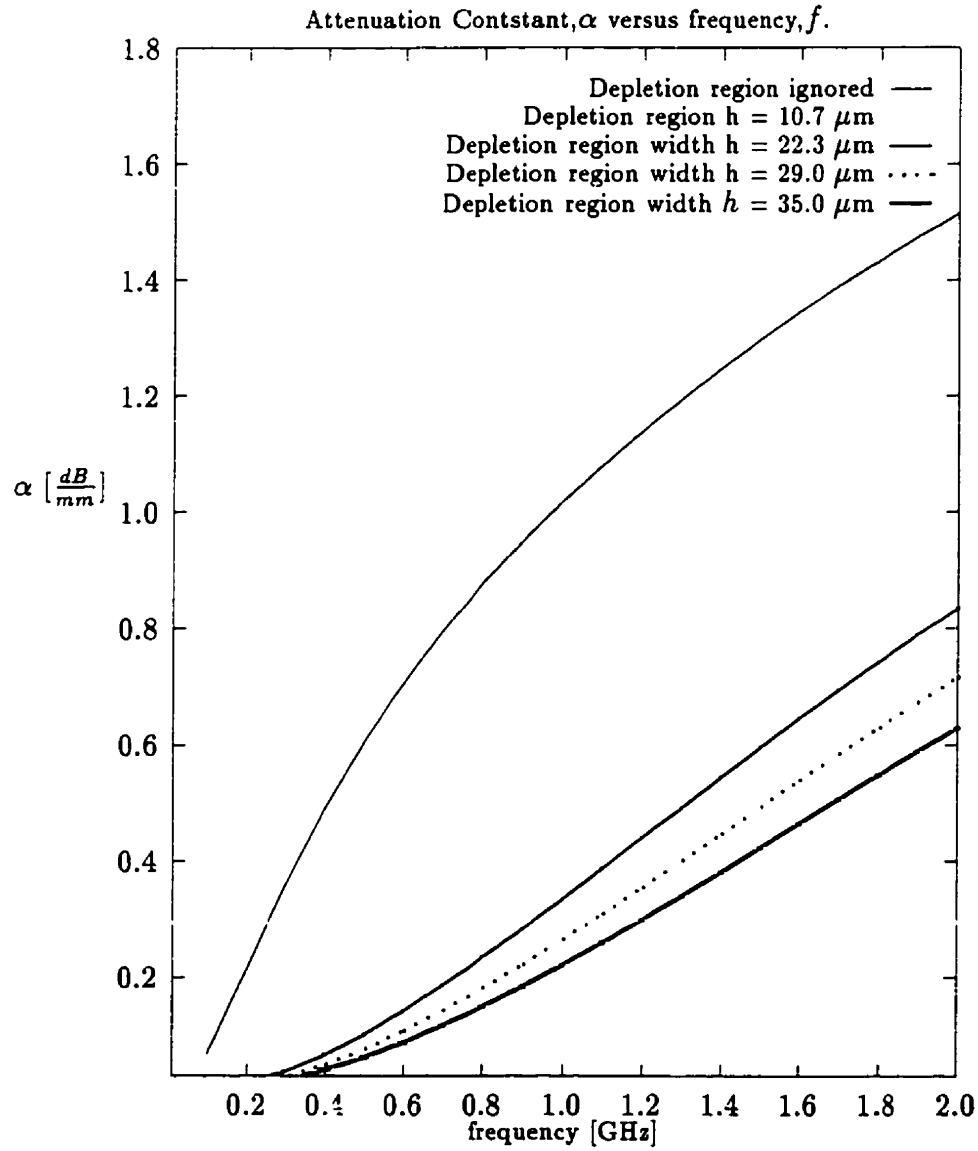

Figure 4.30: The attenuation constant, α [$\frac{dB}{mm}$], versus frequency f [GHz] in the frequency range of the slow-wave mode, for a transmission line of width W= 500 μm. All parameters are as noted in the previous figure.

4.4.6 The Green's Functions for A Rectangular Cavity Partially Filled With Multiple Layers of Lossy Dielectrics

In a procedure analogous to that conducted in the case of a rectangular waveguide, the Green's functions for a rectangular cavity partially filled with multiple layers of lossy dielectrics is obtained. Figure 4.32 illustrates the geometry of the cavity. The structure is loaded with N dielectric layers and contains a point current source, $\vec{J}_s(r')$, located at (x_{01}, y', z'). In response to this current source, an electric field is generated. This electric field directly yields the electric Green's function for the cavity, $\vec{G}_c(\vec{r}, \vec{r}')$, given by

$$\vec{G}_c{}^i(\vec{r}, \vec{r}') = \hat{x}\hat{y}G_c{}^i{}_{xy}(\vec{r}, \vec{r}') + \hat{x}\hat{z}G_c{}^i{}_{xz}(\vec{r}, \vec{r}') + \hat{y}\hat{y}G_c{}^i{}_{yy}(\vec{r}, \vec{r}')$$
$$+ \hat{y}\hat{z}G_c{}^i{}_{yz}(\vec{r}, \vec{r}') + \hat{z}\hat{y}G_c{}^i{}_{zy}(\vec{r}, \vec{r}') + \hat{z}\hat{z}G_c{}^i{}_{zz}(\vec{r}, \vec{r}') \,, \tag{4.198}$$

where the term $\vec{G}_{c_{xy}}^{\,i}(\vec{r}, \vec{r}')$ is the component of the electric Green's function associated with the $\hat{x}$ component of the electric field in region i due to the $\hat{y}$-directed component of the infinitesimal electric surface current source located at $(x' = x_{01}, y', z')$. The other terms are defined similarly. The point current source $\vec{J}_s(r')$, located at $(x = x_{01}, y', z')$, is defined as,

$$\vec{J}_s(r') = \hat{y}J_y + \hat{z}J_z = \left[\delta(x - x_{01})\delta(y - y')\delta(z - z')\right](\hat{y} + \hat{z}) \,, \tag{4.199}$$

The procedure for deriving the Green's function for the cavity problem is identical to that of the rectangular waveguide. A point current source is assumed, and the electric field due to this source defines the desired Green's function. The primary Hertz vectors are derived first, followed by the Hertz vectors of the scattered fields. Both are combined to satisfy the boundary conditions 4.84- 4.85, yielding the amplitude coefficients. The Green's function are constructed from the total Hertz vectors. The analysis is almost identical, and for the sake of brevity will not be reproduced here. The Green's functions obtained are used to compute the fields around a discontinuity of a transmission line and to characterize the discontinuity. For this goal, only the Green's function in the

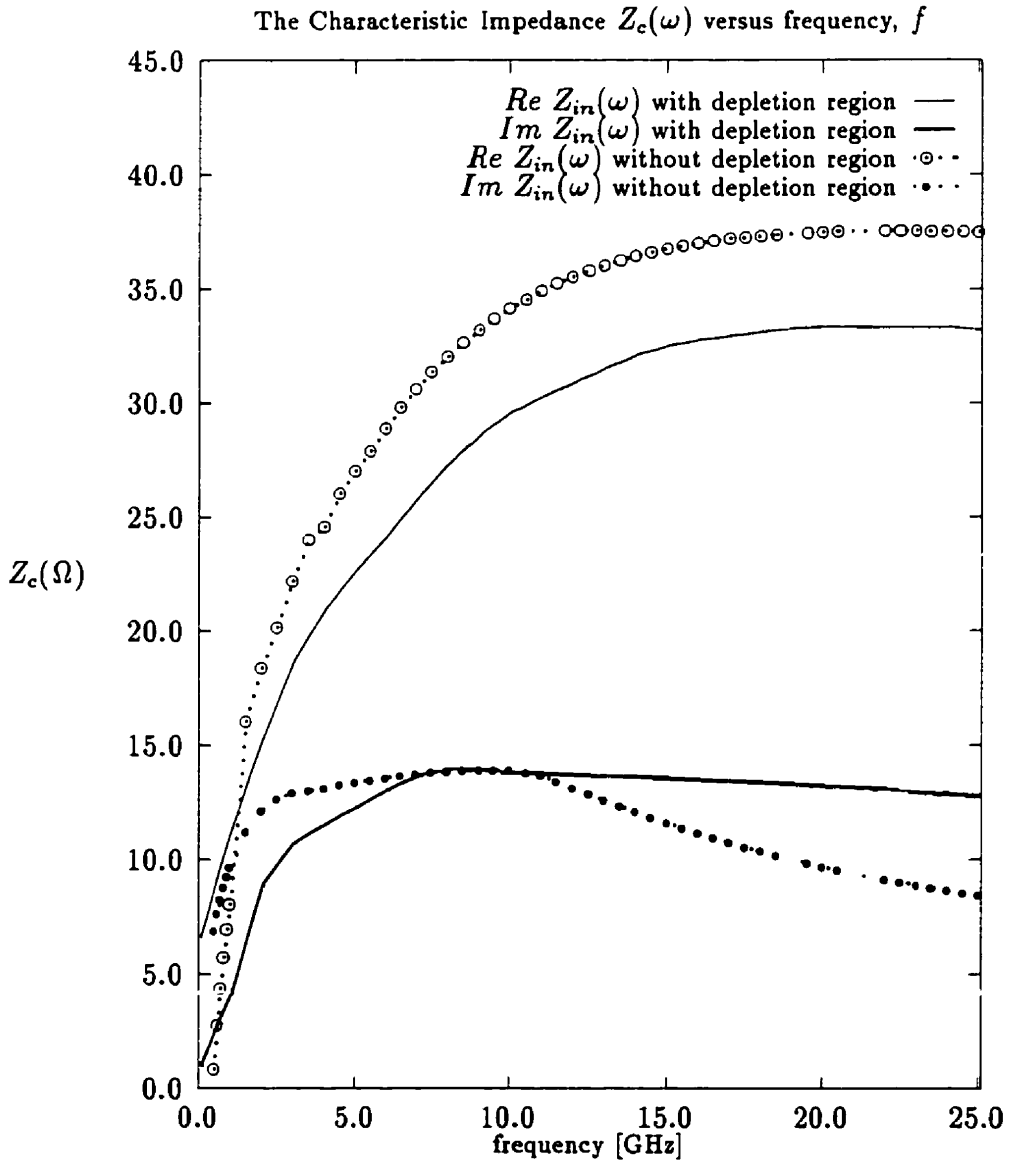

Figure 4.31: The characteristic impedance $Z_c(\omega)$, versus frequency, f [GHz], for a transmission line of width W= 500 μm, and a silicon (ϵ_r=12) substrate of thickness 390 μm, with 1.4 μm of silica (ϵ_r=4) on top of it. A depletion region of width 10 μ is taken into account. Result obtained for a substrate resistivity of 0.12 $\Omega - m$. The shielding structure dimensions are a= 6mm and b= 6.5 mm.

region (0) above the metalization or the Green's function in the region (1) just below the metalization is required. The Green's function will be used to derive the electric fields tangential to the plane of the discontinuity, which is the plane of the metalization. Hence, the evaluation of ${G_{cxy}}^{(0)}$ and ${G_{cxz}}^{(0)}$ is unnecessary. The mathematical task reduced to obtaining the remaining four components of the Green's function dyad: ${G_{yy}}^{(0)}$, ${G_{yz}}^{(0)}$, ${G_{zy}}^{(0)}$, and ${G_{zz}}^{(0)}$. These are given as:

$$ {G_{yy}}^{(0)} = \sum_m \sum_n {g^{(0)}}_{yy_{mn}}(x) \cos\left(\frac{m\pi y}{b}\right) \cos\left(\frac{m\pi y'}{b}\right) \sin\left(\frac{n\pi z}{c}\right) \sin\left(\frac{n\pi z'}{c}\right) \quad (4.200) $$

$$ {G_{yz}}^{(0)} = \sum_m \sum_n {g^{(0)}}_{yz_{mn}}(x) \cos\left(\frac{m\pi y}{b}\right) \sin\left(\frac{m\pi y'}{b}\right) \sin\left(\frac{n\pi z}{c}\right) \cos\left(\frac{n\pi z'}{c}\right) \quad (4.201) $$

$$ {G_{zy}}^{(0)} = \sum_m \sum_n {g^{(0)}}_{zy_{mn}}(x) \sin\left(\frac{m\pi y}{b}\right) \cos\left(\frac{m\pi y'}{b}\right) \cos\left(\frac{n\pi z}{c}\right) \sin\left(\frac{n\pi z'}{c}\right) \quad (4.202) $$

$$ {G_{zz}}^{(0)} = \sum_m \sum_n {g^{(0)}}_{zz_{mn}}(x) \sin\left(\frac{m\pi y}{b}\right) \sin\left(\frac{m\pi y'}{b}\right) \cos\left(\frac{n\pi z}{c}\right) \cos\left(\frac{n\pi z'}{c}\right) \quad (4.203) $$

where

$$ {g^{(0)}}_{yy_{mn}}(x) = \varepsilon_{om} \left[\left(\frac{m\pi}{b}\right)^2 T_1 - \left(\frac{n\pi}{c}\right)^2 T_{LSE}(x_{01}) \right] C(x) , \quad (4.204) $$

$$ {g^{(0)}}_{yz_{mn}}(x) = 2 \left(\frac{m\pi}{b}\right) \left(\frac{n\pi}{c}\right) [T_1 + T_{LSE}(x_{01})] C(x) , \quad (4.205) $$

$$ {g^{(0)}}_{zy_{mn}}(x) = {g^{(0)}}_{yz_m}(x) , \quad (4.206) $$

and

$$ {g^{(0)}}_{zz_{mn}}(x) = \varepsilon_{on} \left[\left(\frac{n\pi}{c}\right)^2 T_1 - \left(\frac{m\pi}{b}\right)^2 T_{LSE}(x_{01}) \right] C(x) , \quad (4.207) $$

where $\varepsilon_{o\nu}$ is defined in 4.41, T_1 is given in 4.126, $C(x)$ is given in 4.127 and T_{LSM} and T_{LSE} are given in 4.128 and 4.129 respectively.

4.4.7 Theoretical Study of Microstrip Discontinuities in Multi-layered Shielded Structures

Formulation

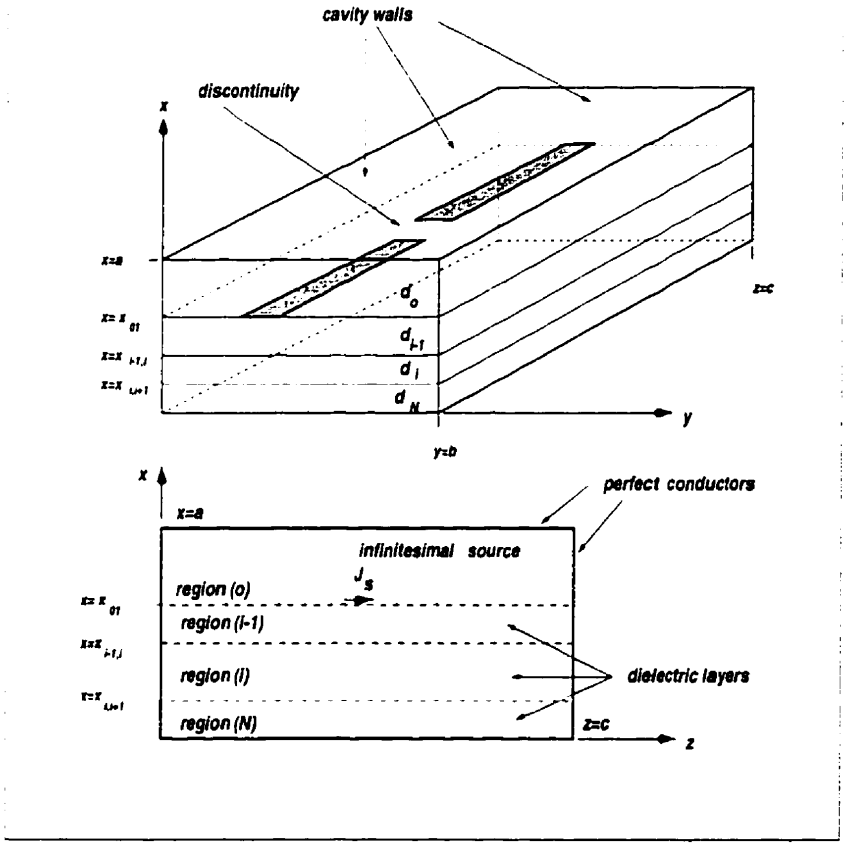

Figure 4.32: A schematic of an inhomogeneously partially filled rectangular cavity.

In the previous section, the electric Green's function for a rectangular cavity partially filled with N layers of lossy dielectrics and semiconductors has been derived. Consider now a certain metalization layout of random shape and of negligible thickness situated on top of the N layers of dielectrics of the previous analysis. This metalization layout is assumed to be made of a perfect conducting material. Such a geometry is characterized as a microwave discontinuity, an example of which is the series gap discontinuity depicted in Figure 4.32. Again, As a result of adding this conducting geometry, the boundary conditions of the original cavity problem have changed. Using the cavity Green's functions obtained earlier and using the current distribution on the metalization, the electric field is recalculated from equation 4.3 subject to a new boundary condition; the tangential component of the electric field must vanish on the metallic strip. As opposed to the problem of the uniform stripline, the surface current distribution for the discontinuity is unknown and is expressed in terms of a series of known basis functions with unknown amplitude coefficients. The electric field in the plane of the metalization is expressed in terms of these basis functions. Enforcing the boundary condition that $\vec{E} = 0$ on the metalization yields a system of linear equations whose unknowns are the unknown amplitude coefficients of the basis function of the surface current density. Solution of this matrix yields the unknown coefficients. Hence, the current distribution is specified everywhere. Fitting the current distribution on the uniform line feeding the discontinuity to a transmission line model, the incident and reflected portions of the current are identified. Using this information, the discontinuity is characterized using a scattering matrix representation or an impedance matrix representation.

It is possible to use the rectangular waveguide Green's function to analyze discontinuities in the line instead of using the rectangular cavity Green's function. It is easier however to use the cavity Green's function. The eigenvalues of the cavity problem are easily determined directly from the separation of variables solution: $k_z = \frac{n\pi}{c}$ and $k_y = \frac{m\pi}{b}$. For the waveguide problem, $k_y = \frac{m\pi}{b}$ but k_z is determined by solving a complicated transcendental equation. It is impractical to evaluate the hundreds of k_z's required for the fields expansions using this method, especially when dealing with lossy substrates where

k_z is a complex number.

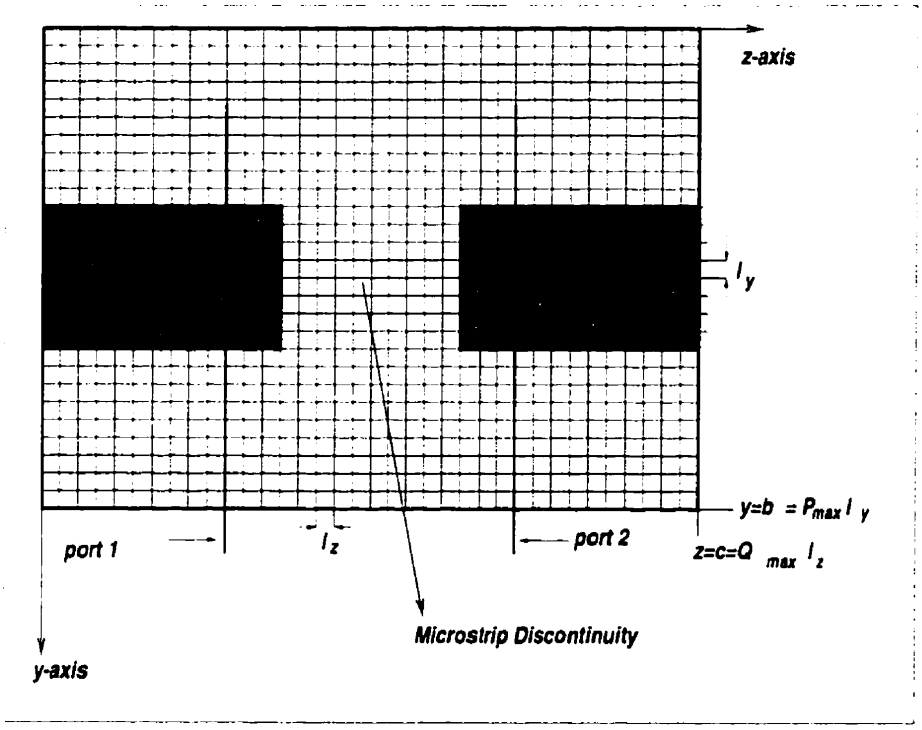

Figure 4.33: Discretization of a discontinuity plane.

The unknown surface current density distribution on the metalization is cast in the form:

$$J_y(y',z') = \sum_{p'}\sum_{q'} I_{y_{p'q'}}\ f_{p'}(y')g_{q'}(z')\ , \tag{4.208}$$

and

$$J_z(y',z') = \sum_{p'}\sum_{q'} I_{z_{p'q'}}\ g_{p'}(y')f_{q'}(z')\ , \tag{4.209}$$

where $f_{p'}(y')\ g_{q'}(z')$ and where $f_{q'}(z')\ g_{p'}(y')$ are basis function expansions for $J_y(y',z')$ and $J_z(y',z')$ respectively with $I_{y_{p'q'}}$ and $I_{z_{p'q'}}$ being the unknown amplitude coefficients of $J_y(y',z')$ and $J_z(y',z')$ respectively. p' and q' are the summation integral indices. The plane of the discontinuity is partitioned into small sections as shown in Figure 4.33. The cavity dimensions b and c are partitioned into P_{max} and Q_{max} segments each of length l_y or l_z respectively. The basis functions define the shape of the current within each subsection

of the plane of the discontinuity. $f_{p'}(y')$ and $g_{q'}(z')$ are defined as

$$f_{q'}(z') = \begin{cases} \frac{\sin h_z(z_{q'+1}-z')}{\sin h_z l_z} & \text{if } z_{q'} \leq z' \leq z_{q'+1} \\ \frac{\sin h_z(z'-z_{q'-1})}{\sin h_z l_z} & \text{if } z_{q'} \leq z' \leq z_{q'} \\ 0 & \text{elsewhere} , \end{cases} \tag{4.210}$$

and

$$g_{p'}(y') = \begin{cases} 1 & \text{if } y_{p'} - \frac{l_y}{2} \leq y' \leq y_{p'} + \frac{l_y}{2} \\ 0 & \text{elsewhere} \end{cases} \tag{4.211}$$

l_z and l_y are the subsection lengths in the $z-$ direction and the $y-$ direction respectively, as shown in Figure 4.33. h_z and h_y are the basis function wave numbers. The above expansions and shaping functions have been previously applied to the problem of modeling microstrip discontinuities with excellent results obtained [238] [169]. The shape functions account for the edge effect on the current distribution. Note that these shape functions exchange coordinates when considering $J_z(y', z')$ rather than $J_y(y', z')$. The coordinates $y_{p'}$ and $z_{q'}$ assume the following discrete coordinate values [194]:

$$y_{p'} = \begin{cases} p' l_y & \text{in } J_y(y', z') \\ (p' + \frac{1}{2}) l_y & \text{in } J_z(y', z') , \end{cases} \tag{4.212}$$

$$z_{q'} = \begin{cases} (q' + \frac{1}{2}) l_z & \text{in } J_y(y', z') \\ q' l_y & \text{in } J_z(y', z') , \end{cases} \tag{4.213}$$

Substituting 4.208 and 4.209 in 4.198 results in expressions for the electric field due to that surface current density distribution. Enforcing $\vec{E_{tan}} = 0$ on the metalization yields the unknown amplitude coefficients. Since only the tangential component of the electric field is of interest at this point, only this component of the field will be evaluated in the forthcoming analysis. The components of the electric field tangential to the metalization are the E_y and E_z components, which can be expressed in the form of a set of two coupled integral equations that can be written in the following short form:

$$E_y^{(0)} = E_{yy}^{(0)} + E_{yz}^{(0)} , \tag{4.214}$$

$$E_z^{(0)} = E_{yz}^{(0)} + E_{zz}^{(0)} , \tag{4.215}$$

where

$$E_{yy}{}^{(0)} = -j\omega\mu_o \int\int G_{cyy}{}^{(0)} J_y(y',z')dy'dz' \ , \tag{4.216}$$

$$E_{yz}{}^{(0)} = -j\omega\mu_o \int\int G_{cyz}{}^{(0)} J_z(y',z')dy'dz' \ , \tag{4.217}$$

$$E_{zy}{}^{(0)} = -j\omega\mu_o \int\int G_{czy}{}^{(0)} J_y(y',z')dy'dz' \ , \tag{4.218}$$

$$E_{zz}{}^{(0)} = -j\omega\mu_o \int\int G_{czz}{}^{(0)} J_z(y',z')dy'dz' \ , \tag{4.219}$$

The superscript (0) denotes the air-filled region of width d_0 above the cavity as shown in Figure 4.32. Evaluating the Green's function for region (0) or region (1) only is sufficient to yields the unknown amplitudes. Expressions for $G_{cyy}{}^{(0)}$, $G_{cyz}{}^{(0)}$, $G_{czy}{}^{(0)}$, and $G_{czz}{}^{(0)}$ were derived in 4.204- 4.207. $J_y(y',z')$ and $J_z(y',z')$ are given in 4.208 and 4.209 respectively. This yields the following expressions for $E_{yy}{}^{(0)}$, $E_{yz}{}^{(0)}$, $E_{zy}{}^{(0)}$, and $E_{zz}{}^{(0)}$:

$$E_{yy}{}^{(0)} = -j\omega\mu_o \int\int \sum_m \sum_n g^{(0)}{}_{yy_{mn}}(x) \cos\left(\frac{m\pi y}{b}\right) \cos\left(\frac{m\pi y'}{b}\right)$$

$$\sin\left(\frac{n\pi z}{c}\right) \sin\left(\frac{n\pi z'}{c}\right) J_y(y',z')dy'dz' \ , \tag{4.220}$$

$$E_{yz}{}^{(0)} = -j\omega\mu_o \int\int \sum_m \sum_n g^{(0)}{}_{yz_{mn}}(x) \cos\left(\frac{m\pi y}{b}\right) \sin\left(\frac{m\pi y'}{b}\right)$$

$$\sin\left(\frac{n\pi z}{c}\right) \cos\left(\frac{n\pi z'}{c}\right) J_z(y',z')dy'dz' \ , \tag{4.221}$$

$$E_{zy}{}^{(0)} = -j\omega\mu_o \int\int \sum_m \sum_n g^{(0)}{}_{zy_{mn}}(x) \sin\left(\frac{m\pi y}{b}\right) \cos\left(\frac{m\pi y'}{b}\right)$$

$$\cos\left(\frac{n\pi z}{c}\right) \sin\left(\frac{n\pi z'}{c}\right) J_y(y',z')dy'dz' \ , \tag{4.222}$$

$$E_{zz}{}^{(0)} = -j\omega\mu_o \int\int \sum_m \sum_n g^{(0)}{}_{zz_{mn}}(x) \sin\left(\frac{m\pi y}{b}\right) \sin\left(\frac{m\pi y'}{b}\right)$$

$$\cos\left(\frac{n\pi z}{c}\right) \cos\left(\frac{n\pi z'}{c}\right) J_z(y',z')dy'dz' \ . \tag{4.223}$$

Substituting with the expressions for $J_y(y',z')$ and $J_z(y',z')$ in the above four equations yields:

$$E_{yy}{}^{(0)} = -j\omega\mu_o \sum_m \sum_n g^{(0)}{}_{yy_{mn}}(x) \cos\left(\frac{m\pi y}{b}\right) \sin\left(\frac{n\pi z}{c}\right) \sum_{p'} \sum_{q'} I_{y_{p'q'}} \int_{y_{p'-1}}^{y_{p'+1}} f_{p'}(y') \cos\left(\frac{m\pi y'}{b}\right) dy' \int_{z_{q'}-\frac{l_z}{2}}^{z_{q'}+\frac{l_z}{2}} g_{q'}(z') \sin\left(\frac{n\pi z'}{c}\right) dz' \tag{4.224}$$

$$E_{yz}{}^{(0)} = -j\omega\mu_o \sum_m \sum_n g^{(0)}{}_{yz_{mn}}(x) \cos\left(\frac{m\pi y}{b}\right) \sin\left(\frac{n\pi z}{c}\right) \sum_{p'} \sum_{q'} I_{z_{p'q'}} \int_{y_{p'}-\frac{l_y}{2}}^{y_{p'}+\frac{l_y}{2}} g_{p'}(y') \sin\left(\frac{m\pi y'}{b}\right) dy' \int_{z_{q'-1}}^{z_{q'+1}} f_{q'}(z') \cos\left(\frac{n\pi z'}{c}\right) dz' \tag{4.225}$$

$$E_{zy}{}^{(0)} = -j\omega\mu_o \sum_m \sum_n g^{(0)}{}_{zy_{mn}}(x) \sin\left(\frac{m\pi y}{b}\right) \cos\left(\frac{n\pi z}{c}\right) \sum_{p'} \sum_{q'} I_{y_{p'q'}} \int_{y_{p'-1}}^{y_{p'+1}} f_{p'}(y') \cos\left(\frac{m\pi y'}{b}\right) dy' \int_{z_{q'}-\frac{l_z}{2}}^{z_{q'}+\frac{l_z}{2}} g_{q'}(z') \sin\left(\frac{n\pi z'}{c}\right) dz' \tag{4.226}$$

$$E_{zz}{}^{(0)} = -j\omega\mu_o \sum_m \sum_n g^{(0)}{}_{zz_{mn}}(x) \sin\left(\frac{m\pi y}{b}\right) \cos\left(\frac{n\pi z}{c}\right) \sum_{p'} \sum_{q'} I_{z_{p'q'}} \int_{y_{p'}-\frac{l_y}{2}}^{y_{p'}+\frac{l_y}{2}} g_{p'}(y') \sin\left(\frac{m\pi y'}{b}\right) dy' \int_{z_{q'-1}}^{z_{q'+1}} f_{q'}(z') \cos\left(\frac{n\pi z'}{c}\right) dz'. \tag{4.227}$$

Carrying-out the above integrals, and simplifying;

$$E_{yy}{}^{(0)} = -j\omega\mu_o \sum_{p'} \sum_{q'} I_{y_{p'q'}} \sum_m \sum_n g^{(0)}{}_{yy_{mn}}(x) \cos\left(\frac{m\pi y}{b}\right) \sin\left(\frac{n\pi z}{c}\right) Int_g(q') Int_f(p') , \tag{4.228}$$

$$E_{yz}{}^{(0)} = -j\omega\mu_o \sum_{p'} \sum_{q'} I_{z_{p'q'}} \sum_m \sum_n g^{(0)}{}_{yz_{mn}}(x) \cos\left(\frac{m\pi y}{b}\right) \sin\left(\frac{n\pi z}{c}\right) Int_g(p') Int_f(q') , \tag{4.229}$$

$$E_{zy}{}^{(0)} = -j\omega\mu_o \sum_{p'} \sum_{q'} I_{y_{p'q'}} \sum_m \sum_n g^{(0)}{}_{zy_{mn}}(x) \sin\left(\frac{m\pi y}{b}\right) \cos\left(\frac{n\pi z}{c}\right) Int_g(q') Int_f(p') , \tag{4.230}$$

$$E_{zz}{}^{(0)} = -j\omega\mu_o \sum_{p'} \sum_{q'} I_{z_{p'q'}} \sum_m \sum_n g^{(0)}{}_{zz_{mn}}(x) \sin\left(\frac{m\pi y}{b}\right) \cos\left(\frac{n\pi z}{c}\right) Int_g(q') Int_f(p') , \tag{4.231}$$

where

$$Int_g(p') = \int_{y_{p'}-\frac{l_y}{2}}^{y_{p'}+\frac{l_y}{2}} g_{p'}(y') \sin\left(\frac{m\pi y'}{b}\right) dy' = l_y sinc\left[\frac{m\pi l_y}{2b}\right] \sin\left(\frac{m\pi y_{p'}}{b}\right) , \tag{4.232}$$

$$Int_g(q') = \int_{z_{p'}-\frac{l_z}{2}}^{y_{p'}+\frac{l_z}{2}} g_{q'}(z') \sin\left(\frac{n\pi z'}{c}\right) dz' = l_z sinc\left[\frac{n\pi l_z}{2c}\right] \sin\left(\frac{n\pi z_{q'}}{c}\right) , \tag{4.233}$$

$$Int_f(p') = \int_{y_{p'-1}}^{y_{p'+1}} f_{p'}(y') \cos\left(\frac{m\pi y'}{b}\right) dy' =$$

$$\frac{l_y}{sinc(h_y l_y)} sinc\left[(\frac{m\pi}{b} + h_y)\frac{l_y}{2}\right] sinc\left[(\frac{m\pi}{b} - h_y)\frac{l_y}{2}\right] \cos\left(\frac{m\pi y_{p'}}{b}\right), \qquad (4.234)$$

and

$$Int_f(q') = \int_{z_{q'-1}}^{z_{q'+1}} f_{q'}(z') \cos\left(\frac{n\pi z'}{c}\right) dz' =$$

$$\frac{l_z}{sinc(h_z l_z)} sinc\left[(\frac{n\pi}{c} + h_z)\frac{l_z}{2}\right] sinc\left[(\frac{n\pi}{c} - h_z)\frac{l_z}{2}\right] \cos\left(\frac{n\pi z_{q'}}{c}\right). \qquad (4.235)$$

Hence, the final expressions for the tangential electric field are given by

$$E_{yy}^{(0)} = -j\omega\mu_o l_y l_z \sum_{p'} \sum_{q'} I_{y_{p'q'}} \sum_m \sum_n g^{(0)}{}_{yy_{mn}} \left[\frac{sinc\left[\frac{n\pi l_z}{2c}\right]}{sinc(h_y l_y)}\right] sinc\left[(\frac{m\pi}{b} + h_y)\frac{l_y}{2}\right]$$

$$sinc\left[(\frac{m\pi}{b} - h_y)\frac{l_y}{2}\right] \cos\left(\frac{m\pi y_{p'}}{b}\right) \sin\left(\frac{n\pi z_{q'}}{c}\right) \cos\left(\frac{m\pi y}{b}\right) \sin\left(\frac{n\pi z}{c}\right), \qquad (4.236)$$

$$E_{yz}^{(0)} = -j\omega\mu_o l_y l_z \sum_{p'} \sum_{q'} I_{y_{p'q'}} \sum_m \sum_n g^{(0)}{}_{yz_{mn}} \left[\frac{sinc\left[\frac{m\pi l_y}{2b}\right]}{sinc(h_z l_z)}\right] sinc\left[(\frac{n\pi}{c} + h_z)\frac{l_z}{2}\right]$$

$$sinc\left[(\frac{n\pi}{c} - h_z)\frac{l_z}{2}\right] \sin\left(\frac{m\pi y_{p'}}{b}\right) \cos\left(\frac{n\pi z_{q'}}{c}\right) \cos\left(\frac{m\pi y}{b}\right) \sin\left(\frac{n\pi z}{c}\right), \qquad (4.237)$$

$$E_{zy}^{(0)} = -j\omega\mu_o l_y l_z \sum_{p'} \sum_{q'} I_{y_{p'q'}} \sum_m \sum_n g^{(0)}{}_{zy_{mn}} \left[\frac{sinc\left[\frac{n\pi l_z}{2c}\right]}{sinc(h_y l_y)}\right] sinc\left[(\frac{m\pi}{b} + h_y)\frac{l_y}{2}\right]$$

$$sinc\left[(\frac{m\pi}{b} - h_y)\frac{l_y}{2}\right] \cos\left(\frac{m\pi y_{p'}}{b}\right) \sin\left(\frac{n\pi z_{q'}}{c}\right) \sin\left(\frac{m\pi y}{b}\right) \cos\left(\frac{n\pi z}{c}\right), \qquad (4.238)$$

$$E_{zz}^{(0)} = -j\omega\mu_o l_y l_z \sum_{p'} \sum_{q'} I_{z_{p'q'}} \sum_m \sum_n g^{(0)}{}_{zz_{mn}} \left[\frac{sinc\left[\frac{m\pi l_y}{2b}\right]}{sinc(h_z l_z)}\right] sinc\left[(\frac{n\pi}{c} + h_z)\frac{l_z}{2}\right]$$

$$sinc\left[(\frac{n\pi}{c} - h_z)\frac{l_z}{2}\right] \sin\left(\frac{m\pi y_{p'}}{b}\right) \cos\left(\frac{n\pi z_{q'}}{c}\right) \sin\left(\frac{m\pi y}{b}\right) \cos\left(\frac{n\pi z}{c}\right). \qquad (4.239)$$

Method of Moments

The z and y components of the electric field, $E_y^{(0)}$ and $E_z^{(0)}$ due to the given surface current density distribution of 4.208 and 4.209 have been found. Enforcing the boundary

condition $\vec{E_{tan}} = 0$ on the perfectly conducting metalization yields the unknown amplitude coefficients. An equivalent boundary condition is that the conduction surface current and the tangential electric field are complementary quantities in the $x = x_{01}$ plane. Hence, this condition is cast as

$$\int\int {E_y}^{(0)} J_y dy\, dz|_{x=x_{01}} = \int\int {E_z}^{(0)} J_z dy\, dz|_{x=x_{01}} = 0 \,. \tag{4.240}$$

In a more explicit form,

$$\int\int_{\Delta s} {E_y}^{(0)} J_y dydz = \int\int_{\Delta s} \left[{E_{yy}}^{(0)} + {E_{yz}}^{(0)}\right] J_y dydz =$$

$$\int\int_{\Delta s} {E_{yy}}^{(0)} f_p(y) g_q(z) dydz + \int\int_{\Delta s} {E_{yz}}^{(0)} f_p(y) g_q(z) dydz = 0 \,, \tag{4.241}$$

and

$$\int\int_{\Delta s} {E_z}^{(0)} J_z dydz = \int\int_{\Delta s} \left[{E_{zy}}^{(0)} + {E_{zz}}^{(0)}\right] J_z dydz =$$

$$\int\int_{\Delta s} {E_{zy}}^{(0)} g_p(y) f_q(z) dydz + \int\int_{\Delta s} {E_{yz}}^{(0)} g_p(y) f_q(z) dydz = 0 \,, \tag{4.242}$$

where Δs is a segment of the plane $x = x_{01}$ with dimensions l_y and l_z in the y and z directions respectively. Conducting the above integrals yield:

$$\int\int_{\Delta s} {E_{yy}}^{(0)} f_p(y) g_q(z) dydz = -j\omega\mu_o (l_y l_z)^2 \sum_{p'} \sum_{q'} I_{y p' q'} \sum_m \sum_n {g^{(0)}}_{yy_{mn}} \left[\frac{sinc\left(\frac{n\pi l_z}{2c}\right)}{sinc(h_y l_y)}\right]^2$$

$$\left[sinc\left(\left(\frac{m\pi}{b} + h_y\right)\frac{l_y}{2}\right) sinc\left(\left(\frac{m\pi}{b} - h_y\right)\frac{l_y}{2}\right)\right]^2$$

$$\cos\left(\frac{m\pi y_{p'}}{b}\right) \sin\left(\frac{n\pi z_{q'}}{c}\right) \cos\left(\frac{m\pi y}{b}\right) \sin\left(\frac{n\pi z}{c}\right) \,, \tag{4.243}$$

$$\int\int_{\Delta s} {E_{yz}}^{(0)} f_p(y) g_q(z) dydz =$$

$$-j\omega\mu_o (l_y l_z)^2 \sum_{p'} \sum_{q'} I_{y p' q'} \sum_m \sum_n {g^{(0)}}_{yz_{mn}} \left[\frac{sinc\left(\frac{n\pi l_z}{2c}\right)}{sinc(h_y l_y)}\right] \left[\frac{sinc\left(\frac{m\pi l_y}{2b}\right)}{sinc(h_z l_z)}\right]$$

$$\left[sinc\left((\frac{m\pi}{b}+h_y)\frac{l_y}{2}\right)sinc\left((\frac{m\pi}{b}-h_y)\frac{l_y}{2}\right)\right]\left[sinc\left((\frac{n\pi}{c}+h_z)\frac{l_z}{2}\right)sinc\left((\frac{n\pi}{c}-h_z)\frac{l_z}{2}\right)\right]$$
$$\sin\left(\frac{m\pi y_{p'}}{b}\right)\cos\left(\frac{n\pi z_{q'}}{c}\right)\cos\left(\frac{m\pi y}{b}\right)\cos\left(\frac{n\pi z}{c}\right), \tag{4.244}$$

$$\int\int_{\Delta s} E_{zy}{}^{(0)} g_p(y) f_q(z) dydz =$$

$$-j\omega\mu_o(l_y l_z)^2 \sum_{p'}\sum_{q'} I_{z_{p'q'}} \sum_m \sum_n g^{(0)}{}_{zy_{mn}} \left[\frac{sinc\left(\frac{n\pi l_z}{2c}\right)}{sinc(h_y l_y)}\right]\left[\frac{sinc\left(\frac{m\pi l_y}{2b}\right)}{sinc(h_z l_z)}\right]$$

$$\left[sinc\left((\frac{m\pi}{b}+h_y)\frac{l_y}{2}\right)sinc\left((\frac{m\pi}{b}-h_y)\frac{l_y}{2}\right)\right]\left[sinc\left((\frac{n\pi}{c}+h_z)\frac{l_z}{2}\right)sinc\left((\frac{n\pi}{c}-h_z)\frac{l_z}{2}\right)\right]$$
$$\cos\left(\frac{m\pi y_{p'}}{b}\right)\sin\left(\frac{n\pi z_{q'}}{c}\right)\sin\left(\frac{m\pi y}{b}\right)\cos\left(\frac{n\pi z}{c}\right), \tag{4.245}$$

and

$$\int\int_{\Delta s} E_{zz}{}^{(0)} g_p(y) f_q(z) dydz = -j\omega\mu_o(l_y l_z)^2 \sum_{p'}\sum_{q'} I_{z_{p'q'}} \sum_m \sum_n g^{(0)}{}_{zz_{mn}} \left[\frac{sinc\left(\frac{m\pi l_y}{2b}\right)}{sinc(h_z l_z)}\right]^2$$

$$\left[sinc\left((\frac{n\pi}{c}+h_z)\frac{l_z}{2}\right)sinc\left((\frac{n\pi}{b}-h_z)\frac{l_z}{2}\right)\right]^2$$
$$\cos\left(\frac{m\pi y_{p'}}{b}\right)\sin\left(\frac{n\pi z_{q'}}{c}\right)\sin\left(\frac{m\pi y}{b}\right)\cos\left(\frac{n\pi z}{c}\right). \tag{4.246}$$

These equations can be written in the following short form:

$$\int\int_{\Delta s} E_{yy}{}^{(0)} g_q(z) f_p(y) dydz = \sum_{p'}\sum_{q'} I_{y_{p'q'}} Z_{yy}(p,q,p',q'), \tag{4.247}$$

$$\int\int_{\Delta s} E_{yz}{}^{(0)} g_q(z) f_p(y) dydz = \sum_{p'}\sum_{q'} I_{z_{p'q'}} Z_{yz}(p,q,p',q'), \tag{4.248}$$

$$\int\int_{\Delta s} E_{zy}{}^{(0)} g_p(y) f_q(z) dydz = \sum_{p'} \sum_{q'} I_{y_{p'q'}} Z_{zy}(p,q,p',q') \ , \tag{4.249}$$

and

$$\int\int_{\Delta s} E_{zz}{}^{(0)} g_p(y) f_q(z) dydz = \sum_{p'} \sum_{q'} I_{z_{p'q'}} Z_{zz}(p,q,p',q') \ , \tag{4.250}$$

which can be written in the following matrix form:

$$\begin{pmatrix} Z_{yy}(p,q,p',q') & Z_{yz}(p,q,p',q') \\ Z_{zy}(p,q,p',q') & Z_{zz}(p,q,p',q') \end{pmatrix} \begin{pmatrix} I_y(p',q') \\ I_z(p',q') \end{pmatrix} = \begin{pmatrix} V_y(p,q) \\ V_z(p,q) \end{pmatrix} \tag{4.251}$$

Here $I_y(p',q')$ and $I_z(p',q')$ are the amplitude coefficients of the surface conduction current components J_y and J_z respectively. It follows that the elements of the LHS matrix of the above system need not be evaluated of all segments Δs of the plane $x = x_{01}$. The coefficients matrix can be evaluated only for the metalized segments of that plane, since the conduction current is, by definition zero everywhere else. The coefficients $Z_{yy}(p,q,p',q')$, $Z_{yz}(p,q,p',q')$, $Z_{zy}(p,q,p',q')$ and $Z_{zz}(p,q,p',q')$ are given by

$$Z_{yy}(p,q,p',q') = \sum_{m=1}^{m=M} \sum_{n=1}^{n=N} g^{(0)}{}_{yy_{mn}} \left[\frac{sinc\left(\frac{n\pi l_x}{2c}\right)}{sinc(h_y l_y)} \right]^2$$

$$\left[sinc\left((\frac{m\pi}{b} + h_y)\frac{l_y}{2} \right) sinc\left((\frac{m\pi}{b} - h_y)\frac{l_y}{2} \right) \right]^2$$

$$\cos\left(\frac{m\pi y_{p'}}{b}\right) \sin\left(\frac{n\pi z_{q'}}{c}\right) \cos\left(\frac{m\pi y}{b}\right) \sin\left(\frac{n\pi z}{c}\right) \ , \tag{4.252}$$

$$Z_{yz}(p,q,p',q') = \sum_{m=1}^{m=M} \sum_{n=1}^{n=N} g^{(0)}{}_{yz_{mn}} \left[\frac{sinc\left(\frac{n\pi l_x}{2c}\right)}{sinc(h_y l_y)} \right] \left[\frac{sinc\left(\frac{m\pi l_y}{2b}\right)}{sinc(h_z l_z)} \right]$$

$$\left[sinc\left((\frac{m\pi}{b} + h_y)\frac{l_y}{2} \right) sinc\left((\frac{m\pi}{b} - h_y)\frac{l_y}{2} \right) \right] \left[sinc\left((\frac{n\pi}{c} + h_z)\frac{l_z}{2} \right) sinc\left((\frac{n\pi}{c} - h_z)\frac{l_z}{2} \right) \right]$$

$$\sin\left(\frac{m\pi y_{p'}}{b}\right) \cos\left(\frac{n\pi z_{q'}}{c}\right) \cos\left(\frac{m\pi y}{b}\right) \cos\left(\frac{n\pi z}{c}\right) \ , \tag{4.253}$$

$$Z_{zy}(p,q,p',q') = \sum_{m=1}^{m=M}\sum_{n=1}^{n=N} g^{(0)}{}_{zy_{mn}} \left[\frac{sinc\left(\frac{n\pi l_z}{2c}\right)}{sinc(h_y l_y)}\right]\left[\frac{sinc\left(\frac{m\pi l_y}{2b}\right)}{sinc(h_z l_z)}\right]$$

$$\left[sinc\left((\frac{m\pi}{b}+h_y)\frac{l_y}{2}\right) sinc\left((\frac{m\pi}{b}-h_y)\frac{l_y}{2}\right)\right]\left[sinc\left((\frac{n\pi}{c}+h_z)\frac{l_z}{2}\right) sinc\left((\frac{n\pi}{c}-h_z)\frac{l_z}{2}\right)\right]$$

$$\cos\left(\frac{m\pi y_{p'}}{b}\right)\sin\left(\frac{n\pi z_{q'}}{c}\right)\sin\left(\frac{m\pi y}{b}\right)\cos\left(\frac{n\pi z}{c}\right), \qquad (4.254)$$

and

$$Z_{zz}(p,q,p',q') = \sum_{m=1}^{m=M}\sum_{n=1}^{n=N} g^{(0)}{}_{zz_{mn}} \left[\frac{sinc\left(\frac{m\pi l_y}{2b}\right)}{sinc(h_z l_z)}\right]^2$$

$$\left[sinc\left((\frac{n\pi}{c}+h_z)\frac{l_z}{2}\right) sinc\left((\frac{n\pi}{b}-h_z)\frac{l_z}{2}\right)\right]^2$$

$$\cos\left(\frac{m\pi y_{p'}}{b}\right)\sin\left(\frac{n\pi z_{q'}}{c}\right)\sin\left(\frac{m\pi y}{b}\right)\cos\left(\frac{n\pi z}{c}\right). \qquad (4.255)$$

The summation over m and n is truncated at $m = M < \infty$ and $n = N < \infty$ respectively. The truncation at M and N is chosen such that the retained terms provide sufficiently accurate results. A criteria for choosing M and N are presented later in this section.

Input Field Excitation and Various Models

The matrix of 4.251 is a system of linear equations obtained from the boundary condition that the electric field at a certain point on the metalization is zero or else the surface conduction current density at this point is zero. Hence the product of these two quantities is zero everywhere on the metalization. It follows that the RHS of the system 4.251 is a vector of zeroes, leading to a homogeneous system of linear equations, whose solution is the trivial solution. However, that boundary condition is violated at one or more points to provide an excitation to the system. Hence, $V_y(p,q)$ and $V_z(p,q)$ are termed the excitation vectors. For a given excitation vector, a certain current distribution is

maintained on the metalization. That distribution is given by the amplitude coefficients $I_y(p',q')$ and $I_y(p',q')$. The point at which $V_y(p,q) \neq 0$ or $V_y(p,q) \neq 0$ is called the gap generator. Hence, $V_y(p,q)$ and $V_y(p,q)$ are defined as [167]:

$$V_y(p,q) = \begin{cases} 1 & \text{if } y_p = y_{gap} \\ 0 & \text{elsewhere on the metalization ,} \end{cases} \tag{4.256}$$

$$V_z(p,q) = \begin{cases} 1 & \text{if } z_q = z_{gap} \\ 0 & \text{elsewhere on the metalization .} \end{cases} \tag{4.257}$$

The gap generator excitation method [239] [167] is a non-physical mathematical tool to excite the circuit. Another technique to excite the circuit is the cavity resonance technique [240] [241], which again is a pure-mathematical tool. A coaxial excitation method is developed in [221], which has its physical foundation in modeling the feed current of a coaxial line leading to the microstrip. The final results, however, compared to the gap generator method, are unaffected by the method of excitation [168].

Matrix Computation and Inversion

All the elements of the matrix 4.251 are evaluated from equations 4.252, 4.253, 4.254 and 4.255 for each segment of the metalization. It is important to note the following symmetries in the impedance matrix:

$$Z_{yy}(p,q,p',q') = Z_{yy}(p',q',p,q) , \tag{4.258}$$

$$Z_{zz}(p,q,p',q') = Z_{zz}(p',q',p,q) , \tag{4.259}$$

and

$$Z_{zy}(p,q,p',q') = Z_{yz}(p',q',p,q) . \tag{4.260}$$

These symmetries are utilized to cut down on the computational effort to calculate the matrix elements of 4.251 by 50%. Based on computational experiences, computing the matrix elements consumes more than 99% of the computation time with the remaining

1% goes to the matrix solution problem. These symmetries also reduce the size of the storage array in half.

A computer code for computing these matrix elements was developed. For the case of a narrow strip of metalization, and where the discontinuity does not lead to a large y-directed current, a sub-set of this matrix can be used. For example, when characterizing a series gap discontinuity in a thin transmission line, the I_y component of current was found to be of negligible magnitude compared to the I_z component of the current. For this type of situation it is sufficient to only consider the problem

$$\left(Z_{zz}(p,q,p',q') \right) \left(I_z(p',q') \right) = \left(V_z(p,q) \right) \tag{4.261}$$

where $I_z(p',q')$ are the amplitude coefficients of the current J_z respectively. The coefficients $Z_{zz}(p,q,p',q')$ are given by 4.255. This step reduces the computational effort and time to one fourth of that required to solve the full matrix. It should be noted, that for the purpose of obtaining the scattering matrix representation, only the knowledge of J_z is required, which eliminates the need to compute J_y. A computer code for evaluating the subset system was also developed.

Once all the elements of 4.251 or 4.261 are computed, a matrix inversion routine is invoked and the unknown surface current amplitude coefficients $I_y(p',q')$ and $I_z(p',q')$ are evaluated. For this purpose, an LU-Decomposition routine for matrices with complex elements is utilized. This routine was written in C language. A complete complex algebra library in C was written and is utilized by this routine and all others used in this PhD research. The output generated by the developed LU-Decomposition routine was compared to that of *Matlab* and yielded the same results.

Curve Fitting and Extraction of the Elements of the Scattering Matrix

It is assumed that a uniform transmission line feeds a discontinuity from all ports. For a two port problem, the longitudinal currents I_{z1} and I_{z2} on ports 1 and 2 are evaluated using $I_z(p',q')$ by a transverse integration. On an input port, on a uniform transmission

line, an ideal transmission line current exists as long as the operating frequency is below the cut-off frequency of the shielding cavity. Thus the current distribution obtained can be fitted to a transmission line current model to obtain the scattering parameters. The current distribution obtained behaves like a transmission line model away from the excitation point and the discontinuity itself, (say by a distance of $d_s = \frac{\lambda_g}{4}$ from each) as shown in Figure 4.34 [169].

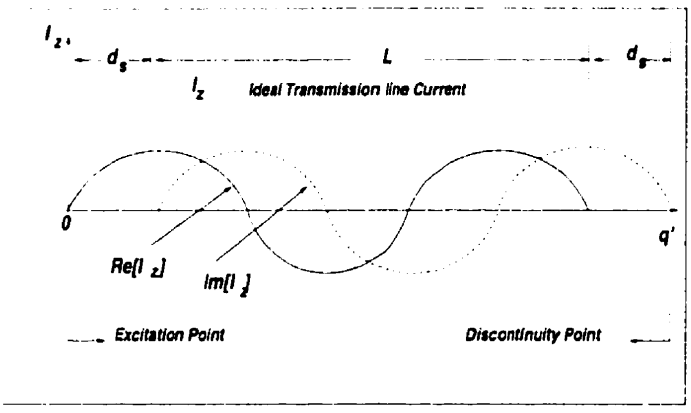

Figure 4.34: Axial current distribution along the transmission line of the input port feeding a discontinuity.

An ideal transmission line current is given by

$$I_z = I_z^+ e^{-jK_z z} + I_z^- e^{jK_z z}, \tag{4.262}$$

where I_z^+ is the incident current, I_z^- is the reflected current and K_z is the complex propagation constant. This expression is used as a fitting model to fit the data obtained from the solution of 4.251. The optimization routine used for this purpose is L-BFGS-B [224]. The error function supplied to the routine for minimization is

$$E = \left[Re(I_{zcomputed} - I_{zideal})\right]^2 + \left[Im(I_{zcomputed} - I_{zideal})\right]^2. \tag{4.263}$$

Minimizing this error function yields the unknown parameters in 4.262, namely I_z^+, I_z^- and K_z. A FORTRAN driver for L-BFGS-B was written. The driver supplies the L-BFGS-B routine with the error function and its gradients with respect to all the six

unknown parameters: I_z^+, I_z^- and K_z, both real and imaginary parts. Notice that K_z is treated here as an unknown that can be found from the optimization routine. K_z can be also computed from the uniform transmission line analysis presented earlier. Comparison of the two approaches were conducted and they show an excellent agreement. A strength of this theory is that it doesn't require the knowledge of K_z on the feed transmission lines to solve the discontinuity problem. From the information obtained by the L-BFGS-B routine, the voltage reflection coefficient for the input port, Γ_{in}, is computed as:

$$\Gamma_{in} = \frac{I_z^-}{I_z^+} e^{j2K_z(L+d_s-d_{ref})} , \tag{4.264}$$

where d_{ref} is the reference plane distance.

Scattering and Impedance Matrices

For a one port discontinuity, the scattering parameter, S_{11} is given by the reflection coefficient of equation 4.264. For a symmetric two-port geometry, two excitations are required: an even excitation and an odd excitation. For an even excitation, the gap generators of 4.257 are equal to one on both ends, and zero everywhere else on the metalization. For an even excitation, the gap generator of 4.257 is equal to 1 at one end and to -1 at the other end, and zero everywhere else on the metalization. Using these two different excitations, two different reflection coefficients are computed: ${\Gamma_{in}}^{even}$ and ${\Gamma_{in}}^{odd}$. The matrix elements, and the LU-Decomposed matrix are computed only once. Only the excitation vector is changed and then multiplied with the same inverse matrix. Using ${\Gamma_{in}}^{even}$ and ${\Gamma_{in}}^{odd}$, the normalized input impedance for the even and odd excitation are derived from:

$${z_{in}}^{even} = \frac{1+{\Gamma_{in}}^{even}}{1-{\Gamma_{in}}^{even}} \tag{4.265}$$

$${z_{in}}^{odd} = \frac{1+{\Gamma_{in}}^{odd}}{1-{\Gamma_{in}}^{odd}} \tag{4.266}$$

From microwave circuit theory, and considering a two-port network symmetric impedance matrix representation, the following relationship between the impedance matrix elements, Z_{11} and Z_{12}, and ${z_{in}}^{even}$ and ${z_{in}}^{odd}$ are obtained:

$$Z_{11} = \frac{{z_{in}}^{even}+{z_{in}}^{odd}}{2} \tag{4.267}$$

$$Z_{12} = \frac{{z_{in}}^{even} - {z_{in}}^{odd}}{2} \tag{4.268}$$

The scattering matrix, $[S]$, is related to the impedance matrix,$[Z]$ through

$$[S] = \begin{pmatrix} S_{11} & S_{12} \\ S_{21} & S_{22} \end{pmatrix} = [Z - U][Z + U]^{-1} , \tag{4.269}$$

where $[U]$ is the unitary matrix. In an explicit form, the above equation can be written as

$$[S] = \begin{pmatrix} S_{11} & S_{12} \\ S_{21} & S_{22} \end{pmatrix} = \begin{pmatrix} Z_{11} - 1 & Z_{12} \\ Z_{12} & Z_{11} - 1 \end{pmatrix} \begin{pmatrix} Z_{11} + 1 & Z_{12} \\ Z_{12} & Z_{11} + 1 \end{pmatrix}^{-1} \tag{4.270}$$

which leads to the following relations between the Impedance matrix elements and the scattering matrix elements.

$$S_{11} = S_{22} = \frac{{Z_{11}}^2 - {Z_{12}}^2 - 1}{{Z_{11}}^2 - {Z_{12}}^2 + 2Z_{11} + 1} , \tag{4.271}$$

$$S_{12} = S_{21} = \frac{2Z_{12}}{{Z_{11}}^2 - {Z_{12}}^2 + 2Z_{11} + 1} . \tag{4.272}$$

Both these representations are utilized in the forthcoming study. The impedance matrix representation is used to obtain more accurate parameters for the π equivalent circuit of Figure 2.7. This equivalent circuit models the optically excited series gap discontinuity. The effect of the optical excitation on the transmission coefficient of the gap being illuminated is studied by examining S_{12} and the return loss of the switch is examined by considering S_{11}.

Convergence Considerations

Detailed convergence and verification studies were conducted in [169] for the same theory but for the special case of a two layered substrate. These were also conducted in [168] for a closely related analysis. As argued earlier, the same convergence considerations remain valid for the case of N layers of dielectrics. These criteria were tested and verified for the N layers case during the course of this research on numerous cases.

The convergence criterion for a uniform line is simple and depends only on the line width and the shielding guide dimensions. This criterion is given in 4.195. For discontinuity analysis, the convergence criteria depend on the modal summation limits M and N, the subsection highest indices P and Q, the cavity dimensions a, b and c, the subsection lengths l_z and l_y, and the subsection wavenumbers h_y and h_z.

These convergence criteria can be summarized as follows:

1. The dimensions of the enclosing cavity must be such that its lowest cut-off frequency is higher than the highest frequency with which the discontinuity is excited. Otherwise, if the cavity were to resonate to a certain frequency, coupling could occur between the microstrip circuit and the resonant cavity.

2. choosing the subsection wavenumbers h_y and h_z to be approximately equal to the phase constant of the microstrip feed lines yield the best results. This is based on extensive numerical testing carried out in [168].

3. To guarantee convergent accurate results, and due to the nature of the overlapping sinusoidal basis functions, the maximum value for the subsection lengths l_z and l_y is governed by

$$h_z l_z \, , h_y l_y \leq \frac{\pi}{2} \, . \tag{4.273}$$

4. Based on computing experience, the relationship between the modal summation limits M and N, and the subsection highest indices P and Q should be such that

$$M \geq 1.25P \text{ and } N \geq 1.25Q \, . \tag{4.274}$$

This minimum summation criterion was also observed with other studies of shielded microstrip such as [174] and [221].

5. For accurate results, the values of l_y and l_z should satisfy the following upper and lower bounds:

$$\frac{\lambda_g}{175} \leq l_y \, , l_z \leq \frac{\lambda_g}{25} \, , \tag{4.275}$$

where λ_g is the guided wavelength. If l_y and l_z are greater than $\frac{\lambda_g}{25}$, inaccurate results for the current distribution are obtained since there aren't enough sampling points per wavelength. If l_y , l_z are smaller than $\frac{\lambda_g}{175}$, inaccurate results for the current distribution are again obtained. This time, the source of error is that the adjacent matrix elements of 4.251 have very close values, leading to a reduced numerical accuracy when computing the matrix inverse. This criterion is not absolute, but recommended.

These criteria were tested and followed closely for all the studies conducted in this research.

A Series Gap Discontinuity Analysis

In this section, a sample test case is presented to demonstrate the theory developed for the discontinuity analysis. As an example of a discontinuity, a series gap is considered. Such series gap is the proposed topology of optically controlled microstrip switch to be studied in chapter six.

Figure 4.35 depicts the frequency dependence of the normalized propagation constant $\frac{\beta}{k_o}$ for a transmission line of width W= 0.5 mm and a silicon substrate of thickness 0.4 mm and relative permittivity ϵ_r=12. It is assumed that this is the topology of a microstrip line to be used for an optically controlled switch. An optical excitation power level that leads to an effective resistivity $\rho = 1.2\ \Omega - m$ for a thickness of 0.2 mm in the upper half of the substrate is assumed. The shielding rectangular waveguide dimensions are $a = 6\ mm$ and b= 1.5 mm. The cut-off frequency for the shielding guide is $\approx$ 25 GHz. Computations were conducted using two values for M: M=2200 modes and M= 5000 modes. The two results fully overlap. These curves are obtained using the dispersion analysis for a continuous transmission line developed in this thesis. The attenuation constant α versus frequency f for this transmission line is shown in Figure 4.36.

The discontinuity analysis developed in this thesis is utilized to study a series gap of length 0.1 mm in this transmission line. The matrix elements of equation 4.251 are evaluated using the method of moments (MOM). The MOM Computation is conducted using

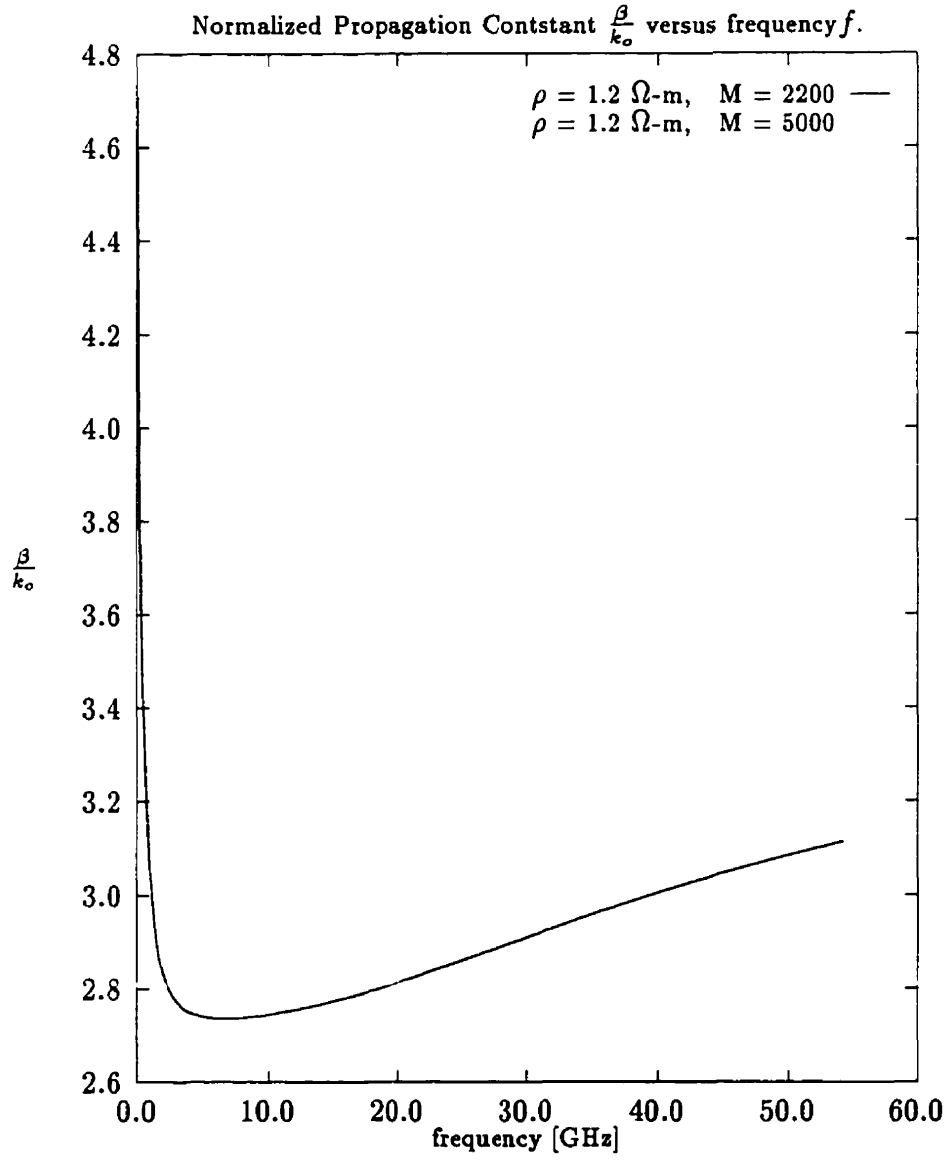

Figure 4.35: The normalized propagation constant $\frac{\beta}{k_o}$ versus frequency f [GHz] for a transmission line of width W= 0.5 mm, and a silicon substrate (ϵ_r=12) of thickness 0.4 mm. It is assumed that optical excitation leads to an effective resistivity, $\rho = 1.2\ \Omega - m$ for a thickness of 0.2 mm in the upper half of the substrate. Shield dimensions: a = 6 mm, and b= 1.5 mm. Computation conducted using M=2200 and 5000 modes.

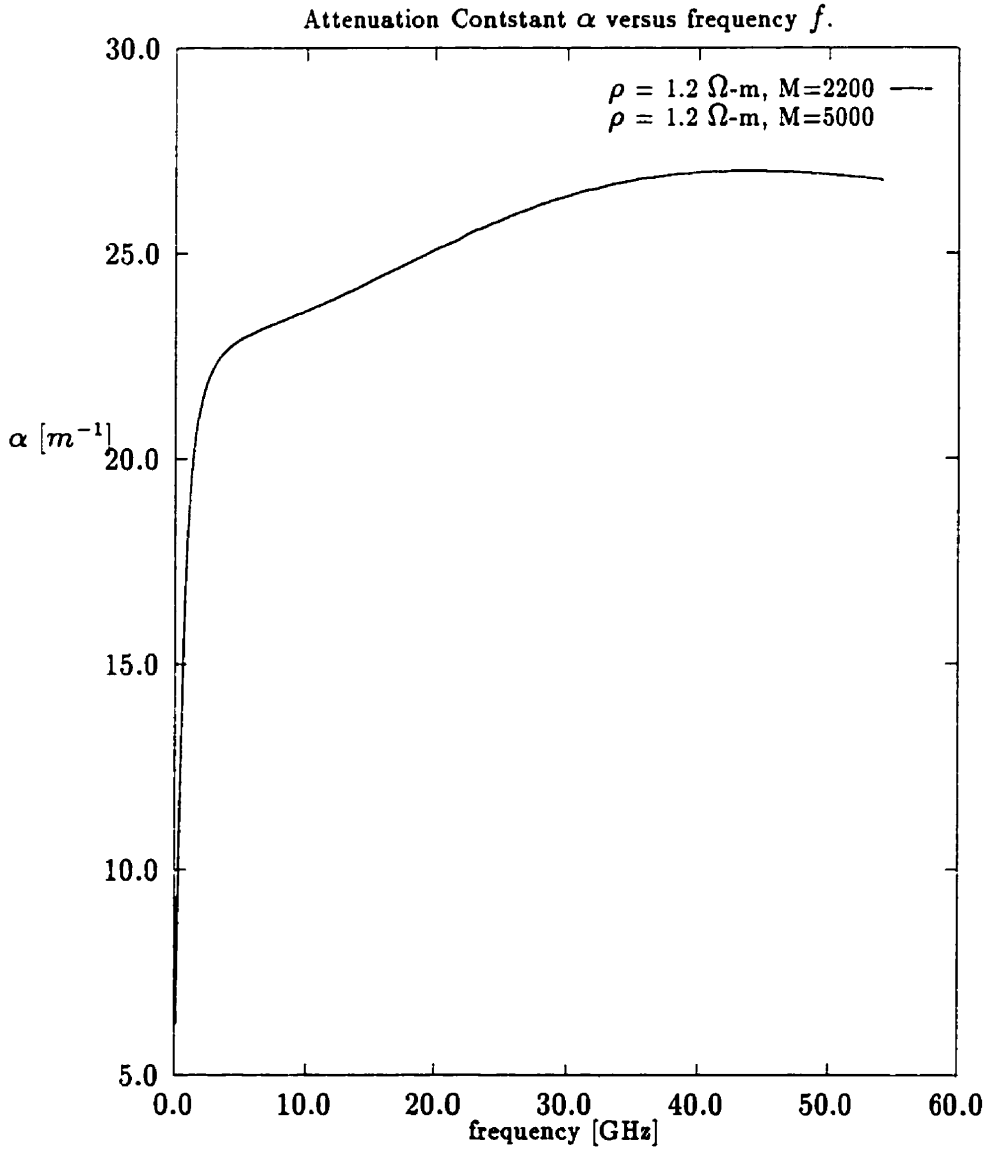

Figure 4.36: The attenuation constant, α, versus frequency, f [GHz], for the transmission line with parameters as per Fig. 4.35

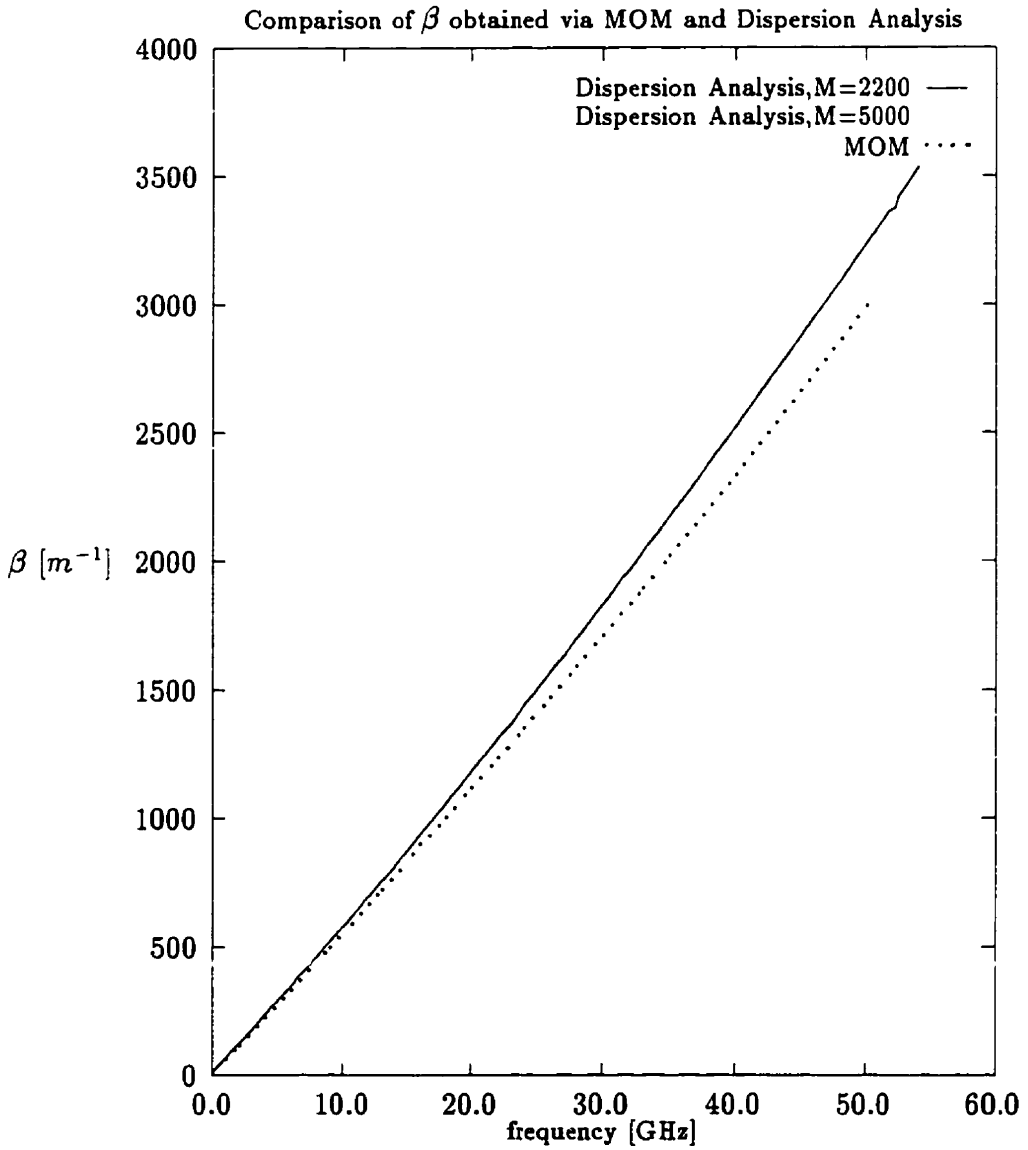

Figure 4.37: Comparison of propagation constant β obtained via the Method of Moments (MOM) to that obtained via direct dispersion analysis computation, versus frequency f [GHz], for the transmission line described in Fig 4.35. MOM Computation conducted using MxN=300x300 modes. Parameter extraction obtained using curve fitting to 85 sampling points.

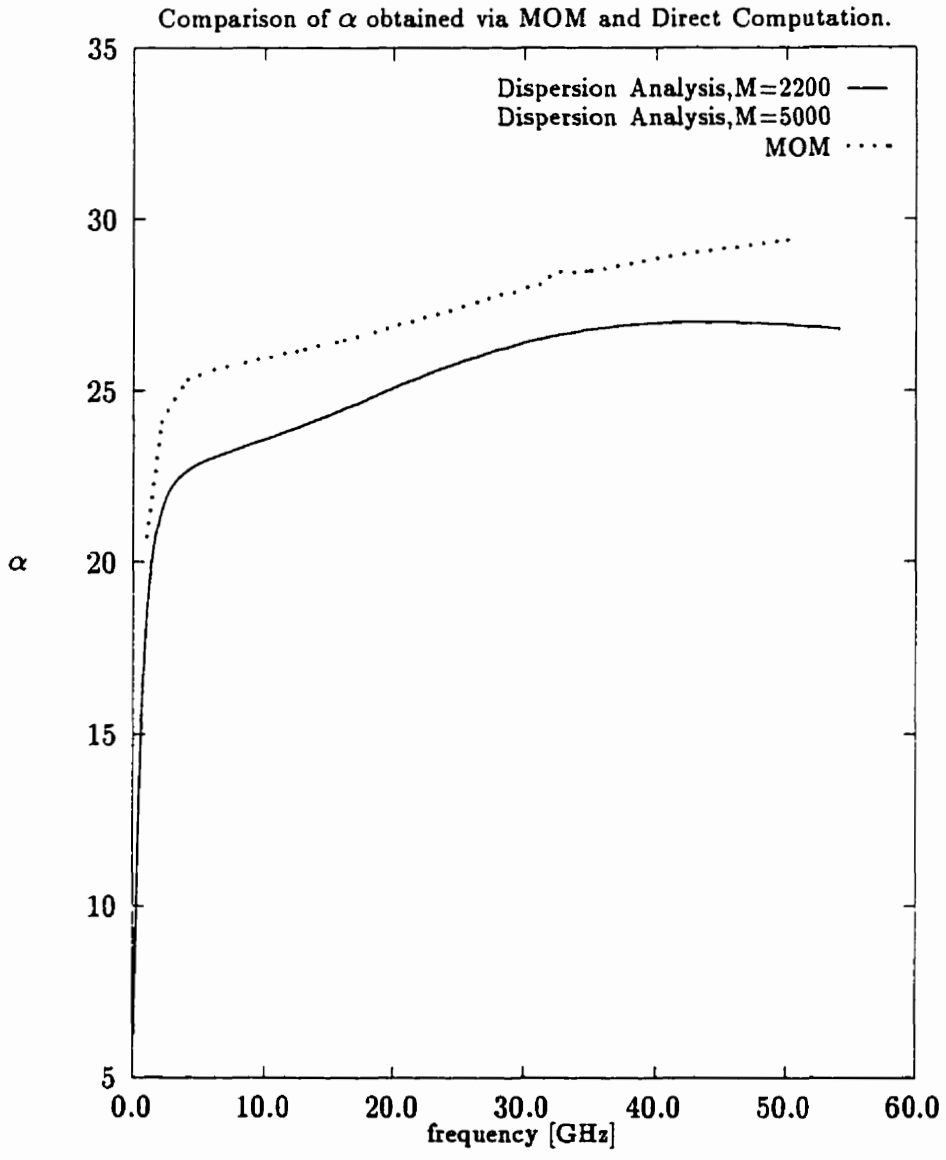

Figure 4.38: Comparison of the attenuation constant α obtained via the Method of Moments (MOM) and that obtained via direct dispersion analysis computation versus frequency, f [GHz]. All parameters are as per Fig 4.35.

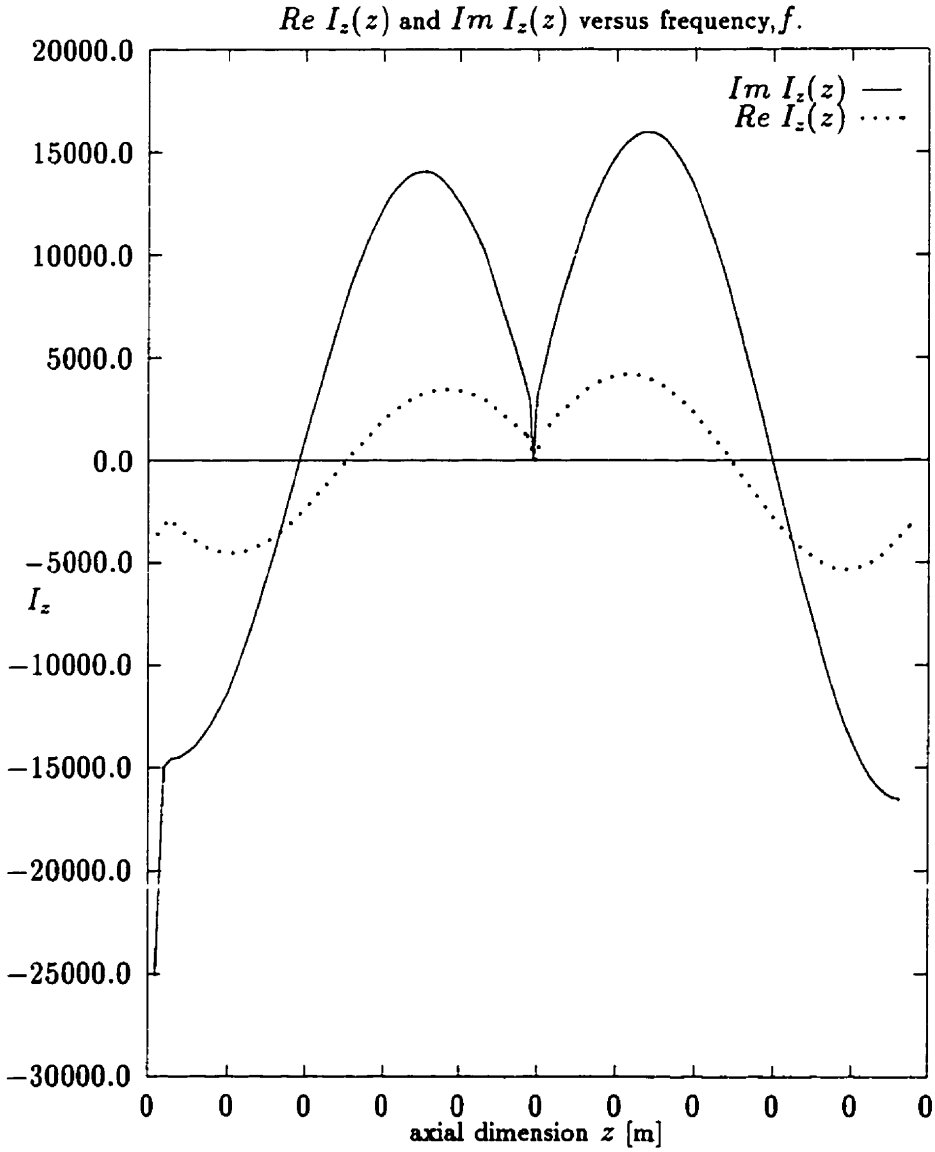

Figure 4.39: Axial current, $I_z(z)$, versus z at f= 9 GHz for an even excitation of a series gap of length 0.1 mm. All parameters as per Fig. 4.35

M= 300 and N=300 for a cavity of length c =20 mm, with subsection discretization of P = 3 and Q =200. These dimensions and parameters lead to l_y = l_z =0.1 mm. h_y and h_z were chosen to approximately match the propagation constant computed in Figure 4.35. Hence, all convergence criteria were met. Using even and odd excitation, as described earlier, two distinct current distributions are obtained. Those current distributions are curve-fitted to a transmission line model, where incident and reflected currents are extracted, along with a value for β and α. These parameters derived from the transmission line model are used, as explained earlier, to characterize the gap in the form of a scattering matrix or an impedance matrix. Parameter extraction was obtained using curve fitting to 85 sampling points utilizing the L-BFGS-B optimization routine.

The propagation constant β obtained via the method of moments (MOM) from the discontinuity analysis is compared to that obtained using the dispersion analysis developed in this thesis with excellent agreement at lower frequencies and good agreement at higher frequencies (within 7%) The comparison for the attenuation constant α is shown in Figure 4.38. Discrepencies are due to difference in model between an infinite uniform transmission line and a short segment of that line enclosed in a cavity.

A typical axial current distribution $I_z(z)$ along the propagation direction z at f= 9 GHz for the given transmission line with a series gap of length 0.1 mm is shown in Figure 4.39 for the case of even excitation. The real component of the current is the one associated with the loss in the transmission line. For a lossless transmission line, the axial current is 90° out of phase with the excitation.

The magnitude of the scattering matrix elements, S_{11} and S_{12}, versus frequency is shown in Figure 4.40 for the given series gap. The phase of S_{11} and S_{12} versus frequency is depicted in Figure 4.41. This structure is symmetric. Alternatively, the impedance matrix elements z_{11} and z_{12} versus frequency for this structure are depicted in Figures 4.42 and 4.43. The real components of the impedance matrix are associated with the loss in the transmission line. For a lossless transmission line, the impedance matrix elements are imaginary. For these results, the reference planes on both sides of the discontinuity are

placed at a distance of a quarter wavelength from the center of the discontinuity.

4.5 Conclusion

In this chapter, a rigorous theory for analyzing shielded transmission line structures and their discontinuities was developed. The present analysis can model multi-layered lossy substrates and multi-conductor structures.

The formulation utilizes the concepts of the Green's function in the space domain and the principle of scattering superposition to obtain the propagation characteristics. For a uniform microstrip line, the general shape of the current distribution is known, and is deployed in the EFIE to obtain the dispersion equation. In doing so, the computationally expensive step of using the Method of Moments (MOM) is avoided. The dispersion relation is a complex equation of complex roots. Complex root searching is conducted using *Müller* method and the roots of the dispersion equation are obtained. These are the complex propagation constants for the microstrip propagating modes. Once the propagation constant is known, the fields of the transmission line propagating mode are obtained, and are used to compute the line characteristic impedance through a power/current relationship. Samples of the results obtained using this method were presented.

To analyze a discontinuity, the unknown surface current maintained on the microstrip discontinuity is expanded in terms of basis functions. The electric field components in the plane of the discontinuity region are then written in terms of the current. Imposing the condition that the component of the electric fields tangential to the metalization is zero, (E_{tan}=0), yields an integral equation known as the Electric field integral equation (EFIE). The moment method is applied to the EFIE to obtain a system of linear equations. An LU-Decomposition routine is deployed in order to obtain the matrix inverse. The elements of this matrix are complex in general. For a given voltage excitation of the discontinuity, a current distribution profile can be obtained. To obtain the discontinuity characteristics, this current distribution profile is fitted to transmission line current model. This curve

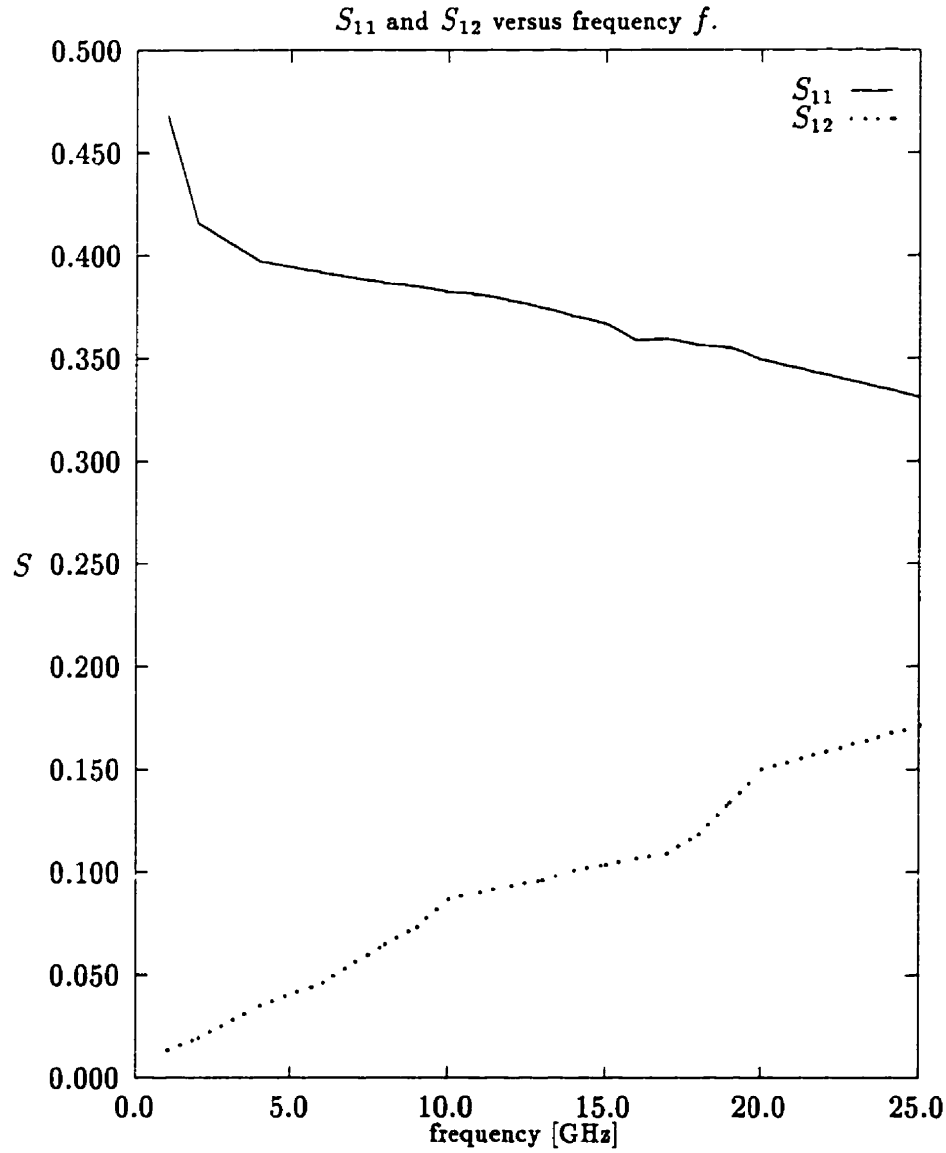

Figure 4.40: The scattering matrix elements S_{11} and S_{12} versus frequency, f [GHz]. All parameters are as per Fig 4.35.

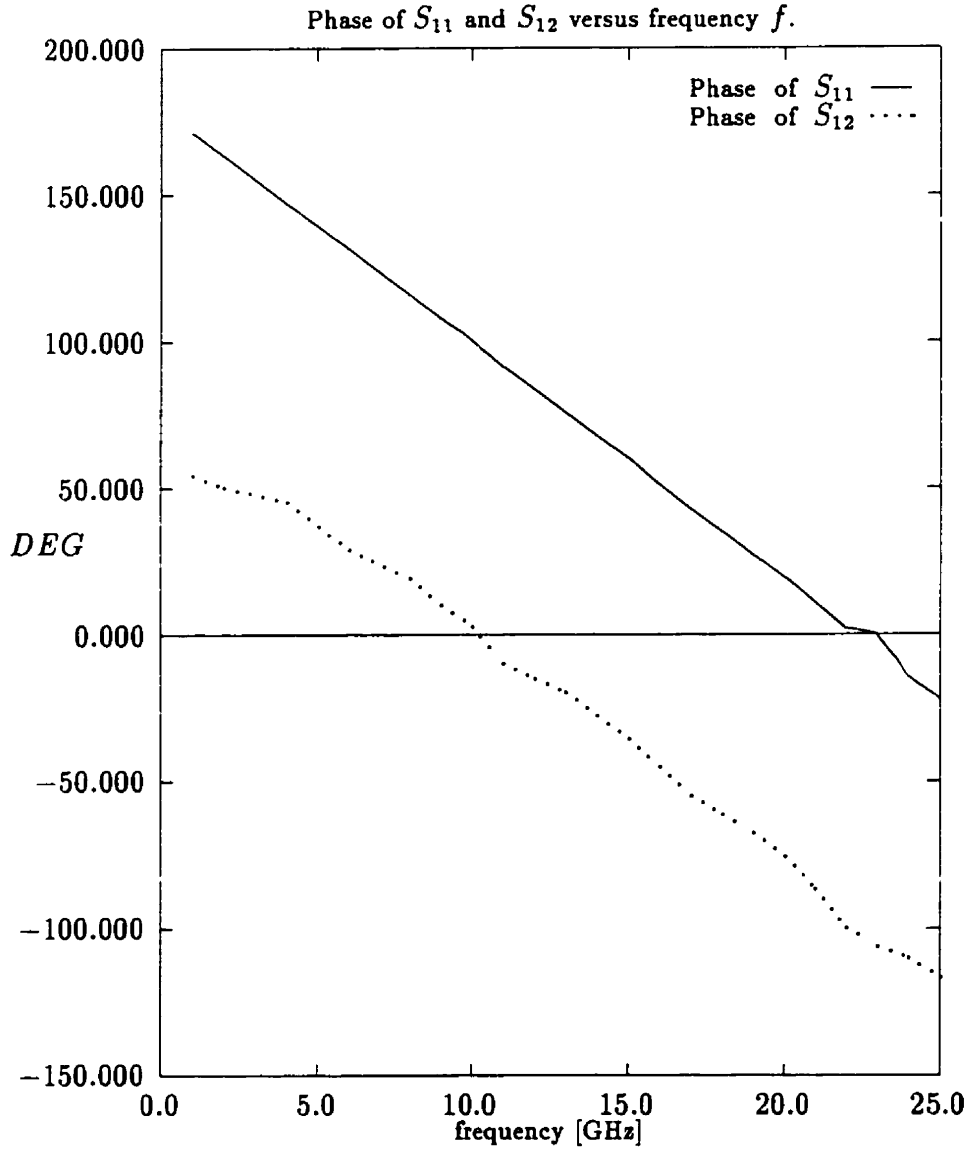

Figure 4.41: The phase of S_{11} and S_{12} versus frequency f [GHz]. All parameters are as per Fig 4.35.

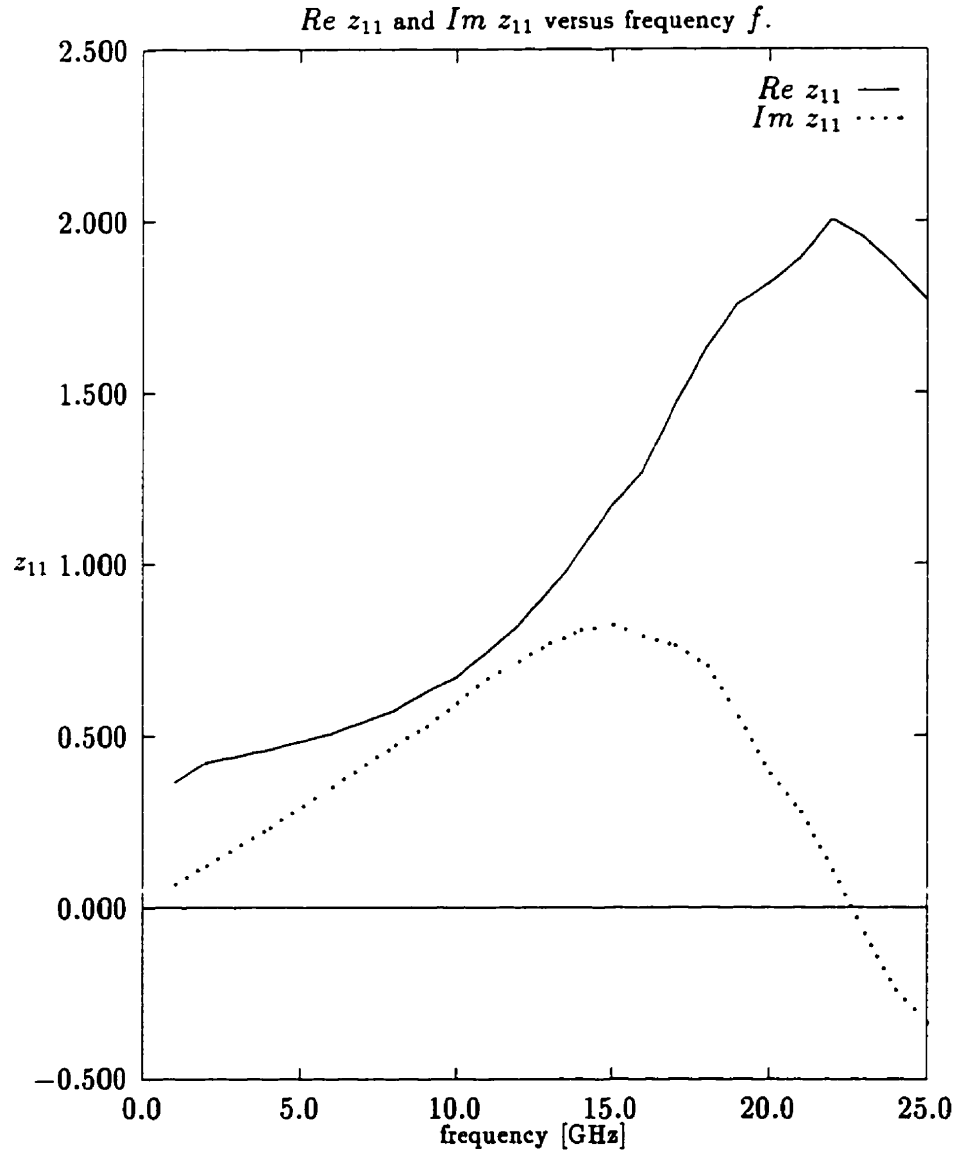

Figure 4.42: The impedance matrix element z_{11} versus frequency f [GHz]. All parameters are as per Fig 4.35.

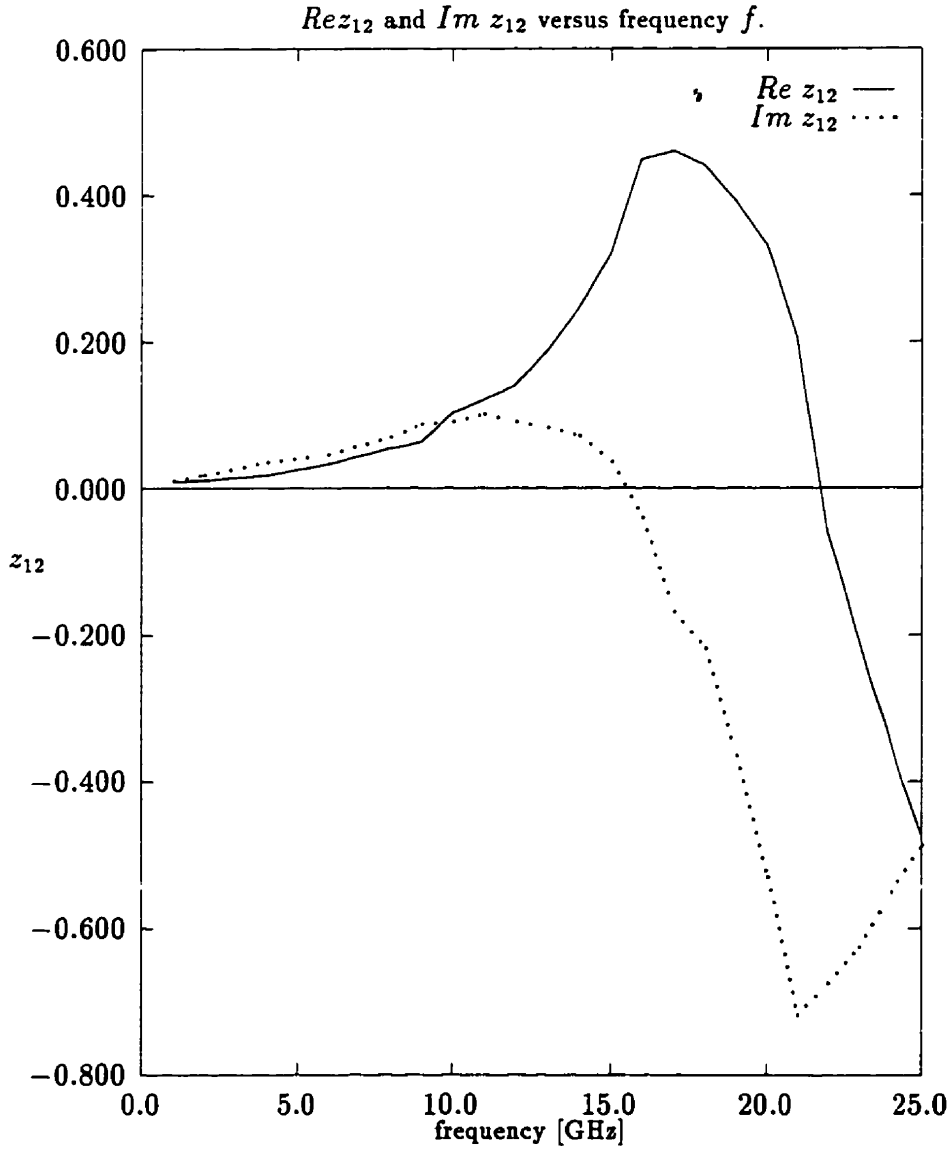

Figure 4.43: The impedance matrix element z_{12} versus frequency f [GHz]. All parameters are as per Fig 4.35.

fitting is used for the extraction of the incident and reflected current amplitudes at the discontinuity, as well as the complex propagation constant. The computer optimization code L-BFGS-B was used for the curve-fitting task. Using a 2-port network representation, the incident and reflected currents are used to compute the scattering matrix and the impedance matrix representing the discontinuity.

The obtained semi-analytical expressions were developed into computer codes, and were used to conduct accurate modeling of a variety of structures. The validity and accuracy of this method was established through comparison with other published data for a wide range of structures. Convergence consideration and criteria were outlined and verified.

In Chapter Five, the above analyses are used to conduct accurate modeling of a series gap discontinuity in the microstrip line. This series gap is a model of the microwave switch. The gap transmission behavior is studied for varied substrate conductivity, gap separations, and frequency ranges. The substrate conductivity represents the effect of photo-excitation generated by the optical control element. The current approach of modeling optically controlled microwave switches using equivalent circuit models based on quasi-TEM assumptions is assessed and compared to the more accurate Green's function formulation. The domain of validity of these simplified models is defined.

Chapter 5

Overall Device Performance Characteristics

5.1 Introduction

In this chapter, a detailed design of an integrated optically switched microstrip gap is conducted. The design procedure goes through all the necessary steps to design the optical and microwave sections of the device.

In the previous chapters, a systematic knowledge base for the technology of optical guided wave control of microwave devices was developed. As shown, a theory for the accurate modeling of the microstrip switch was developed. The switch is a series gap in a microstrip line on top of several layers of lossy substrate materials. The entire device is enclosed in a shielding cavity. This theory was presented in Chapter 4, along with its verification and convergence studies. This tool is used here to model the microstrip circuit behavior under optical excitation.

Modeling the optical power propagation in the structure was presented in Chapter 3. The algorithm presented in Chapter 3 is used in this chapter to compute the modal fields that can propagate in such a highly lossy optical structure. Simulation tools such as

the Vector Finite Difference Time Domain (VFDTD) and the Vector Beam Propagation Method (VBPM) were applied to the optical propagation problem. The modeling issues related to the optical guiding system and optical absorption were discussed in chapter 3.

The application of the theories and tools of chapters 3 and 4 makes it possible to accurately model the proposed integrated device, subject to the design issues and requirements discussed in chapter 3.

In what follows, an optical guided-wave controlled microwave switch will be characterized quantitatively and accurately. The first step in this process is to design the microwave structure in terms of various substrate layers and parameters with due consideration to the optical guiding system buried in the substrate. The propagation characteristics of the transmission line under different substrate conductivities will be computed. These lead to the choice of a microstrip mode of operation that helps minimize the optical power required to achieve the desired switching. The choice of the mode of operation of the transmission line ensures a spatially limited microwave signal that can be switched with a much reduced optical power requirement.

Next, a gap in the microstrip metalization will be considered. The optically generated carriers in the substrate leads to a change in the substrate conductivity and to a certain switching behavior for the microwave gap. The effect of various parameters such as the gap length, the operating frequency, and substrate conductivity on the switching performance of this device is studied.

Earlier studies in this area were conducted using approximate models and utilized only bulk illumination techniques. The present work is pioneering in two aspects: in terms of considering the integrated device, and in terms of conducting an accurate and in-depth modeling approach. The present work also addresses some practical aspects of the device fabrication technology and incorporates that into the electromagnetic model.

Using the developed accurate model, the conventional approach of modeling optically controlled microwave switches using quasi-TEM assumptions is assessed and compared to the more accurate Green's function formulation. The domain of validity of these simpli-

fied models is defined. It is established that the quasi-static models are only valid at low frequencies, and for very high optical injection levels. These two conditions ensure that an optically illuminated gap will have a resistivity which is much smaller than the accompanying shunt capacitances. For practical optical excitation levels at higher frequencies, effects of these capacitances become significant, and the more accurate frequency-dependent modeling approach of this thesis becomes necessary.

5.2 The Device Structure

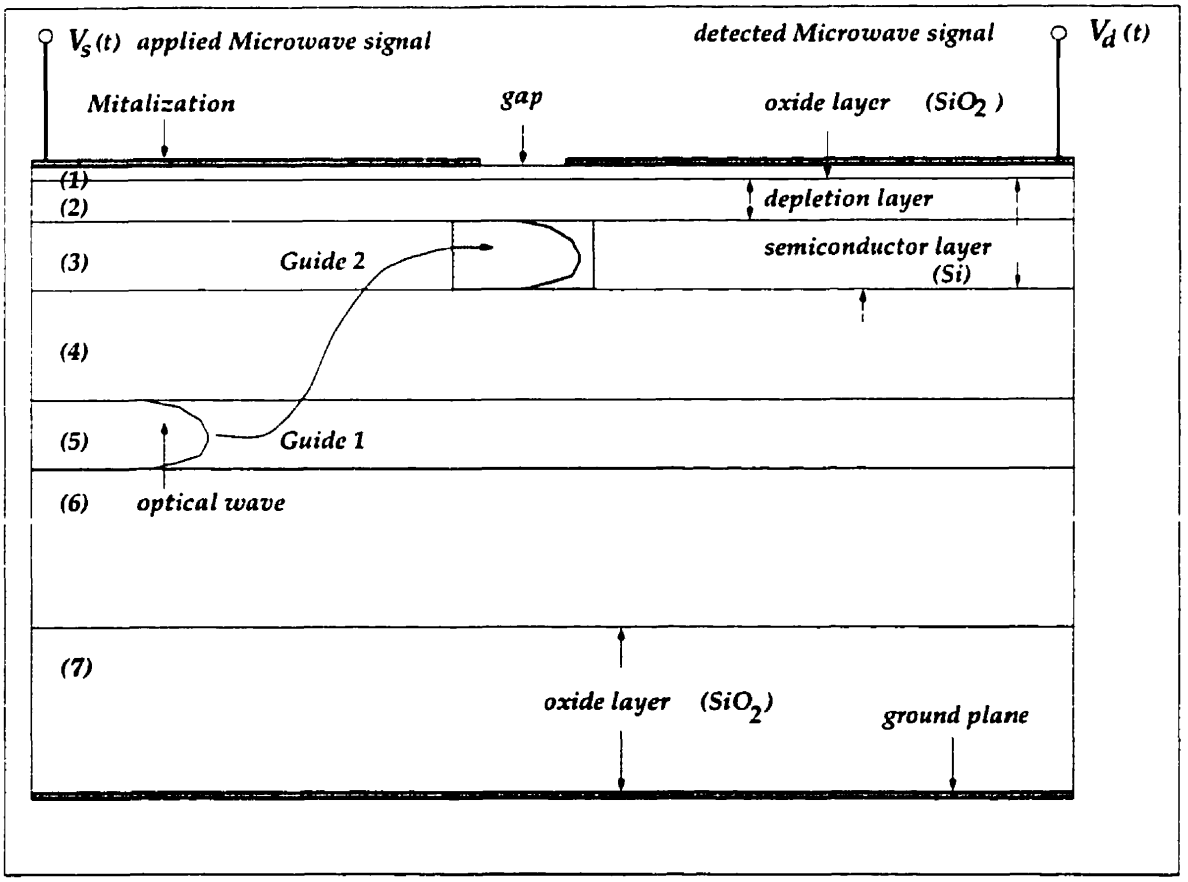

Figure 5.1: A schematic cross-section of an optical guided wave controlled microwave switch showing all the substrate layers.

Figure 5.1 show a schematic cross-section of proposed device structure: a microstrip transmission line comprised of a ground plane and a top metal strip situated above a multi-layered substrate. Normally, gold is used for these metallic strips. Just below the metalization, a thin oxide layer is grown. This layer is denoted by layer 1 in Figure 5.1. Normally, a semiconductor surface will be oxidized during the fabrication process to prevent the self oxidation of the surface, known as the *native* oxide. The native oxide grows in a non-uniform manner whose characteristics are unreliable. Also, the adhesion between the native oxide and the layer above it can be very weak. To avoid the growth of a native oxide, a uniform oxide layer is grown on top of the semiconductor as a part of any standard fabrication technology. The depth is this layer is usually chosen in the 1-20 μm range. Thinner oxide thicknesses are also possible, as long as they prevent the irregular self-oxidation of the semiconductor surface. It is advantageous for the proposed devices to make this layer as thin as possible. This maximizes the interaction of the optically-generated carriers in the semiconductor region with the microwave fields, as it brings the semiconductor region closer to the metalization. In the forthcoming analysis, the width of this oxide layer is set to 1 μm. Previous studies of free-space optical illumination of microstrip gaps such as [13] [89] [22] ignore this layer alltogether. The modeling of the switch in these studies assumes the metallic strip to be right above the semiconductor substrate. Hence, the mathematical model obtained projects a photo-generated conductance whose magnitude is more than an order of magnitude higher than the measured one. This is attributed to a variety of reasons that were discussed in chapters 2 and 3, along with the fact that it is impossible to realize this metal-semiconductor arrangement without the intermediate oxide layer.

In Figure 5.1, region 3 is the semiconductor layer, where optical energy is absorbed. Region 2 is the depletion region that forms at an insulator-semiconductor interface. The effect of this layer on the transmission characteristics of MIS structures have been discussed in chapter 4. Again, earlier studies ignored such an effect, despite its prominent effect on the propagation characteristics. For the study presented in this chapter, the width of this layer was calculated to be around 1μm or less as explained in the following

Material	λ= 1.55 μm	λ= 0.83 μm	f = 20 GHz
Silicon (Si)	3.4764 -j 1.07x10^{-9}	3.6810 -j 0.006	3.3701 -j 1.40x10^{-3}
SiO_2(Glass)	1.4440 -j 0	1.4529 -j 0	1.5500 -j 7.96x10^{-3}
SiO_2(Type α,Crystal)	1.5277 -j0	1.5377 - j 0	2.1063 -j 7.96x10^{-4}
Gallium Arsenide $GaAs$	3.3737- j 0	3.6660 -j 0.0789	3.587- j 1.01x10^{-3}
Gold (Au)	0.5590 -j 11.5	0.188 -j 5.39	σ=4.098x10^{7}℧/m

Table 5.1: Complex refractive index of silicon, silica, $GaAs$ and gold at the optical and microwave frequencies of interest.

section.

The layers denoted by 4, 5 and 6 in Figure 5.1 are designed in such a way that the refractive index of each layer is slightly different to realize an optical waveguide whose core is layer 5. Optical energy is propagated in the lower guide where it couples into the absorbing layer (region 3) just below the gap. The width of layer 4 dictates the strength of the coupling between the two guides, which in turn dictates the photo-generated carrier profile in the gap region. These issues were discussed in Chapter 3. The rest of the substrate (layer 7) is a low loss dielectric. The study presented here assumes a silica-silicon system. Alternate designs can use $GaAs$-based structures which have an inherent high switching speed. $GaAs$ has a much smaller minority carrier life time than crystalline silicon, and hence it has faster recombination and faster switching performance. Means to enhance the speed of response in silicon and other materials were discussed in detail in chapter 2.

Table 5.1 lists the complex refractive index of silicon (Si) ,silica (SiO_2), gallium arsenide ($GaAs$) and gold at the optical and microwave frequencies of interest. These data were obtained from [242]. The band gap of silicon is 1.124 eV at 300°K. The wavelength of a 1.124 eV quantum is 1.1 μm. The band gap of $GaAs$ is 1.424 eV at 300°K. The wavelength of a 1.424 eV quantum is 0.87 μm [24]. Incident optical energy with a wavelength

Layer	Material	Width (μm)	n at λ= 0.83 μm	n at f = 20 GHz
1	SiO_2	1.0	1.4529 -j 0	1.5500 -j 7.96×10^{-3}
2	Si-Dep.Reg.	0.1-1.0	3.6810 -j 0	3.3701 -j 0
3	Si	1.0	3.6810 -j 0.006	3.3701 -j n_r''
4	Si [low-loss]	0.1-1.0	3.6700 -j 0	3.3600 -j 7.96×10^{-4}
5	Si [low-loss]	1.0	3.6810 -j 0	3.3701 -j 7.96×10^{-4}
6	Si [low-loss]	5.0	3.6700 -j 0	3.3600 -j 7.96×10^{-4}
7	SiO_2	300.0	1.4529 -j 0	1.5500 -j 7.96×10^{-3}

Table 5.2: The Width and Complex Refractive Index of All The Layers Comprising The Substrate of The Proposed Structure.

shorter than 1.1 μm is absorbed in silicon, and those with a wavelength shorter than 0.87 μm are absorbed in $GaAs$. Here, an incident optical energy of a wavelength λ= 0.83 μm is assumed throughout. Vital data about these materials are listed in table 5.1.

5.3 Optimized Transmission Line Design

The widths of all the layers comprising the substrate of the structure depicted in Figure 5.1 along with their refractive indices at the optical and microwave frequencies of interest are shown in table 5.2. The imaginary part of the refractive index of layer 3 in the microwave frequency range n_r'' is variable depending on the level of optical excitation. The imaginary component of the the refractive indices of the other layers at the microwave frequencies amounts to a microwave signal attenuation of less than 0.005 dB/mm and hence is ignored. Further, gold microstrip conductor losses for a line of width 500 μm is 0.01 dB/mm at 1 GHz and reduces at higher frequencies [225]. Hence, the microstrip line is assumed to be made of a perfect conductor.

The choice of these dimensions were deduced based on several design considerations.

The width of the oxide layer (layer 1) is assumed here to be 1 μm. The width of the oxide layer was minimized in order to maximize the interaction between the optically-generated carriers in the semiconductor region and the microwave signal. This is achieved by placing the semiconductor region in a close proximity to the metallic strip. Oxide layers of less than 1 μm are also possible.

The depletion region (region 2) width was computed using the expressions presented in Chapter 4 assuming microwave signal levels around 1V. For silicon, using equation 4.196, the depletion region thickness is $\approx \frac{2[\mu m]}{\sqrt{\sigma}}$, where σ is the photo-generated conductivity in region 3. A width of 1 μm is the worst case value given the conductivity level requirement of these switches. The values of these conductivity levels are discussed later in this section.

The width of the optical guide of region 3 was chosen based on the following justification. The design objective is to minimize the optical power required to obtain the desired switching feature. By limiting the spatial extent of the microwave fields to a small depth, only a moderate optical power level is required to provide a high photo-generated carrier density within this depth. For a thin layer 3 with a high photo-generated carrier density, and hence high optically-induced conductivity, the mode of propagation of the microwave signal in the proposed switch is designed to be the skin-effect mode. This can be deduced from the figures of merit presented in chapter 4 (section 4.4.4).

For this mode of operation, and as explained in chapter 4, the microwave fields will be essentially localized in regions 1 and 2 only and shielded from the rest of the substrate, as the highly conductive region of layer 3 acts as a conducting ground plane. For comparison, the Quasi-TEM mode of operation, where the microwave fields extends throughout the substrate, would require a much higher optical energy levels to achieve a photo-generated carrier density capable of realizing the proposed switching. For the skin-effect mode, however, a photo-absorbing layer of width 1 μm is sufficient to achieve the desired switching. Table 5.3 shows the effect of varying the conductivity σ of layer 3 on the mode of operation of the transmission line.

As shown in this table, for conductivities higher than 1000 $\mho$/m, and for the above

σ [℧/m]	1.0	10.0	100.0	1000.0	6700.0
f_e [GHz]	1.327	13.266	132.66	1326.6	8887.9
f_s [GHz]	0.028	0.281	2.806	28.06	188.0
f_d [GHz]	2748.0	274.8	27.48	2.7	0.41
f_o [GHz]	0.028	0.281	2.627	3.539	0.613
Slow Wave Mode	$f \leq 0.01$	$f \leq 0.10$	$f \leq 0.8$	$f \leq 1.0$	$f \leq 0.2$
Quasi-TEM Mode	$f \geq 2.0$	$f \geq 20.0$	$4 \leq f \leq 27$	$1 \leq f \leq 2.7$	$0.2 \leq f \leq 0.6$
Skin Effect Mode	-	-	$f \geq 100$	$f \geq 10$	$f \geq 1.6$

Table 5.3: **The Effect of varying the conductivity σ of layer 3 on the mode of operation of the transmission line.**

noted dimensions, the device is operated in the skin effect mode of operation, for all frequencies of interest, i.e. those in excess of 10 GHz. This conductivity level is quite reasonable given the limited width of region 3. The ability to limit optical field extent is one of the major strengths of the proposed optical guided-wave device.

Having decided on the conductivity level required for the optimum operation of the device, we proceed to compute the optical energy requirement. The conductivity σ of layer 3 in Figure 5.1 is proportional to the number of photo-generated carriers n and is given by

$$\sigma = ne\mu \ , \tag{5.1}$$

where μ is the carrier mobility, and e is the electron charge. In turn, the number of photo-generated carriers is related to the absorbed optical power P_{abs} given by

$$P_{abs} = n \ V \ h \ \nu = (n * V)\frac{hc}{\lambda_{opt}} \ , \tag{5.2}$$

where h is Planck's constant, ν is the optical frequency, V is the volume of the gap region, c is the speed of light, and λ_{opt} is the optical wavelength. Hence, the conductivity σ is

related to the optical power absorbed by

$$\sigma = \frac{e\mu\lambda_{opt}}{Vhc} P_{abs} \ . \tag{5.3}$$

Hence, the imaginary part of the refractive index of layer 3 is given by

$$\epsilon_r'' = \frac{-\sigma}{\omega_{mic}\epsilon_o} = \frac{-e\mu\lambda_{opt}P_{abs}}{Vhc\omega_{mic}\epsilon_o} \ . \tag{5.4}$$

where ω_{mic} is the microwave radian frequency. For silicon, the hole mobility μ = 505 cm^2/V-s at 300 K. At an incident optical wavelength of 0.83 μm, each 1μwatt of absorbed optical power in the volume of the gap yields a change of conductivity of 6.7558x10^3 $\mho$/m (ρ= 1.48x10^{-4}). Typical gap dimensions are a length of 100-1000 μm in a 500 μm-wide transmission line whereas the depth of the optical field is 1 μm. Hence the gap volume is $\approx$ 5x10^{-14} - 5x$10^{-13}m^3$. The overall change in the resistance of the gap, due to a 1μW of absorbed optical power reduces this resistance to 0.3 Ω for a 100 μm long gap, and 3.0 Ω for a 1000 μm long gap. The characteristic impedance of a line of width 500 μm on top of the substrate characterized above is about 30 Ω in the frequency ranges of interest, as discussed later. This makes the gap almost a short circuit under optical excitation conditions as those described above. For comparison, convertional devices have an interaction depth $\frac{1}{\alpha}$= 125 μm, which increases the amount of optical power requirement by two orders of magnitude [89].

5.4 Optical System Design

Design of the optical component of the device was conducted using VBPM and VFDTD. VBPM is less computationally demanding than VFDTD and was used to simulate longer sections of the device. VFDTD was used to confirm the obtained results for shorter simulation lengths. The input field profile and effective index were computed using the algorithm presented in Chapter 3 and then supplied to these numerical simulators. The simulator used is a two-dimensional (2D) one. As discussed earlier, the width of the

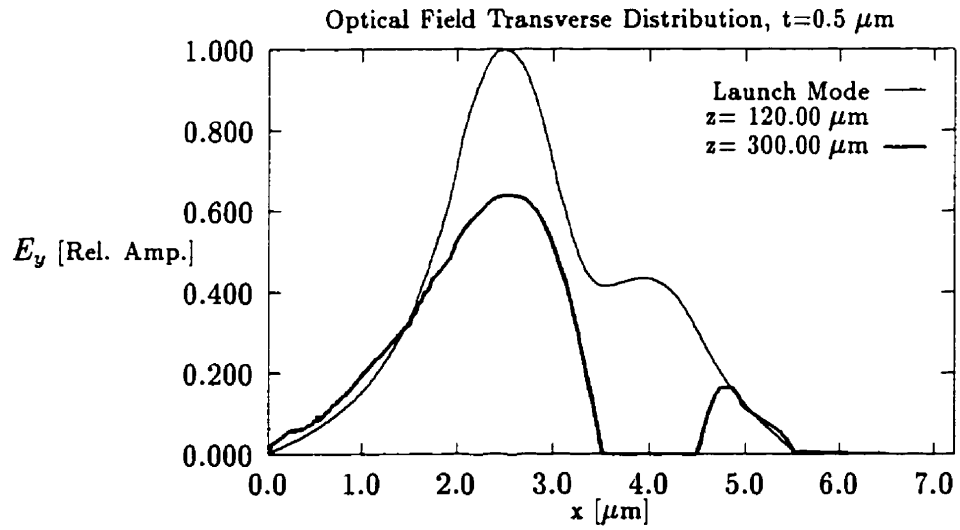

Figure 5.2: The optical field distribution along the transverse direction for the optical system whose parameters are depicted in table 5.2. Here a silicon absorbing layer of width 1 μm and an index 3.6810 -j 6x10^{-3} is assumed. The separation between the guides is 0.5 μm. Optical energy is launched into the lossless (lower) guide.

optical wave-guide in the direction normal to the axial-transverse $(z-x)$ plane is several hundreds of optical wavelengths, and hence a 2D optical simulation is quite adequate. This is dictated by the width of the microstrip line itself, here chosen to be 500 μm wide.

The input field profile and effective index were computed using the algorithm presented in Chapter 3 and then supplied to these numerical simulators. As discussed earlier, the boundary conditions at the edges of the simulation window assimilates that of a metallic conductor. This is actually useful for this study since the optical waveguide system is the substrate of the microstrip line. Hence, the top metalization and the bottom ground plane are conveniently modeled by these boundary conditions. Normally, the simulation window has to be chosen wide enough to minimize the effect of the boundary conditions of the simulation window. Being unconstrained by this condition, the moderate size of the simulation window allows for running simulations that are less computationally expensive.

The simulations assume an incident TE mode, which is less prone to attenuation due

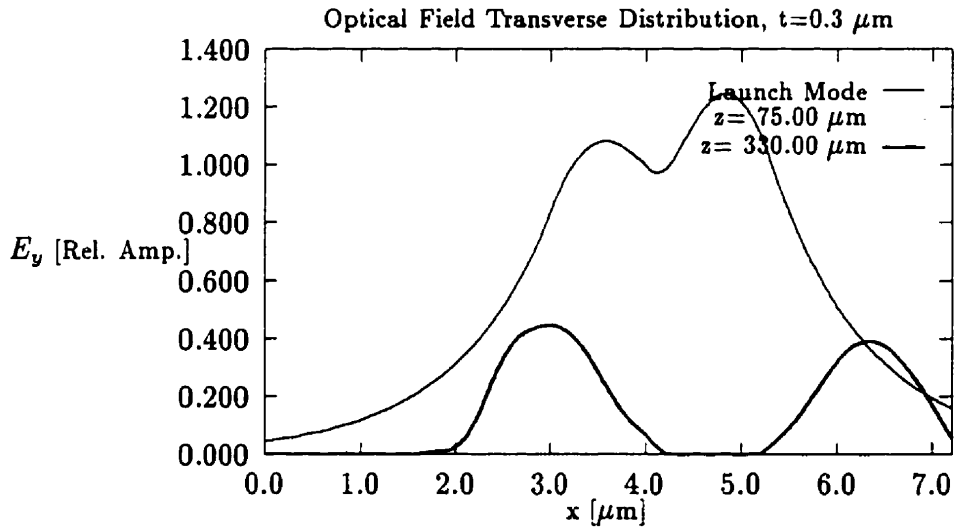

Figure 5.3: The optical field distribution along the transverse direction for the optical system whose parameters are depicted in table 5.2. Here a silicon absorbing layer of width 1 μm and an index 3.6810 -j $6\text{x}10^{-3}$ is assumed. The separation between the guides is 0.3 μm. Optical energy is launched into the lossless (lower) guide.

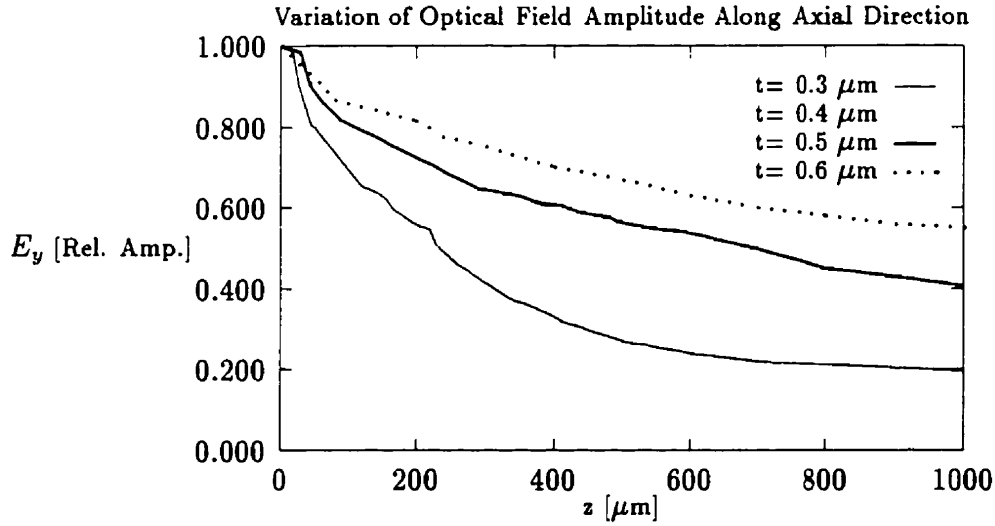

Figure 5.4: The variation of the field amplitudes along the axial direction in the launching guide for the optical system whose parameters are depicted in table 5.2, for different guide separations t.

to proximity with metallic surface [121]. Guides comprising the directional coupler are single mode guides at the optical wavelength of interest.

The optical field distribution along the transverse direction for the case where separation between the guides is 0.5 μm is shown in figure 5.2. All design parameters are shown in table 5.2. Here the optical energy is launched into the lower lossless guide, and is coupled and absorbed gradually in the upper semiconductor guide. The optical field distribution along the transverse direction for the case where separation between the guides is 0.3 μm is shown in figure 5.3.

The objective of the design of the coupling system is to obtain the kind of approximately uniform distribution of photo-generated carriers within the gap as that described in Chapter 3. As explained, the carrier distribution profile is the same as that of the optical energy absorbed. The amount of optical energy coupled into the lossy guide is used to adjust this profile. The width of layer 4 dictates the strength of the coupling between the two guides, which in turn dictates the photo-generated carrier profile in the gap region.

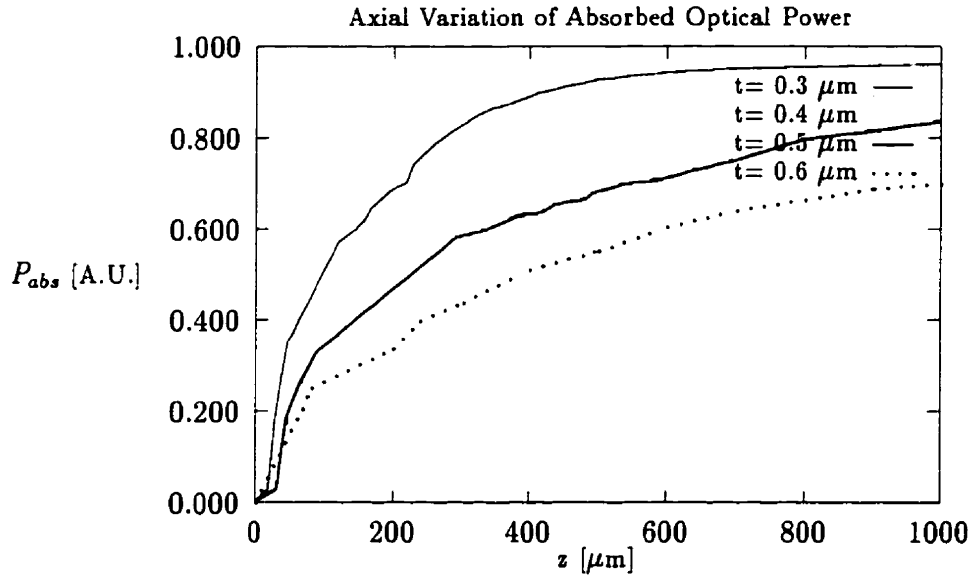

Figure 5.5: The axial variation of the absorbed optical power (relative magnitude) for the optical system whose parameters are depicted in table 5.2, for different guide separations t.

Depending on the gap width, the separation between the guides is adjusted accordingly in order to achieve a coupling length within which the carriers are evenly distributed. A longer gap require a weaker coupling. Simulations for different guide separations t are shown in Figure 5.4. The figure depicts the axial attenuation of the E_y field amplitude in the lossless guide as it propagates along the structure. The amount of optical energy absorbed in shown in Fig.5.5. For a strong coupling, the incident optical energy is mostly absorbed in a relatively short distance. As discussed in chapter 3, this may lead to a high local resistivity at the other end of the gap.

The conductance ΔG of a length Δz along the gap for a variety of gap separations t is shown in Figure 5.6 for the given structure. ΔG is computed using the formulae supplied in Chapter 3. The modeling approach of this thesis does not require the development of an equivalent circuit model with G being the effective gap conductance. ΔG is used here merely as a guideline to design the optimum separation t. The separation t is assumed optimum when the magnitude of ΔG does not drop to less than one half its original

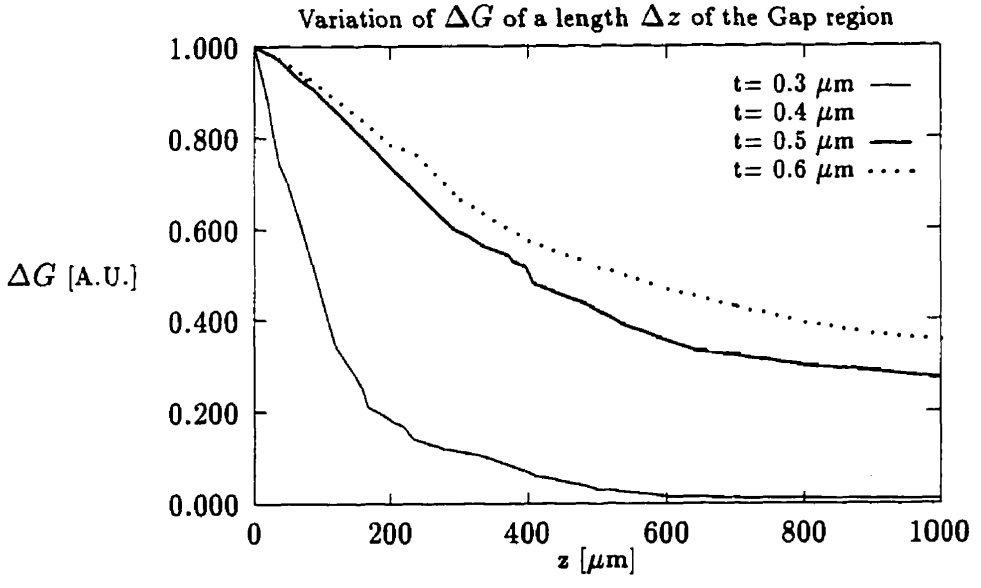

Figure 5.6: The variation of the optically induced conductance ΔG (normalized magnitude) of a length Δz along the axial direction for the optical system whose parameters are depicted in table 5.2, for different guide separations t.

Gap length	Guide separation t
0.10 mm	0.30 μm
0.20 mm	0.40 μm
0.40 mm	0.50 μm
0.50 mm	0.60 μm

Table 5.4: The optimum guide separation t for a given gap length for the proposed structure whose parameters are depicted in table 5.2.

magnitude along the gap length, hence avoiding the situation of a "cold" area at the end of the gap, where the resistivity is high. From the results of Figure 5.6, table 5.4 is drawn up where an optimum separation t is suggested for various gap lengths. The specific gap length is designed depending on the frequency of operation of the switch, as discussed in the following section.

5.5 Microwave Modeling and Switch Characterization

In this section, the frequency response of the device in the microwave frequency range is characterized, and based on this frequency response, a suitable gap length is chosen. The gap length is the only remaining parameter to be defined.

First, the propagation characteristics of the microstrip line is analyzed. The complex propagation constant and the characteristic impedance of the microstrip feed lines are computed using the theory presented in Chapter 4. Figure 5.7 depicts the effective index $n_{eff} = \frac{\beta}{k_o}$ versus resistivity $\rho(\Omega-\text{m})$ at different frequencies for a transmission line of width 500 μm with the multi-layered substrate described in section 5.3. The figure shows the transmission line operating in the slow wave mode at f=0.1 GHz for all conductivity

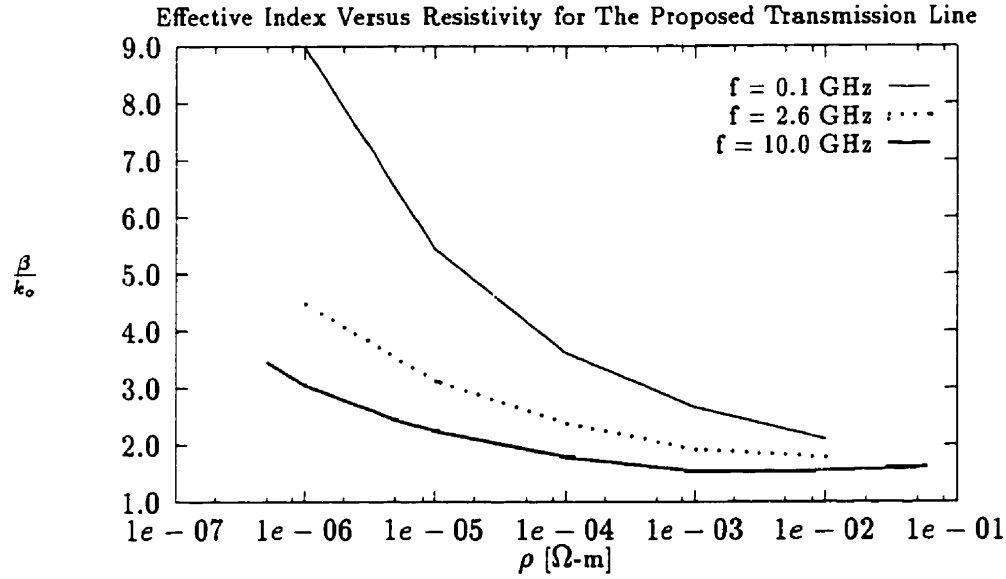

Figure 5.7: The effective index $\frac{\beta}{k_o}$ versus resistivity $\rho(\Omega-m)$ at different frequencies for a transmission line of width 500 μm with the substrate described in section 5.3.

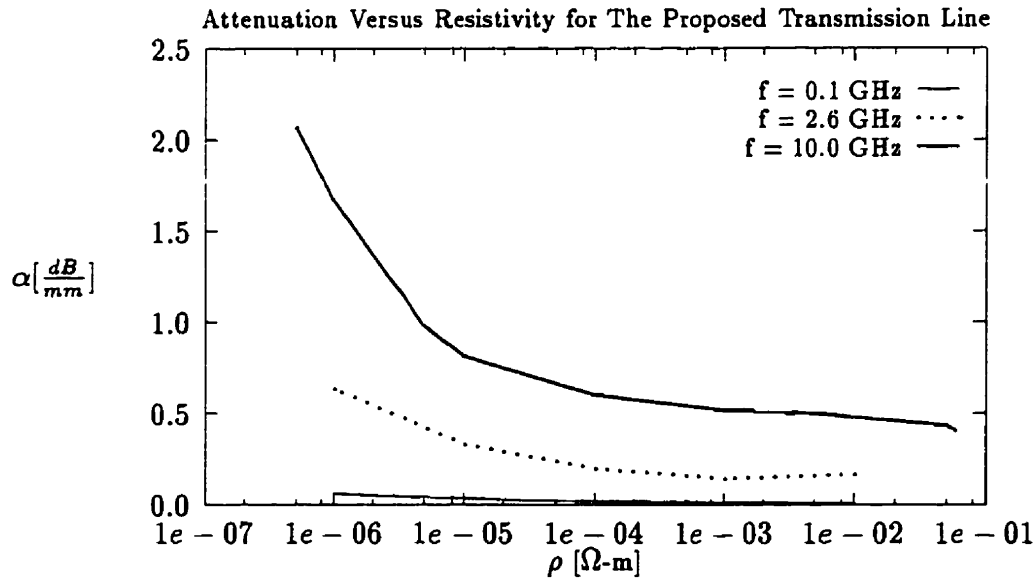

Figure 5.8: The attenuation $\alpha[\frac{dB}{mm}]$ versus ρ for a transmission line of width 500 μm with the substrate described in section 5.3.

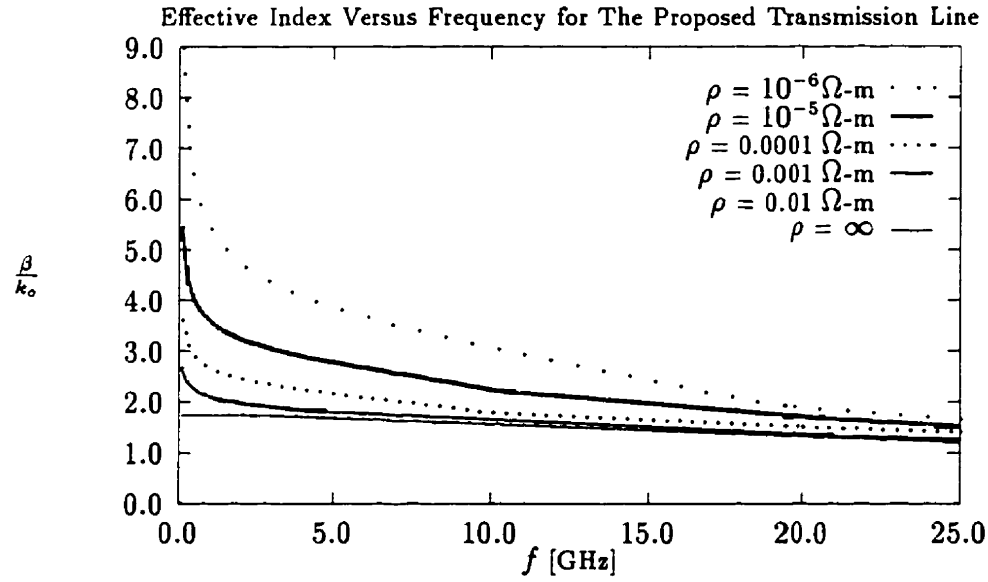

Figure 5.9: The effective index $\frac{\beta}{k_o}$ versus frequency f for a transmission line of width 500 μm with the substrate described in section 5.3.

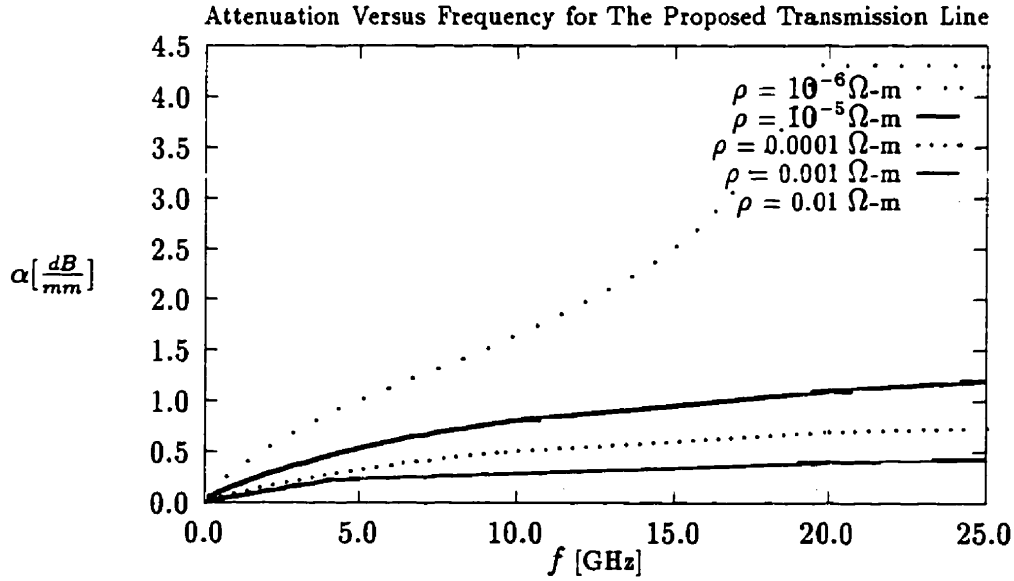

Figure 5.10: Attenuation $\alpha\frac{dB}{mm}$ versus frequency f for a transmission line of width 500 μm with the substrate described in section 5.3.

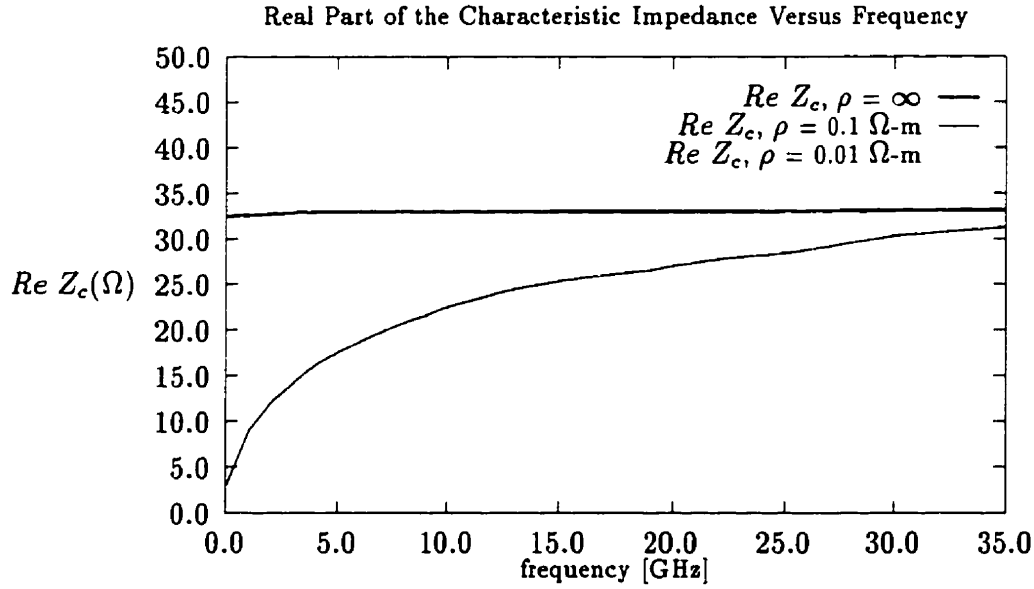

Figure 5.11: The real component of the characteristic Impedance $Re\ Z_c$ [Ω] versus frequency f for a transmission line of width 500 μm with the substrate described in section 5.3.

levels. The slow wave mode is characterized by its high effective index. On the other hand, at ρ = 0.001 Ω-m (i.e. σ = 1000 $\mho$/m), the device operates in the slow-wave mode at 0.1 GHz, in the Quasi-TEM mode at 2.6 GHz, and in the skin-effect mode at 10 GHz as shown. This is in agreement with the calculations tabulated in table 5.3. The corresponding attenuation curves in dB/mm for the same transmission line are depicted in Figure 5.8.

The frequency dependence of the normalized phase constant (effective index) and attenuation are depicted in Figures 5.9 and 5.10 for varied conductivities of the photo-excited regions. The anticipated operating frequency of these devices is at 20 GHz and beyond. At these frequencies, based on the criteria discussed earlier, the device is operating in the skin effect mode for a substrate conductivity σ = 100 $\mho$/m, and higher. Within the portion of the transmission line interacting with the photo-generated carriers, the microwave signal will suffer a loss of about 0.2 dB/mm at 20 GHz, as shown in Figure 5.8.

Figures 5.11 and 5.12 depict the frequency dependence of the real and imaginary com-

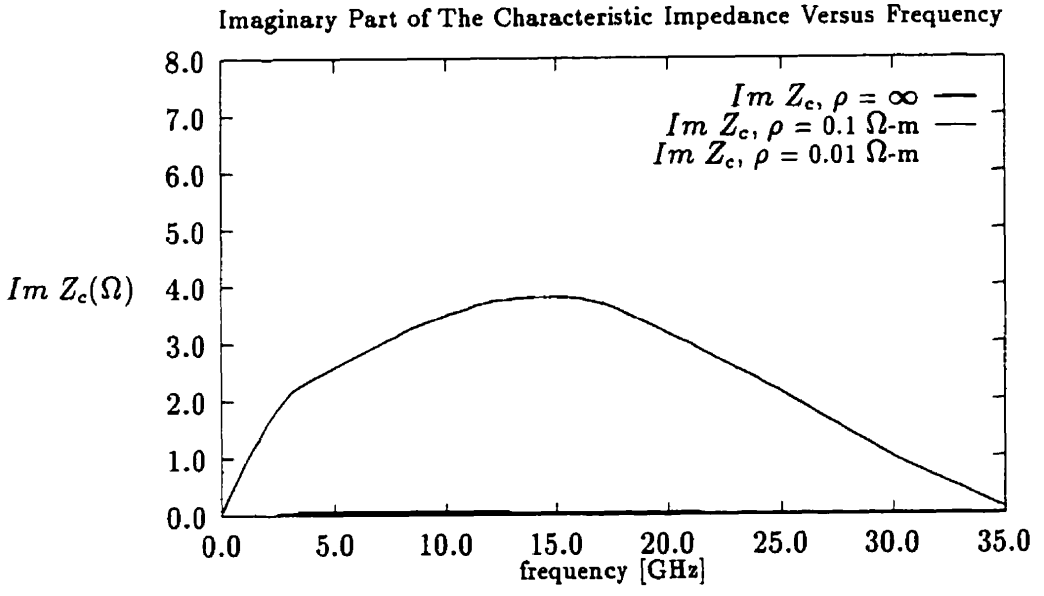

Figure 5.12: The imaginary component of the characteristic Impedance $Im\ Z_c$ [Ω] versus frequency f for a transmission line of width 500 μm with the substrate described in section 5.3.

ponents of the characteristic impedance Z_c [Ω]. The imaginary part of the characteristic impedance corresponds to the loss in the transmission line, and hence drops for higher frequencies.

Figure 5.13 depicts variation of the magnitude of S_{11} with frequency f at different gap lengths varying from 0.0 to 0.5 mm when no optical excitation is applied. $|S_{12}|$ is shown in Figure 5.14. The reference planes are located at a distance of 1 mm from each side of the gap. The gap length should be optimized for a given operating frequency of the switch. At this frequency, the gap is wide enough to yield an almost open circuit condition in the absence of optical excitation. On the other hand, this gap should not be wide enough to require excessive optical excitation for switching.

Consider a switch operating at 20 GHz. At this frequency, the magnitude of S_{12} in the absence of optical excitation is 0.0154 which is sufficiently low to consider the switch practically OFF. At these conditions, almost all the incident microwave signal is reflected. The variation of the scattering matrix parameters with the gap width at $f = 20$ GHz for different conductivity levels were computed, and depicted in Figures 5.15 and 5.16. For the case where $\rho = 0.01$ Ω-m, S_{12} is equal to 0.6366 for a gap length of 0.5 mm. In comparative terms, the extinction ratio (the difference in power levels at the output side of the gap between the ON and OFF states) is 32.3 dB. The output power is 3.9 dBs below the input power. Under these conditions, S_{11} is equal to 0.6729. Hence, the return loss is about 3.4 dBs.

Based on these numbers, a typical switch operating at 20 GHz with a series gap of 0.5 mm width will have the above noted performance characteristics for a photo-induced conductivity of 100 $\mho$/m.

5.6 Assessment of Quasi-TEM modeling Approximations

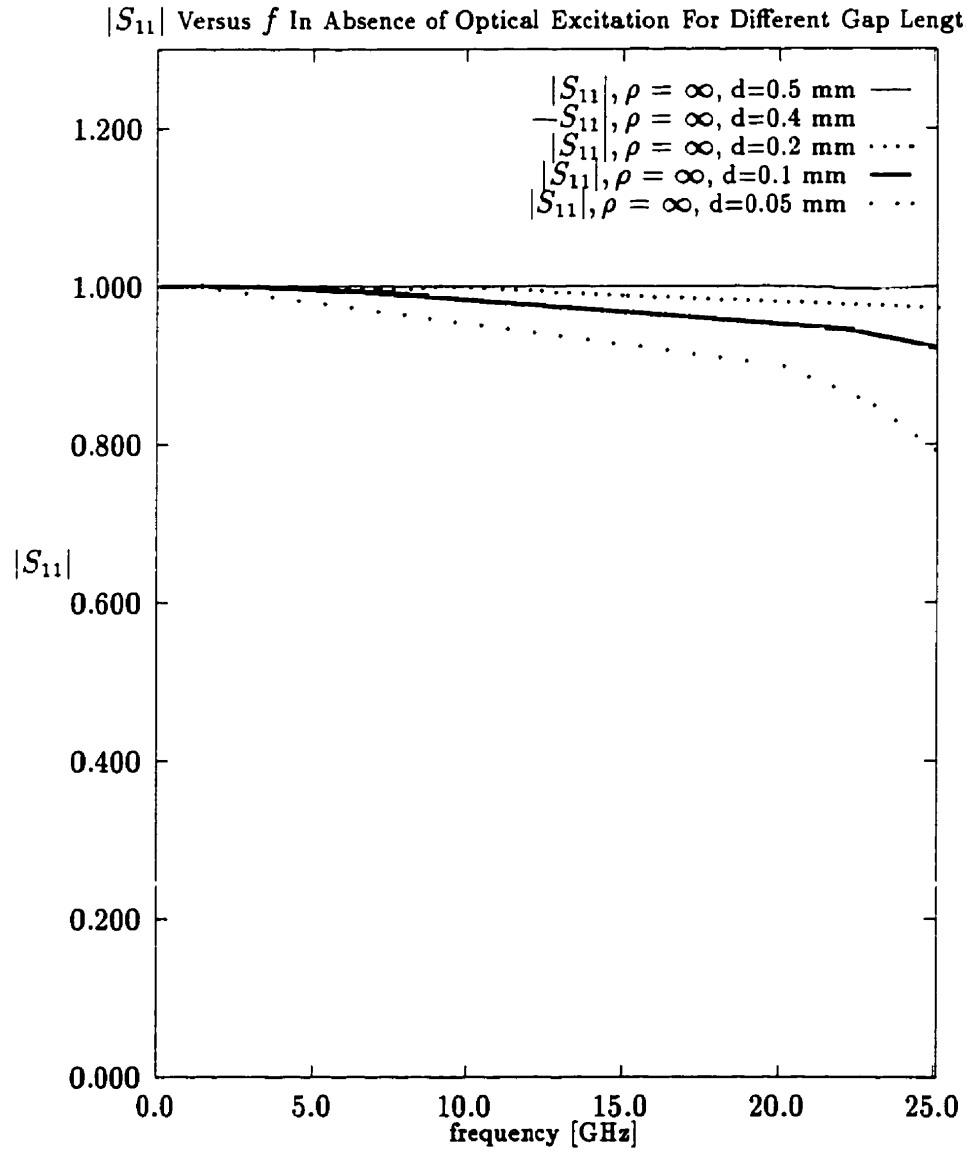

Figure 5.13: The magnitude of the scattering matrix element S_{11} versus frequency f of the proposed device for different gap widths, d.

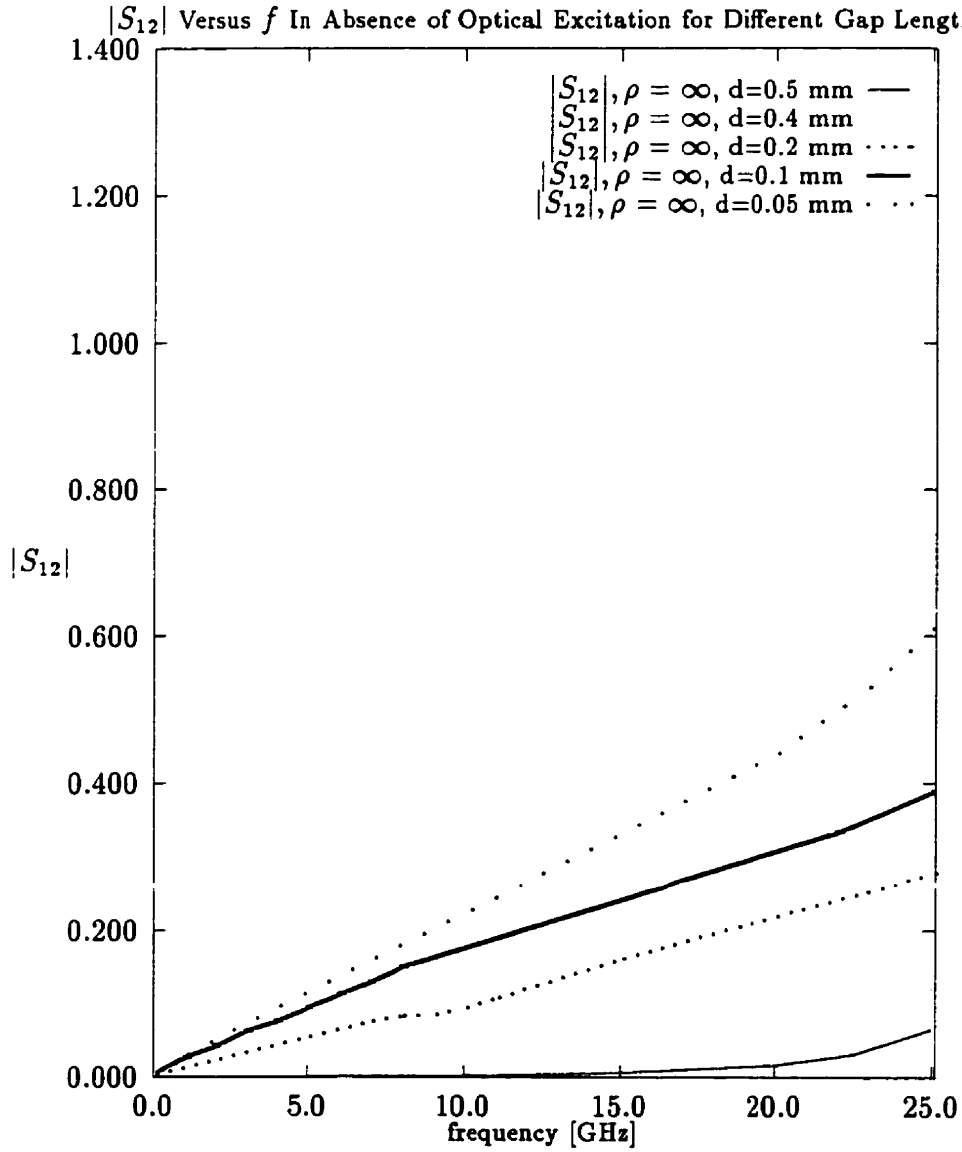

Figure 5.14: The magnitude of the scattering matrix element S_{12} versus frequency f of the proposed device for different gap widths, d.

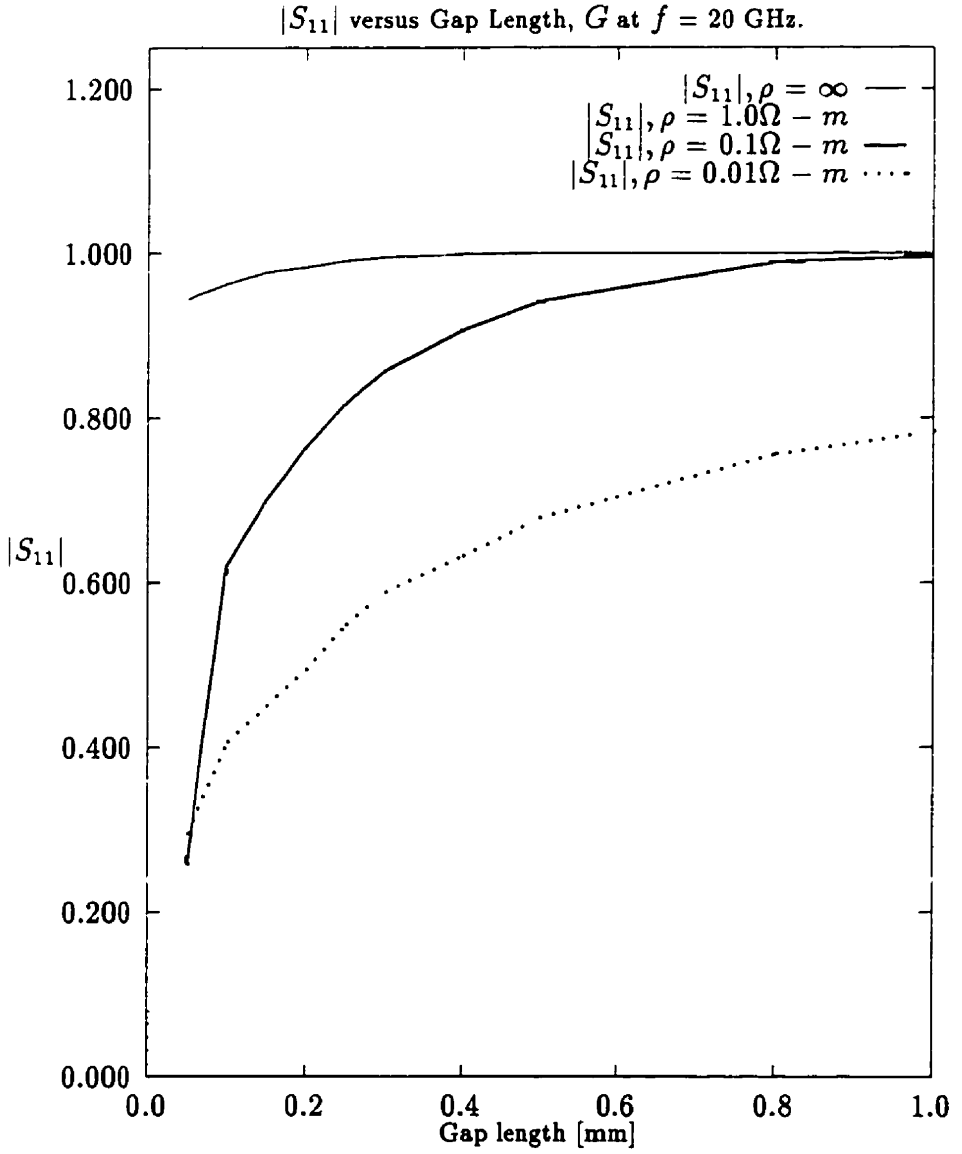

Figure 5.15: The magnitude of the scattering matrix element S_{11} versus gap length, G, [mm]. All parameters are as per table 5.2.

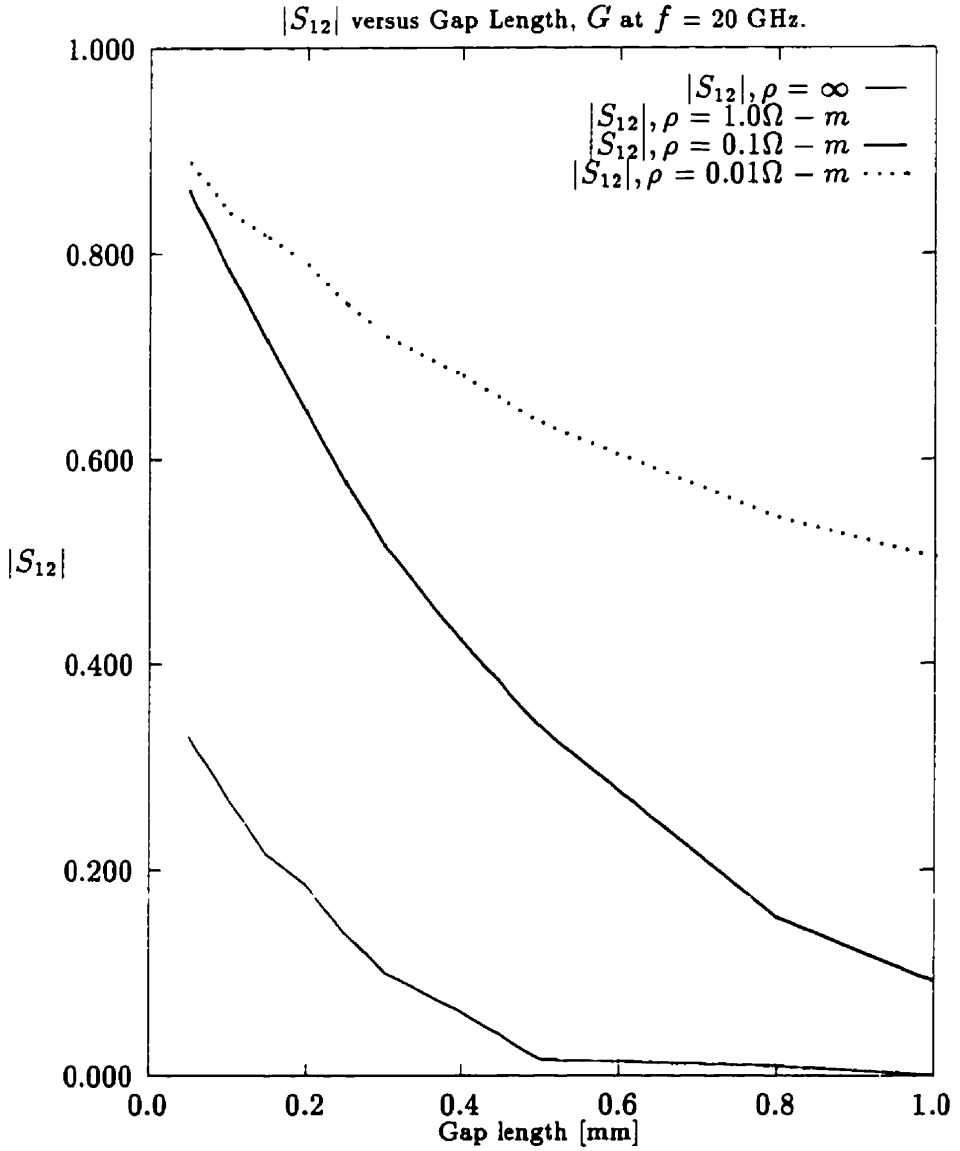

Figure 5.16: The magnitude of the scattering matrix element S_{12} versus gap length, G, [mm]. All parameters are as per table 5.2.

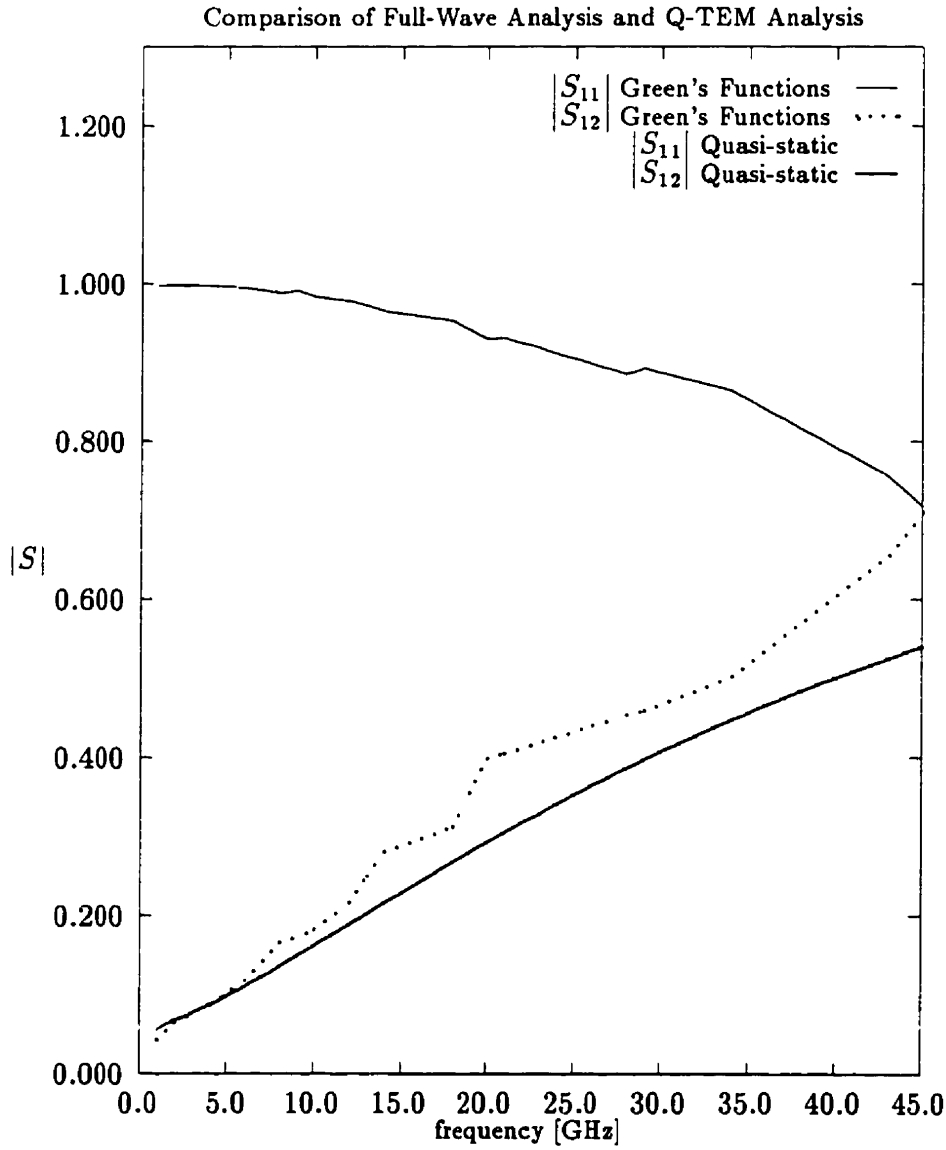

Figure 5.17: The magnitude of the scattering matrix elements, S_{11} and S_{12} of a gap of length 0.1 mm, versus frequency, f, [GHz]. Optical excitation leads to an effective resistivity of 1.2 Ω/m for a depth of 200 μm. Computation is obtained using the quasi-static approach of [104] and the theory developed in Chapter 4. The Green's function numerical computation is conducted using M= 300 and N=300 for a cavity of length c =20 mm, with subsection discretization of P_{max} = 300 and Q_{max} =300.

Quasi-static modeling approximations have been traditionally used in studying free-space optical control of microwaves [23][16] [17] [18] [15] [19] [20] [21]. This approach is valid essentially for low frequency operation of the device. In general, all quasi-TEM approaches are intended for low frequency analysis. Analytical and experimental results such as [23] for example assume a microwave operating frequency of 0.47 GHz. For this reason, a full-wave analysis such as the one developed in Chapter 4 is essential for the accurate modeling of these switches at higher frequencies. The multiple layer substrate feature of this analysis is of particular interest in the analysis of the device proposed in this thesis. Moreover, the operation of the proposed switch in the skin effect mode cannot be studied using a quasi-static model.

Quasi-TEM analysis was used in the former studies coupled with the use of a lumped equivalent circuit representation of the gap whose elements are derived from the quasi-TEM analysis. Chapter 2 described the conditions under which the lumped equivalent circuit model is valid (see section 2.5). The photoexcited region of the series gap in a microstrip line can be modeled by equivalent lumped circuit elements provided that these conditions are met:

1. The operating microwave frequency is such that the microwave skin depth in the semiconductor $\delta = \frac{1}{\sqrt{\omega\mu\sigma}}$ is much bigger than $\frac{1}{\alpha}$ where α is the radiation absorption coefficient of the semiconductor. The quantity $\frac{1}{\alpha}$ represents the depth of the active photoexcited region. In the device proposed herein, this condition is violated as the switch is operated in the skin-effect mode. This condition is valid in the Quasi-TEM mode of operation only, and is therefore tied to the validity of the TEM analysis.

2. The operating microwave signal's wavelength, λ_g, when propagating along the microstrip line must be much bigger than the length and width of the light spot size. This condition is violated for frequencies of operation in excess of $\approx$ 30 GHz, given the gap size of length 1mm.

It follows that equivalent circuit modeling is not an accurate approach for the type of

devices proposed in this thesis nor for the high frequency operation of optically switched microstrip devices in general. In this thesis, a scattering matrix representation of the device performance was utilized. Moreover, the equivalent circuit model is good for modeling the device in the OFF and the very high optical injection ON states only. Moderate excitation levels render the equivalent circuit model inaccurate, as it models the gap with a simple resistance whose magnitude is directly related to incident optical energy.

Quasi-static models and equivalent circuit modeling are only accurate at low frequencies, and for very high optical injection levels. These two conditions ensure that an optically illuminated gap will have a resistance which is much smaller than the shunt capacitive reactance as well as the line characteristic impedance. For moderate optical excitation levels at higher frequencies, effects of these capacitances become significant, and the more accurate frequency-dependent modeling becomes necessary.

The following study was conducted to establish the domain of validity of the quasi-static approximations. Consider a transmission line of width W= 0.5 mm and a silicon substrate of thickness 0.5 mm, with a series gap of width 0.1 mm. These values are typical to those stated in [95] and [23]. Using bulk optical illumination, the gap region is exposed to optical excitation, and light is absorbed in the substrate to an effective depth of $\frac{1}{\alpha}$ = 200 μm, where α is the absorption coefficient of silicon of an incident light with $\lambda \approx 1$ μm. To model this substrate, it is assumed that the substrate is comprised of two layers, one with a relative permittivity ϵ_r=12, resistivity $\rho = 1.2\ \Omega - m$ and a thickness of 0.2 mm, and beneath that, an insulating layer of a relative permittivity ϵ_r=12.

The discontinuity analysis developed in Chapter 4 is compared to the quasi-static approach for modeling the gap reported in [104]. The analysis developed in [104] is utilized to model the gap switching behavior in [95] and [23]. The numerical computation is conducted using M= 300 and N=300 for a cavity of length c =20 mm, with subsection discretization indices P_{max} = 300 and Q_{max} =300. These dimensions and parameters lead to $l_y = l_z$ =0.1 mm. K_y and K_z were chosen to approximately match the propagation constant for the structure [computed in Figure 4.35]. Hence, all convergence criteria were

met. These results are depicted in Figure 5.17. For these plots, the reference planes on both sides of the discontinuity were placed at a distance 1.05 mm from the center of the discontinuity. This is done to obtain the gap-only scattering matrix from the scattering matrix representing the entire transmission line.

The quasi-TEM analysis shows a good agreement with the current Full-wave analysis up to about 10 GHz. At higher frequencies, quasi-TEM analysis becomes less accurate. It is concluded that for the range of frequencies in which the future generation of optically controlled microwave devices is expected to operate, quasi-TEM analysis is not an adequate modeling tool.

5.7 Summary

In this chapter, a detailed design of an integrated optically controlled microstrip switch was conducted. Both the optical and microwave components of the device were considered. The tools presented in chapter 3 were utilized in analyzing the optical guiding system, and the theory developed in chapter 4 was utilized in analyzing the microwave device.

The device was designed in terms of defining the various substrate layers' thicknesses and their refractive indices. The optical guiding system buried in this substrate was designed and analyzed. The microwave transmission line was characterized in terms of its frequency response and the propagation characteristics of the transmission line were computed.

This transmission line analysis was utilized in determining the choice of dimensions of the microwave system to allow for operating the device in the skin-effect mode. This mode helps minimize the optical power requirement to achieve the desired switching.

The discontinuity analysis of the device was used to compute the scattering matrix of the series gap constituting the microwave switch. The size of this gap is designed for a given operating frequency of the switch.

Finally, an assessment of the conventional quasi-TEM modeling technique used in modeling optically controlled microwave switching was conducted and its limitations were pointed out.

Chapter 6

Conclusions and Suggestions for Future Work

6.1 Contribution of This Thesis

This thesis proposed and studied a future generation of optically controlled microwave devices. This future generation uses guided optical wave excitation in an integrated optical-microwave environment.

The building block of these devices is an optically-controlled microwave switch utilizing a microstrip transmission line with a series gap. The optical signal is brought into the gap region using an optical waveguiding system buried in the semiconductor substrate of the microwave transmission line. Photo-generated carriers in the gap region produce a change in the transmission characteristics of the microstrip line.

The bulk of this thesis was dedicated to developing an accurate model of the microwave component of the switch. To model the propagation characteristics and the microwave discontinuity, an analysis that utilizes spatial Green's functions formulations was developed. This analysis is capable of modeling continuous and discontinuous shielded microstrip multi-conductor transmission lines with lossy multi-layer substrates. The formulation

utilized the concepts of the Green's function in the space domain and the principle of scattering superposition to obtain the propagation characteristics. The analysis was kept broad to allow for multi-layered substrates in which one or more of the layers are lossy.

The Green's functions of the enclosing shielding structure along with the boundary condition imposed by the transmission line metalization yield a complex function representing the dispersion equation for the transmission line. This equation was solved using Muller Method to yield the unknown complex propagation constant, the characteristic impedance and the EM field patterns for the microwave signals propagated on the continuous microstrip transmission line. Samples of the results obtained using this method were presented.

Using the method of moments (MOM) coupled with the electric field integral equation (EFIE), another formulation was developed to analyze the discontinuities in the transmission line. The MOM along with the EFIE, yield the current distribution on a transmission line with a certain discontinuity for a given excitation of the system. Using a curve fitting and optimization routine, the essential design and performance parameters are extracted from the current distribution and are used to compute the scattering ([S]) matrix and Impedance ([Z]) matrix of the structure.

The above analyses were developed into computer codes, and were used to conduct accurate modeling of a series gap discontinuity in the microstrip line. This series gap is a model of the microwave switch. The gap transmission behavior was studied for varied substrate conductivity, gap separations, and frequency ranges. The substrate conductivity represents the effect of photo-excitation generated by the optical control element.

The optical component of the proposed devices was also studied. The optical power distribution within the microstrip gap region was accurately modeled using a Vector Beam Propagation Method (VBPM) and a Vector Finite Difference Time Domain (VFDTD) numerical simulators. Means to most effectively use the available optical power were studied. The optical guiding system proposed is an optical directional coupler. An iterative exact solution for the fields and effective index of the propagating optical power within

the structure was presented and utilized in computing the input optical excitation field profile for the noted numerical simulators.

Further, using the developed accurate model, the current approach of modeling optically controlled microwave switches using equivalent circuit models based on quasi-TEM assumptions was assessed and compared to the more accurate Green's function formulation. The domain of validity of these simplified models was defined.

An important contribution of this thesis is that it considered all the design aspects of this device ranging from the optical and microwave aspects of it and spanning semiconductor properties and practical considerations of the fabrication technology to be employed in its fabrication.

6.2 Conclusions

The introduction of guided optical waves as a replacement of bulk optics creates an integrated version of optically controlled microwave devices. This integration advantage has the potential of enhancing the fabrication yield. This also leads to the improvement in the overall performance of the device. Unless an integrated version of these devices is available, the commercialization of these devices is not an easy task. This thesis proposed and studied an integrated optically controlled microwave device.

More complex devices and systems and complicated control mechanisms could be implemented using guided wave optics. Examples of the proposed complex devices were presented. The availability of the optical energy in a guided format enables the design of these complex systems. Bulk optical control is not an adequate approach for controlling a multi-junction device.

Most of the current work in the area utilize microwave devices that are not specifically designed or packaged for optical control. In these devices, the injection efficiency of an optical beam into that part of the device which is most sensitive to light and actually performs the control function is low and usually unspecified. Several reasons could be

given for the low efficiency. First, the air-semiconductor interface constitutes a high refractive index discontinuity, which reflects a sizable portion of the incident light. Second, not all of the coupled energy is utilized effectively, because of metalization overshadowing and uneven distribution of the photo-generated carriers. These issues were addressed in this thesis. The proposed optical directional coupler provides for efficient optical energy coupling and utilization. Uniform optical illumination of the gap is possible through designing the optical directional coupler feeding the microstrip gap with light.

The thesis also presents a model for the guided optical energy conversion into electronic plasma. The plasma distribution in space and its relation to the optical field distribution leads to suggesting specific guiding characteristics and optimized optical field distribution patterns that can be more effective in achieving the control function with less optical power and hence enhancing the device performance. Through guiding of optical energy, profiling of both the optical beam and the resulting plasma distribution is possible, which reduces optical losses, and reduces the optical energy requirement, among other advantages.

This thesis also provided a more accurate and systematic analysis of these devices than the traditional approach. The traditional analysis approach of using quasi-static models are only valid at low frequencies, and for very high optical injection levels. These two conditions require that an optically illuminated gap will have a resistivity which is much smaller than the accompanying shunt capacitances. For moderate optical excitation levels and/or for higher frequencies, effects of these capacitances become significant, and the more accurate frequency-dependent modeling of this thesis becomes necessary.

Further, previous models ignored several important effects such as the depletion layer at the semiconductor interface, and the surface oxide layer. This were included in the current analysis which makes it a more accurate model even for conventional bulk optics devices.

The Quasi-TEM mode of operation by itself is not the optimum mode of operation of these devices. Operating these devices in the skin effect mode leads to a spatially limited microwave signal that can be effectively switched with much less optical power. This

mode of operation was utilized in the design of the simple optically controlled switch of chapter 5.

6.3 Suggestions for Future Work

Within the course of this thesis, an array of complex optical guided-wave controlled systems were presented. These systems, such as the optically controlled logic elements, are based on the microstrip switch studied in this thesis. It is suggested that an accurate analysis of these devices be carried out. The present analysis serves as a complete study of the module used in building these complex devices.

Further, exploring other topologies and layouts of the proposed integrated version of the switch may lead to other enhancements of the device performance. These include comparing different orientations of the optical waveguide with respect to the microstrip line as means of reducing optical losses, and as means of timing the time delay between successive optical excitations at different locations of an optically controlled system. These issues were discussed in chapter 3.

MIS transmission lines can exhibit large changes in the phase constant when subjected to optical excitation. Utilizing this optically induced phase change in an integrated environment may lead to numerous advantages. Transmission characteristics of uniform transmission lines can be efficiently controlled in that manner without resorting to discontinuities in the line. The present study presents an ideal tool for exploring this approach as an alternative to optical guided wave control of microwave signals in discontinuities.

Bibliography

[1] N. K. Das and H. L. Bertoni, *Directions for the Next Generation of MMIC Devices and Systems.* New York, USA: Plenum, 1997.

[2] R. N. Simons, *Optical Control of Microwave Devices.* Boston, MA, USA: Artech House, 1990.

[3] C. Lee, "Picosecond optics and microwave technology," *IEEE Transactions on Microwave Theory and Techniques*, vol. 38, pp. 596–607, 1990.

[4] D. M. Cutrel, J. B. Georges, T. H. Le, and K. Y. Lau, "Dynamic range requirements for analog fiber-optic links in fiber-fed wireless microcells," in *Optical Fiber Conference (OFC'95), San Diego, California*, p. THF1, February 26-March 3,1995.

[5] S. Gopalakrishnan, M. Kimura, H. Shiomi, T. Wakabayashi, M. Funabashi, and K. Ohata, "Optical control of MMIC oscillators and model parameter analysis of an illuminated FET at the Ka- and V- band," in *1995 IEEE MTT-S International Microwave Symposium*, pp. 1287–1290, May 16-20,1995.

[6] J. O'Reilly and P. Lane, "Remote delivery of video services using mm-waves and optics," *IEEE/OSA Journal of Lightwave Technology*, vol. 12, pp. 369–375, 1994.

[7] A. J. Seeds, "Evolution of optics in microwave radars," in *24th European Microwave Conference Workshop Proceedings*, pp. 58–67, 1994.

[8] k. Horikawa, I. Ogawa, and T. Kitoh, "Photonic switched true time delay beam forming network integrated on silica waveguide circuits," in *1995 IEEE MTT-S International Microwave Symposium*, pp. 65–68, May 16-20,1995.

[9] R. Esman, M. Frankel, J. Dexter, L. Goldberg, M. Parent, D. Stilwell, and D. Cooper, "Fiber-optic prism true time-delay antenna feed," *IEEE Photonics Technology Letters*, vol. 5, pp. 1347–1349, Nov. 1993.

[10] D. Auston and M. Nuss, "Electrooptic generation and detection of femtosecond electrical transients," *IEEE Journal of Quantum Electronics*, vol. QE-24, pp. 184–197, 1988.

[11] W. Platte, "Optoelectronic microwave switching," *Proceedings of the Institution of Electrical Engineers, pt. J*, vol. 132, pp. 126–132, 1985.

[12] A. J. Seeds and A. A. A. de Salles, "Optical control of microwave semiconductor devices," *IEEE Transactions on Microwave Theory and Techniques*, vol. 38, pp. 577–585, May 1990.

[13] A. Johnson and D. Auston, "Microwave switching by picosecond photoconductivity," *IEEE Journal of Quantum Electronics*, vol. QE-11, pp. 283–287, 1975.

[14] D. Auston and C. Shank, "Picosecond ellipsometry of transient electron-hole plasmas in germanium," *Phys. Rev. Lett.*, vol. 32, pp. 1120–1123, 1974.

[15] W. Platte, "Optimum gapwidth in light-controlled microstrip modulators," *Electronics Letters*, vol. 12, pp. 189–190, 1976.

[16] W. Platte, "Spectral dependence of microwave power transmission in laser controlled solid-state microstrip switches," *Proceedings of the Institution of Electrical Engineers, pt. I*, vol. 2, pp. 97–103, 1978.

[17] W. Platte, "Optoelectronic generation of short microwave bursts via pulse subtraction," *Arch. Elek. Ubertragung.*, vol. 32, pp. 377–378, 1978.

[18] D. H. Auston and P. R. Smith, "Generation and detection of the millimeter waves by picosecond photoconductivity," *Applied Physics Lettters*, vol. 43, pp. 631–633, 1983.

[19] D. H. Auston, , A. M. Johnson, P. R. Smith, and J. C. Bean, "Picosecond optoelectronic detection, sampling and correlation measurements in amorphous semiconductors," *Applied Physics Lettters*, vol. 37, pp. 371–373, 1980.

[20] P. Schmid and H. Melchior, "High speed optoelectronic sampling with semiconductor-laser pulsed coplanar photoconductor," *Electronics Letters*, vol. 20, pp. 684–687, 1984.

[21] D. E. Cooper and S. C. Moss, "Picosecond measurement of the high-frequency scattering parameters of a GaAs FET," *IEEE Journal of Quantum Electronics*, vol. QE-22, pp. 94–100, 1986.

[22] P. Lefur and D. H. Auston, "A kilovolt picosecond optoelectronic switch and pockels cell," *Applied Physics Lettters*, vol. 28, pp. 21–23, 1977.

[23] W. Platte, "Spectral dependence of microwave power transmission in laser controlled solid-state microstrip switches," *Solid-State and Electron Devices*, vol. 2, pp. 97–103, 1978.

[24] S. M. Sze, *Modern Semiconductor Device Physics.* New York, NY, USA: John Wiley & Sons, 1998.

[25] E. S. Yang, *Microelectronic devices.* New York, NY, USA: McGraw-Hill, 1988.

[26] S. M. Sze, *Physics of Semiconductor Devices.* New York, NY, USA: John Wiley & Sons, 1981.

[27] A. Rose, *Concepts in photoconductivity and allied problems.* New York: Kreiger, 1963.

[28] T. S. Moss, *Optical Properties of Semiconductors.* London, UK: Butterworths Scientific Publications, 1959.

[29] W. Kaiser, *Ultrashort laser pulses and applications.* New York: Springer-Verlag, 1988.

[30] F. E. Doany, D. Grischkowsky, and C. C. Chi in *Digest of the second topical Conference on picosecond electronics and optoelectronics, Optical Society of America, Washington DC*, pp. 127–134, 1987.

[31] C. Erginsoy *Phys. Rev. Lett.*, vol. 79, pp. 1013–1014, 1950.

[32] G. Betts, "Optical link for cellular telephone microcells," in *Optical Fiber Conference (OFC'95), San Diego, California*, p. THF2, February 26-March 3,1995.

[33] R.-P. Braun, G. Grosskopf, H. Heidrich, C. von Helmot, R. Kaiser, K. Krügler, U. *Krü*gler, D. Rohde, F. Schmidt, R. Stenzel, and D. Trommer, "Optical microwave generation and transmission experiments in the 12- and 60-ghz region for wireless communication," *IEEE Transactions on Microwave Theory and Techniques*, vol. MTT-46, pp. 320–330, April 1998.

[34] G. Gustafson and M. Bendett, "GaAs circuits for nonolishic optical controler," *The International Society for Optical Engineers (SPIE) Optoelectronics Signal processing for phased-array Antennas*, vol. SPIE 886, pp. 80–87, 1988.

[35] SPIE, "The international society for optical engineers," in *Optoelectronics Signal processing for phased-array Antennas*, p. SPIE 886, 1988.

[36] SPIE, "The international society for optical engineers," in *Optoelectronics Signal processing for phased-array Antennas II*, p. SPIE 1217, 1990.

[37] L. Fujiang, "Optical control of microwaves and its appplication to phased array antenna systems," *Acta Electronics Sinica*, vol. 21, pp. 38–43, Dec. 1993.

[38] N. Riza, "An optical control system for millimeter wave phase array antennas," *Proceedings of the SPIE - The International Society for Optical Engineering*, vol. 2026, pp. 311–351, Jan. 1993.

[39] W. Ng, D. Yap, A. Narayanan, and A. Walston, "High-prediction detector-switched monolithic GaAs time-delay network for the optical control of phased arrays," *IEEE Photonics Technology Letters*, vol. 6, pp. 231–234, Feb. 1991.

[40] X. Zhou and A. Daryoush, "Analytical and experimental modeling of a push-pull self-oscillating mixer," in *23rd. European Microwave conference Proceedings*, p. 770 vol.1, 1993.

[41] J. Spanos, Z. Rahman, C. Chu, and J. O'Brien, "Control structure interaction in long baseline space interferometers," in *Automatic Control in Aerospace 1992. Selected Papes from the 12th IFAC Symposium*, pp. 163–170, 1993.

[42] R. Ohmoto, H. Ohtsuka, and K. Araki, "Wide dynamic range technologies for fiber-optic microcell radio system," in *Optical Fiber Conference (OFC'95), San Diego, California*, p. THF3, February 26-March 3,1995.

[43] G. Grimes, "Where microwaves and optics meet," *Photonics Spectra*, vol. 23, No.5, pp. 101–110, 1989.

[44] G. Mourou, D. Bloom, and C. Lee, *Picosecond Electronics and optoelectronics.* Springer, Berlin, Heidelberg: Springer-Verlag, 1985.

[45] F. Leonberger, *Picosecond Electronics and optoelectronics II.* Springer, Berlin, Heidelberg: Springer-Verlag, 1984.

[46] D. Auston and K. Eisenthal, *Ultrafast Phenomena IV.* Springer, Berlin, Heidelberg: Springer-Verlag, 1984.

[47] G. Fleming and A.E.Siegman, *Ultrafast Phenomena IV.* Springer, Berlin, Heidelberg: Springer-Verlag, 1984.

[48] S. Shapiro, *Ultrafast light pulses.* Springer, Berlin, Heidelberg: Springer-Verlag, 1977.

[49] W. Kaiser, *Ultrashort Optical pulses.* New York: Springer-Verlag, 1984.

[50] J. Herrmann and B. Wilhelmi, *Lasers for ultrashort light pulses.* Amsterdam, The Netherlands: North-Holland, 1987.

[51] W. Platte, "Pulse shaping by laser-excited solid=state plasmas in silicon," *Electronic Letters*, vol. 12, pp. 631–633, 1976.

[52] G. J. Simonis and K. G. Purchase, "Optical generation and distribution of microwave signals," in *Thirteenth International Conference on Infrared and millimeter Waves, SPIE 1039*, pp. 102–103, 1988.

[53] G. J. Simonis and K. G. Purchase, "Optical generation, distribution, and control of microwaves using laser heterodyne," *IEEE Transactions on Microwave Theory and Techniques*, vol. MTT-38, pp. 667–669, 1990.

[54] R. Castagne, S. Laval, and R. Laval, "Picosecond 1-wavelength optoelectronic gate," *Electronic Letters*, vol. 12, No.17, pp. 438–439, 1976.

[55] Y. Horii, M. Hira, T. Nakagawa, and S. Kurazono, "Optical control of the short-terminatted microstrip filter utilizing current distribution of the standing wave," *IEICE Transactions on Fundamentals of Electronics, Communications and Computer Sciences*, vol. E76-A, pp. 2085–2088, Dec. 1993.

[56] Y. Horii, K. Inata, T. Nakagawa, and S. Kurazono, "Optical control of microstrip band elimination filter utilizing semiconductor plasma," *IEICE Transactions on Fundamentals of Electronics, Communications and Computer Sciences*, vol. E76-A, pp. 2082–2084, Dec. 1993.

[57] S. E. Saddow and C. Lee, "Scattering parameter measurements on an optoelectronic attenuator," in *1994 IEEE Microwave Theory and Techniques Symposium (MTT-s)*

International Microwave Symposium Program, San Diego, California, May 23-27, 1994, pp. TH1D-3, 1994.

[58] G. J. SImonis, R. G. Hay, and K. G. Purchase, "Optical control of microwaves with iii-v semiconductor optical waveguide," *The International Society for Optical Engineers (SPIE) Optoelectronics Signal processing for phased-array Antennas II*, vol. SPIE 1217, pp. 83–91, 1990.

[59] Y. Shen, K. Nichrson, C. Wu, J. Litha, and D. Conn, "Full-wave analysis of optically controlled semiconductor coplanar waveguides," in *IEEE Antennas and Propagation International Symposium*, pp. 838–841, 1993.

[60] P. Cheung, D. P. Neikirt, and T. Itoh, "Optically controlled coplanar waveguide phase shifters," *IEEE Transactions on Microwave Theory and Techniques*, vol. MTT-38, pp. 568–595, 1990.

[61] J. R. Forrest and A. A. de Salles, "Optics control microwaves," *Microwave Syst. News*, pp. 112–122, June 1981.

[62] R. G. Hunsperger, "Optical control of microwave devices," *Integrated Optical Circuit Engineering II*, vol. (SPIE vol.578) S. Sriramm,Ed. Bellingham: SPIE, pp. 40–45, 1985.

[63] Q. Z. Lin and R. I. MacDonald, "Very high isolation optoelectronic switch using Pin-PD and GaAs MESFET transmission gate," in *1994 IEEE Microwave Theory and Techniques Symposium (MTT-s) International Microwave Symposium Program, San Diego, California, May 23-27, 1994*, pp. TH1D-4, 1994.

[64] P. Bhattacharya, "GaAs and InP-Based monolithically integrated transmitters and photorecievers," in *1994 IEEE Microwave Theory and Techniques Symposium (MTT-s) International Microwave Symposium Program, San Diego, California, May 23-27, 1994*, pp. TH2D-1, 1994.

[65] M. Karakucuk, W. Lee, P. Freeman, J. East, G. I. Haddad, and P. Bhatacharya, "Transparent emitter contact hbts for direct optical injection locking of the oscillators," in *1994 IEEE Microwave Theory and Techniques Symposium (MTT-s) International Microwave Symposium Program, San Diego, California, May 23-27, 1994*, pp. TH1D–5, 1994.

[66] J. H. Schaffner and R. R. Hayes, "Velocity-matching in millimeter wave integrated optic modulators with periodic electrodes," *IEEE/OSA Journal of Lightwave Technology*, vol. 12, pp. 503–511, 1994.

[67] V. Hietala, S. H. Kravitz, M. G. Armendariz, G. A. Vawter, and R. F. Carson, "Integrated optically driven millimeter wave sources and recievers," in *1994 IEEE Microwave Theory and Techniques Symposium (MTT-s) International Microwave Symposium Program, San Diego, California, May 23-27, 1994*, pp. TH2D–3, 1994.

[68] K. Matsui, E. Suematsu, T. Takenaka, and H. Ogawa, "An one-chip integrated optical/rf transducer using a hemt opto-microwave mixer and slot antenna," in *1994 IEEE Microwave Theory and Techniques Symposium (MTT-s) International Microwave Symposium Program, San Diego, California, May 23-27, 1994*, pp. TH2D–5, 1994.

[69] H. R. Fetterman, D. P. Prakash, D. Scott, W. Wang, and B. Jalali, "Integrated optically driven millimeter wave sources and recievers," in *1994 IEEE Microwave Theory and Techniques Symposium (MTT-s) International Microwave Symposium Program, San Diego, California, May 23-27, 1994*, pp. TH2D–2, 1994.

[70] A. Petersen, F. Ebskamp, R. Pedersen, and X. Zhang, "Wide-band low noise distributed front-end for multi-gigabit cpfsk receivers," in *1994 IEEE Microwave Theory and Techniques Symposium (MTT-s) International Microwave Symposium Program, San Diego, California, May 23-27, 1994*, pp. TH1D–1, 1994.

[71] C.-G. Shih, D. Barlage, J. Wang, and M. Feng, "Design and fabrication of 5 gb/s fully integrated OEIC receivers using direct ion implanted GaAs MESFET-MSM,"

in *1994 IEEE Microwave Theory and Techniques Symposium (MTT-s) International Microwave Symposium Program, San Diego, California, May 23-27, 1994*, pp. TH1D-2, 1994.

[72] C. Shu, H. Choy, and T. She, "Optical control of polarity in short electrical pulses generated from coplanar waveguide metal-semiconductor-metal photodetectors," *Journal of Applied Physics*, vol. 75, pp. 8228–8230, June 1991.

[73] B. Mishra, V. Pradeep, and P. Chakrabarti, "Microwave characterization of an optically controlled high electron mobility transistor," *Journal of the Institute of Electronics and Telecommunication Engineers*, vol. 39, pp. 361–373, Dec. 1993.

[74] R. N. Simons and K. B. Bhasin, "Microwave performance of AlGaAs/GaAs high electron mobility transistors and GaAs MESFET," in *1987 IEEE MTT-S Int. Microwave Symp. Digest*, pp. 339–371, June 1987.

[75] M. Romero, L. B. Jr., and P. H. Herczfeld, "Internal photovoltaic effect in microwave devices," in *1994 IEEE Microwave Theory and Techniques Symposium (MTT-s) International Microwave Symposium Program, San Diego, California, May 23-27, 1994*, pp. TH2D-5, 1994.

[76] A. Bangert, J. Rosenzweig, M. Ludwig, W. Broner, P. Hoffman, and K. Kohler, "Optical response of pseudomorphic HFET up to 10 GHz," in *1994 IEEE Microwave Theory and Techniques Symposium (MTT-s) International Microwave Symposium Program, San Diego, California, May 23-27, 1994*, pp. TH1D-5, 1994.

[77] R. A. Keihel, "Behavior and dynamics of optically controlled TRAPPAT oscillators," in *IEEE Trans. Electron devices*, pp. ED–25, June 1978.

[78] T. F. Carruthers, *Picosecond optical control of transferred-electron devices in Picosecond optoelectronic Devices C.H. Lee Ed.* New York: Academic Press, 1984.

[79] S. Rossek and C. Free, "Optical control of microwave signals using GaAs FETs," *Electronics and Communication Engineering Journal*, vol. 6, pp. 21–30, Feb. 1991.

[80] A. A. A. DeSalles, "Optical control of GaAs MESFETs," *IEEE Transactions on Microwave Theory and Techniques*, vol. MTT-31, pp. 812–820, Oct. 1983.

[81] R. N. Simons and K. B. Bhasin, "Analysis of optically controlled microwave / millimeter wave device structures," in *1986 IEEE MTT-S Int. Microwave Symp. Digest*, pp. 551–554, June 1986.

[82] B. Biswas, P. Lahiri, D. Mandal, and A. Sinha, "Direct optical control of impatt oscillators," *Indian Journal of Pure and Applied Physics*, vol. 31, pp. 709–717, Oct. 1993.

[83] H. W. Yen, M. K. Barnoski, R. G. Hansperger, and R. T. Melville, "Switching to GaAs IMPATT oscillator by optical illumination," *Applied Physics Lettters*, vol. 31, pp. 120–122, July 1977.

[84] J. R. Forrest and A. J. Seeds, "Optical control of IMPATT microwave oscillators," in *1978 IEEE Int. Electron Device Meeting Tech. Dig.*, pp. 282–258, Dec. 1978.

[85] H. W. A. Gerlach and R. Willman, "The behavior of a pulsed millimeter wave (70 GHz) IMPATT diode oscillator during laser illumination," in *1980 IEEE MTT-S Int. Microwave Symp. Digest*, pp. 70–72, May 1980.

[86] A. Kost, L. West, T. Hasenberg, and J. White, "Optical control of microwaves with semiconductor n-i-p-i structures," *Applied Physics Lettters*, vol. 63, pp. 3191–3196, Dec. 1993.

[87] G. K. Gopalakrishnan, "A broadband low-loss analog fiber-optic link for concurrent detection and down conversion of microwave signals," in *Optical Fiber Conference (OFC'95), San Diego, California*, p. THF5, February 26-March 3,1995.

[88] E. Suematsu and N. Imai, "Signal-to-noise performance of a fiber optic subcarrier link using an hbt optoelectronic upconverter," in *1994 IEEE Microwave Theory and Techniques Symposium (MTT-s) International Microwave Symposium Program, San Diego, California, May 23-27, 1994*, pp. TH2D–4, 1994.

[89] D. H. Auston, "Picosecond optoelectronic gating and switching in silicon," *Applied Physics Lettters*, vol. 26, pp. 101–103, 1975.

[90] R. A. Lawton and A. Scavannec *Electronics Letters*, vol. 11, pp. 74–75, 1975.

[91] W. Platte, "Optoelectronic microwave switching," in *Proceedings of Military Microwave Conference*, pp. 276–286, 1984.

[92] W. Platte, "On the excitation-dependent decay of photo-conductivity in laser-controlled solid-state switches," *Frequenz*, vol. 32, pp. 57–62, 1978.

[93] W. Platte, "Diffusion controlled decay of laser-excited photoconductivity in opto-electronic switches," *Electron. Lett.*, vol. 13, pp. 321–323, 1977.

[94] W. Platte, "Switched optoelectronic microwave load," *IEE Proceedings, Pt I.*, vol. 129, pp. 193–199, 1982.

[95] W. Platte and G. Applehans, "Optoelectronic gating of microwave signals using a silicon microstrip shunt modulator," *Electronics Letters*, vol. 11, pp. 270–271, 1976.

[96] R. A. Lawton and J. R. Andrews *Electronics Letters*, vol. 11, p. 138, 1975.

[97] R. A. Lawton and J. R. Andrews *IEEE Transactions on Intrumentation and Measurements*, vol. 25, pp. 56–60, 1976.

[98] S. Forrest *IEEE/OSA Journal of Lightwave Technology*, vol. LT-3, pp. 347–354, Mar. 1985.

[99] D. H. Auston, P. Lavallard, N. Sol, and D. Kaplan *Applied Physics Lettters*, vol. 35, pp. 66–68, 1980.

[100] D. H. Auston *IEEE Journal of Quantum Electronics*, vol. QE-19, pp. 639–648, 1983.

[101] M. Ketchen, D. Grischkowsky, T. C. Chen, C. C. Chi, N. J. Duling, and N. J. Halas *Applied Physics Lettters*, vol. 48, pp. 751–753, June 1986.

[102] W. J. Gallagher, C. C. Chi, I. Duling, D. Grischkowsky, and N. Halas *Applied Physics Lettters*, vol. 50, pp. 350–351, 1987.

[103] P. R. Smith, D. H. Auston, and W. M. Augustyniak *Applied Physics Lettters*, vol. 41, pp. 739–741, 1981.

[104] M. Maeda, "An analysis of gap in microstrip transmission lines," *IEEE Transactions on Microwave Theory and Techniques*, vol. MTT-20, pp. 390–396, 1972.

[105] P. Benedek and P. Silvester, "Equivalent capacitances for microstrip gaps and steps," *IEEE Transactions on Microwave Theory and Techniques*, vol. MTT-20, pp. 729–733, 1972.

[106] R. Garg and I. J. Bahl, "Microstrip discontinuities," *Int. J. Electronics*, vol. 45, pp. 81–87, 1978.

[107] K. Li, J. R. Whinnery, and A. Dienes, **In** *Picosecond Optoelectronic Devices* **edited by C. H. Lee** . New York: Academic Press, 1987.

[108] G. Haisnan, G. Arjavalingam, A. Dienes, and J. R. Whinnery in *Proc. SPIE Conf. on Picosecond Electro-optics, San Diego*, 1983.

[109] G. A. Mourou and K. E. Meyer *Applied Physics Lettters*, vol. 45, pp. 492-494, 1987.

[110] D. Cooper *Applied Physics Lettters*, vol. 47, pp. 33–35, 1985.

[111] K. W. Goosen and R. B. Hammond *IEEE Transactions on Microwave Theory and Techniques*, vol. MTT-33, pp. 33–35, 1985.

[112] G. A. Mourou, **In** *High Speed Electronics* **edited by B. Kallback and H. Benek-ing** . Springer, Berlin, Heidelberg: Springer Series Electronics and Photonics, Volume22, 1986.

[113] J. A. Buck, K. K. Li, and J. R. Whinnery *Journal of Applied Physiscs*, vol. 51, pp. 769–772, 1980.

[114] W. Margulis and R. Persson *Rev. Sci. Instr.*, vol. 56, pp. 1586–1588, 1986.

[115] C. S. Chang, V. K. Mathur, M. J. Rhee, and C. H. Lee *Applied Physics Lettters*, vol. 41, pp. 392–394, 1982.

[116] R. Landauer *IBM Journal Res. Dev.*, vol. 4, pp. 391–401, 1960.

[117] R. V. Khokhlov *Radio Eng. Electr. Phys. (USSR)*, vol. 6, pp. 817–824, 1961.

[118] P. Paulus, B. Wedding, A. Gasch, and D. Jager *Phys. Lett.*, vol. 102 A, pp. 89–92, 1984.

[119] M. C. Nuss and D. Auston *Phys. Rev. Lett.*, vol. 58, pp. 2355–2356, 1987.

[120] W. Platte and B. Sauerer, "Optically cw-induced losses in semiconductors coplanar waveguides," *IEEE Transactions on Microwave Theory and Techniques*, vol. 37, pp. 139–149, 1989.

[121] E. K. Sharma and M. P. Singh, "Multilayer waveguide devices with absorbing layers: An exact analysis," *Journal of Optical Communications*, vol. 14, pp. 134–137, 1993.

[122] E. K. Sharma and M. P. Singh, "Exact multilayer waveguide design including absorbing or metal layers," *Electronics Letters*, vol. 27, pp. 408–410, 1991.

[123] C. Ma and S. Liu *J. Opt. Soc. Am.*, vol. A 7, pp. 1577–1581, 1993.

[124] S. X. She *Opt. Lett.*, vol. 15, pp. 990–992, 1990.

[125] M. R. Ramadas, E. Garmire, A. K. Ghatak, K. Thyagarajan, and M. R. Shenoy, "Analysis of absorbing and leaky planar waveguides: a novel method," *Opt. Lett.*, vol. 14, pp. 376–378, 1989.

[126] A. K. Ghatak, K. Thyagarajan, M. R. Shenoy, K. Thyagarajan, and M. R. Shenoy, "Numerical analysis of planar optical waveguides using matrix approach," *IEEE/OSA Journal of Lightwave Technology*, vol. LT-5, pp. 660–667, 1987.

[127] A. W. Snyder and J. D. Love, *Optical Waveguide Theory.* London: Chapman and Hell, 1983.

[128] P. N. 1, "Topical meeting on photonics research," in *Monterey, California, USA*, pp. April 6–12, 1991.

[129] W. P. Huang, S. T. Chu, and S. K. Chaudhuri, "A semivectorial finite-difference time-domain method," *IEEE Photonics Technology Letters*, vol. 3, pp. 803–806, 1991.

[130] S. T. Chu and S. K. Chaudhuri, "A finite-difference time-domain method for the design and analysis of guided-wave optical structures," *IEEE/OSA Journal of Lightwave Technology*, vol. 7, pp. 2033–2038, 1991.

[131] S. T. Chu, W. P. Huang, and S. K. Chaudhuri, "Simulation and analysis of waveguide based optical integrated circuits," *Computer Physics Communications*, vol. 68, pp. 451–484, 1991.

[132] D. E. Apnes, S. M. Kelso, R. A. Logan, and R. Bhat, "Optical properties of $Al_xGa_{1-x}As$," *Journal of Applied Physics*, vol. 60, pp. 754–767, 1986.

[133] W. Huang, C. Xu, S. T. Chu, and S. K. Chaudhuri, "The finite-difference vector beam propagation method: Analysis and assessment," *IEEE/OSA Journal of Lightwave Technology*, vol. 10, pp. 295–305, 1992.

[134] W. Huang, C. Xu, S. T. Chu, and S. K. Chaudhuri, "A vector beam propagation method for guided-wave optics," *IEEE Photonics Technology Letters*, vol. 3, pp. 910–913, 1991.

[135] W. Huang, C. Xu, and S. K. Chaudhuri, "A vector beam propagation method based on h fields," *IEEE Photonics Technology Letters*, vol. 3, pp. 1117–1120, 1991.

[136] J. V. Roey, J. V. D. Donk, and P. E. Lagasse, "Beam-propagation method: analysis and assessment," *Proceedings of the Institution of Electrical Engineers, pt. J*, vol. 135, pp. 343–349, 1981.

[137] J. J. Gribble and J. M. Arnold, "Beam propagation method and geometrical optics," *Journal of the Optical Society of America*, vol. 71, pp. 803–809, 1988.

[138] D. Yevick and B. Hermansson, "Efficient beam propagation techniques," *IEEE Journal of Quantum Electronics*, vol. 26, pp. 109–112, 1990.

[139] D. Mirshekar-Syahkal, *Spectral Domain Method for Microwave Integrated Circuits.* Taunton, Somerset, England: John Wiley and Sons Inc., 1990.

[140] J. B. Faria, *Multiconductor Transmission-Line Structures, Modal Analysis Techniques.* New York, NY, USA: John Wiley & Sons Inc., Wiley Series in Microwave and Optical Engineering, 1993.

[141] M. Aikawa, "Microstrip line directional couplers with tight coupling and high directivity," *Electronics and Communication in Japan*, vol. J60-B, pp. 253–258, Apr. 1977.

[142] T. Itoh and W. S. Hebert, "A generalized spectral domain analysis for coupled syspended microstrip lines with tuning septums," *IEEE Transactions on Microwave Theory and Techniques*, vol. MTT-26, pp. 820–826, Oct. 1978.

[143] T. Itoh, "Generalized spectral domain method for multiconductor printed lines and its application to turnable suspended microstrips," *IEEE Transactions on Microwave Theory and Techniques*, vol. MTT-26, pp. 983–987, Dec. 1978.

[144] J.-S. Ko, B.-K. Kim, and K. Lee, "Simple modeling of coplanar waveguide on thick dielectric over lossy substrate," *IEEE Transactions on Electron Devices*, vol. 44, pp. 856–861, 1997.

[145] J. R. Wait, *Electromagnetic waves in stratified media.* New York and Oxford: New York: Institute of Electrical and Electronics Engineers; Oxford:Oxford University Press, c1996., 1996.

[146] A. Bhattacharyya, *Electromagnetic fields in multilayered structures : theory and applications.* Boston, MA, USA: Artech House, 1994.

[147] R. A. Pucel, "Design considerations for monolithic microwave circuits," *IEEE Transactions on Microwave Theory and Techniques*, vol. 29, pp. 513–534, 1981.

[148] R. S. Pengelly, "Hybrib versus monolithic microwave circuits - a matter of cost," *Microwave Syst. News*, pp. 77–114, 1983.

[149] S. Compact, *Compact Software.* New Jersey: Peterson, 07504.

[150] Libra, *EEsof.* CA: Westlake Village, 91362.

[151] IE3D, *Zeland Software, Inc.* CA: Fremont, 94538.

[152] W. J. Getsinger, "Microstrip dispersion model," *IEEE Transactions on Microwave Theory and Techniques*, vol. MTT-21, pp. 34–39, 1973.

[153] G. Kompa and R. Mehran, "Planar waveguide model for calculating microstrip components," *Electron. Lett.*, vol. 11, pp. 459–460, 1975.

[154] H. A. Wheeler, "Transmission line properties of parallel wide strips by conformal mapping approximation," *IEEE Transactions on Microwave Theory and Techniques*, vol. MTT-12, pp. 280–289, 1964.

[155] H. A. Wheeler, "Transmission line parallel strips separated by a dielectric sheet," *IEEE Transactions on Microwave Theory and Techniques*, vol. MTT-13, pp. 172–185, 1965.

[156] E. Chen and S. Y. Chou, "Characteristics of coplanar transmission lines on multilayer substrates: modeling and experiments," *IEEE Transactions on Microwave Theory and Techniques*, vol. MTT-45, pp. 939–945, June 1997.

[157] M. Y. Frankel, R. H. Voelker, and J. N. Hilfiker, "Coplanar transmission lines on thin substrates for high-speed low-loss propagation," *IEEE Transactions on Microwave Theory and Techniques*, vol. MTT-42, pp. 396–402, Mar. 1994.

[158] P. Silvester, "TEM properties of microstrip lines," *Proceedings of the IEEE*, vol. 115, pp. 42–49, 1968.

[159] E. Yamashita and R. Mittra, "Variational method for the analysis of microstrip lines," *IEEE Transactions on Microwave Theory and Techniques*, vol. MTT-16, pp. 251–256, 1968.

[160] T. Sphicopoulos, V. Theodoris, and F. Gardiol, "Dyadic green function for the electromagnetic field in multilayered isotropic media: an operator approach," *Proceedings of the Institution of Electrical Engineers, pt. H*, vol. 132, no.5, pp. 329–334, 1985.

[161] J. Wang, "General method for the computation of radiation in stratified media," *Proceedings of the Institution of Electrical Engineers, pt. H*, vol. 132, no.1, pp. 58–62, 1985.

[162] J. Mosig and T. Sargar, "Comparison of quasi-static and exact electromagnetic fields from a horizontal electric dipole above dielectric above a lossy dielectric backed by an imperfect ground plane," *IEEE Transactions on Microwave Theory and Techniques*, vol. 34, pp. 379–387, 1986.

[163] L. Beyne and D. D. Zutter, "Green's function for layered lossy media with special application to microstrip antennas," *IEEE Transactions on Microwave Theory and Techniques*, vol. 36, pp. 875–881, 1988.

[164] N. K. Das and D. M. Pozar, "A generalized spectral-domain green's function for multilayer dielectric substrates with application to multilayer transmission line," *IEEE Transactions on Microwave Theory and Techniques*, vol. 35, pp. 326–335, 1987.

[165] T. Itoh and W. Menzel, "A full-wave analysis method for open microstrip structures," *IEEE Transactions on Antenna and Propagation*, vol. AP-29, pp. 63–67, 1981.

[166] C. Roudot, C. Terret, and J. P. Daniel, "Fundamental surface-wave effects on microstrip antenna radiation," *Electronics Letters*, vol. 132, pp. 1112–1113, 1985.

[167] J. C. Rautio and R. F. Harrington, "An electromagnetic time-harmonic analysis of shielded microstrip circuits," *IEEE Transactions on Microwave Theory and Techniques*, vol. MTT-35, pp. 726–730, Aug. 1987.

[168] L. P. Dunleavy, *Discontinuity analysis in Shielded Microstrip: A theoretical and experimental study.* University of Michigan: Ph.D. Dissertation, 1988.

[169] T. G. Livernois, *Numerical and Experimental Analysis of Metal - Insulator - Semiconductor Microstrip Structures.* University of Michigan: Ph.D. Dissertation, 1991.

[170] J. Mosig and F. Gardiol, "General integral equation formulation for microstrip antennas and acatterers," *Proceedings of the Institution of Electrical Engineers, pt. H*, vol. 132, no.7, pp. 424–432, 1985.

[171] R. Mittra and T. Itah, "A new technique for the analysis of the dispersion characteristics of microstrip lines," *IEEE Transactions on Microwave Theory and Techniques*, vol. MTT-19, pp. 47–56, 1971.

[172] E. J. Denlinger, "A frequency dependent solution for microstrip transmission lines," *IEEE Transactions on Microwave Theory and Techniques*, vol. MTT-19, pp. 30–39, Jan. 1971.

[173] C. Railton and T. Rozzi, "The rigorous analysis of cascaded step discontinuities in microstrip," *IEEE Transactions on Microwave Theory and Techniques*, vol. MTT-36, pp. 1177–1185, 1988.

[174] W. Wertgen and R. H. Jansen, "Efficient direct and iterative electrodynamic analysis of geometrically complex MIC and MMIC structures," *Int. J. Numer. Modeling*, vol. 2, pp. 153–186, 1989.

[175] A. H. Hamade, A. B. Kouki, and F. M. Ghannouchi, "A cad-suitable approach for the analysis of nonuniform MMIC and MHMIC transmission lines," *IEEE Transactions on Microwave Theory and Techniques*, vol. MTT-44, pp. 1614–1617, Sept. 1996.

[176] M.-S. D. and D. J.B., "An accurate, unified solution to various finline structures," *IEEE Trans. Micrawave Theory Tech.*, vol. MTT-30, pp. 1854–1861, 1982.

[177] M.-S. D. and D. J.B., "Accurate analysis of coupled strip-finline structure," *IEEE Trans. Micrawave Theory Tech.*, vol. MTT-30, pp. 577–579, 1982.

[178] M.-S. D. and J. B., "Analysis of bilateral finline couplers," *Electron. Lett.*, vol. 23, pp. 577–579, 1987.

[179] W. J. R. Hoefer, "Accelerated spectral domain analysis of e-plane circuits suit able for computer aided design," *URSI International Symposium on Electromagnetic Theory*, vol. 2, pp. 495–497, 1986.

[180] T. Itoh and R. Mittra, "Spectral domain approach for calculating dispersion characteristics of microstrip lines," *IEEE Transactions on Microwave Theory and Techniques*, vol. MTT-21, pp. 496–499, 1973.

[181] R. H. Jansen, "Shielded rectangular microstrip disc resonators," *Electron. Lett.*, vol. 10, pp. 299–300, 1974.

[182] R. H. Jansen, "Computer analysis of edge-coupled planar structures," *Electron. Lett.*, vol. 10, pp. 520–522, 1974.

[183] Y. Rahmat-Samii, T. Itoh, and R. Mittra, "A spectral domain analysis for solving microstrip discontinuity problems," *IEEE Transactions on Microwave Theory and Techniques*, vol. MTT-22, pp. 372–378, 1974.

[184] T. Itoh and R. Mittra, "A technique for computing dispersion characteristic impedance of microstrip lines," *IEEE Transactions on Microwave Theory and Techniques*, vol. MTT-22, pp. 896–898, 1974.

[185] J. B. Davies and D. Mirshekar-Syahkal, "Spectral domain solution of arbitrary coplanar transmission line with multilayer substrate," *IEEE Transactions on Microwave Theory and Techniques*, vol. MTT-25, pp. 143–146, 1977.

[186] T. Itoh, "Spectral domain immitance approach for dispersion characteristics of generalized printed transmission lines," *IEEE Transactions on Microwave Theory and Techniques*, vol. MTT-28, pp. 733–736, 1980.

[187] R. W. Jackson and D. M. Pozar, "Full-wave analyis of microstrip open-end and gap discontinuities," *IEEE Transactions on Microwave Theory and Techniques*, vol. MTT-33, pp. 1036–1042, Oct. 1985.

[188] T. Itoh, *Planar Transmission Line Structures.* New York, NY, USA: IEEE Press, 1987.

[189] T. Itoh, *Numerical Techniques for Microwave and Millimeter-Wave Passive Structures.* New York, NY, USA: Wiley Interscience, 1989.

[190] D. A. Mohamed, "A more comprehensive analysis of microstrip gap discontinuity in the spectral domain," *IEEE MTT-S Int. Microwave Symp. Dig.*, vol. 2, pp. 688–691, 1993.

[191] E. Yamashita and K. Atsuki, "Analysis of microstripi-like transmission lines by non-uniform discretization of integral equations," *IEEE Transactions on Microwave Theory and Techniques*, vol. MTT-24, pp. 195–200, Apr. 1976.

[192] J. C. Goswami, A. K. Chan, and C. K. Chui, "Spectral domain analysis of single and coupled microstrip open discontinuities with anisotropic substrates," *IEEE Transactions on Microwave Theory and Techniques*, vol. MTT-44, pp. 1174–1178, July 1996.

[193] C. T. Tai, "Dayadic green's function for a rectangular waveguide filled with two dielectrics," *Journal of Electromagnetic Waves and Applications*, vol. 2, no.3/4, pp. 245–253, 1988.

[194] M. F. Catedra, J. G. Cuevas, and L. Nuno, "A scheme to analyze conducting plates of resonant size using the conjugate-gradient method and the fast fourier transform," *IEEE Transactions on Antenna and Propagation*, vol. 36, pp. 1744–1752, Dec. 1988.

[195] I. Park and R. Mittra, "Numerically effcient analysis of planar microstrips configurations using closed-form Green's functions," *IEEE Transactions on Microwave Theory and Techniques*, vol. MTT-43, pp. 394–400, Feb. 1995.

[196] T. G. Livernois and P. B. Katehi, "A generalized method for deriving the space-doamin green's function in a shielded, multiplayer substarte structure with applications to MIS slow-wave transmission lines," *IEEE Transactions on Microwave Theory and Techniques*, vol. 37, pp. 1761–1767, 1989.

[197] T. G. Livernois and P. B. Katehi, "A simple method for characterizing planar transmission line discontinuities on dissipative substrates," *IEEE Transactions on Microwave Theory and Techniques*, vol. MTT-39, pp. 369–370, 1991.

[198] N. Uzunoglu, C. Capsalis, and C. Chronopoulos, "Frequency dependent analysis of a shielded step discontinuity using an efficient mode-matching technique," *IEEE Transactions on Microwave Theory and Techniques*, vol. MTT-36, pp. 976–984, 1988.

[199] Q. Xu, K. Webb, and R. Mittra, "Study of modal solution procedures for microstrip step discontinuities," *IEEE Transactions on Microwave Theory and Techniques*, vol. MTT-37, pp. 381–387, 1989.

[200] Y. L. Chow, J. J. Yang, D. J. Fang, and G. E. Howard, "A closed-form spatial green's function for the thick microstrip substarte," *IEEE Transactions on Microwave Theory and Techniques*, vol. MTT-39, pp. 588–592, Mar. 1991.

[201] L. Vietzorreck and R. Pregla, "Hybrid analysis of three-dimensional MMIC elements by the method of lines," *IEEE Transactions on Microwave Theory and Techniques*, vol. MTT-44, pp. 2580–2586, 1989.

[202] S. Nam, H. Ling, and T. Itoh, "Time domain method of lines applied to planar guide structures," *IEEE Transactions on Microwave Theory and Techniques*, vol. MTT-37, pp. 897–901, 1989.

[203] Z. Chen and B. Gao, "Full-wave analysis of multiconductor coupled lines in MICs by the method of lines," *Proceedings of the Institution of Electrical Engineers, pt. H*, vol. 136, p. no. 5, Oct. 1989.

[204] N. Georgieva and E. Yamashita, "Time domain vector-potential analysis of transmission-line problems," *IEEE Transactions on Microwave Theory and Techniques*, vol. MTT-46, pp. 404–410, 1998.

[205] N. Georgieva and E. Yamashita, "Finite-difference approach to the solution of time-domain integral equations for layered structures," *IEEE Transactions on Microwave Theory and Techniques*, vol. MTT-45, pp. 984–990, 1997.

[206] D. Sheen, S. Ali, M. Abouzahra, and J. Kong, "Application of the three-dimensional finite-difference imethod to the analysis of planar microstrip circuits," *IEEE Transactions on Microwave Theory and Techniques*, vol. MTT-38, pp. 849–857, 1990.

[207] X. Zhang and K. Mei, "Time-domain finite difference approach to a calculation of the frequency-dependent characteristics of microstrip discontinuities," *IEEE Transactions on Microwave Theory and Techniques*, vol. MTT-36, pp. 1775–1787, 1988.

[208] R. N. Simons, N. I. Dib, and L. P. B. Katehi, "Modeling of coplanar stripline discontinuities," *IEEE Transactions on Microwave Theory and Techniques*, vol. MTT-44, pp. 711–716, May 1996.

[209] D. Bica and B. Beker, "Analysis of microstrip discontinuities using the spatial network method with absorbing boundary conditions," *IEEE Transactions on Microwave Theory and Techniques*, vol. MTT-44, pp. 1157–1161, July 1996.

[210] W. J. R. Hoefer, "The transmission line matrix method-theory and applications," *IEEE Transactions on Microwave Theory and Techniques*, vol. MTT-33, pp. 882–893, 1985.

[211] C. Tzuang and T. Itoh, "Finite element analysis of slow-wave schottky contact printed lines," *IEEE Transactions on Microwave Theory and Techniques*, vol. MTT-34, pp. 1483–1489, Dec. 1986.

[212] G. Hughes and R. White, "MIS and schottky barrier microstrip devices," *Proceedings of the IEEE*, vol. 60, pp. 1460–1461, Dec. 1972.

[213] H. Hasegawa and S. Seki, "Analysis of interconnection delay on very high-speed LSI/VLSI chips using an MIS microstrip line model," *IEEE Transactions on Microwave Theory and Techniques*, vol. MTT-32, pp. 1721–1727, 1984.

[214] S. Sali, "Modeling of resistive and geometrical discontinuities in microstrip interconnections on integrated circuits," *IEE Proceedings*, vol. 137, pp. pt. H., no. 5, 1990.

[215] H. Hasegawa, M. Furukawa, and H. Yanai, "Proporties of microstrip line on Si-Sio$_2$ system," *IEEE Transactions on Microwave Theory and Techniques*, vol. MTT-19, pp. 869–881, 1971.

[216] R. A. Lawton and W. T. Anderson, "Two-layer dielectric microstrip line structures: SiO_2 on si and GaAs on si: Modeling and measurement," *IEEE Transactions on Microwave Theory and Techniques*, vol. MTT-36, 1988.

[217] M. Aubourg, J. Villotte, F. Godon, and Y. Garault, "Finite element analysis of lossy waveguides - application to microstrip lines on lossy substrates," *IEEE Transactions on Microwave Theory and Techniques*, vol. MTT-31, pp. 326–331, 1983.

[218] C. Krowne, "Slow-wave propagation in generalized cylindrical waveguides loaded with a semiconductor," *Int. J. Electron.*, vol. 58, No. 2, pp. 249–269, 1985.

[219] P. Kennis and L. Faucon, "Rigorous analysis of planar MIS transmission line," *Electronics Letters*, vol. 17, No. 13, pp. 454–456, 1981.

[220] L. P. Dunleavy and P. B. Katehi, "Shielding effects in microstrip discontinuities," *IEEE Transactions on Microwave Theory and Techniques*, vol. MTT-36, pp. 1767–1774, 1988.

[221] L. P. Dunleavy and P. B. Katehi, "A generalized method for analysing shielded thin microstrip discontinuities," *IEEE Transactions on Microwave Theory and Techniques*, vol. MTT-36, pp. 1758–1766, 1988.

[222] T. G. Livernois and P. B. Katehi, "Characteristic impedance and electromagnetic field distribution in metal-insulator-semiconductor microstrip," *IEEE Transactions on Microwave Theory and Techniques*, vol. MTT-38, pp. 1740–1743, 1990.

[223] A. Sommerfeld, *Partial differential equations in physiscs.* New York, USA: Academic Press, 1949.

[224] C. Zhu, R. H. Byrd, P. Lu, and J. Nocedal, "L-BFGS-B: FORTRAN subroutine for large-scale bound constrained optimization," *Northwestern Uninersity, Departement of Electrical Engineering and Computer Science technical report*, vol. NAM12, pp. 1–12, October 1996.

[225] T. E. VanDeventer, P. B. Katehi, and A. C. Cangellaris, "An integral equation method for evaluation of conductor and dielectric losses in high frequency interconnects," *IEEE Transactions on Microwave Theory and Techniques*, vol. MTT-37, pp. 1964–1972, 1989.

[226] M. Zambuto, *Semiconductor Devices.* New York, NY, USA: McGraw Hill, 1989.

[227] C. T. Tai, *Dyadic Green's Function in Electromagnetic Theory.* Scranton, PA: Intext, 1971.

[228] M. Yousefi and S. K. Chaudhuri, "Dielectrectic resonator-microstrip interactive circuit analysis and design using integral equation techniques," *IEEE Transactions on Microwave Theory and Techniques*, vol. MTT-43, July 1995.

[229] S. Caorsi and M. Raffetto, "Electromagnetic boundary value problem in the presence of a partly lossy dielectric: Consideration about the uniqueness of the solution," *IEEE Transactions on Microwave Theory and Techniques*, vol. MTT-44, pp. 1511–1513, August 1996.

[230] R. H. Harrington, *Field Computations by moment method.* Malabar, FL, USA: Krieger Publishing Company, 1982.

[231] P. P. Silvester, *Finite Elements for Electronic Engineers.* Cambridge, UK: Cambridge University Press, 1983.

[232] L. W. Johnson and R. D. Riess, *Numerical Analysis, 2nd ed.* Reading, MA, USA: Addison-Wesley, 1982.

[233] Y. R. Kwon, V. M. Hietala, and K. S. Champlin, "Quasi-TEM analysis of slow wave mode of propagation on coplanar microstructure MIS transmission lines," *IEEE Transactions on Microwave Theory and Techniques*, vol. MTT-35, pp. 545–551, 1987.

[234] G. Kowalski and R. Pregla, "Dispersion characteristics of shielded microstrips with finite thickness," *Arch. Elektron. Uebertragungstech*, vol. 25, pp. 193–196, July 1971.

[235] R. Pregla and F. Schmuckle, "The method of lines the analysis of planar waveguide structures with finite metalization thickness," *Kleinheubacher Ber.*, vol. 31, pp. 431–438, July 1988.

[236] M. A. Morich, *Broadband Dispersion Analysis of Coupled Microstrip on anisotrip substrates by perturbation-iteration theory.* Cleveland, OH, USA: MS Thesis, Case Western Reserve University, May 1987.

[237] R. E. Collin, *Field Theory of Guided Waves, Second Edition.* New York, NY, USA: IEEE Press, 1991.

[238] W. P. Harokopus and L. P. B. Katehi, "Electromagnetic coupling and radiation loss considerations in microstrip (M)MIC design," *IEEE Transactions on Microwave Theory and Techniques*, vol. MTT-39, pp. 413–421, March 1991.

[239] P. B. Katehi and N. Alexopoulos, "Microstrip discontinuity modeling for millimetric integrated circuits," *1985 IEEE Microwave Theory and Techniques Symposium (MTT-S) Digest*, vol. 2, pp. 571–573, 1985.

[240] R. H. Jansen, "Hybrid mode analysis of end effects of planar microwave and millimeter-wave transmission lines," *IEEE Preceedings*, vol. 128, pp. 77–86, 1981.

[241] T. Itoh, "Analysis of microstrip resonators," *IEEE Transactions on Microwave Theory and Techniques*, vol. MTT-24, pp. 946–951, 1974.

[242] E. D. P. (Editor), *Handbook of Optical Constants of Solids.* New York: Academic Press Handbook Series, 1985.

[243] E. S. Tony and S. K. Chaudhuri, "Analysis of shielded lossy multi-layered-substrate transmission line," *IEEE Transactions on Microwave Theory and Techniques*, vol. Submitted For Publication, 1999.

[244] E. S. Tony and S. K. Chaudhuri, "Analysis of shielded lossy multi-layered-substrate microstrip discontinuities," *IEEE Transactions on Microwave Theory and Techniques*, vol. Submitted For Publication, 1999.

[245] E. S. Tony and S. K. Chaudhuri, "Effect of depletion layer on the propagation characteristics of MIS transmission lines," *IEEE Transactions on Microwave Theory and Techniques*, vol. Submitted For Publication, 1999.

[246] E. S. Tony and S. K. Chaudhuri, "Optical guided wave control of microwave devices and signals," in *Integrated Photonics research (IPR) Topical Meeting, Boston, Massachusetts, USA*, April 29-May 2 1996.

[247] E. S. Tony and S. K. Chaudhuri, "Electromagnetic modeling of optical guided-wave controlled microstrip circuits," in *Integrated Photonics research Topical Meeting, Boston, Massachusetts, USA*, April 29-May 2 1996.